Advances in Heat Transfer

Edited by
Young I. Cho and George A. Greene

Volume 42

Advances in

HEAT TRANSFER

Volume Editors/Serial Editors

Young I. Cho
Department of Mechanical Engineering and Mechanics
Drexel University
Philadelphia, Pennsylvania

and

George A. Greene
Energy Sciences and Technology
Brookhaven National Laboratory
Upton, New York

Volume 42

ELSEVIER

AMSTERDAM • BOSTON • HEIDELBERG • LONDON
NEW YORK • OXFORD • PARIS • SAN DIEGO
SAN FRANCISCO • SINGAPORE • SYDNEY • TOKYO
Academic Press is an imprint of Elsevier

Academic Press is an imprint of Elsevier
525 B Street, Suite 1900, San Diego, CA 92101-4495, USA
30 Corporate Drive, Suite 400, Burlington, MA 01803, USA
32 Jamestown Road, London NW1 7BY, UK
Radarweg 29, PO Box 211, 1000 AE Amsterdam, The Netherlands

First edition 2010

British Library Cataloguing in Publication Data
A catalogue record for this book is available from the British Library

Library of Congress Cataloging-in-Publication Data
A catalog record for this book is available from the Library of Congress

ISBN: 978-0-12-378645-6
ISSN: 0065-2717

Printed and bound in USA
10 11 12 10 9 8 7 6 5 4 3 2 1

CONTRIBUTORS

Numbers in parentheses indicate the pages on which the author's contributions begin.

Rupak K. Banerjee (137), Department of Mechanical Engineering, University of Cincinnati, Cincinnati, OH, USA; Department of Biomedical Engineering, University of Cincinnati, Cincinnati, OH, USA

Young I. Cho (179), Department of Mechanical Engineering and Mechanics, Drexel University, Philadelphia, PA, USA

Subhashish Dasgupta (137), Department of Mechanical Engineering, University of Cincinnati, Cincinnati, OH, USA

Bakhtier Farouk (1), Department of Mechanical Engineering and Mechanics, Drexel University, Philadelphia, PA, USA

Alexander Fridman (179), Department of Mechanical Engineering and Mechanics, Drexel University, Philadelphia, PA, USA

Zhiheng Lei (1), Department of Mechanical Engineering and Mechanics, Drexel University, Philadelphia, PA, USA

Yiqiang Lin (1), Department of Mechanical Engineering and Mechanics, Drexel University, Philadelphia, PA, USA

Yong Yang (179), Department of Mechanical Engineering and Mechanics, Drexel University, Philadelphia, PA, USA

PREFACE

For more than 40 years, *Advances in Heat Transfer* has filled the information gap between regularly published journals and university-level textbooks. The series presents review articles on topics of current interest, starting from widely understood principles and bringing the reader to the forefront of the topic being addressed. The favorable response by the international scientific and engineering community to the 42 volumes published to date is an indication of the success of our authors in fulfilling this purpose.

In recent years, the editors have published topical volumes dedicated to specific fields of endeavor. Examples of such volumes are Volume 22 (*Bioengineering Heat Transfer*), Volume 28 (*Transport Phenomena in Materials Processing*), Volume 29 (*Heat Transfer in Nuclear Reactor Safety*), and Volume 40 (*Transport Phenomena in Plasma*). The editors intend to continue publishing topical volumes as well as the traditional general volumes in the future. Volume 32, a cumulative author and subject index for the first 32 volumes, has become a valuable tool to search the series for contributions relevant to their current research interests.

The editorial board expresses its appreciation to the contributing authors of Volume 42, who have maintained the high standards associated with *Advances in Heat Transfer*. Finally, the editors would like to acknowledge the efforts of the staff at Academic Press and Elsevier, who have maintained the attractive presentation of the volumes over the years.

Acoustic Wave Induced Flows and Heat Transfer in Gases and Supercritical Fluids

BAKHTIER FAROUK*, YIQIANG LIN, and ZHIHENG LEI

Department of Mechanical Engineering and Mechanics, Drexel University, Philadelphia, PA 19104

I. Introduction

Acoustic waves can be generated in a compressible media by various sources. Usually acoustic waves are generated by mechanical vibrations, such as wall/surface vibration or shaking of a chamber. They can also be created by thermal perturbations, such as rapid heating/cooling, combustion, by special arrangement of heat sources and sinks, and so on. In this chapter, we focus on the acoustic waves in fluids that are induced either by wall/surface vibrations or by the rapid heating of a confining surface, and the associated convection and transport phenomena under different gravity conditions.

It is well known that sound sources may generate an acoustic field in which the particle velocities are not simply sinusoidal, and a pattern of time-independent vortical flows or steady circulations is often found in the body of compressible media. These second-order steady flow patterns are known as acoustic streaming, which always have rotational characteristics. The streaming velocity increases with the sound intensity. Acoustic streaming may be effective in accelerating certain kinds of rate processes and has applications in localized micro-mixing, convective cooling, acoustic compressors, micro-fluidic devices, acoustic levitation, ultrasonic medical diagnostic devices and ultrasonic cleaning of contaminated surfaces. Acoustic streaming also attracted a lot of attention in the past due to its effect on the heat transfer enhancement.

When a confining boundary wall/surface is subjected to rapid temperature increase, the fluid in the immediate vicinity of the boundary gets heated by conduction and tends to expand. The sudden expansion of the fluid due to the energy input, constrained by the inertia of the unperturbed media creates a local pressure disturbance, which then leads to the production of a pressure

* Current address: Department of Mechanical Engineering and Mechanics, Drexel University, Philadelphia, PA 19104.

Advances in Heat Transfer
Volume 42 ISSN 0065-2717
DOI: 10.1016/S0065-2717(10)42001-8

wave. The pressure wave generated from the hot wall impinges on the opposite wall, and is reflected back. The wave repeatedly traverses between the walls, and its amplitude eventually damps out due to the viscous and thermal losses within the fluid and wall boundary [1]. The fluid velocities induced by the acoustic wave may be sufficient to cause a convective heat transfer mode. Consequently, the fluid is heated more rapidly than it would have been by pure conduction. In normal gravity conditions, the velocities generated by the acoustic waves may also affect the development of buoyancy-induced flow, because the velocities in both modes are expected to be of the same order. Hence, the interaction between a thermally induced acoustic wave and gravity creates an interesting problem, particularly at reduced gravity environments.

Previous studies show that though the heat transfer effects of such waves are usually not appreciable under standard conditions, they may be very significant when other modes of convection are weak or absent, such as under zero-gravity conditions, or when the fluid is close to its thermodynamic critical point [2]. Because of the high density and compressibility character of the high-pressure fluid, strong thermally induced acoustic waves can be produced and heat transfer effects of these waves become significant even when the system undergoes a small temperature variation. The thermally induced acoustic waves may also cause unwanted disturbances in static processes like cryogenic storage systems, which involve rather weak diffusive and convective transport of heat, especially in a reduced-gravity environment.

The thermal-acoustic interactions are found in many natural phenomena and industrial applications, such as thermoacoustic refrigerators and engines. All of these and other applications involve mechanically or thermally driven acoustic fields in chambers with various media. A sound wave in a compressible fluid is usually regarded as consisting of coupled pressure and motion oscillations, but temperature oscillations are also present. For instance, when the sound travels in small channels, oscillating heat transfer occurs along the channel walls. For intense sound waves in pressurized gases, the acoustic energy can be harnessed to produce powerful engines, pulsating combustion, heat pumps, refrigerators, and mixture separators.

The interactions between a standing wave and a stack (thin low-conductivity parallel plates) or between a traveling wave and a regenerator (conductive wire-mesh screens) introduces one of the important industrial applications: thermoacoustic engines and refrigerators [3]. A thermoacoustic engine absorbs heat at a high temperature and exhausts heat at a low temperature while producing acoustic power as an output. A thermoacoustic refrigerator works in the opposite way. It absorbs heat at a low temperature, and requires the input of acoustic power to exhaust heat to a high temperature.

In this chapter, the important transport phenomena resulting from mechanically driven acoustic waves and thermally induced acoustic waves under the microgravity and normal gravity conditions are also considered. The fundamental characteristics of these problems are investigated and the results show interesting features. The chapter first focuses on the flow patterns and energy transport in high-intensity sound fields driven by pure mechanical vibrations in gas-filled resonators. Thermally induced pressure waves and associated convective flows for different kinds of fluids under different pressures are considered next. The interactions between flow fields generated by acoustic waves and the buoyancy induced flows in different heating enclosures are studied. Finally, the generation and propagation of thermally induced acoustic waves in supercritical carbon dioxide are considered. Recent results on the generation, propagation and decay of thermally induced acoustic waves in supercritical carbon dioxide are presented.

A. Mechanically Driven Acoustic Waves

Mechanically driven sound waves are sometimes associated with second-order, steady, circulatory fluid motion, viz. acoustic streaming flow structures. Acoustic streaming is a net mean flow generated by sound. Acoustic streaming can be classified on the basis of the different mechanisms by which the streaming is generated [4]. Rayleigh streaming [5] is referred to as "boundary layer driven" streaming inside a standing wave resonator, as the shear viscosity close to a solid boundary is responsible for the induced flow. Rayleigh streaming also describes the mean fluid motion outside the boundary layer, where it is often referred to "outer streaming". Schlichting streaming (also known as "inner streaming") is the mean flow motion inside the boundary layer of a standing wave field. The size of Schlichting streaming vortices is estimated to be $\lambda/4 \times \Delta$. Here, Δ is approximately equal to $1.9\delta_\nu$ where $\delta_\nu = (2\nu/\omega)^{1/2}$ is the viscous penetration depth. Inner and outer streaming can be formed inside a channel where the acoustic wave propagates longitudinally or there is oscillation of solid boundary wall inside the bulk medium. Eckert streaming is driven by dissipation within the fluid volume and is predominant in the high frequency range. This kind of streaming has been used in ultrasonic applications and can be referred to as "bulk dissipation driven" streaming.

Andres and Ingard [6,7] analytically investigated acoustic streaming around a cylinder and discussed the distortion of the streaming flow patterns as a function of sound intensity, under different Reynolds numbers. Lee and Wang [8] studied the effect of compressibility on the streaming pattern. Lee and Wang concluded that compressibility could affect the inner but not the outer streaming flow for the flow between parallel plates, but that for two or

three-dimensional objects, such as a cylinder or a sphere, the compressibility also affects the outer streaming pattern. They used the limiting velocity at the edge of the inner streaming layer as a slip boundary condition to solve for the large outer streaming for the different geometries.

The effect of compressibility on acoustic streaming near a rigid boundary was investigated by Qi [9]. Qi tried to resolve an existing inconsistency: while the compressibility is a necessary condition for the propagation of acoustic waves, previous analyses of acoustic streaming were limited to incompressible fluids. This inconsistent description is due to adapting the incompressible boundary layer solutions obtained by Schlichting to solve acoustic streaming near rigid boundaries. Qi's results showed that the consideration of compressibility leads to a larger streaming velocity outside the boundary layer. The effect was found to be significant in gases, but not in liquids. The study was extended to investigate acoustic streaming in a circular tube [10].

Vainshtein [11] combined the problems of Rayleigh streaming and Couette flow and investigated the effect of streaming on shear flow. Menguy and Gilbert [12] studied nonlinear acoustic streaming in a guide with a perturbation calculation using asymptotic expansions. A noticeable distortion of the acoustic field due to the fluid inertia was demonstrated and a comparison of slow and nonlinear acoustic streaming was presented. Andrade [13] experimentally studied the streaming flows occurring outside the boundary layers in a tube and around cylindrical and spherical obstacles. The outer streaming structures were visualized in air around a cylindrical rod immersed in a standing sound wave. The fluid particles flow towards the cylinder from above and from below, and move away in both directions parallel to the acoustic oscillations (horizontal).

The phenomenon of flow reversal in the circulation occurring in the vicinity of oscillating cylinders was experimentally observed by West [14]. The results of this investigation showed that, as soon as the amplitude of the excited sound wave exceeds a critical value, the direction of the circulation near the cylinder reverses and streaming outside the boundary layer forms. Holtsmark *et al.* [15] studied the vortices in air near a cylindrical rod in a Kundt's tube. The streaming in and outside the boundary layer was observed. The boundary layer streaming structures around a cylinder were visualized by Raney *et al.* [16] in a water-glycerin mixture. Coppens and Sanders [17] measured the acoustic wave in a resonator. They found that the microphone output waveforms become irregular when the sound intensity increases. A similar measurement was carried out by Cruikshank [18]. This kind of non-harmonic wave shape is believed to be the non-linear source of the acoustic streaming.

Trinh and Robey [19] investigated the streaming flows associated with ultrasonic levitators. In this experimental study, the streaming flow field was

caused by an ultrasonic vibrating wall of an enclosure. The circulation induced by the presence of a sample in the enclosure was studied. As initially described by Kempton [20] and Morfey [21], the mixing of several "lumps" of fluid with different temperatures can act as a sound source mainly due to the fact that the physical properties of the medium are not uniform. As another example, a heated surface can maintain large amplitude acoustic oscillations. Kempton [20] analytically examined the role of heat diffusion as an internal noise source. He considered a number of problems: sound induced by unsteady heat transfer from a solid body; fluctuation flow over a hot body, and unsteady heat transfer between gas streams. Morfey [21] analytically examined the radiation of sound from a free turbulent jet. The sound was generated due to thermal dissipation and composition gradient.

Acoustic streaming has received attention as a heat transfer enhancement mechanism. Fand and Kave [22] used photography to study the streaming around a circular cylinder in standing wave tube. The experimental results showed that the streaming around the heated cylinder was much stronger than the isothermal streaming for the same geometry and sound intensity. The mean flow motion due to streaming not only contributes to the convective heat transfer but also promotes the transition to turbulence. Richardson [23] analytically studied the effect of sound on natural convection along a horizontal cylinder which is immersed in sound fields. Later, Richardson [24] presented shadowgraphs for a heated horizontal circular cylinder, subjected to transverse horizontal and vertical sound fields. The shadowgraph demonstrated the local changes in boundary layer thickness and heat transfer coefficient.

Engelbrecht and Pretorius [25] experimentally studied the influence of sound waves on the transition from laminar to turbulent flow in the boundary layer associated with natural convection from a vertical flat plate with uniform heat flux. The transition has been shown to occur at a Grashof number lower than the normally cited value. Gopinath and Mills [26] estimated the convective heat transfer from an isolated sphere in a standing sound field due to acoustic streaming in large streaming Reynolds numbers. The Nusselt number correlations for a wide range of Prandtl numbers were obtained. Later, Gopinath and Mills [27] extended their study to the air-filled tube, modeling an acoustic levitation chamber. The flow was treated as incompressible. Analytical techniques were used along with a commercial numerical solver for the solution of the complete elliptic form of the equations governing the steady transport due to the streaming motion.

Vainshtein *et al*. [28] performed a theoretical analysis on the heat transfer between two horizontal parallel plates in presence of a steady sonic wave propagated in the longitudinal direction. An acoustic Peclet number, which represents the interaction between heat conduction and forced convection,

was introduced, and the mean Nusselt number in terms of the Peclet number was derived. Mozurkewich [29] placed a heated cylindrical wire at a velocity antinode of a standing wave and measured the rate of heat transfer from the wire to the acoustic medium. The Nusselt number showed a distinctive variation with acoustic amplitude. A similar experiment was reported by Gopinath and Harder [30].

Recently Kawahashi and Arakawa [31] numerically studied acoustic streaming induced by finite-amplitude oscillation in a closed duct driven by a piston. The results showed velocity distributions in the oscillatory boundary layer and the change of the streaming profile due to the increase in the amplitude of oscillation, and the existence of a double layer near the duct wall. Kawahashi *et al.* [32] performed experimental studies on the interaction of acoustic streaming with natural convection in a closed rectangular duct, and observed intensified steady streaming. Loh *et al.* [33] investigated the acoustic streaming induced by ultrasonic vibrations in an open space and the associated convection enhancement using both theoretical and numerical methods. Later, Loh and Lee [34] measured the heat transfer enhancement capability of acoustic streaming generated by ultrasonic vibration. The cooling effect was found to have a strong correlation with the gap size between the ultrasonic device and the heat source. The cooling effect was maximized when the gap corresponded to a multiple of the half-wavelength of the ultrasonic wave.

Mozurkewich [35] measured the heat transfer within a cylindrical resonance tube, mediated by acoustic streaming. For an empty resonator with heated wall segment, the radial heat flux varied with position in a manner consistent with the global streaming pattern within the tube. Wan and Kuznetsov [36] numerically studied the fluid flow and heat transfer due to acoustic streaming in the gap between two horizontal beams, the part of the lower of which is vibrating. By utilizing the perturbation method, the compressible Navier-Stokes equations were decomposed into the first-order acoustic equations and second-order streaming equations. A similar problem was experimentally studied by Wan and co-workers [37]. The visualization clearly showed that vertical streaming could be induced by bimorph vibration, which enhanced the heat transfer between the heated surface and surrounding air. Hamilton *et al.* [38] derived an analytic solution for the average mass transport velocity generated by a standing wave which is excited by shaking the system harmonically between parallel plates. In their study, both the streaming structure and streaming velocity were described for various channel widths. They found that the inner vortices increase in size relative to the outer vortices as channel width is reduced, and the outer vortices disappear when the width of channel is less than 5.7. The analysis method was extended to a gas in which heat conduction and

dependence of viscosity on temperature were taken into account [39]. It was revealed that for channel widths 10–20 times the viscous velocity penetration depth, thermal effects may alter the streaming velocity substantially. For significantly wider or narrower channels, thermal effects influence the streaming velocity by only a few percent.

Wang and Kuznetsov [40] analytically solved for the acoustic streaming in a channel bounded by one beam at rest and one beam vibrating at ultrasonic frequency. The flow field was found to be highly dependent on the aspect ratio. The classical theory of acoustic streaming is restricted to slow or linear streaming. It is assumed that in the second-order governing equations, any nonlinear term that involves a second-order quantity is negligible. As a result, the second-order equations are linear in the dependent variables. This is why it usually referred to as linear streaming. The numerical method that directly solves the Navier-Stokes equations provides a new method to overcome this limit.

Yano [41] used an upwind TVD scheme to solve the full Navier-Stokes equation to investigate the turbulent acoustic streaming in a resonator. When $M << 1$ (and hence $\mathrm{Re} >> 1$), shock waves are formed and the gas oscillation attains a quasi-steady state, where the magnitude of the streaming velocity is linearly proportional to the acoustic Mach number. Aktas and Farouk [42] directly solved the compressible Navier-Stokes equations by an FCT scheme. They classified acoustic streaming into classical streaming and irregular streaming. The transfer line between the two streaming patterns was determined by the two following non-dimensional variables: wall vibration amplitude and width of channel. Aktas *et al.* [43] numerically investigated thermal convection in a two-dimensional resonator due to acoustic excitations induced by the vibration of the left side wall. In this case, the left and right walls were held at different temperatures. The mechanically induced periodic oscillations in the fluid were found to have an insignificant effect on the heat transfer characteristics of the system.

B. Thermally Induced Acoustic Waves in Gases

Trilling [1] treated the problem of thermally induced sound fields in a semi-infinite body of a perfect gas, subjected to a step change in temperature at the solid wall. The one-dimensional compressible flow equations were linearized and a closed-form asymptotic solution was obtained using a Laplace transform technique. He also determined how sound intensity depended on wall temperature history by developing analytical solutions.

Larkin was apparently the first to use the numerical method to study the thermally induced fluid motion in a confined medium as a result of step increase in temperature on one wall [44]. In his numerical model,

one-dimensional equations of motion, continuity and energy were considered, while the kinetic energy and dissipation terms were omitted. He used the explicit finite-difference scheme for the motion and energy equations, but an implicit scheme for the continuity equation. The acoustic nature of the fluid motion was observed, but the behavior of pressure oscillation was not completely captured due to high numerical diffusion. The fluid motion was observed to greatly increase the rates of both heat flow and pressure rise. Solutions to the problem of the response of a perfect gas in a slot to a monotonically varying temperature disturbance at the boundaries were developed by Kassoy [45] employing a variety of perturbation methods. Radhwan and Kassoy [46] studied the response of a gas confined between infinite parallel planar walls subjected to significant heat addition. Solutions were developed in terms of asymptotic expansions, valid only when the ratio of acoustic to conduction time scales is small. Numerical studies of one- and two-dimensional thermoacoustic convection in a confined region have been carried out by Ozoe and co-workers [47,48]. The compressible Navier-Stokes equations for a gas with constant viscosity and conductivity and negligible viscous dissipation were non-dimensionalized. Numerical solutions were obtained by employing a first-order upwind scheme. The pressure waves were captured, but it showed effects of substantial numerical diffusion. The effects of various parameters, such as gravity, viscosity, wall temperature, and fluid properties on the development of convection were discussed in their paper.

A simplified model (the hyperbolic equation of conduction) for thermoacoustic motion was compared with the one-dimensional Navier-Stokes equations model of the phenomena, and limitations of the simplified approach were discussed by Brown and Churchill [49]. By using finer discretization, Brown and Churchill's numerical results of one-dimensional compressible Navier-Stroke equations showed that rapid heating of a solid surface bounding a region of gas generates a slightly supersonic wave with positive amplitude in pressure, temperature, density and mass velocity [50]. Huang and Bau [51] solved the linearized equations for thermally induced acoustic waves in a semi-infinite medium, suffering step and gradual changes in the boundary temperature, by using a numerical inverse Laplace transform method. They also solved equations of the nonlinear wave model by using a finite differences scheme modified with a Galerkin finite element interpolation in space. A similar theoretical analysis for thermally induced acoustic waves in a confined medium was repeated more recently by Huang and Bau [52]. Their results illustrated that thermally induced acoustic waves have a characteristic shape consisting of a sharp front and a long tail, which is different from the round symmetric wave shape predicted by the earlier numerical method.

Farouk *et al.* [53] used a control-volume-based flux-corrected transport algorithm to predict the early time behavior of thermally induced acoustic waves in a compressible-fluid filled cavity. In their numerical model, the temperature dependent fluid properties were used. Aktas and Farouk [54] recently studied the effect of gravity on the fluid motion generated by the thermally induced acoustic waves in a rectangular enclosure. The gravitational acceleration was found to have a negligible effect on the behavior of thermal induced acoustic wave for early times. Only a uniformly heated sidewall was considered and the flow development of thermally induced acoustic waves under zero gravity conditions was not studied.

The generation of thermally induced acoustic waves in gases has been studied experimentally by only a few investigators. Parang and Salah-Eddine [55] investigated the thermoacoustic convection phenomena in a cylinder containing air in both normal and reduced gravity environments. In their resulting measurements of air temperature, no oscillations was recorded due to the small oscillation amplitude and low sample rate of measurement, but the air temperatures were found to rise much faster than in the computational results for the case of pure conduction. No pressure measurement was reported.

Experimental measurements of pressure waves generated by rapid heating of a surface were reported by Brown and Churchill [56]. In their experiments, the rapid heating procedure was achieved by an R-C circuit. These pressure measurements in the wall of the closed chamber clearly demonstrated the generation of acoustic waves by rapid heating of a wall.

C. Thermoacoustic Waves in Supercritical Fluids

A fluid is called supercritical, when its temperature and pressure are above its critical temperature and pressure. Supercritical fluids exhibit a number of specific properties, such as large density, high conductivity, high specific heat, low viscosity and low thermal diffusivity, which make them intermediate between gases and liquids. For carbon dioxide, the critical temperature and pressure are 304.13 K and 7.3773 MPa respectively. At the critical point, the thermal conductivity of carbon dioxide achieves its maximum value. At any given pressure, the thermal conductivity also has a pseudo maximum at the corresponding critical temperature. The thermal conductivity in supercritical region, especially near the critical point, is higher than that in the ideal gas region.

The thermal diffusivity D_{T} vanishes near the liquid-vapor critical point. Until recently this fact plus the usual equation of heat conduction

$$\frac{\partial T}{\partial t} = D_T \nabla^2 T \qquad (\mathrm{I}-1)$$

were seen by most researchers as the complete picture for the very slow relaxation times often observed in one-phase critical point experiments. In the one-phase region, these times are of the order of $T \sim L^2/D_T$, where L is the characteristic length of the fluid's container. However Straub and his coworkers [57,58] measured very short temperature equilibration times close to the critical point even when low gravity was used to suppress convection. This and related puzzles led to the realization that the divergence of the fluid's compressibility near its critical point significantly affects thermal equilibration [59–61]. The heat transport in a pure fluid near its critical point is thus strongly enhanced due to the very high compressibility, even though the thermal diffusivity near the critical point tends to zero. Beysens and co-workers [62] carried out quantitative interferometry experiments under microgravity conditions in sample cells filled with supercritical CO_2 at different densities and temperatures around the critical point. They showed two interrelated mechanisms when the fluid was heated: a diffusing thermal boundary layer and fast adiabatic density increase in the bulk fluid via propagation of pressure waves. The border of the expanding thermal layer acts as a piston, and hence the phenomenon has been termed as *the piston effect* [62]. Further details of thermally induced acoustic waves and their characteristics are given in Section VI.

The fundamental process associated with the *piston effect* is due to the propagation of acoustic waves in the near-critical fluid media. It is interesting to note here that acoustic speed of a fluid close to its critical point is not small, even though the compressibility diverges at the critical point. For example, the sound velocity in SF_6 close to its critical point ($T - T_c = 0.01$ K) is 50 m/s [63]. The high compressibility of the near-critical fluids with moderate acoustic speed give rise to the fast heat transport due to the *piston effect*.

Recent experiments in the absence of effects due to gravity, and especially those in the NASA Space Shuttle and the International Space Station have ushered in a new era in our understanding of the property behavior and transport modes in fluids near their critical point. In order to investigate the different aspects of the transport of heat in the absence of gravity [64], performed a thermal cycle close to and around the critical point of CO_2 at critical density. Reduced gravity was provided during a 6-min flight of a sounding rocket (TEXUS 25). A cell was designed which allowed surface and bulk phenomena to be distinguished. The thermal cycle of the experiments in weightlessness started at $T_c + 2.5$ mK where the authors studied the relaxation of the perturbations caused by liftoff in the fluid flow and density and temperature gradients. They also investigated the effect of a quench from $T_c + 2.3$ mK to T_c +v1.3 mK and the expected

mechanism of heat transport by the *piston effect* was experimentally evidenced. In particular, they observed homogeneous thermalization, with a time of thermalization less than a few seconds in a cell with dimensions 10.1 mm (diameter) and 9.025 mm (length). Regarding other related studies abroad the Space Shuttle [65], used a novel, over damped oscillator to measure the viscosity of xenon near its critical density ρ_c and temperature T_c. In microgravity, useful data were obtained within 0.1 mK of T_c corresponding to a reduced temperature $T^* = (T - T_c)/T_c = 3 \times 10^{-7}$. The data directly reveal the expected power law behavior. The same group of researchers [66] reported viscoelastic behavior of xenon when the reduced temperature T^* was less than 10^{-5}.

II. Mathematical Model and Numerical Methods

A. Overview

A sound field is formed by a series of compressions and expansions of a substance, which obey the laws of thermodynamics, heat transfer, and fluid mechanics. It is essentially characterized by the pressure p, corresponding density ρ, temperature T, and velocities. Hence, an accurate mathematical model must be able to describe the compressible behavior of the substance in question. In this study, the compressible form of the Navier-Stokes equations, including the conservation of mass, momentum and energy, along with a state equation, are used as the governing equations.

B. Mathematical Model

1. Conservation Equations in Two-Dimensional Cylindrical Coordinates

In two-dimensional cylindrical coordinates (r, z), these equations can be expressed in the conservative form as

$$\frac{\partial \rho}{\partial t} + \frac{1}{r}\frac{\partial (\rho r u_r)}{\partial r} + \frac{\partial (\rho u_z)}{\partial z} = 0 \qquad \text{(II} - 1\text{)}$$

$$\frac{\partial (\rho u_r)}{\partial t} + \frac{1}{r}\frac{\partial (r\rho u_r^2)}{\partial r} + \frac{\partial (\rho u_r u_z)}{\partial z} = -\frac{\partial p}{\partial r} + \rho f_r + \frac{1}{r}\frac{\partial (r\tau_{rr})}{\partial r} + \frac{\partial \tau_{rz}}{\partial z} - \frac{\tau_{\theta\theta}}{r} \qquad \text{(II} - 2\text{)}$$

$$\frac{\partial (\rho u_z)}{\partial t} + \frac{1}{r}\frac{\partial (r\rho u_r u_z)}{\partial r} + \frac{\partial (\rho u_z^2)}{\partial z} = -\frac{\partial p}{\partial z} + \rho f_z + \frac{1}{r}\frac{\partial (r\tau_{rz})}{\partial r} + \frac{\partial \tau_{zz}}{\partial z} \qquad \text{(II} - 3\text{)}$$

$$\frac{\partial E}{\partial t}+\frac{1}{r}\frac{\partial\left(ru_rE+ru_rp\right)}{\partial r}+\frac{\partial\left(u_zE+u_zp\right)}{\partial z}=\frac{1}{r}\frac{\partial\left(rq_r\right)}{\partial r}+\frac{\partial q_z}{\partial z}+\varphi+\rho\vec{f}\bullet\vec{V} \tag{II-4}$$

Here, E is the total energy, and ϕ is the viscous dissipation rate. The components of stress tensor τ are

$$T_{rr}=\lambda\left[\frac{1}{r}\frac{\partial(ru_r)}{\partial r}+\frac{\partial u_z}{\partial z}\right]+2\mu\frac{\partial u_r}{\partial r} \tag{II-5}$$

$$T_{zz}=\lambda\left[\frac{1}{r}\frac{\partial(ru_r)}{\partial r}+\frac{\partial u_z}{\partial z}\right]+2\mu\frac{\partial u_z}{\partial z} \tag{II-6}$$

$$\tau_{\theta\theta}=\lambda\left[\frac{1}{r}\frac{\partial(ru_r)}{\partial r}+\frac{\partial u_z}{\partial z}\right]+2\mu\frac{u_r}{r} \tag{II-7}$$

$$\tau_{rz}=\tau_{zr}=\mu\left(\frac{\partial u_z}{\partial r}+\frac{\partial u_r}{\partial z}\right) \tag{II-8}$$

where the bulk viscosity $\mu'=\lambda+(2/3)\mu$ is assumed to be negligible and the second coefficient of viscosity λ is set equal to $-(2/3)\mu$ (zero bulk viscosity). The components of the heat flux vector are written as:

$$q_r=-k\frac{\partial T}{\partial r} \tag{II-9}$$

$$q_z=-k\frac{\partial T}{\partial z} \tag{II-10}$$

The viscous dissipation term is given as:

$$\phi=\frac{\partial[(\tau_{rr}u_r+\tau_{rz}u_z)r]}{\partial r}+\frac{\partial[(\tau_{zr}u_r+\tau_{zz}u_z)r]}{\partial z} \tag{II-11}$$

An equation of state for perfect gas is used to relate the temperature to the other thermodynamic characteristics:

$$p=\rho RT \tag{II-12}$$

Here, R is the specific gas constant of the medium. For supercritical carbon dioxide, the p-ρ-T relations are obtained from the NIST Reference Database 12 [67].

The definition of the speed of sound waves in compressible fluid is expressed as

$$c = \sqrt{\frac{c_p}{c_v}\frac{\partial p}{\partial \rho}\bigg|_T} \qquad (II-13)$$

Here c_p and c_v are the specific heats at constant pressure and constant volume, respectively. For an ideal gas, this equation can be expressed as a function of temperature only:

$$c = \sqrt{\frac{c_p}{c_v}RT} \qquad (II-14)$$

The internal energy of ideal gas can be expressed using the following simple equation:

$$i = \frac{P}{\gamma - 1} \qquad (II-15)$$

Here, γ is the ratio of specific heat. For supercritical fluids (Section VI), the internal energy

$i = f(p, \rho)$ and the relations are obtained from the NIST Reference Database 12.

In three-dimensional Cartesian coordinates (x, y, and z), these equations can be expressed in the conservative form as:

$$\frac{\partial \rho}{\partial t} + \frac{\partial(\rho u)}{\partial x} + \frac{\partial(\rho v)}{\partial y} + \frac{\partial(\rho w)}{\partial z} = 0 \qquad (II-16)$$

$$\frac{\partial(\rho u)}{\partial t} + \frac{\partial(\rho uu)}{\partial x} + \frac{\partial(\rho uv)}{\partial y} + \frac{\partial(\rho uw)}{\partial z} = \rho f_x - \frac{\partial p}{\partial x} + \frac{\partial}{\partial x}\left[-\frac{2}{3}\mu\left(\frac{\partial u}{\partial x} + \frac{\partial v}{\partial y} + \frac{\partial w}{\partial z}\right)\right] + \frac{\partial}{\partial x}\left[2\mu\frac{\partial u}{\partial x}\right] + \frac{\partial}{\partial y}\left[\mu\left(\frac{\partial v}{\partial x} + \frac{\partial u}{\partial y}\right)\right] + \frac{\partial}{\partial z}\left[\mu\left(\frac{\partial w}{\partial x} + \frac{\partial u}{\partial z}\right)\right] \qquad (II-17)$$

$$\frac{\partial(\rho v)}{\partial t} + \frac{\partial(\rho uv)}{\partial x} + \frac{\partial(\rho vv)}{\partial y} + \frac{\partial(\rho vw)}{\partial z} = \rho f_y - \frac{\partial p}{\partial y} + \frac{\partial}{\partial y}\left[-\frac{2}{3}\mu\left(\frac{\partial u}{\partial x} + \frac{\partial v}{\partial y} + \frac{\partial w}{\partial z}\right)\right] + \frac{\partial}{\partial x}\left[\mu\left(\frac{\partial u}{\partial y} + \frac{\partial v}{\partial x}\right)\right] + \frac{\partial}{\partial y}\left[2\mu\frac{\partial v}{\partial y}\right] + \frac{\partial}{\partial z}\left[\mu\left(\frac{\partial w}{\partial y} + \frac{\partial v}{\partial z}\right)\right] \qquad (II-18)$$

$$\frac{\partial(\rho w)}{\partial t}+\frac{\partial(\rho u w)}{\partial x}+\frac{\partial(\rho v w)}{\partial y}+\frac{\partial(\rho w w)}{\partial z}=\rho f_z-\frac{\partial p}{\partial z}+\frac{\partial}{\partial z}\left[-\frac{2}{3}\mu\left(\frac{\partial u}{\partial x}+\frac{\partial v}{\partial y}+\frac{\partial w}{\partial z}\right)\right]$$
$$+\frac{\partial}{\partial x}\left[\mu\left(\frac{\partial u}{\partial z}+\frac{\partial w}{\partial x}\right)\right]+\frac{\partial}{\partial y}\left[\mu\left(\frac{\partial v}{\partial z}+\frac{\partial w}{\partial y}\right)\right]+\frac{\partial}{\partial z}\left[2\mu\frac{\partial w}{\partial z}\right] \qquad (\text{II}-19)$$

and considering zero bulk viscosity, $\mu'=\lambda+(2/3)\mu$ and setting $\lambda=-(2/3)\mu$, we get

$$\frac{\partial E}{\partial t}+\frac{\partial(Eu)}{\partial x}+\frac{\partial(Ev)}{\partial y}+\frac{\partial(Ew)}{\partial z}=\rho(f_x u+f_y v+f_z w)-\left[\frac{\partial(pu)}{\partial x}+\frac{\partial(pv)}{\partial y}+\frac{\partial(pw)}{\partial z}\right]$$
$$+\frac{\partial}{\partial x}\left\{2\mu\left[\frac{\partial u}{\partial x}u+\frac{1}{2}\left(\frac{\partial v}{\partial x}+\frac{\partial u}{\partial y}\right)v+\frac{1}{2}\left(\frac{\partial u}{\partial z}+\frac{\partial w}{\partial x}\right)w\right]-\frac{2}{3}\mu\left(\frac{\partial u}{\partial x}+\frac{\partial v}{\partial y}+\frac{\partial w}{\partial z}\right)u\right\}$$
$$+\frac{\partial}{\partial y}\left\{2\mu\left[\frac{1}{2}\left(\frac{\partial v}{\partial x}+\frac{\partial u}{\partial y}\right)u+\frac{\partial v}{\partial y}v+\frac{1}{2}\left(\frac{\partial w}{\partial y}+\frac{\partial v}{\partial z}\right)w\right]-\frac{2}{3}\mu\left(\frac{\partial u}{\partial x}+\frac{\partial v}{\partial y}+\frac{\partial w}{\partial z}\right)v\right\}$$
$$+\frac{\partial}{\partial z}\left\{2\mu\left[\frac{1}{2}\left(\frac{\partial u}{\partial z}+\frac{\partial w}{\partial x}\right)u+\frac{1}{2}\left(\frac{\partial w}{\partial y}+\frac{\partial v}{\partial z}\right)v+\frac{\partial w}{\partial z}w\right]-\frac{2}{3}\mu\left(\frac{\partial u}{\partial x}+\frac{\partial v}{\partial y}+\frac{\partial w}{\partial z}\right)w\right\}$$
$$+\frac{\partial}{\partial x}\left(k\frac{\partial T}{\partial x}\right)+\frac{\partial}{\partial y}\left(k\frac{\partial T}{\partial y}\right)+\frac{\partial}{\partial z}\left(k\frac{\partial T}{\partial z}\right) \qquad (\text{II}-20)$$

Here, E is the total energy and i is the internal energy and u, v, and w are the velocity components in the x, y and z directions respectively:

$$E=i+\frac{1}{2}\rho(u^2+v^2+w^2) \qquad (\text{II}-21)$$

C. Numerical Methods

For the results presented in this chapter, the governing equations (except for the diffusion terms) are discretized using a finite-volume method based on the flux-corrected transport (FCT) algorithm [68]. FCT is a high-order, nonlinear, monotone, conservative and positivity-preserving method designed to solve a general one-dimensional continuity equation with appropriate source terms. This scheme has fourth-order phase accuracy and is able

to resolve step gradients with minimum numerical diffusion. The diffusion terms (the viscous term in the momentum equations and the conduction terms in the energy equation) were discretized using a second-order central difference approach. Time-step splitting was also used to couple all of the representative physical effects.

No-slip boundary conditions were used at all solid walls. In the present computational method, the treatment proposed by Poinsot and Lele [69] was followed for implementing the boundary conditions for the density.

1. Evaluation of Boundary Conditions

A high-order non-dissipative algorithm such as FCT requires rigorous formulation of boundary conditions [70]. Otherwise, numerical solutions may show spurious wave reflections at the regions close to boundaries and nonphysical oscillations arising from instabilities. In the present computational method, the treatment proposed by Poinsot and Lele [69] was followed for implementing the boundary conditions for density. This method based on the theory of wave characteristics, avoids incorrect extrapolations and overspecified boundary conditions.

Along any solid wall, the density is calculated from

$$\left(\frac{\partial \rho}{\partial t}\right)_w + \frac{1}{c_w}\left(\frac{\partial p}{\partial n} + \rho c \frac{\partial u_n}{\partial n}\right)_w = 0 \qquad (\text{II} - 22)$$

where the subscript w signifies the location of the wall, and n is the direction normal to the wall.

Following the procedure described by Poinsot and Lele, the density along a vibrating wall (for ideal gases) is calculated by

$$\frac{\partial \rho}{\partial t} = \frac{\rho\gamma}{c_w}\frac{\partial u_w}{\partial t} + \frac{\rho\gamma(u_w - c_w)}{c_w}\frac{\partial u}{\partial x} - \frac{\gamma(u_w - c_w)}{c_w^2}\frac{\partial p}{\partial x} \qquad (\text{II} - 23)$$

III. Mechanically Driven Acoustic Waves in Gas-Filled Enclosures

A. Overview

Interaction of acoustic waves in compressible fluids and solid boundaries creates challenging problems. It is a well-known fact that sound sources may generate a flow field in which the particle velocities are not simply sinusoidal and a pattern of time-independent vortical flows or steady circulations is

often found in the body of compressible media [71]. Sound at high intensity levels in gases and liquids is accompanied by these second order steady flow patterns known as "acoustic streaming". These steady flows always have rotational character and their velocity increases with the sound intensity. However, even at the high intensity levels, the secondary streaming velocity magnitude remains smaller than the primary oscillatory particle velocity magnitude.

While various analytical models are available for describing acoustic streaming phenomena, they are usually based on substantial approximations and the solutions are often limited to idealized conditions. The study of acoustic streaming started with the theoretical work of Lord Rayleigh [72]. He considered vortex flows occurring in a long pipe (Kundt's tube) because of the presence of a longitudinal standing wave. Westervelt [73] obtained a general vorticity equation and developed a general procedure for evaluating the streaming velocity induced by acoustical disturbances that can be specified in a first-order manner by a wave equation—linear in the field variables. The treatment presented in the above study was not applicable to problems where the wave amplitudes are large and the field values cannot be described by a linear wave equation because of the fact that no first-order specification of the field exists. The vorticity equation was thus subject to the restrictions: solenoidal first order motion and irrotational first order motion. Andres and Ingard investigated low [7] and high Reynolds number acoustic streaming analytically and discussed the distortion of the streaming flow patterns as a function of sound intensity. Nyborg reviewed the theories for calculating steady streaming associated with sound fields. He worked out two illustrative problems, both for rectilinear flow due to irrotational sound fields: the first deals with a single attenuated plane wave traveling down a tube and the second one deals with a pair of crossed plane waves. An approximate solution was also developed by Nyborg [74] for sonically-induced steady flow near a fluid-solid interface subjected to the condition of known irrotational oscillatory velocity distribution in the vicinity of the interface. The previously developed theoretical approaches are based on successive approximations to solutions of nonlinear hydrodynamic equations, where the first and second order solutions in each approximation must satisfy the boundary conditions.

B. Flows in an Acoustically Driven Rectangular Enclosure

A rigorous method for predicting acoustically excited flow fields in a resonator is described in this section [75]. A perfectly sinusoidal primary standing wave field in the domain of interest is assumed and the investigation is started from this point. The study [75] is specifically concerned with

the modeling of the actual physical processes, i.e. the formation of the sound field and streaming processes in the resonator. No pre-defined sound field in the computational domain is assumed for the simulation of acoustic streaming. Instead, we directly compute and fully describe the formation of the acoustic field in the domain. A rectangular enclosure filled with a compressible fluid is considered. The left wall of the enclosure is modeled as a rigid boundary, which vibrates harmonically in time representing the motion of a loudspeaker diaphragm or vibration of a commercial ultrasonic mixer probe. The vibrating boundary is the acoustic source in this geometry and sound field in the enclosure is created by this source. We are able to model the physical processes including the compression of the fluid and the generation of the wave, acoustic boundary layer development and finally the interaction of wave field with viscous effects and formation of streaming structures. We consider five different enclosure heights with various wall displacement values for the geometries considered in this study. This present model is a flexible tool that can analyze acoustic streaming in various geometries, and with different fluids. The results of the current study will also be a good reference and starting point for more advanced studies involving heat transfer analysis in acoustically induced flow fields with streaming.

The pressure amplitude in the enclosure (see Fig. 1) is determined by adjusting the maximum displacement of the wall (X_{MAX}). The calculations were started with the vibration of the left wall at $x = 0$ and with uniform values of pressure (101,325 Pa), temperature (300 K) and density (1.138 kg/m^3) within the quiescent medium. For the duration of each cycle of the vibration of the wall, about 25,000 time steps were used for the explicit numerical scheme described earlier.

The cases considered [75] are summarized in Table I. The dimensionless channel width (y_0/δ_ν), the maximum displacement of the left wall (X_{MAX}), and the aspect ratio of the enclosure ($H/L = 2y_0/L$) are included in Table I for each case.

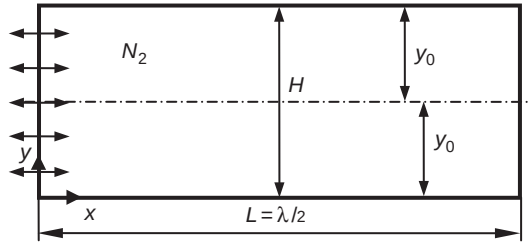

FIG. 1. Schematic of the problem [75].

TABLE I
SUMMARY OF CASES CONSIDERED FOR ACOUSTIC STREAMING ANALYSIS [75]

Case	y_0/δ_ν	X_{MAX} (μm)	H/L
A	10	10	0.0358
B-1	20	10	0.0716
B-2	20	3	0.0716
C-1	30	10	0.1074
C-2	30	2	0.1074
C-3	30	1	0.1074
D-1	40	10	0.1432
D-2	40	0.5	0.1432
E-1	50	10	0.1790
E-2	50	0.5	0.1790
E-3	50	0.2	0.1790

In the first case considered (Case-A), the enclosure half-width is the smallest ($y_0/\delta_\nu = 10$) and the maximum displacement of the wall was set to $X_{MAX} = 10\,\mu m$. Figures 2(a) and (b) show the pressure and velocity distributions respectively along the symmetry axis ($y = y_o$) of the enclosure at $\omega t = 0$, $\pi/2$, π, $3\pi/2$ for Case A (during cycle # 100). Pressure distribution for $\omega t = 2\pi$ (not shown here) is identical to the curve given for $\omega t = 0$. Perfectly sinusoidal profile of the emitted wave by the oscillating wall is distorted due to viscous and nonlinear effects. At $\omega t = 0$ and $\omega t = \pi$, the amplitude of the pressure waves reach a maximum value in the enclosure. At the beginning of the cycle ($\omega t = 0$), the pressure is maximum on the vibrating wall of the enclosure and decreases with distance from the wall and reaches a minimum at the opposite wall ($x = L$). In the middle of the cycle ($\omega t = \pi$) the pressure profile is symmetric respect to vertical mid-plane ($x = L/2$) to the profile given for $\omega t = 0$ and reaches a maximum at the right wall.

The pressure profiles given for different time levels intersect at approximately $x = L/2$ and creates a pressure node. Corresponding u-velocity profile for this case is given in Fig. 2 (b). Unlike the pressure field, velocity maximums and minimums are observed at $\omega t = \pi/2$ and $\omega t = 3\pi/2$. The left wall is stationary at $\omega t = \pi/2$ and $\omega t = 3\pi/2$. The primary oscillatory flow is periodic and the maximum value of the velocity is predicted to be approximately 12 m/s. Due to attenuation caused by viscous and nonlinear effects, both pressure and velocity profiles slightly differ from a perfect sinusoidal wave field.

Predicted secondary flow field for Case-A is shown in Fig. 3 for the enclosure. This flow field is based on the average mass transport velocity values in the enclosure. The average mass transport velocity was given by

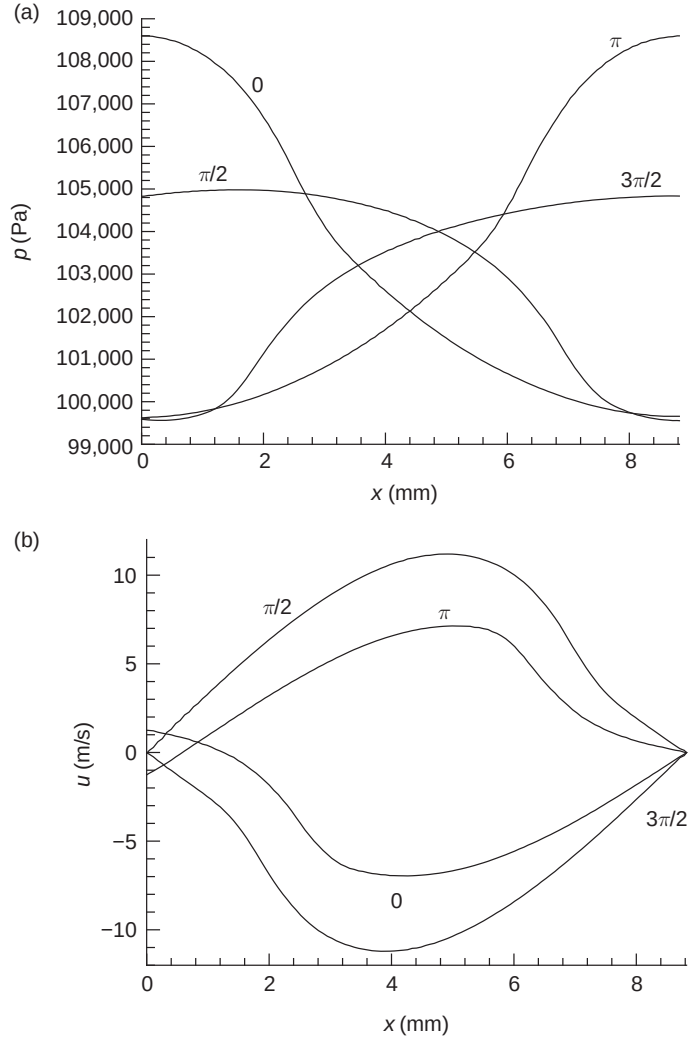

FIG. 2. Variation of (a) pressure and (b) u-velocity along the symmetry axis of the enclosure at four different instant ($\omega t = 0$, $\pi/2$, π, $3\pi/2$) during the acoustic cycle # 100 (Case A) [75].

$$u_{st} = \frac{\langle \rho u \rangle}{\langle \rho \rangle} \quad v_{st} = \frac{\langle \rho v \rangle}{\langle \rho \rangle} \tag{III - 1}$$

which describes the x- and y-components of the streaming velocities, respectively. Here $\langle\ \rangle$ indicates the time averaged quantities.

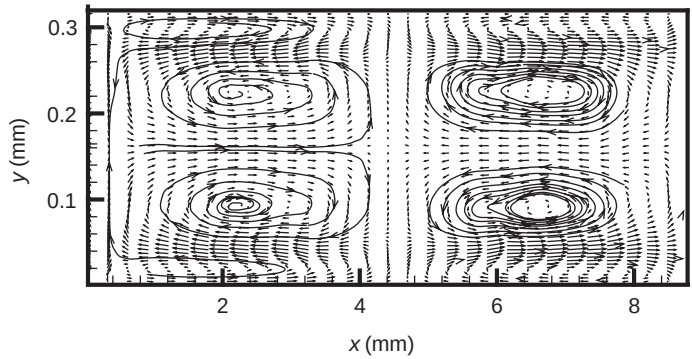

FIG. 3. Mean flow field in the enclosure at $t = 0.005$ s (Case A) [75].

The time averaging was applied during the 100th vibration cycle (between cycle # 99 and # 100) and gives the streaming velocity values near $t = 5$ ms. The streaming velocities calculated based on the time averaging during 150th ($t = 7.5$ ms) and 200th ($t = 10$ ms) cycles do not differ significantly from the values computed at $t = 5$ ms. Hence, the average mass transport velocities were assumed to be cycle-independent by this time ($t = 5$ ms). The maximum streaming velocity value is found to be approximately 0.06 m/s while the maximum instantaneous velocities reach 12 m/s in the primary oscillatory flow field in the enclosure. Four clockwise and four counter clockwise circulations are observed in the enclosure. Two of these vortical structures, namely inner streaming structures, formed at the vicinity of the bottom wall. The height of the circulatory flow structures (inner streaming) observed near the horizontal walls is characterized by the thickness of the acoustic boundary layer. The streaming structures seen in the middle section of the enclosure (outer streaming) have larger sizes. The horizontal length of both the inner and the outer streaming vortices is characterized by quarter wavelength ($\lambda/4$). Predicted streaming structures are in good agreement with the results reported by Hamilton *et al.* [38,39] in their recent studies.

Figure 4 (a) shows the variation of the x-component of streaming velocity along the enclosure semi-height at $x = 3L/4$ for case A. In this figure, the vertical axis is the x-component of the dimensionless streaming velocity (u_{st}/u_R) and u_R is the reference velocity given by $u_R = 3u_0^2/16c_0$ where u_0 is the maximum oscillatory velocity. This reference velocity value represents the maximum streaming velocity in case of a perfect sinusoidal waveform obtained by Rayleigh. Results from Hamilton *et al.* [39] are also included in the same figure (dashed curve). The predictions of the current study for Case A compare well with the results from Hamilton *et al.* [38]. Figure 4 (b)

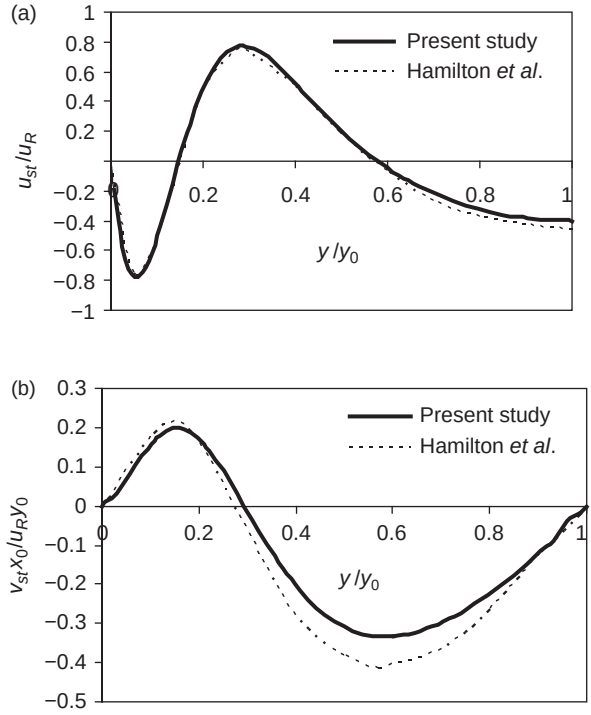

FIG. 4. Variation of the streaming velocity along the semi-height of the enclosure (Case A) [75], (a) u-component of the streaming velocity at $x = 3L/4$ and (b) v-component of the streaming velocity at $x = L/2$.

shows the variation of the y-component of streaming velocity along the enclosure semi-height at $x = L/2$. The vertical axis represents the y-component of the non-dimensional streaming velocity ($v_{st}x_0/u_Ry_0$). The maximum difference between the predictions of the current study and the reference solution (dashed curve) [38] is approximately 10%. The results given in the reference solution are for a resonator in which the sound field is assumed to be formed by shaking the system with a harmonic excitation. Since the present study considers a resonator with a vibrating boundary, the resulting velocity fields slightly differ.

In the next case considered (Case B-1), the enclosure height ($y_0/\delta_\nu = 20$) was doubled compared to Case A. The maximum wall displacement was kept the same ($X_{\mathrm{MAX}} = 10\,\mu\mathrm{m}$). Figure 5 shows the pressure distribution in the enclosure for this case during acoustic cycle # 100. Pressure waves emanating from the sinusoidal displacement of the oscillating wall is strongly distorted by the

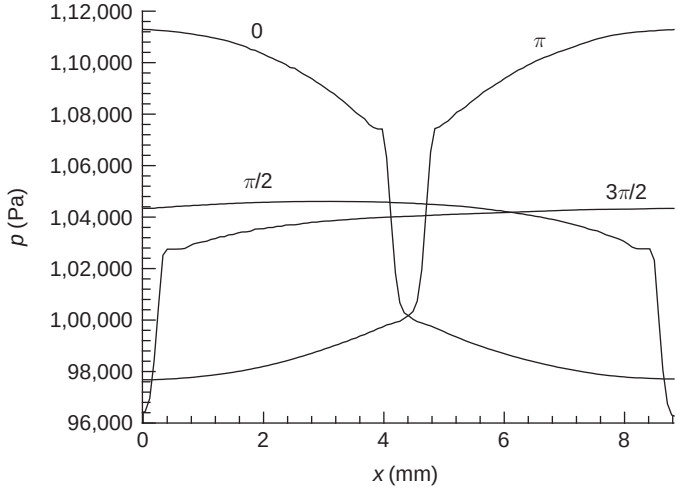

FIG. 5. Variation of the pressure along the symmetry axis of the enclosure at four different instant ($\omega t = 0$, $\pi/2$, π, $3\pi/2$) during the acoustic cycle # 100 (Case B-1) [75].

nonlinear effects. Since we have a wider system ($y_0/\delta_\nu = 20$), the viscous effects are weaker and shear forces along the top and the bottom walls have less effect on the bulk of the gas. This leads to higher-pressure amplitudes and more "shock wave" type profiles in the enclosure due to less attenuation. Similar wave profiles were reported by Chester [76] and several other researchers for resonant gas oscillations in closed tubes. Corresponding flow structures based on the average mass transport velocity in the enclosure is shown in Fig. 6. The figure depicts the flow field in the bottom half of the enclosure. For this case, the secondary flow patterns are observed in the shape of irregular vortical structures. Several second order vortices form the streaming flow field. Circulation loops apparently become unstable and non-symmetric vortex patterns are observed. The inner streaming structures are destructed but visible. The maximum primary oscillatory flow velocity is predicted as 20 m/s while the maximum flow speed is 0.54 m/s in the secondary quasi-steady streaming flow field. For this case, we qualitatively compare our results with the predictions of Yano [41]. The aspect ratio of the enclosure 0.07 is quite close to that of 0.1, considered by Yano. Yano's definition of streaming Reynolds number can be expressed as $\pi X_{\mathrm{MAX}} c_0/\nu$ using the present nomenclature. Based on this definition, streaming Reynolds number for Case B-1 is 699. This value is close to the minimum streaming Reynolds number (560) considered by Yano. However, the pressure amplitudes and the oscillatory flows are much stronger in Case B-1, compared to those addressed by

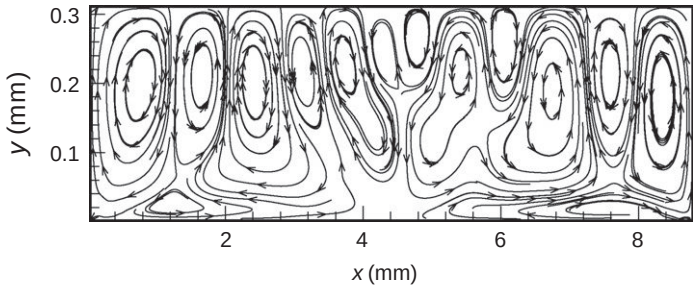

FIG. 6. Mean flow field in the enclosure at $t = 0.005$ s (Case B-1) [75].

Yano. Yano's computations demonstrate streaming structures localized near the tube wall. A number of vortices are visible in the bottom half of the tube distributed non-homogeneously and in skewed form. The streaming currents are not strong enough to position the vortex near two ends of the tube. The present computations show more homogeneous streaming pattern distribution in the enclosure due to larger streaming velocities.

In the next case considered (Case B-2), we decreased the maximum wall displacement value to $X_{MAX} = 3\,\mu$m to reduce the sharp pressure and velocity gradients observed for Case B-1 in the enclosure. The enclosure height is kept the same ($y_0/\delta_\nu = 20$) as in Case B-1. Figure 7 compares the temporal variation of the pressure for Case B-1 and B-2 at the mid-point of the left wall at the end of 100th vibration cycle. The pressure amplitude reaches approximately

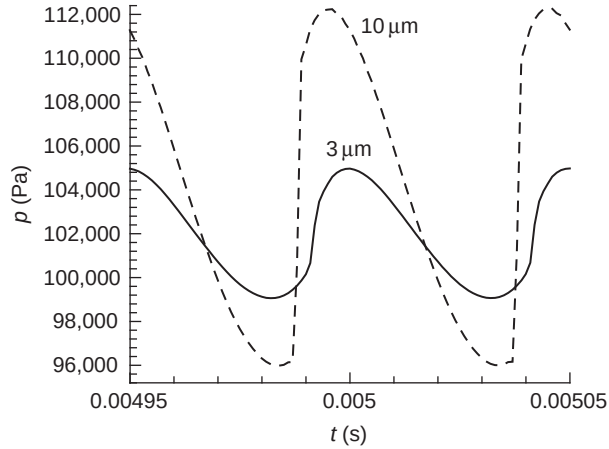

FIG. 7. Time evolution of left wall pressure at the mid-point (Case B-1, B-2) [75].

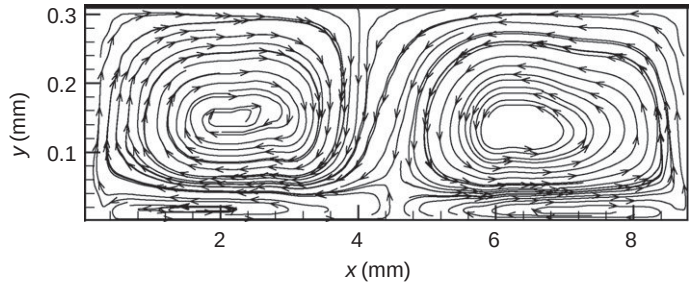

FIG. 8. Mean flow field in the enclosure at $t = 0.005$ s (Case B-2) [75].

16 kPa with 10 μm maximum wall displacement (Case B-1) while it is 6 kPa with 3 μm maximum wall displacement (Case B-2). In addition, with higher wall displacement value (10 μm), the pressure waveform is much sharper and shock wave type profile is observed. For small wall displacement (3 μm), the pressure profile depicts slightly attenuated sinusoidal wave in the system. The temporal variation of the pressure at the left wall is characterized by sudden amplitude increase for Case B-1 while a more gradual increase is observed for Case B-2. Corresponding quasi-steady (time-averaged) flow structure in the enclosure for Case B-2 is shown in Fig. 8 at $t = 5$ ms. For this case, the flow patterns are observed in the shape of regular structures. The inner and outer acoustic streaming structures are clearly visible. The maximum primary oscillatory flow velocity is computed as 7 m/s while the maximum flow speed is 0.03 m/s in the secondary steady streaming flow field.

For the next three cases the enclosure height was increased further ($y_0/\delta_\nu = 30$). In this geometry, $X_{MAX} = 10$ μm, $X_{MAX} = 2$ μm and $X_{MAX} = 1$ μm were considered as maximum wall displacement values for Case C-1, C-2 and C-3, respectively. The pressure profiles obtained for these three cases are presented in Fig. 9. Larger wall displacement creates higher-pressure amplitudes. In addition, the pressure gradients in the sound field increases with larger wall displacement. Sharp wave profile indicates the presence of higher harmonics in the wave field in addition to fundamental component, which describes a perfectly sinusoidal wave. The maximum pressure amplitudes are approximately 19.2 kPa, 5.2 kPa and 3.1 kPa for Case C-1, C-2 and C-3, respectively. Figures 10 (a), (b) and (c) show the instantaneous flow field in the enclosure for these cases at $t = 5$ ms which corresponds to the beginning of acoustic cycle # 101 ($\omega t = 0$). These are representative figures and although the flow direction changes during the acoustic cycle due to periodic oscillations, the nature of the flow structure is preserved. The maximum oscillatory flow velocities are 25 m/s, 6.8 m/s and 3.6 m/s for cases C-1, C-2 and C-3, respectively. In Fig. 10 (a), a strongly two-dimensional flow pattern is observed. Near the bottom wall, flow is uniform.

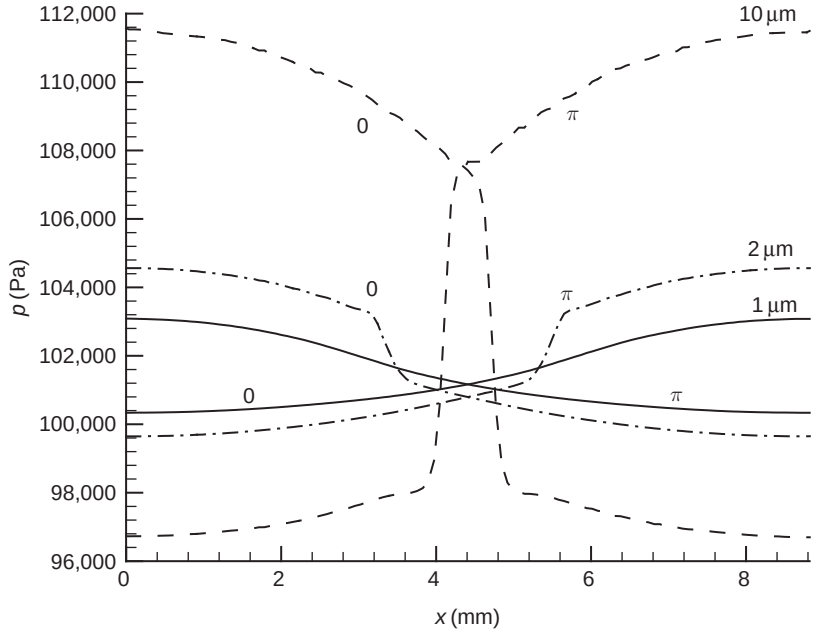

FIG. 9. Variation of the pressure along the symmetry axis of the enclosure at two different instant ($\omega t = 0,\ \pi$) during the acoustic cycle # 100 for Case C-1 ($X_{MAX} = 10\,\mu m$), Case C-2 ($X_{MAX} = 2\,\mu m$) and Case C-3 ($X_{MAX} = 1\,\mu m$) [75].

As the wall displacement amplitude decreases (case C-2), two-dimensional form of the transient flow field approaches to a one-dimensional form (Fig. 10 (b)) and a circulation pattern resulting from viscous interactions is present at $x \cong 4$ mm. For case C-3, the flow field is mostly one-dimensional except regions close to the bottom wall (Fig. 10 (c)).

The time-averaged flow fields predicted for these three cases are given in Fig. 11 (a), (b) and (c). In Fig. 11 (a), the flow pattern in the enclosure in the form of number of vortical structures and five streaming structures are observed per quarter wavelength. This irregular streaming flow pattern is a result of two-dimensional transient (periodic) flow field (Fig. 10 (a)). The maximum streaming flow speed is 2.1 m/s. In Fig. 11 (b), three outer streaming structures are observed per quarter wavelength while one inner streaming structure exists per quarter wavelength. The transform of oscillatory flow field from a two-dimensional form to one-dimensional form is reducing the number of streaming structures and the irregularity of the streaming field. The streaming pattern is steady but quite different from that of classical Rayleigh streaming.

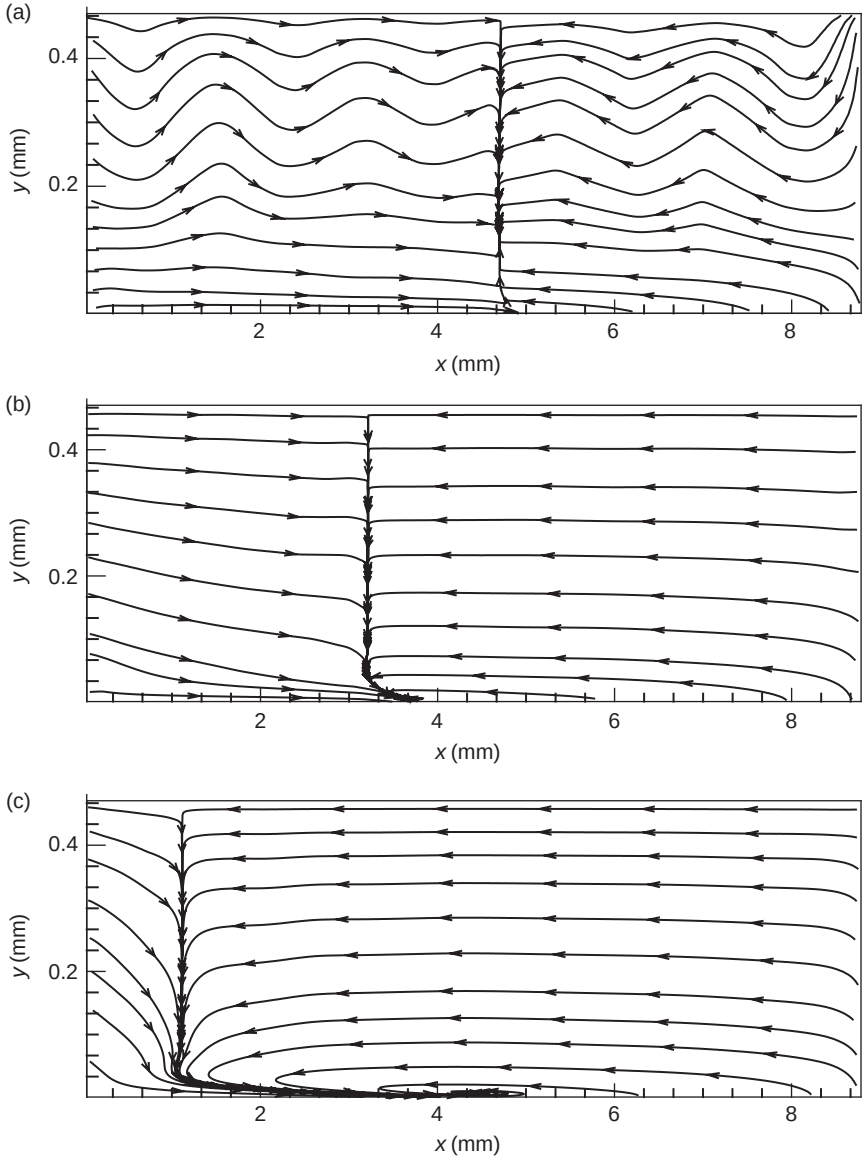

FIG. 10. Oscillatory flow field in the enclosure at $t = 0.005$ s for (a) Case C-1; (b) Case C-2; (c) Case C-3 [75].

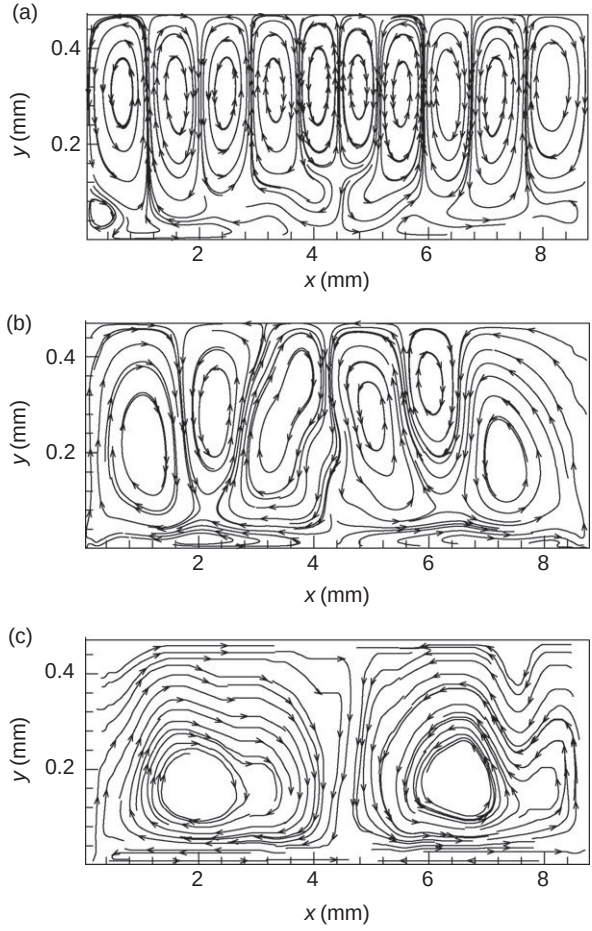

FIG. 11. Mean flow field in the enclosure at $t = 0.005\,\mathrm{s}$ for (a) Case C-1; (b) Case C-2; (c) Case C-3 [75].

The maximum streaming flow speed is 0.044 m/s. In Fig. 11 (c), two inner and two outer streaming structures are present in the system and the maximum streaming flow speed is 0.008 m/s.

In the last three cases considered (Case E-1, E-2, E-3), the dimensionless enclosure height was chosen as $y_0/\delta_\nu = 50$. In this geometry we consider $X_{\mathrm{MAX}} = 10\,\mu\mathrm{m}$, $X_{\mathrm{MAX}} = 0.5\,\mu\mathrm{m}$ and $X_{\mathrm{MAX}} = 0.2\,\mu\mathrm{m}$ as maximum wall displacements for Case E-1, E-2 and E-3, respectively. Figure 12 compares the temporal variation of the pressure for these three cases at the mid-point of

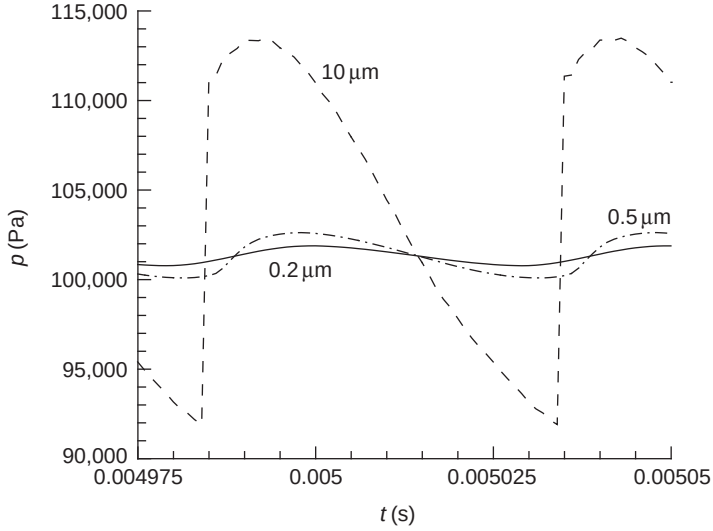

FIG. 12. Time evolution of left wall pressure at the mid-point for Case E-1 ($X_{MAX} = 10\,\mu m$), Case E-2 ($X_{MAX} = 0.5\,\mu m$) and Case E-3 ($X_{MAX} = 0.2\,\mu m$) [75].

the left wall at the end of the 100th vibration cycle. The pressure amplitude reaches a value of approximately 21.2 kPa for the 10 μm wall displacement (Case E-1), 2.5 kPa for 0.5 μm (Case E-2) and 1.1 kPa for 0.2 μm (Case E-3) wall displacements. In addition, with higher wall displacement value, the pressure waveform is much sharper and distorted. The temporal variation of pressure at the left wall is characterized by sudden amplitude increase for Case E-1 while a more gradual increase is observed for Cases E-2 and E-3. Corresponding streaming structures in the enclosure for all three cases are shown in Figs. 13(a), (b), and (c). All three figures demonstrate highly irregular flow structure for the nonlinear sound fields. For Case E-1, approximately four outer streaming rolls are observed per quarter wavelength. In Fig. 12 the pressure profiles seem linear for Case E-2 ($X_{MAX} = 0.5\,\mu m$) and for Case E-3 ($X_{MAX} = 0.2\,\mu m$) though the (weak) attenuation effects are present. However, the corresponding flow structures do not contain the classical streaming field having two inner and two outer vortices per half wavelength. Approximately four and half streaming rolls are observed per quarter wavelength for the cases E-2 and E-3. The pressure variations (Fig. 12) are weaker in the domain for cases E-2 (2.5 kPa) and E-3 (1.1 kPa) compared to the classical streaming cases A (Fig. 2, 9.6 kPa), B-2 (Fig. 7, 6 kPa)), and C-3 (Fig. 9, 3.1 kPa) though weakly attenuated pressure fields predicted for all five cases. Similar behavior is observed also for the maximum velocity

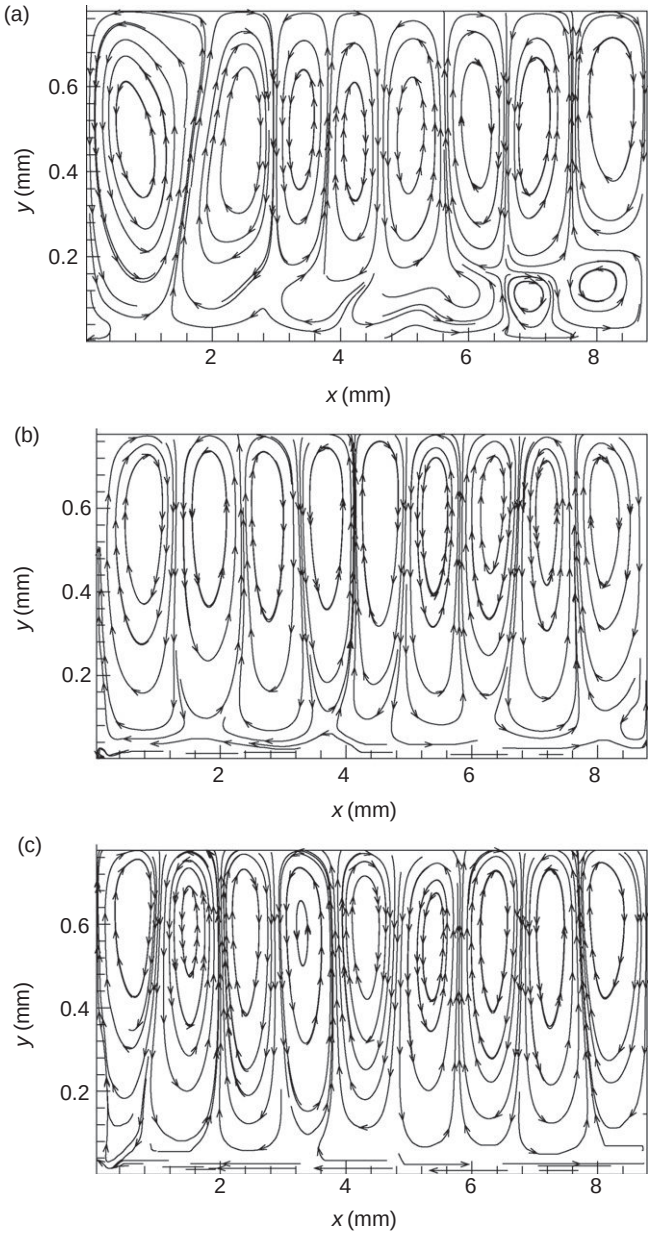

FIG. 13. Mean flow field in the enclosure at $t = 0.005$ s for (a) Case E-1; (b) Case E-2; (c) Case E-3 [75].

TABLE II
CHARACTERISTIC RESULTS FOR THE CASES STUDIED

Case	u_{MAX}	v_{stMAX} (m/s)	Re_s	Streaming structure
A	12	0.06	73	Classical
B-1	20	0.51	203	Irregular
B-2	7	0.03	24.8	Classical
C-1	25	2.1	317	Irregular
C-2	6.8	0.044	23.4	Irregular
C-3	3.6	0.008	6.6	Classical
D-1	26.5	3.17	356	Irregular
D-2	2.5	0.005	3.2	Irregular
E-1	28	4.25	397	Irregular
E-2	3	0.047	4.5	Irregular
E-3	1.3	0.02	0.86	Irregular

values (u_{MAX}) in the oscillatory flow fields (Table II). These two points appear to be the major factor resulting in irregular streaming motion. When the enclosure is sufficiently high, ($H/L > 0.14$) Rayleigh streaming patterns are not observed even for small vibration amplitudes. Compared to narrow enclosures having oscillatory velocity amplitudes of the same order, wide systems are associated with larger streaming velocities and irregular flow structures. The maximum oscillatory flow velocities are 28 m/s, 3 m/s, and 1.3 m/s for cases E-1, E-2 and E-3, respectively, while the maximum streaming flow speeds are 4.5 m/s, 0.047 m/s and 0.02 m/s. Since the thickness of the acoustic boundary layer is small compared to the enclosure height, inner streaming structures diminish.

Figure 14 shows the variation of normalized pressure amplitude ($\Delta p/\Delta p_1$) calculated at resonance with the modified acoustic Reynolds number ($Re_a^{1/3}/\Lambda$). Here Δp indicates the amplitude of the pressure variation at the right wall ($\Delta p = p_{max} - p_{min}$) and $\Delta p_1 = 8\gamma\varepsilon p_0/[\pi(\gamma+1)]^{1/2}$, where $\varepsilon = (\pi X_{MAX}/L)^{1/2}$ and p_0 is the initial pressure. Acoustic Reynolds number is defined as $Re_a = c_0 X_{MAX}/\nu$ and $\Lambda = L/H$ is the dimensionless length of the enclosure. In this figure dashed curve indicates the values computed based on the correlation suggested by Alexeev and Gutfinger [77]. This correlation is given for $0.05 < \varepsilon < 0.25$. The data from present study (symbols in the figure) are in the range of $0.03 < \varepsilon < 0.06$. The pressure amplitude predictions of the present study compare well with the above correlation [77]. The authors also reported recirculating flow patterns at each half of the tube resulting from acoustic streaming for $\varepsilon = 0.137$ and $H/L = 0.016$. In their predictions, the direction of streaming at resonance was opposite to that at non-resonance frequencies, when gas oscillations are continuous. In the

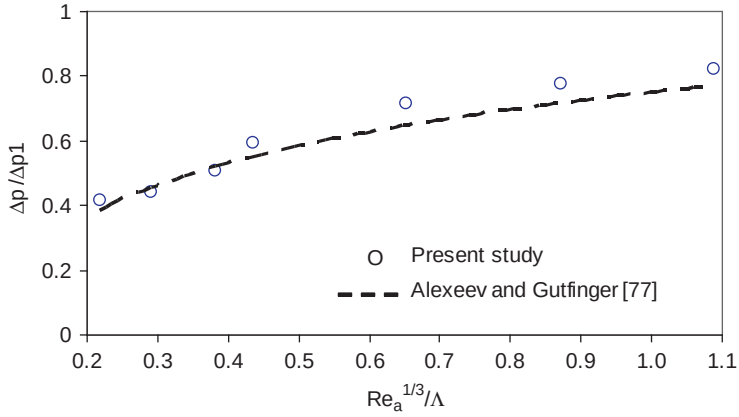

FIG. 14. Normalized pressure amplitude at resonance versus dimensionless parameter $Re_a^{1/3}/\Lambda$ [75].

present computations, we did not observe flow reversal for the circulatory structures having width of quarter wavelength for $\varepsilon \leq 0.06$ and $H/L \geq 0.036$.

Merkli and Thomann observed similar irregular circulations resulting from the transition to turbulence in their experiments. They considered gas oscillations excited with non-resonant frequencies (the flow properties varied sinusoidally in time) in a tube and reported a number of vortices non-uniformly distributed in the tube for $H/L \cong 0.01$. In this study, the critical Reynolds number for transition was found as $A_c = 2u_{MAX}/(\nu\omega)^{1/2} \cong 400$. The predictions of the present study differ from the observations of Merkli and Thomann especially for the distribution of streaming patterns. For the cases we considered, irregular streaming structures appear in uniform form in the enclosure. However, for the present computations, the maximum value of A_c is 40 and the time variations of flow properties are not sinusoidal.

Some characteristic results obtained for each case and the forms of streaming fields are summarized in Table II. The maximum velocity in the oscillatory flow field (u_{MAX}), the maximum acoustic streaming velocity and streaming Reynolds number ($Re_s = u^2{}_{MAX}/\nu\omega$) are included in the table. An observation from this data is that the relative magnitude of the streaming velocity respect to the oscillatory flow velocity (v_{stMAX}/u_{MAX}) is much larger for irregular streaming conditions compared to classical streaming.

The regions (defined by the aspect ratio of the enclosure and the maximum displacement of the wall amplitude) for which classical streaming patterns are shown in Fig. 15. The symbols in Fig. 15 indicate the cases

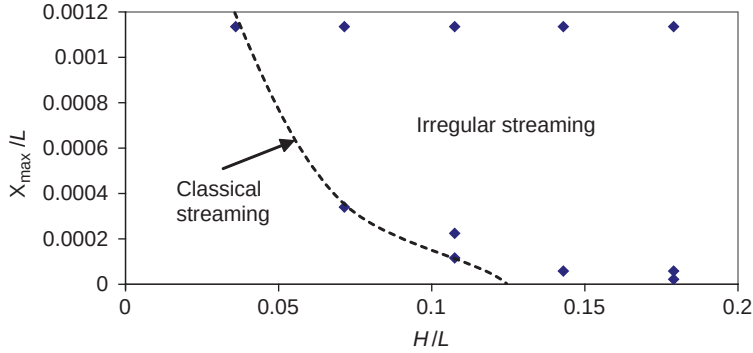

FIG. 15. Map of the cases considered as a function of the normalized maximum wall displacement and the enclosure aspect ratio. The symbols (♦) indicate the cases considered in terms of the geometrical condition and the normalized maximum wall displacement [75].

considered in terms of the enclosure aspect ratio and the normalized maximum wall displacement. The dashed line indicates the combinations of the aspect ratios and wall vibrational amplitudes that result in the formation of the classical acoustic streaming flow patterns characterized by two outer streaming vortices per half wavelength. Based on our results, the line defines the upper bound of the geometrical and vibrational amplitude conditions where the classical Rayleigh streaming patterns form. Clearly, both the vibrational amplitude and the height of the enclosure (wall induced viscous effects) play roles in the formation of the classical Rayleigh streaming structures. On the right hand side of the line, the acoustic streaming structures appear in complex and irregular forms. The number of streaming rolls increases as the enclosure height and the wall displacement increases.

The formation of pressure (acoustic) waves, acoustic-viscous boundary layer interactions and associated flows in a rectangular enclosure are studied by solving the unsteady compressible Navier-Stokes equations in 2-D Cartesian coordinate system. The acoustic field in the enclosure is created due to the harmonic vibration of the left wall. The effects of the maximum amount of wall displacement on the wave field and the formed flow structures are determined by utilizing a highly accurate flux corrected transport (FCT) algorithm. Observed primary oscillatory and secondary steady flow fields demonstrate the significant effects of the wall displacement and the enclosure height. Flow structure is strongly dependent on the pressure waveform in the enclosure. For a given enclosure height, increasing pressure amplitude induces stronger streaming motion (large u_{st}/u_R) and greatly changes the flow structures. Up to a certain enclosure height, the vibrational motion

causes steady streaming flows, which usually appear as two streaming, roll per half wavelength as reported in previous studies. However, when the enclosure height is increased beyond this limit, the streaming structures become irregular and complex.

C. Flows in an Acoustically Driven Cylindrical Enclosure

Acoustic streaming motion generated by finite-amplitude resonant oscillations in an air-filled two-dimensional cylindrical enclosure was experimentally studied and numerically simulated [78]. The oscillatory flow field in the enclosure was created by the vibration of one end of the cylindrical resonator ($L = 325$ mm, R=12.5 mm). The frequency of the wall vibration was chosen as $f = 1062$ Hz, such that the corresponding wavelength was equal to the length of the resonator. A standing wave was then generated in the closed tube. The pressure wave in the axial points was measured by a piezoresistive pressure transducer (Endevco #4428A). To simulate the flow field, the full compressible form of the Navier-Stokes equations in cylindrical coordinates was considered and solved by a highly accurate flux-corrected transport algorithm for convection terms and a central differencing scheme for the viscous and diffusive terms. In both of the experimental and numerical studies, outer acoustic streaming due to interaction of acoustic waves with viscous boundary layers was observed, and the effects of sound field intensity on the formation of streaming structures were studied.

1. Experimental Apparatus

An experimental system was designed and constructed [79] for the investigation of the streaming motion in air. The resonator was a cylindrical tube made of Plexiglas. The inside diameter of the tube was 25 mm and the length was 295 mm. The acoustic chamber was mounted horizontally with the sound driver on the left end and an aluminum plug, which closed the right end. The source of sound waves in this system was a compression driver type loudspeaker (JBL 2426H). The sinusoidal driving signal of the acoustic driver was provided by a GoldStar FG-8002 function generator and amplified by a Crown CE1000 type power amplifier.

An Endevco 8507C-1 series piezoresistive pressure transducer was used to detect and quantify the acoustic field. The transducer was installed in a 1/8" steel tube, which could be moved along the axis of the tube to measure the pressure at different locations. The cross-sectional area of the microphone was approximately one percent of the resonator area, therefore the error introduced by the presence of the probe in the sound field was assumed negligible. An Endevco 4428A pressure signal conditioner was used to

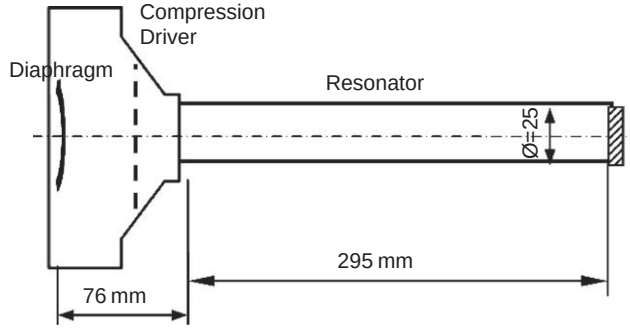

FIG. 16. The compression driver with the mounted resonator [79].

process the signal from the transducer and provide excited voltage. Finally, the pressure signal was collected by an NI 6052E DAQ system.

Flow visualization experiments in the resonator were performed by utilizing a laser system and a smoke injection technique. The laser beam generated by a Spectra-Physics 120S Helium-Neon 15 mW laser system passes through a cylindrical lens. An expanded beam was then obtained to illuminate a thin horizontal layer of the resonator. An Aristo-Craft ART-29308 U-25B smoke unit was used to produce smoke in the system. The smoke was injected into the chamber from the driver side through an inlet hole (see Fig. 16). During the filling procedure, a small discharging hole on the other side of tube was opened to allow smoke to freely flow into the chamber. After the filling procedure was completed, both the filling and discharging holes were closed. A Canon ZR80 digital camera recorder was used to record and store the visualized flow patterns in the experiments.

2. *Experimental Results*

Figure 17 shows the sketch of the acoustic driver and the resonator with critical dimensions of the system. As the figure illustrates, the vibrating diaphragm of the driver is located 76 mm behind the driver end of the cylindrical chamber.

The series of experiments were run under the following ambient conditions: $P = 0.1017$ MPa, $T = 297.15$ K. First, a number of experiments were conducted to find a resonant frequency for the cylindrical chamber and driver geometry. Figure 17 indicates the variations of the pressure amplitude in the right wall of the tube with the driving frequency of the loudspeaker. The maximum pressure amplitude was received at approximately 1062 Hz. At this frequency, the pressure fluctuations in the cylindrical chamber

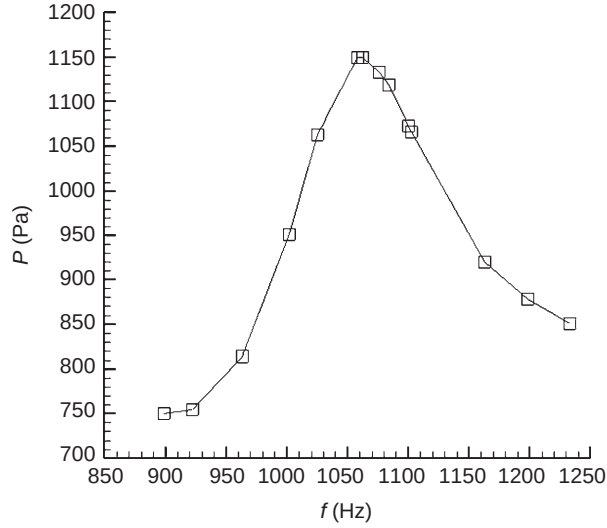

FIG. 17. Variation of pressure amplitude in the right wall with frequency of loudspeaker for driving power 22.4 mW (experimental) [79].

reached resonance. Since the speed of sound could be calculated from the air temperature, $c = \sqrt{\gamma RT} = 345.54$ m/s, the wavelength of the oscillations was given by $\lambda = c/f$. Figure 18 shows the peak-to-peak pressure values along the axial direction for a loudspeaker power of 91.5 mW at 1062 Hz. The maximum pressure antinode (AN) was located in the middle of the resonator, with two minimum nodes (N) symmetrically located on the two sides. According to this rule, we were able to calculate the effective length of resonator to be about 325 mm (indicated by the vertical dashed line in Fig. 16), which is same as the length that we calculated from the wavelength. The pressure wave was not very symmetrical because the boundary conditions and geometries of the two endplates are not the same. Figure 19 shows the root-mean-square pressure values along the axial direction for three different power values with the frequency held at 1062 Hz. While the root-mean-square pressure values decrease with decreasing loudspeaker power, the positions of the nodes and antinodes remain the same.

The instantaneous pressure fluctuation on the node ($z = 3L/4$) is shown in Fig. 20 for three different power levels. A sinusoidal pressure wave was recorded when the power of loudspeaker was low. When the power was increased, the pressure wave could not keep its regular form and it became more and more skewed. This signifies the existence of acoustic streaming because the generation of steady vertical structures destroys the regular

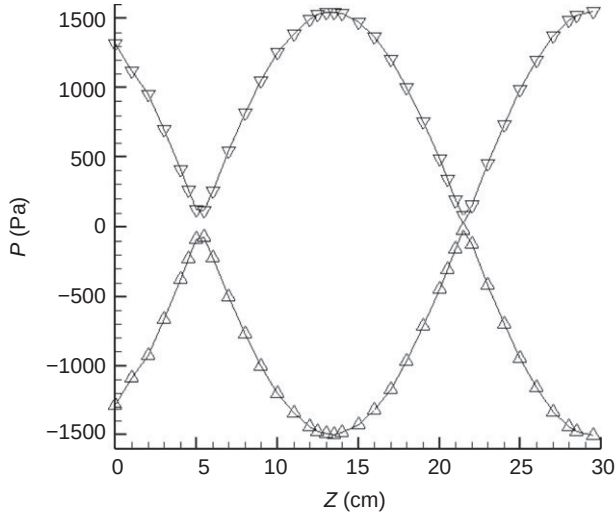

FIG. 18. Peak-to-peak value of the standing pressure wave along the axis of the tube for loudspeaker power 91.5 mW and $f = 1062$ Hz (experimental) [79].

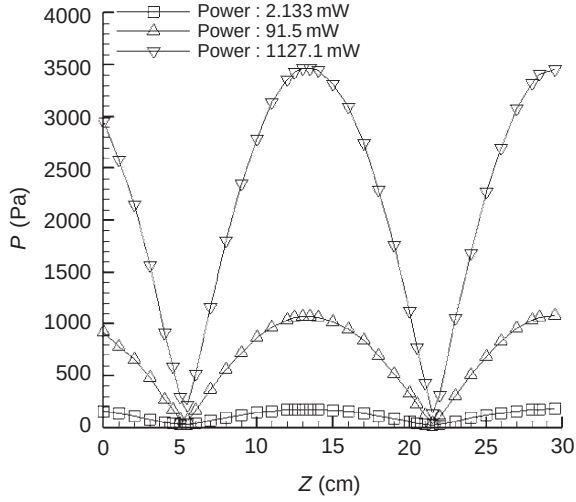

FIG. 19. RMS value of the standing pressure wave along the axis of the tube for different loudspeaker powers and $f = 1062$ Hz (experimental).

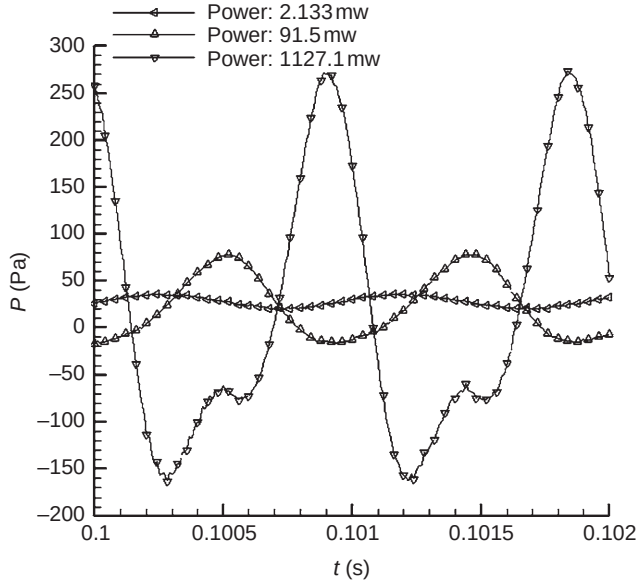

FIG. 20. Instantaneous pressure fluctuations at $z = 21.5\,\text{cm}$ $(3L/4)$ for different loudspeaker powers and $f = 1062\,\text{Hz}$ [79].

harmonic pressure distribution. Figure 21 shows the frequency spectra of the pressure fluctuations at the right wall of the tube for a driving frequency of 1062 Hz and a loudspeaker power of 91.5 mW. A strong first harmonic frequency was found at 1062 Hz, the driving frequency. Weaker higher harmonics are also present.

For the flow visualization experiments, visualization results were recorded under driving frequency $f = 1062\,\text{Hz}$ and a loudspeaker power of 81.6 mW. The time evolution of the structures is presented here. Figure 22 (a) shows the separated flow field structure in the resonator. A sudden flow separation was observed in the middle section of the chamber once the standing wave was formed by the loudspeaker. Since the pressure is highest in this zone (lowest velocity), the smoke particles were pushed in both horizontal directions and formed the separated flow regions. A few seconds later, the formation of the streaming vortices was observed in the resonator. Figure 22 (b) depicts this flow pattern in the half portion of the tube near the right fixed end. The length of clockwise and counterclockwise circulation was approximately a quarter wavelength of the standing sound field (as expected). The four vortices shown in Fig. 22 (b) were found to be nearly symmetric with respect to the resonator axis.

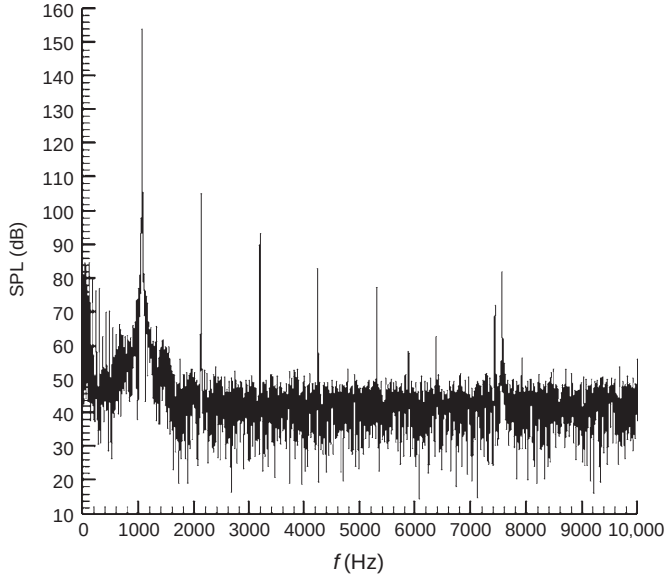

FIG. 21. Frequency spectra of the pressure fluctuations at the right wall of the tube for loudspeaker power 91.5 mW and $f = 1062$ Hz.

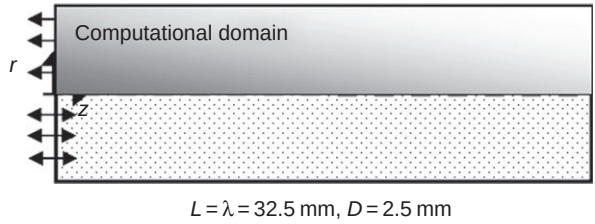

FIG. 22. Schematic of the computational domain.

3. *Numerical Study*

The time-varying primary flow field in the resonator was numerically simulated. To simplify the computations, the resonator was modeled as a cylindrical domain whose length is from the driver end to the fixed end. To maintain high grid density (as required for the high resolution calculations here), the scale of the computational model is reduced to 1/10 of the experimental resonator ($L = 32.5$ mm and $D = 2.5$ mm). The schematic of the computational domain is shown in Fig. 23. Due to symmetry, only the

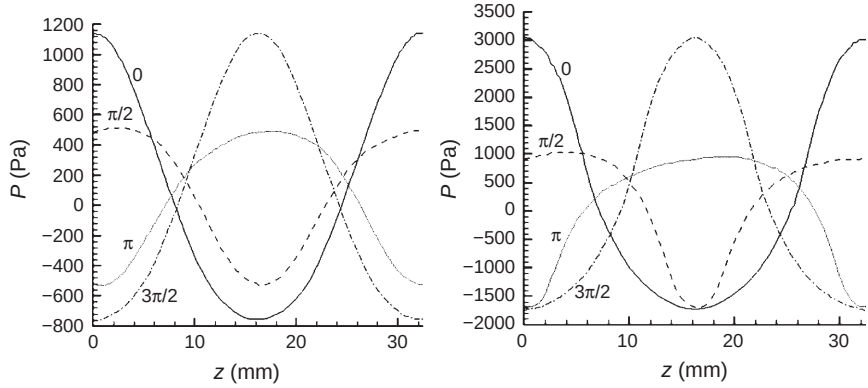

FIG. 23. Variation of pressure along the axis of the enclosure at four different instants with $f = 10{,}620$ Hz (computational): (a)$X_{max} = 4$ μm; (b)$X_{max} = 10$ μm.

top half of the domain was considered for the simulations. Initially, the air in the chamber is considered as quiescent everywhere. At $t > 0$, the left wall starts to vibrate sinusoidally. The displacement of the vibrating wall is given as

$$X = X_{max}\sin(\omega t) \qquad (\text{III} - 2)$$

Here, X_{max} is the maximum displacement; and w is the angular frequency of the vibration, $\omega = 2\pi f$. Since the computation domain is scaled down by a factor of 10 compared to the experimental system, the driving frequency for the computations was scaled up by a factor of 10 ($f = 10{,}620$ Hz) so that the wavelength $\lambda = L$ for both the measurements and the computations.

The input power of the speaker is simulated by adjusting the maximum displacement of the left wall, X_{max}. In the presented paper, the calculations are run for two values of $X_{max:}$ 10 μm and 4 μm. The initial conditions of the air are same as those in the experiment: $P = 0.1017$ MPa, $T = 297.15$ K. For every cycle of left wall vibration, about 28,778 time steps were used; the flow is found to be quasi-steady after 100 cycles.

Figures 23 and 24 show the pressure and axial velocity distributions, respectively, along the axis of the tube at $wt = 0$, $\pi/2$, π, and $3\pi/2$ for two driver amplitudes at $f = 10{,}620$ Hz. Both pressure and velocity profiles repeat as a cycle from $\omega t = 0$ to 2π, and the values at $\omega t = 2\pi$ are identical to those at $\omega t = 0$. The perfect sinusoidal profile of the input sound source is distorted by the viscous effects between the fluid and solid walls. Since the length of the enclosure is equal to the wavelength, the pressure profiles are symmetrical with respect to the vertical mid plane. At the beginning of

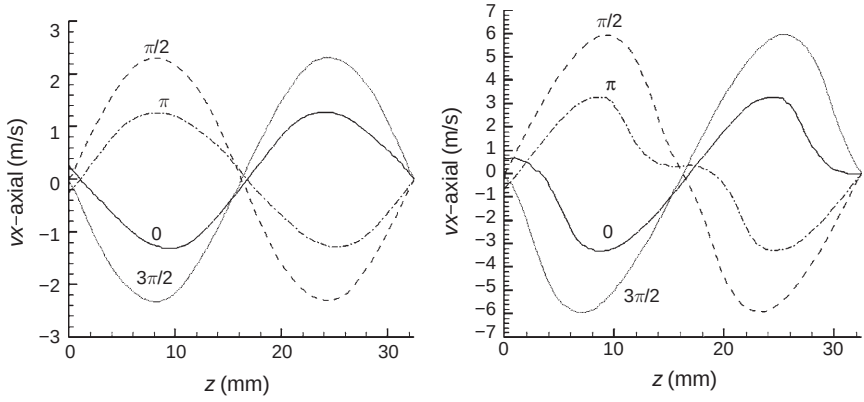

FIG. 24. Variation of axial velocity along the axis of enclosure at four different instants with $f = 10{,}620$ Hz (computational) [79]: (a) $X_{\max} = 4$ μm; (b) $X_{\max} = 10$ μm.

the cycle ($\omega t = 0$), the amplitude of the pressure wave is maximum at the two walls of the enclosure and minimum at the middle of the enclosure. When $\omega t = \pi$, the maximum pressure appears at the middle of the enclosure and decreases to both of the walls. For the axial velocity profiles, the value changes with time at the left wall due to the vibration of the wall, and is stationary at the right wall. It has a zero point near the mid zone of the enclosure.

Figure 25 shows the root-mean-square pressure values along the axial direction for different vibration amplitudes and $f = 10{,}620$ Hz. These profiles are similar to those for the experiments: there is one maximum pressure antinode (AN) in the middle of the resonator, with two minimum nodes (N) symmetrically located on the two sides. In addition, the absolute values are found to increase with increasing left wall vibration amplitude.

Figure 26 compares the temporal pressure distribution at the location $3L/4$ for two left wall vibration amplitudes with $f = 10{,}620$ Hz. The time interval shown in the figure is one cycle. The standing wave is found to be irregular. The larger the wall vibration amplitude is, the more irregular it becomes.

The time-averaged (steady acoustic streaming) flow fields are shown in Fig. 27 (for the top half of the cylindrical enclosure) for two different vibrational amplitudes and $f = 10{,}620$ Hz. The mean velocity is based on the average mass transport velocity in the enclosure. The average mass transport velocity is given by

$$u_{z,\text{mean}} = \frac{\langle \rho u_z \rangle}{\langle \rho \rangle}, \quad u_{r,\text{ mean}} = \frac{\langle \rho u_r \rangle}{\langle \rho \rangle} \qquad \text{(III} - 3\text{)}$$

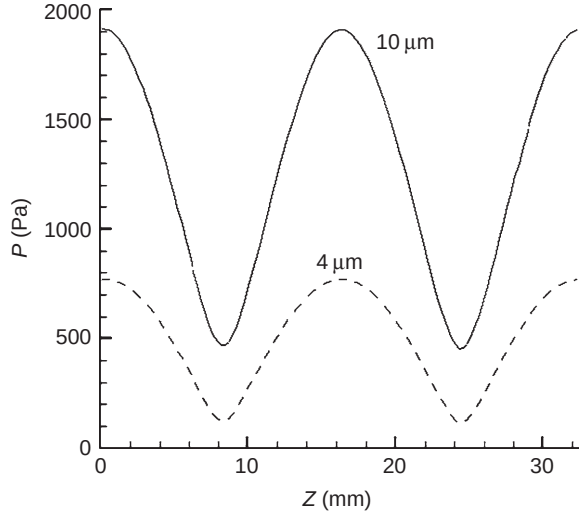

FIG. 25. Computed RMS value of the standing pressure wave along the axis of the tube for different left wall vibration amplitudes.

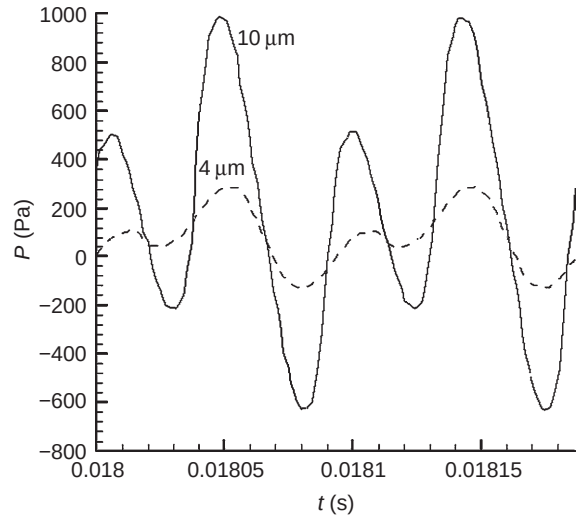

FIG. 26. Computed instantaneous pressure fluctuations at $3L/4$ for different left wall vibration amplitudes.

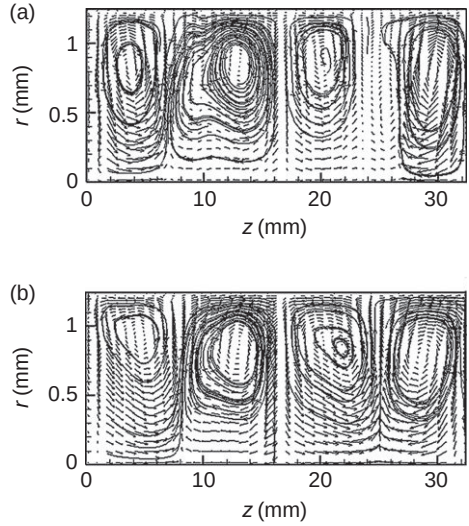

FIG. 27. Mean flow field in the resonator in the symmetric computational domain, $f = 10{,}620$ Hz (computational): (a)$X_{\max} = 4$ μm; (b)$X_{\max} = 10$ μm.

Here, $\langle\ \rangle$ indicates time-averaged quantities. The time average is applied during the 100th cycle of the pressure wave. As in the experimental results, four circular flow patterns are observed in each (top or bottom) half of the resonator. The four vortical structures are equally arranged along the axial direction, and the rotational directions of the neighbor vortices are opposite. Due to the large diameter of the resonator, $R/\delta_\nu = 57.6$, only the outer streaming is generated, and no inner streaming is observed.

The comparison of the root-mean-square values of the standing pressure wave along the axis of the tube for the computational and experimental results is shown in Fig. 28 where $\lambda = L$ for both cases. For the experiments, loudspeaker power was 66.1 mW, and for the computations, wall vibration amplitude was $X_{\max} = 4\,\mu$m. Since direct measurement of the loudspeaker vibrational amplitude was not possible, the applied power was varied until reasonable agreements were obtained for the computations done with the above vibrational amplitude. The experimental and computational results are found to agree well.

4. *Conclusions*

The formation of acoustic standing waves, acoustic-boundary layer interactions, and associated flows in a cylindrical resonator are studied by experimental

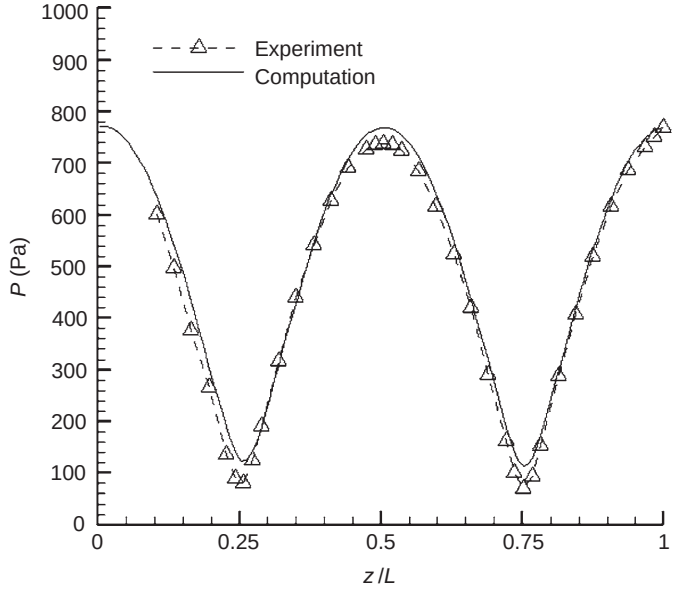

FIG. 28. Comparison of RMS value of the standing pressure wave along the axis of the tube for computational and experimental results.

and numerical methods. The dimension of the computational model is reduced to 1/10 of that of the experimental setup and the computational frequency is increased to 10 times the experimental value, so that $l = L$ for both the experiments and the computations. The computational and experimental results demonstrate the same characteristics of the standing wave characteristics and acoustic streaming and match each other very well. For the studied resonator characteristics, the pressure wave is found to be distorted from the perfect sinusoidal profile and the outer streaming structures are observed.

D. Interactions of Mechanically Driven Acoustic Waves with Heat Transfer in a Rectangular Chamber

Heat transfer in differentially heated enclosures has been studied extensively in the past both experimentally and computationally. However, the effects of acoustically driven oscillatory flow fields on the convective heat transfer processes have been primarily studied experimentally. A detailed understanding of thermal energy transport in these problems is challenging. Sound sources whose elements move essentially sinusoidally may generate a flow field in which the particle velocities are not simply sinusoidal but

a pattern of steady vortices (*streaming*) is often found in the body of the irradiated fluid. Sound at high intensity levels in gases and liquids are accompanied by these second order steady flow patterns.

Acoustic streaming is often observed where a standing wave is formed in a resonator driven by vibrating surface. With suitable design, this steady vortex flow can be employed for cooling of electronic systems in micro-gravity environment where free convective flows in fluids are greatly reduced or eliminated. Such flows can also aid mixing processes in containers and augment heat and mass transfer from resonator walls. Acoustically enhanced convection can be significant zero- or micro-gravity environments where conduction is the only heat transfer mode.

In this chapter, acoustic streaming generated by standing waves and the associated heat transfer in gas-filled closed enclosures is investigated numerically. To simulate the flow field, the full compressible form of the Navier-Stokes equations is considered and solved by a highly accurate flux-corrected transport algorithm. In the numerical model, temperature-dependent heat conductivity and viscosity are taken into account. The study is focused on the channels having intermediate widths (30–50 times the viscous penetration depth). The simulations are run for different wall temperature conditions: $T_t = T_b = T_0$ and $T_t = T_b + \Delta T$.

1. Problem Geometry

A two-dimensional rectangular enclosures filled with nitrogen is considered (Fig. 29). The left wall of the enclosure vibrates harmonically, either completely or partially. The vibrating wall boundary condition is thus the acoustic energy source in this geometry. The displacement of vibration is given as $x = X_{\max} \sin(\omega t)$, where $\omega = 2\pi f$ is the angular frequency. The length of the enclosure is chosen as $L = 2x_0 = 8.825$ mm for all cases studied. The width of the enclosure (H) is varied in the cases studied. The frequency of the wall vibration is set as $f = 20$ kHz, and the corresponding wavelength of the sound waves is $\lambda = 17.65$ mm based on the undisturbed enclosure temperature $T_0 = 300$ K and pressure $P_0 = 1$ atm. Hence for the cases studied, $\lambda = 2L$.

One of the important parameters in the resonator is the viscous penetration depth $\delta_\nu = (2\nu/2\pi f)^{1/2} = 0.0158$ mm. Here f is the frequency of the wall vibration and ν is the kinematic viscosity of the fluid. Previous studies already showed that the ratio of the resonator width H over δ_ν play an important role in the acoustic-fluid dynamic interactions. In the present study, the resonator widths are limited to the range: H ($=2y_0$): $30\delta_\nu$ to $50\delta_\nu$ (Table III). In this width range, the behaviors of acoustic streaming are most significant. The width of resonator was kept small such that the viscous penetration depth δ_ν can be well resolved in the simulation.

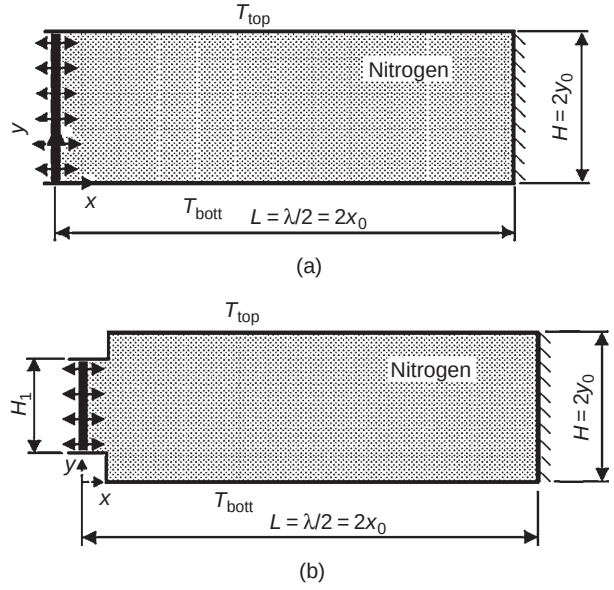

FIG. 29. Schematic of the computational domain [80]. (a) Entire left wall vibration; (b) Part left wall vibration.

TABLE III
LIST OF CASES STUDIED

No.	y_0/δ_ν	x_0/δ_ν	X_{max} (m)	H_1/H	ΔT (K)
1A		279			0
1B	20		1.0×10^{-5}	1.0	20
1C					60
2	20		0.5×10^{-5}	1.0	20
3	20		1.5×10^{-5}	1.0	20
4	15		1.0×10^{-5}	1.0	20
5	25		1.0×10^{-5}	1.0	20
6A	20		1.0×10^{-5}	0.4	0
6B					20
7	20		1.0×10^{-5}	0.1	0

In the present study [80], the aspect ratios of resonators L/H varied from 11 to 18. The high aspect ratio is due to the order of wavelength λ is much higher than that of viscous penetration depth δ_ν. To investigate the interaction between acoustic waves (propagating primarily in the x-direction) and heat transfer (in the y-direction), the top and bottom walls are set at different

temperatures. As mentioned earlier, the vibrating left sidewall and the right sidewalls are thermally insulated. Typically, a grid size of 150×98 is used for the rectangular domain. Resolving the boundary layer in the computational method is essential for accurately simulating the formation of acoustic streaming structures and heat transfer along the walls. For this reason, we employ a non-uniform grid structure. This structure has finest grids near the walls and the grid quality gradually decreases as the distance from the horizontal walls increases. For the present calculations, there are always 3–5 grids inside the boundary layer. To model the wall vibration, moving cell boundaries were considered for a few cells next to the left wall. The number of moving cell is chosen such that the maximum variation of a cell size is less than 25%.

2. *Results and Discussion*

a. Validation Results. To verify the numerical model and grid size, the numerical model is first used to simulate the analytical results given by Hamilton [39] under the following conditions: $P_r = 0.67$, $\gamma = 5/3$, $y_0 = 20\delta_\nu$. The predicted steady streaming flow field (at the end of the 120th cycle) obtained by the present numerical method (where $f = 20\,\text{kHz}$) for the conditions given in Hamilton *et al.* [39] is shown in Fig. 30. This cycle-averaged flow field is

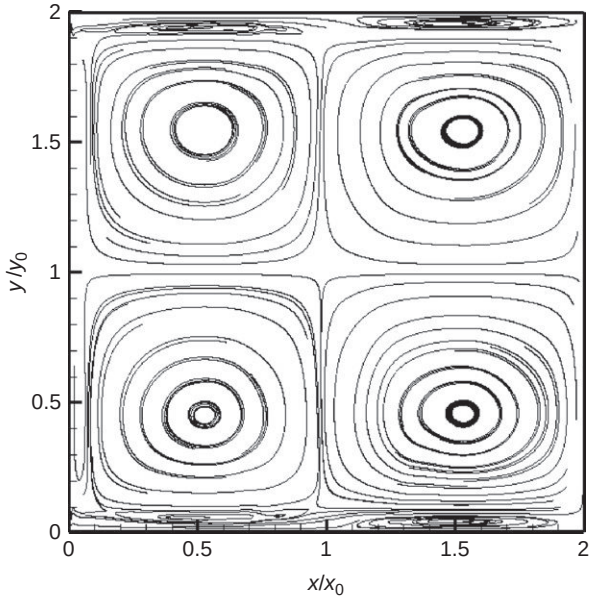

FIG. 30. End wall oscillation induced acoustic streaming (cycle averaged values for the 120th cycle) [80] for conditions given by Hamilton *et al.* [39].

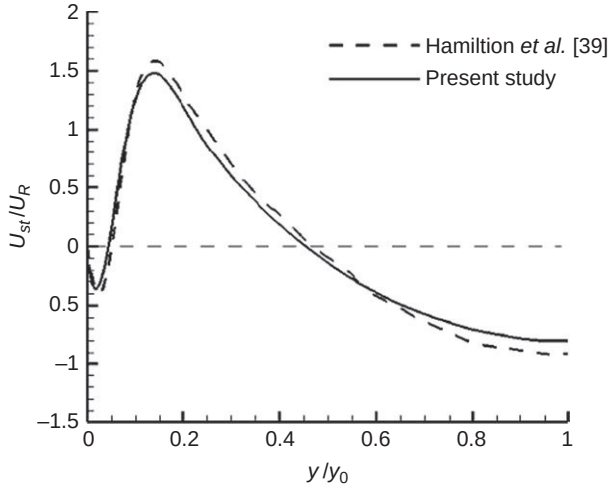

FIG. 31. Comparison of the transverse distribution of x-component streaming velocity at $x/x_0 = 1.5$ [80] with the results by Hamilton *et al.* [39].

based on the average mass transport velocity values in the enclosure. The predicted streaming pattern and size are similar to those given by Hamilton *et al.* (not shown here), except that, the left and right vortices are not symmetric along the middle vertical plane of resonator for the present calculations. In the present case, only the left wall vibrates, however for the results given in Hamilton *et al.* the entire resonator vibrates, albeit with the same frequency and amplitude considered in the present simulations.

Figure 31 shows the comparison of the variation of the x-component of the cycle-averaged velocity along the enclosure height at $x/(L/2) = x/x_0 = 1.5$ of the present model predictions with the results given by Hamilton *et al.* Figure 32 gives similar comparisons for the variation of the y-component of the cycle-averaged velocity along the enclosure height at $x/(L/2) = x/x_0 = 1.0$. In these two figures, the cycle-averaged velocities are nondimensionalized by, which is Rayleigh's result for the maximum streaming velocity in the center of a wide channel containing a pure viscous fluid. The maximum error that is found in Fig. 31 is 6%, which can be perhaps explained by the non-symmetric streaming structure due to the different wall conditions in the two studies.

b. Parametric Case Studies. After the verification of the mathematical formulation and the solution procedure, we investigate the effects of transverse acoustic waves on the convective heat transfer in the enclosure with imposed longitudinal temperature difference. Table III lists the cases reported in this

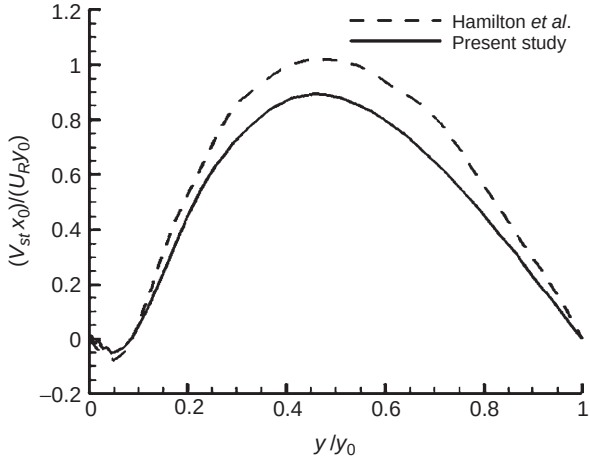

FIG. 32. Comparison of the transverse distribution of the y-component streaming velocity at $x/x_0 = 1.0$ with the results by Hamilton *et al.* [39].

paper. For each case, the calculations were started by keeping the top and bottom walls at the same temperatures. After the system achieves steady state, then the top wall temperature is changed to investigate the interaction between heat transfer and acoustically driven flows.

In the first case considered (Case 1A), the maximum displacement of the entire left wall vibration is set to $x = X_{\max} \sin(\omega t)$ with $X_{\max} = 10\,\mu\text{m}$, and $f = \omega/2\pi = f = 20\,\text{kHz}$. The width of channel is set to $y_0 = 20\delta_\nu$. At first, the temperature of the top and bottom walls are kept at the initial temperature $T_0 = 300\,\text{K}$. The cycle-averaged steady state flow condition is achieved at about the 120th acoustic cycle.

Figure 33 shows the pressure distribution along the horizontal mid-plane of the enclosure at $\omega t = 0$, $\pi/2$, π, $3\pi/2$ (during cycle # 120) for Case 1A. These pressure profiles remain essentially the same at any other horizontal plane away from the bottom and top walls and this indicates the near-one-dimensional character of the acoustic field in the bulk medium. The pressure distribution for $\omega t = 2\pi$ (not shown in Fig. 33) is identical to the curve given for $\omega t = 0$. At $\omega t = 0$ and $\omega t = \pi$, the amplitude of the pressure waves reach a maximum and a minimum value at the ends of the enclosure. At the beginning of the cycle ($\omega t = 0$), the pressure is maximum on the vibrating (left) wall of the enclosure and decreases with increasing distance from the wall and reaches a minimum value at $x \cong L$. The behavior is quite opposite at $\omega t = \pi$ where the pressure is minimum on the vibrating (left) wall of the enclosure and increases with increasing distance from the wall and reaches a

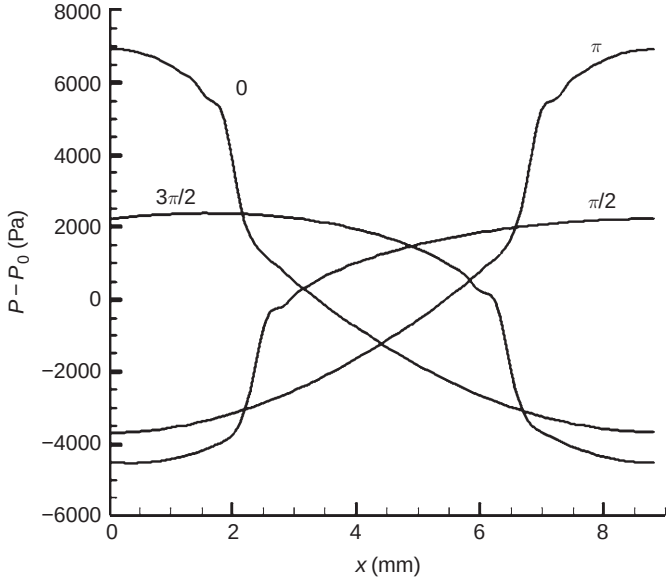

FIG. 33. Variation of pressure along the horizontal mid-plane of the enclosure at four different instants ($\omega t = 0$, $\pi/2$, π, $3\pi/2$) at the 120th cycle, isothermal top and bottom walls, $y_0/\delta_v = 20$, $X_{max} = 1.0 \times 10^{-5}$ (CASE 1A).

maximum value at $x \cong L$. The u velocity profiles given in Fig. 34 for $\omega t = 0$, $\pi/2$, π and $3\pi/2$, along the horizontal midplane show that the velocity node is formed at approximately $x = L/2$. Cycle-averaged (120th cycle) solutions from the present simulations predict steady streaming flows in the enclosure. The predicted steady streaming flow field is shown in Fig. 35. At this stage, the predicted cycle-averaged velocity fields were found to be cycle-independent.

After the steady state is achieved (120th cycle), the top wall temperature is then increased to 320 K ($\Delta T = 20$ K), while the bottom wall is still kept at the initial temperature (Case 1B). Figure 36 shows that cycle-averaged velocity field (121st cycle) changes drastically immediately after the heating is initiated. The steady streaming structure is destroyed due to the temperature change of the top wall. Instead, the gas flows from top to bottom, as heating of the top wall increases the local pressure in the upper part. The flow field is found to attain steady-state conditions again (in a cycle-averaged sense) by the 360th cycle. The new steady streaming flow field at the 360th cycle is shown in Fig. 38, where only two vortices (instead of the four shown in Fig. 36 earlier) are found. Thus, the temperature difference between the top and the bottom walls affect the acoustically driven flow field in a significant way.

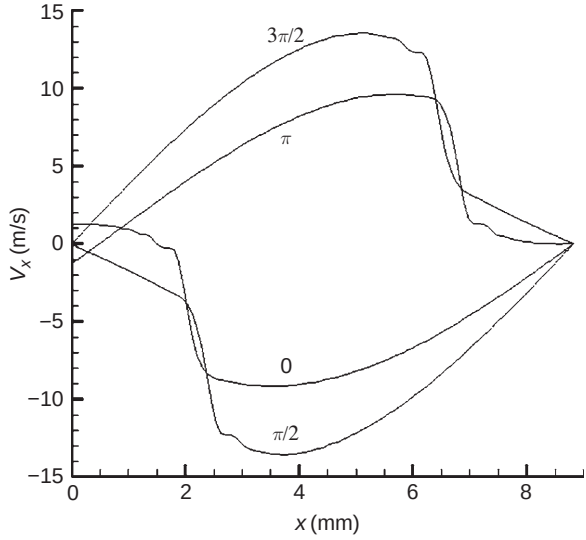

FIG. 34. Variation of the x-component velocity along the horizontal mid-plane of the enclosure at four different instants ($\omega t = 0$, $\pi/2$, π, $3\pi/2$) in 120th cycle, isothermal top and bottom walls, $y_0/\delta_v = 20$, $X_{\max} = 1.0 \times 10^{-5}$ (Case 1A).

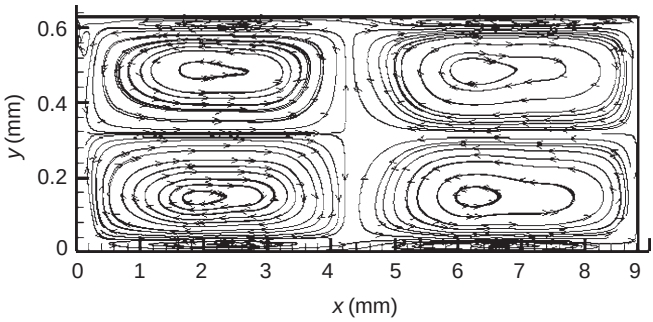

FIG. 35. Cycle averaged flow field showing acoustic streaming at the 120th cycle, isothermal top and bottom walls, y_0/δ_v=20, $X_{\max}$=1.0×10^{-5} (Case 1A).

Since the density, viscosity and conductivity values of the gas are temperature dependent, the symmetric streaming structure in Fig. 37 is distorted and we essentially have a rather asymmetric (cycle-averaged) flow field.

To further study the effect of temperature difference on streaming velocity, we increase the top wall temperature to 360 K from 320 K (Case 1C). For the three different heating cases (1A, 1B and 1C), x-component of the

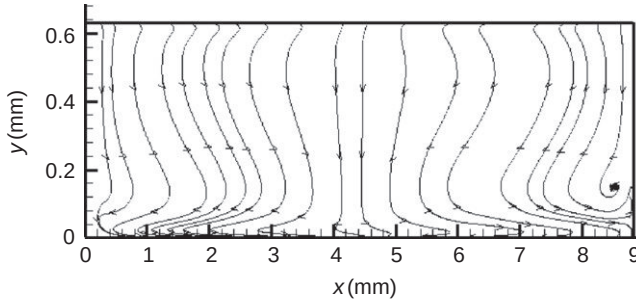

FIG. 36. Streamlines (cycle-averaged) immediately after differential heating along the top and the bottom walls, at 121st cycle, $y_0/\delta_v = 20$, $X_{\max} = 1.0 \times 10^{-5}$ (Case 1B).

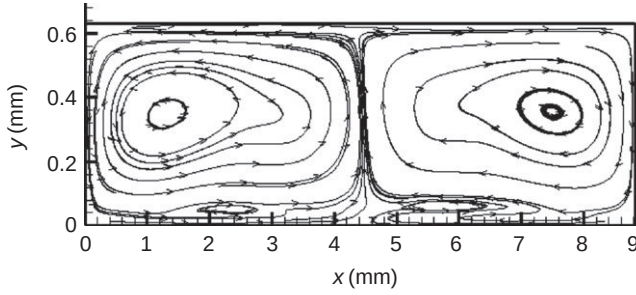

FIG. 37. Acoustic streaming in 360th cycle, differential heating along the top and the bottom walls, $y_0/\delta_v = 20$, $X_{\max} = 1.0 \times 10^{-5}$ (Case 1B).

cycle-averaged streaming velocity profiles along the vertical-plane at $x = 3L/4$ are given in Fig. 38, and the y-component of the cycle-averaged streaming velocity profiles along the vertical-plane at $x = L/2$ are shown in Fig. 39. Compared with the unheated case (1A), velocity profiles change dramatically due to the streaming structure changes for cases 1B and 1C. The streaming-velocity components also increase when the top wall temperature increase. Consequently, differential heating increases the strength of acoustic streaming, though the symmetrical structure found in Fig. 35 is destroyed.

The cycle-averaged temperature contours are shown in Fig. 40 for T_{top}=320 K (Case 1B). The effect of the cycle-averaged flow field (Fig. 41) on the temperature field is evident. The variation of cycle-average temperature along the vertical plane of the enclosure at three different locations ($x = L/4$, $L/2$, $3L/4$) are given in Fig. 41 (Case 1B) along with the conduction profile for no acoustic perturbation. The heat transfer to the horizontal walls is found at the middle of resonator, where the mean streaming flow is

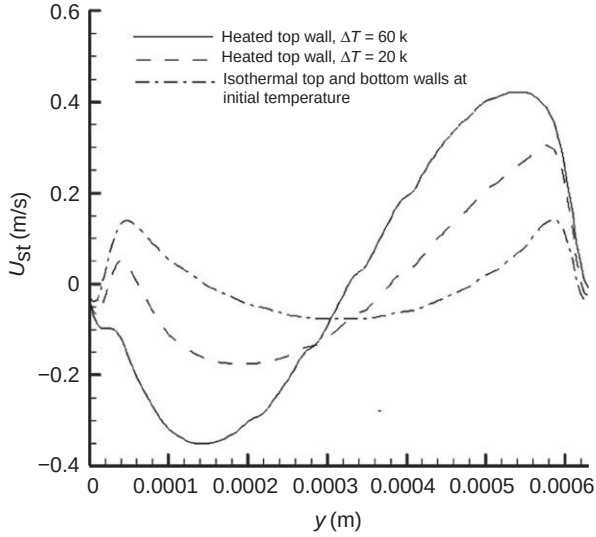

FIG. 38. x-component of the cycle-averaged velocity along the vertical-plane at $x=3L/4$ for different heating conditions along the top and bottom walls (Cases 1A, 1B and 1C).

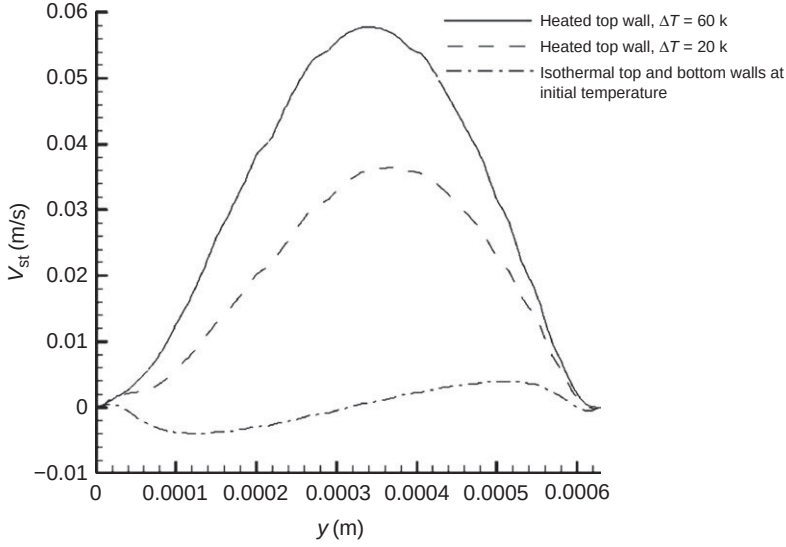

FIG. 39. y-component streaming velocity along the vertical-plane at $x=L/2$ for different for different heating conditions along the top and bottom walls (Cases 1A, 1B and 1C).

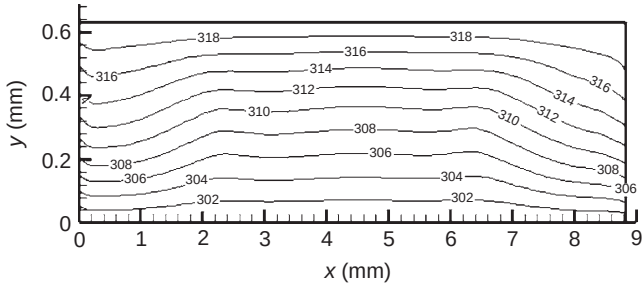

FIG. 40. Cycle-average temperature contours, at the 360th cycle, differentially heated top and bottom walls, $y_0/\delta_v = 20$, $X_{\max} = 1.0 \times 10^{-5}$ (Case 1B).

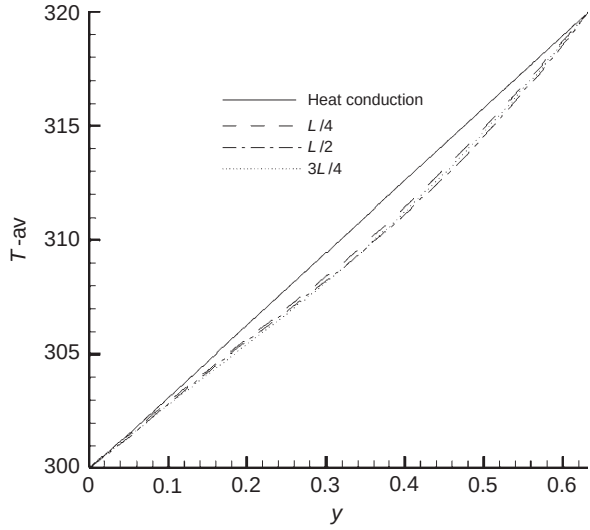

FIG. 41. Variation of cycle-averaged temperature along the vertical plane of the enclosure at three different locations ($x = L/4$, $L/2$, $3L/4$), at the 360th cycle, differentially heated top and bottom walls, $y_0/\delta_v = 20$, $X_{\max} = 1.0 \times 10^{-5}$ (Case 1B).

strongest. The cycle-averaged Nu values along the top and bottom walls are found to be 0.998 and 1.231, respectively. The asymmetry is due to the acoustic power input from the left wall vibration. The acoustic power input to the system is converted to thermal energy by the viscous dissipation, which increases the bottom wall heat load, compared to the top wall. Considering the temperature dependent thermal conductivity, Nu number is 0.975 for the case of steady heat conduction (no wall vibration). Hence, the

acoustic streaming increases the Nu number by 2.4% in the top wall and by 26.3% for the bottom wall for the geometry considered here.

To further study the effects of wall vibration amplitude on the heat transfer, simulations are run for different amplitudes: $X_{\max} = 0.5 \times 10^{-5}$ m (Case 2) and $X_{\max} = 1.5 \times 10^{-5}$ m (Case 3) with $\Delta T = 20$ K. For the different wall vibration amplitudes, there is no significant difference on the streaming structure compared to the results obtained for case 1B ($X_{\max} = 1.0 \times 10^{-5}$ m). The corresponding cycle-averaged (360th cycle) temperature contours are shown in Figs. 42 and 43. For lower acoustic power input (Case 2), the isotherms are similar to those obtained for the heat conduction case. For higher acoustic power input (Case 3) compared to Case 1B, the temperature field undergoes further distortion to accommodate the larger acoustic power input.

Cases 4 and 5 are run for different channel widths $y_0 = 15\delta_\nu$, and $25\delta_\nu$ respectively with $\Delta T = 20$ K. In this range, the predicted streaming structures do not change much compared to results obtained for Case 1B. However the

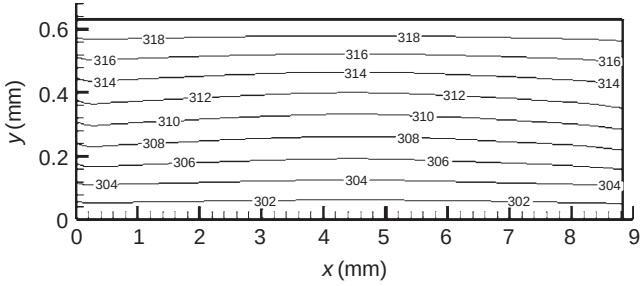

FIG. 42. Cycle-average temperature contour, in 360th cycle, differentially heated top and bottom walls, $y_0/\delta_v = 20$, $X_{\max} = 0.5 \times 10^{-5}$ m (Case 2).

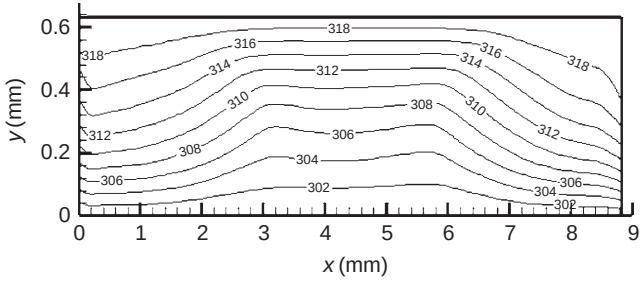

FIG. 43. Cycle-average temperature contour in 360th cycle, differentially heated top and bottom walls, $y_0/\delta_v = 20$, $X_{\max} = 1.5 \times 10^{-5}$ m (Case 3).

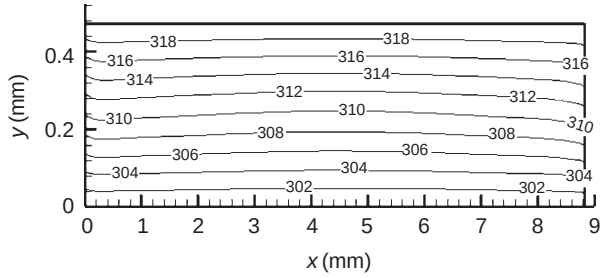

FIG. 44. Cycle-average temperature contour, at the 360th cycle, differentially heated top and bottom walls, $y_0/\delta_v = 15$, $X_{\max} = 1.0 \times 10^{-5}$ (Case 4).

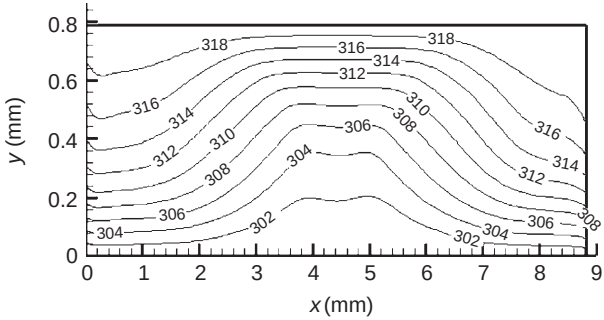

FIG. 45. Cycle-average temperature contour, in 360th cycle, differentially heated top and bottom walls, $y_0/\delta_v = 25$, $X_{\max} = 1.0 \times 10^{-5}$ (Case 5).

temperature contours for $y_0 = 15\delta_\nu$ (Fig. 44) and $y_0 = 25\delta_\nu$ (Fig. 45) show significant differences. For a larger enclosure height, the acoustic power input is higher and the temperature field shows more distortion. The effect of enclosure height on Nu number is given in the Table IV. Nu along the bottom wall increases significantly with the increasing channel width, but the Nu along top wall does not change much. To compensate for the energy addition by the vibrating wall, the heat addition from the hot wall to the fluid is lesser than the heat removal from the bottom wall.

Next, we discuss a more realistic system where the vibration of the left wall is limited to the central part of the wall. To investigate this kind of problem, we vibrate the part of left wall vibration: $H_1/H = 0.4$ and 0.1, in the cases 6 and 7. The schematic is given in Fig. 29 (b).

Figure 46(a) shows the cycle-averaged flow field (360th cycle) for Case 6, where 40% of the left wall vibrates, under unheated (isothermal top and bottom walls) condition. In the bulk zone, four outer streaming and four

TABLE IV
EFFECT OF ENCLOSURE WIDTH ON NU

Case	y_0/δ_ν	Top wall	Bottom
1B	20	0.998	1.231
4	15	1.016	1.114
5	25	1.098	1.395

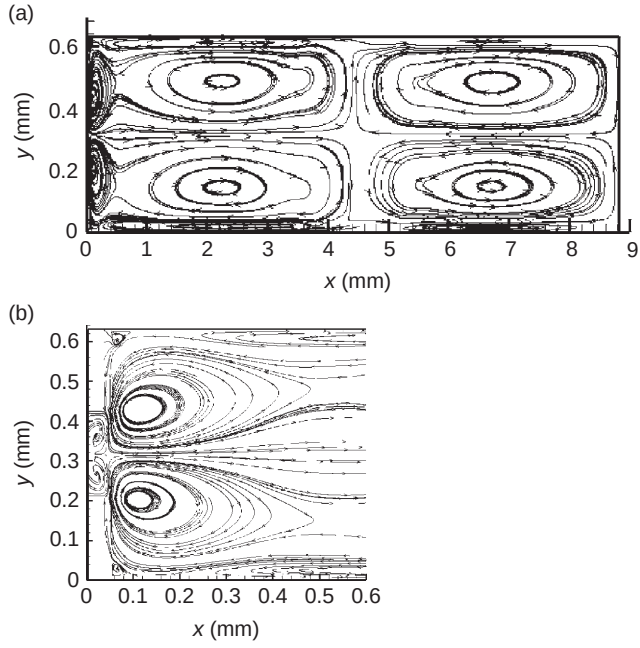

FIG. 46. Acoustic streaming, at 120th cycle, isothermal top and bottom walls, $y_0/\delta_v = 20$, $X_{\max} = 1.0 \times 10^{-5}$, differentially heated top and bottom walls, partial (40%) left wall vibration, (Case 6A).

inner streaming rolls are observed, similar to the case of the full wall vibration (see Fig. 35). However, two other additional vortices are found near the central vibrating part of the left wall. The steaming patterns near the left wall are enlarged in the Fig. 46 (b), which clearly shows the effects of the partial vibration on the flow field.

Following earlier simulations with full wall vibration (Cases 1A and 1B), the top wall temperature is now increased to 320 K, while the bottom wall is held at 300 K (Case 6B). The cycle-averaged flow field (after an additional

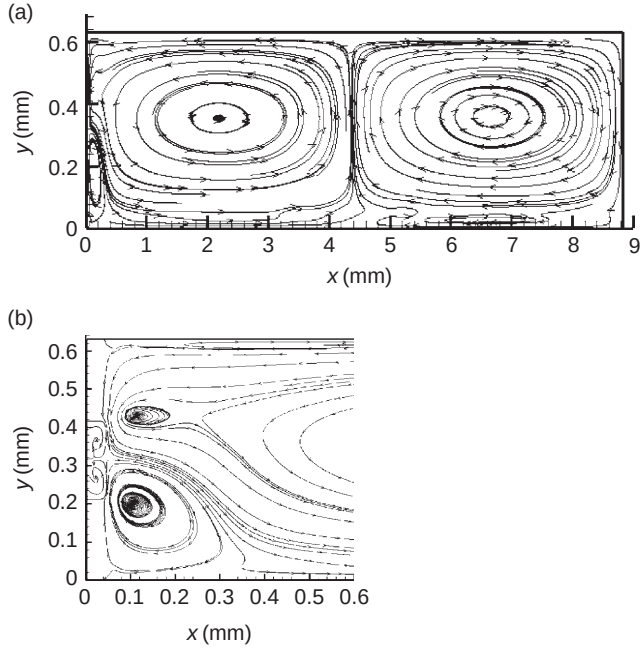

FIG. 47. Acoustic streaming, at 360th cycle, $y_0/\delta_v = 20$, $X_{\max} = 1.0 \times 10^{-5}$, 40% of left wall vibrating (Case 6B).

360 cycles) is given in Fig. 47. The results are similar to those reported earlier in Fig. 37 (for the full wall vibration). The effect of the partial wall vibration is only limited to the vicinity to the left wall, considering. Figure 48 shows the temperature contour in the steady state. It is closed to the results of heat conduction, because of the weak streaming velocity.

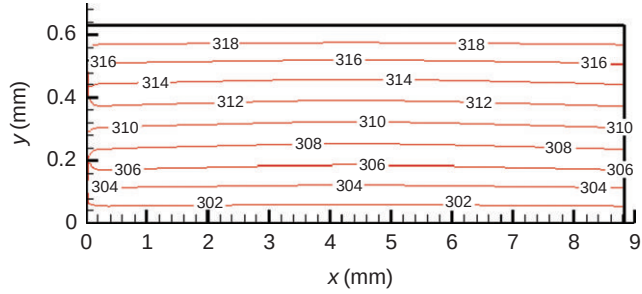

FIG. 48. Cycle-average temperature contour, in 360th cycle, heating, $y_0/\delta_v = 20$, $X_{\max} = 1.0 \times 10^{-5}$, 40% of left wall vibrates (Case 6B).

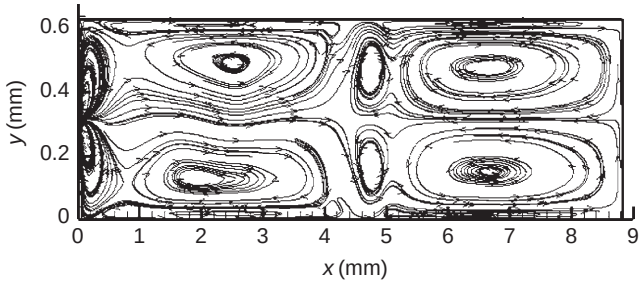

FIG. 49. Acoustic streaming, in 120th cycle, isothermal top and bottom walls, $y_0/\delta_v = 20$, $X_{max} = 1.0 \times 10^{-5}$, 10% of left wall vibrating (Case 7).

In Case 7, the vibrating part of the left wall is further deceased to 10%. The acoustic streaming when the top and bottom walls are kept at the initial temperature is shown in Fig. 49. The streaming structure becomes irregular from the case of whole wall vibration, because of stronger nonuniform boundary condition in the left wall and weaker acoustic streaming in the field.

3. *Conclusions*

The structure and strength of acoustic streaming excited by wall vibration, the effect of heating on acoustic streaming, and acoustic streaming induced thermal convection process in a nitrogen-filled closed enclosure were studied numerically. The formation of pressure (acoustic) waves and associated thermal and flows phenomena are dominated by the unsteady compressible Navier-Stokes equations with temperature dependent viscosity and conductivity. The steady second-order acoustic streaming is predicted by mechanically induced periodic oscillations in the fluid. After one wall temperature of the closed system is increased, the structure of the streaming is changed due to the nonuniform fluid properties. Furthermore, the streaming velocity increases when the temperature of the heated wall is increased. Hence, heating is another way to increase the acoustic streaming, other than increasing the amplitude of wall vibration. To a closed system, the wall vibration has mixed effects on the heat transfer along the walls. First, the mean velocity induced by acoustic streaming can enhance the heat transfer. Second, the acoustic power input to the system adds a new heat load to the cooling plate. Therefore, acoustic streaming is not always conducive to cooling down the hot source. Finally, the effect of partial wall vibration is studied. The nonuniform wall condition is found to be the significant effect on streaming structure. Acoustic streaming introduces an additional convective heat transfer mode into

systems in a zero gravity environment where it is assumed that conduction is the only heat transfer mode. The model developed can be a valuable tool in the optimized design of heat exchangers with acoustically enhanced performance and other applications of acoustic streaming.

IV. Numerical Study of Thermally Induced Acoustic Waves in Gases

A. Introduction

The physics of thermally induced acoustic waves and the effects of gravity on the flows induced are considered in this section. First, the early time behavior of acoustic waves produced by rapid heating in carbon dioxide gas are studied for initial pressures ranging from 0.1 MPa to 8.0 MPa. Here we try to understand the effects of the variation of fluid properties with pressure on the generation, propagation and damping of thermally induced acoustic waves. Then the flow fields generated by thermally induced waves under different gravity conditions are studied. The effects of gravity are investigated under two categories: sidewall heating and bottom wall heating.

B. Thermally Induced Acoustic Waves in Atmospheric and High Pressure Gases

1. Property Variations

An earlier study [54] showed that the behaviors of thermally induced acoustic waves are somewhat different for different gases, due to the variation of their properties. It is known that the effect of pressure on other thermodynamic properties is very small when the gas pressure is low. However, for a high-pressure fluid such as a real gas or super-critical fluid, the effect of pressure cannot be neglected. In this section, we investigate the behavior of thermally induced acoustic waves for carbon dioxide gas under different initial pressures. The pressure range is from 0.1 MPa to 8 MPa.

For high-pressure gas and super-critical fluid, the P-ρ-T relations are quite different from the ideal gas law, and the internal energy and sound speed are functions of temperature and density (or pressure). Instead of using published correlations for high pressure gases, which are limited in applicability, we use the NIST Standard Reference Database 12 [81] to evaluate the P-ρ-T relations and other thermodynamic properties for real gases and supercritical fluids.

Figure 50 gives the variation of density for carbon dioxide as a function of pressure (from 0.1 to 8.0 MPa) for different temperatures. The density is strongly nonlinear with respect to pressure. Figure 51 shows the variation

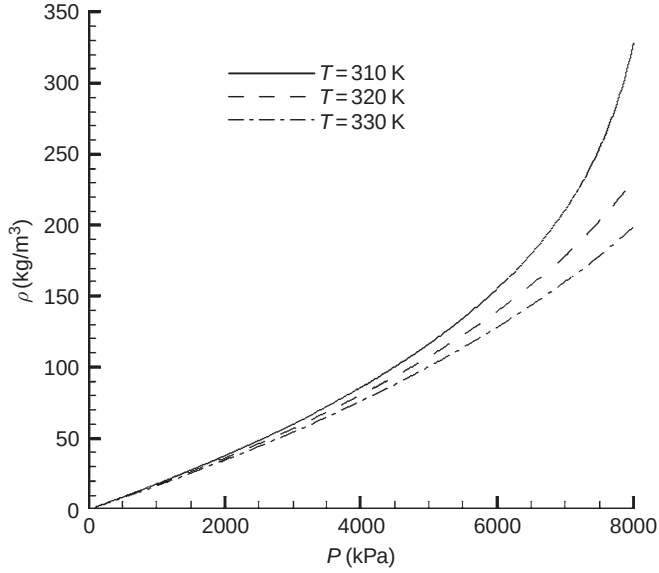

FIG. 50. Variation of density for carbon dioxide as a function of pressure at constant temperatures.

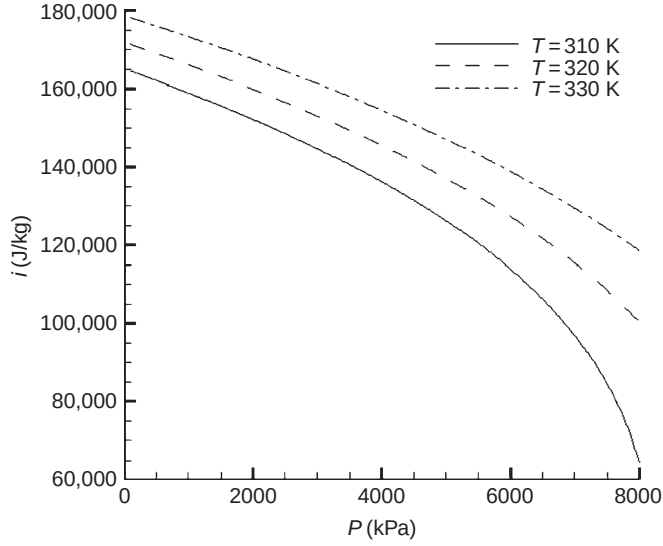

FIG. 51. Variation of internal energy for carbon dioxide as a function of pressure at constant temperatures.

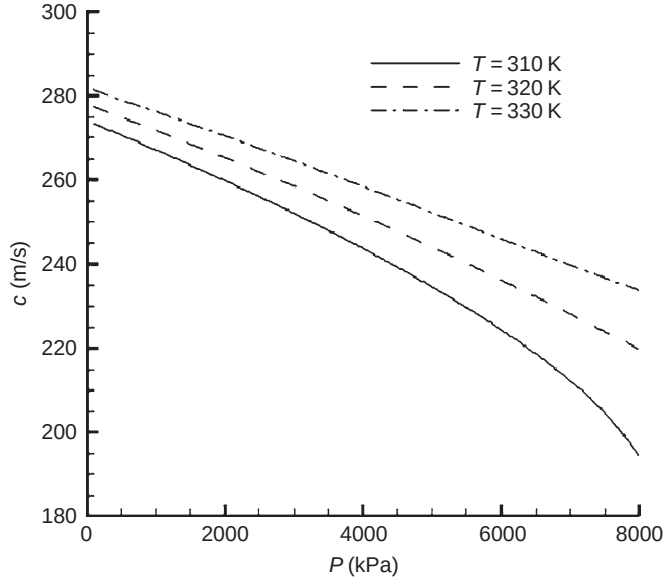

FIG. 52. Variation of sound speed for carbon dioxide as a function of pressure at constant temperatures.

of internal energy as a function of pressure at different temperatures. It is interesting to observe that at high pressure, the internal energy is not only a function of temperature, but also a function of pressure (density). The other thermodynamic properties, such as sound speed, viscosity and heat conductivity are also shown in Figs. 52–54. All fluid properties show strong dependence on pressure, and these relationships become more dramatic when pressure approaches the critical point, $P_{crit} = 7.377$ MPa, $T_{crit} = 304.128$ K.

To use the data provided by the NIST Standard Reference Database 12 in our computational model, polynomial fits were obtained to build the property equations in the specific data regions. The six relation equations are used in the numerical models: $P = f(T, \rho)$, $i = f(T, \rho)$, $c = f(T, \rho)$, $\mu = f(T, \rho)$, $k = f(T, \rho)$, $T = f(i, \rho)$.

2. Problem Statement

The effects of pressure on the thermally induced acoustic waves are reported for a two-dimensional cavity ($L = 0.001$ m) containing carbon dioxide. As shown in Fig. 55, the sidewalls of the cavity are held at specified temperatures and the horizontal surfaces are thermally insulated. Initially,

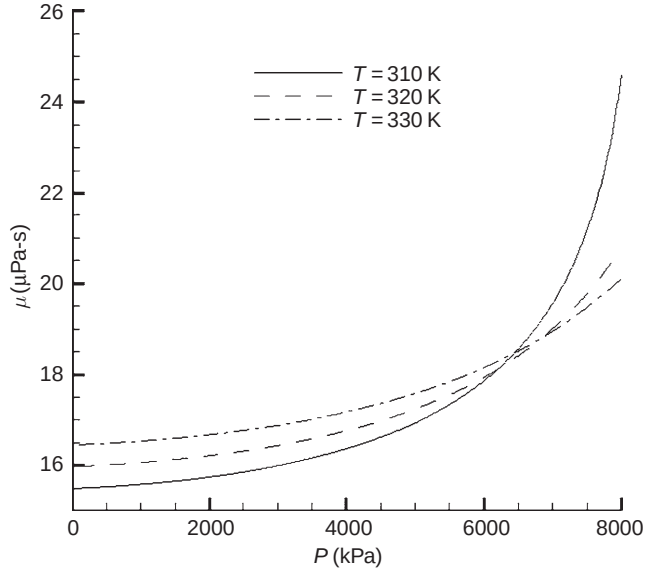

FIG. 53. Variation of viscosity for carbon dioxide as a function of pressure at constant temperatures.

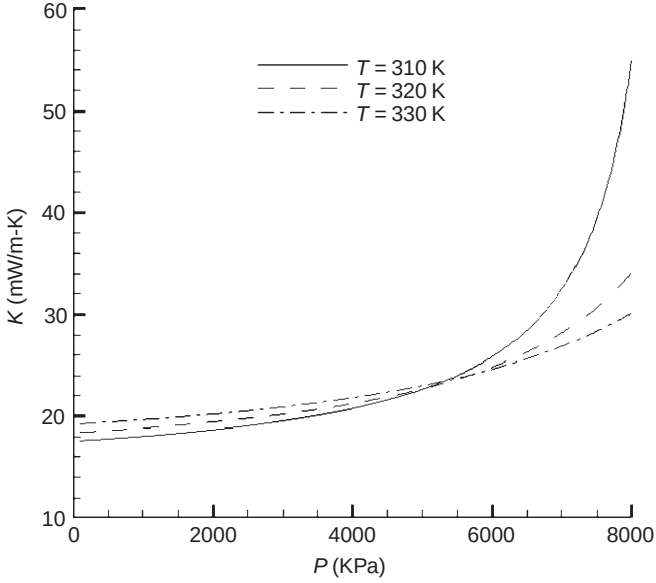

FIG. 54. Variation of heat conductivity for carbon dioxide as a function of pressure at constant temperatures.

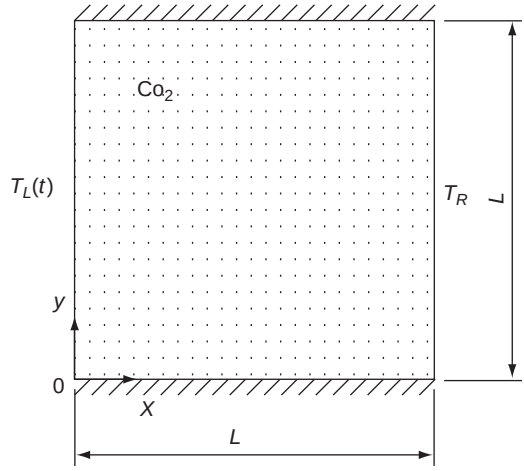

FIG. 55. Geometry and boundary conditions of the problem.

the fluid is quiescent ($u = v = 0$ everywhere) at a constant temperature and pressure (P_0 and T_0). At the given time, the temperature along the left vertical wall is raised impulsively or gradually, while the right wall is kept at the initial temperature. This triggers a thermally induced acoustic wave in the medium. The temperature history of the left wall is governed by the following equation:

$$T_L(t) = T_0\left[1 + \left(\frac{T_{\max} - T_0}{T_0}\right)\left(1 - e^{-\frac{t}{\tau_h}}\right)\right] \qquad \text{(IV.1)}$$

In Eq. (IV.1), $T_{\max}$ is the maximum temperature that the heated left wall can attain. The increase rate of the wall temperature can be controlled by varying the time constant τ_h value in Eq. (IV.1). All the cases presented in this section were carried out for a zero gravity condition.

3. *Results and Discussions*

To study the behavior of the thermally induced acoustic wave for different fluid pressures, eight cases are simulated, as shown in Table V. For all cases, the initial temperature in the enclosure is assumed to be 310 K and the right wall temperature was impulsively raised to 320 K. For Case 1, $P_0 = 0.1$ MPa where ideal gas assumptions can be used. From Case 2 to 7, the initial enclosure pressure is increased gradually and $P_0 = 8$ MPa for Case 8. For this case ($T_0 = 310$ K, $P_0 = 8$ MPa) carbon dioxide exists as a supercritical

TABLE V
LIST OF COMPUTATIONAL CASES

Case	T_0 (K)	P_0 (MPa)	Properties table		T_{max} (K)	τ_h (s)
			ρ (kg/m^3)	T (K)		
1	310	0.1	1.62–1.90	308–324	320	3.57×10^{-7}
2	310	1	16.9–18.4	308–324	320	3.57×10^{-7}
3						
4	310	3	55–61	308–324	320	7.14×10^{-7}
5						
6	310	5	78–120	308–324	320	3.57×10^{-7}
7	310	7	170–221	308–324	320	3.57×10^{-7}
8	310	8	210–450	308–324	320	3.57×10^{-7}

fluid. The density and temperature ranges showed in the table were used to construct the property relations from the NIST Reference Database 12.

The time constant $\tau_h = 3.57 \times 10^{-7}$ s for Case 1. For this Case, the ideal gas law applies. Figure 56 shows the computed pressure variation at the mid point of the enclosure for Case 1. Results are shown for the cases where the

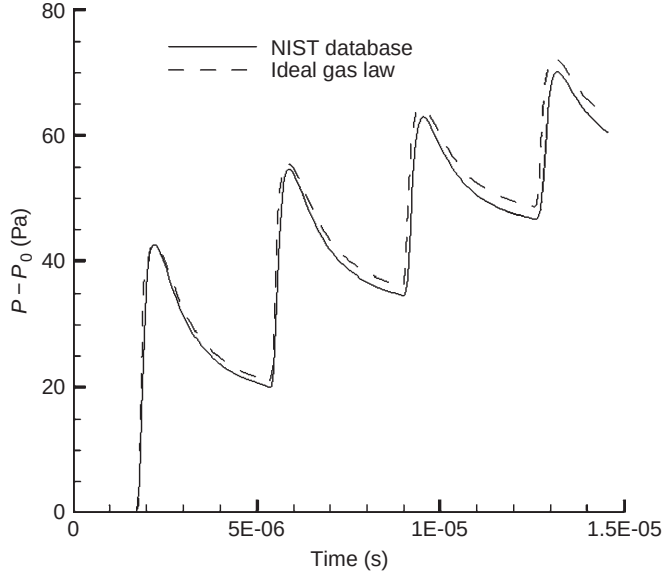

FIG. 56. Variation of pressure at the mid point of the enclosure: (a) ideal gas law and (b) NIST database, case 1 (P_0=0.1 MPa, $\tau_h = 3.57 \times 10^{-7}$ s).

P-ρ-T relation is either obtained from the ideal gas law or the NIST Reference Database 12. The two relations predict the same wave speed and very similar wave shape. The pressure in the middle point remains unchanged until the acoustic wave reaches it. The local pressure rises almost instantaneously, and then decreases gradually. After the pressure wave passes the middle point, it hits the right wall and then is reflected. Eventually, these repeated oscillations are damped due to viscous dissipation. The overall pressure in the chamber increases because of the energy input to the system by the heated left wall.

For the remaining cases (high pressure), we obtained the P-ρ-T and other property relations from the NIST Reference Database 12. Figure 57 shows the variation of pressure with time at the mid point of the enclosure for Case 3 ($P_0 = 3$ MPa, $T_0 = 310$ K). The corresponding of time variation of x-velocity component at the middle point is given in Fig. 58.

The effect of the rapidity of the wall heating process on the thermally induced wave behavior was investigated and the results are shown in Fig. 59. The heating rate is controlled by selecting the value of τ_h in Eq. (IV.1). The rapidity of the wall heating process has a very significant effect on the strength of the pressure wave.

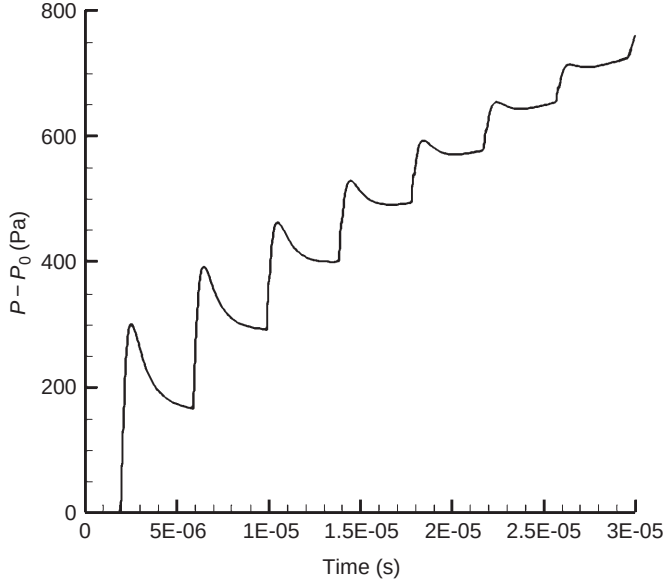

FIG. 57. Variation of pressure with time at the mid point of the enclosure, P_0=3 MPa, $\tau_h = 3.57 \times 10^{-7}$ s (Case 3).

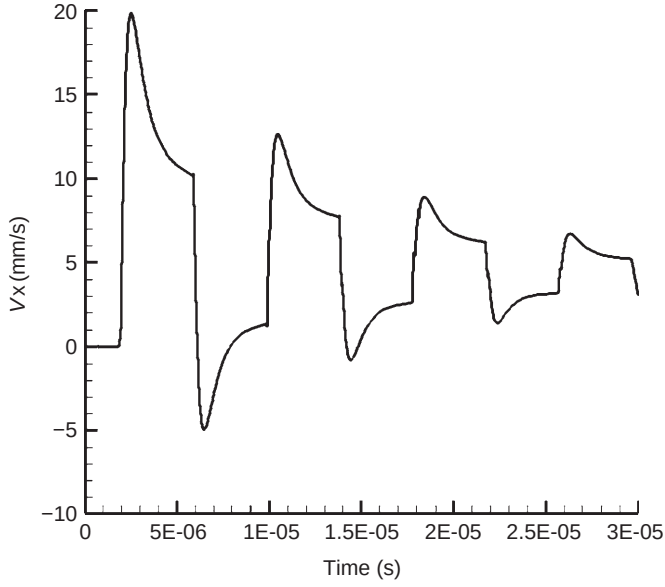

FIG. 58. Variation of velocity with time at the mid point of the enclosure, P_0=3 MPa, $\tau_h = 3.57 \times 10^{-7}$ s (Case 3).

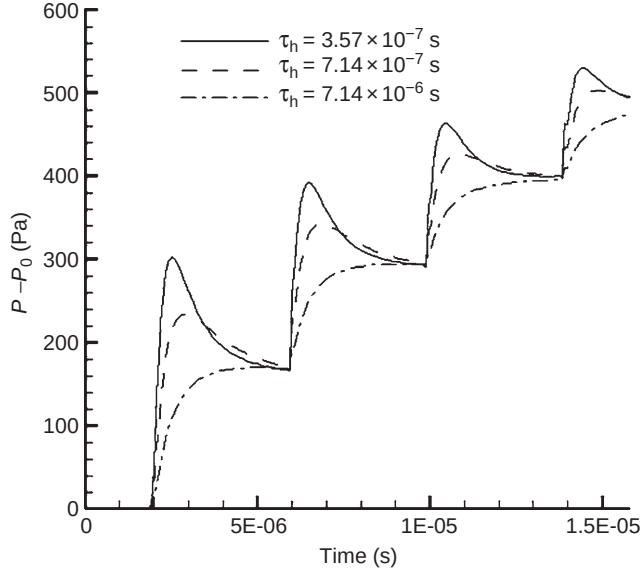

FIG. 59. Variation of pressure at the midpoint of the enclosure for different heating rates, $P_0 = 3$ MPa (Cases 3, 4 and 5).

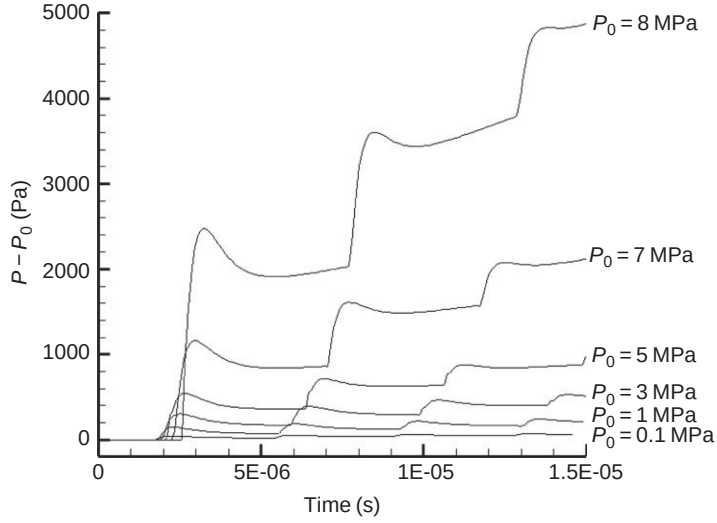

FIG. 60. Variation of pressure at the mid point of the enclosure for different initial pressures, $\tau_h = 3.57 \times 10^{-7}$ s (cases 1, 2, 3, 6, 7 and 8).

The effect of the initial pressure on the thermally induced acoustic wave is shown in Fig. 60 for cases 1–3 and 6–8 (Table V). All six cases have the same initial temperature, maximum wall temperature and heating rate. Carbon dioxide is at supercritical conditions for Case 8. Although the shapes of pressure wave are very similar for all cases, stronger acoustic waves are observed when the initial pressure is higher. The pressure also increases faster in cases with higher initial pressure. It is also observed that the waves damp out much faster for higher initial pressure conditions, because of higher viscosity. No qualitative difference is observed for Case 8 (supercritical fluid conditions). It is noted that initial conditions for Case 8 ($P_0 = 8$ MPa, $T_0 = 310$ K) is not near the critical point ($P_{crit} = 7.377$ MPa, $T_{crit} = 304.128$ K). The behavior of thermoacoustic waves near the critical point are further explored in Section VI.

Figure 61 shows the variation of temperature at the mid point of the enclosure for the above cases as shown in Fig. 60. It is interesting to note that the strongest temperature wave occurs when P_0=0.1 MPa, then that the wave amplitude decreases with initial pressure increase until the weakest temperature wave is observed in the case with $P_0 = 3$ MPa. After that, the temperature waves become stronger with initial pressure increase.

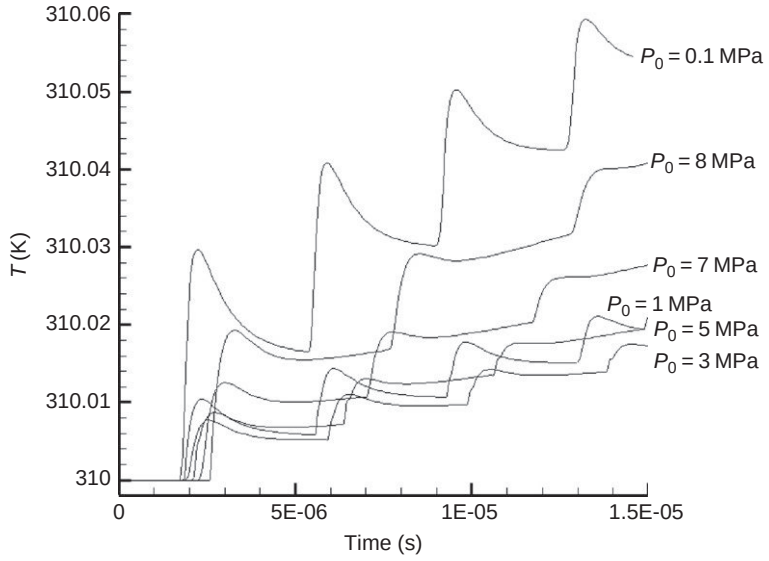

FIG. 61. Variation of temperature at the mid point of the enclosure for different initial pressures, $\tau_h = 3.57 \times 10^{-7}$ s (Cases 1, 2, 3, 6, 7 and 8).

C. Interactions of Thermally Induced Acoustic Waves with Buoyancy Induced Flows: Side-Wall Heated Enclosures

1. *Problem Statement*

The flow field generated by a thermally induced acoustic wave and the effect of gravity on this field are studied in a square enclosure filled with nitrogen gas at 1 atm. and 300 K. The heating is applied on the left wall of the square enclosure, which has a side of length $L = 13$ mm (Fig. 62). The horizontal walls of the square enclosure are adiabatic. Initially the gas and all of the walls are in thermal equilibrium ($T = T_R$ everywhere). At later times $t > 0$, the left-wall temperature is increased to T_L ($T_L > T_R$), either suddenly or gradually. We examine the effects of increases in temperature that are either spatially uniform or nonuniform.

2. *Results and Discussion*

Numerical simulations of the flows generated by thermally induced acoustic waves were performed in a square enclosure filled with nitrogen gas at 1 atm. and 300 K [82]. Results were obtained for four cases: uniform

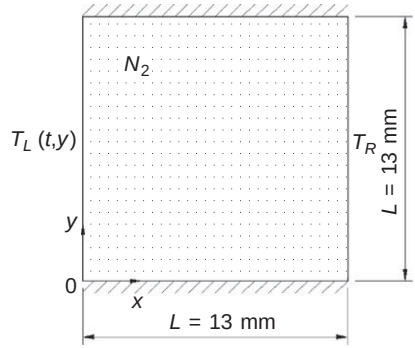

FIG. 62. Geometry and boundary conditions of the problem.

impulsive heating without gravity, uniform gradual heating without gravity, spatially nonuniform gradual heating without gravity, and spatially nonuniform gradual heating with gravity.

Results of a prior investigation [53] on the very short time behavior of the thermally induced acoustic waves generated by impulsive and gradual heating of a wall were in very good agreement with the results given in the literature. In the present study, longer time behavior of the velocity fields, produced by either step impulsive heating or gradual heating of the left wall was investigated under zero- and normal-gravity conditions. In the numerical scheme, "impulsive heating" can be approximated by changing the value of the temperature in the first time step. In the present computations, the first time step is small, 2.81×10^{-8} s, compared to the characteristic acoustic and diffusion times of the system.

a. Uniform Impulsive Heating at Zero Gravity. For impulsive heating, the temperature of the left wall is given as

$$T_L(t) = T_0[1 + A] \tag{IV.2}$$

where the overheat ratio A is given by

$$A = \frac{T_L - T_0}{T_0} \tag{IV.3}$$

and is equal to 1/3 for all cases presented for spatially uniform wall heating.

The variation of pressure at the mid point of the enclosure is shown in Fig. 63 for early times; a distinctive peak is observed whenever the thermally induced acoustic wave crosses the mid point. This wave periodically reflects

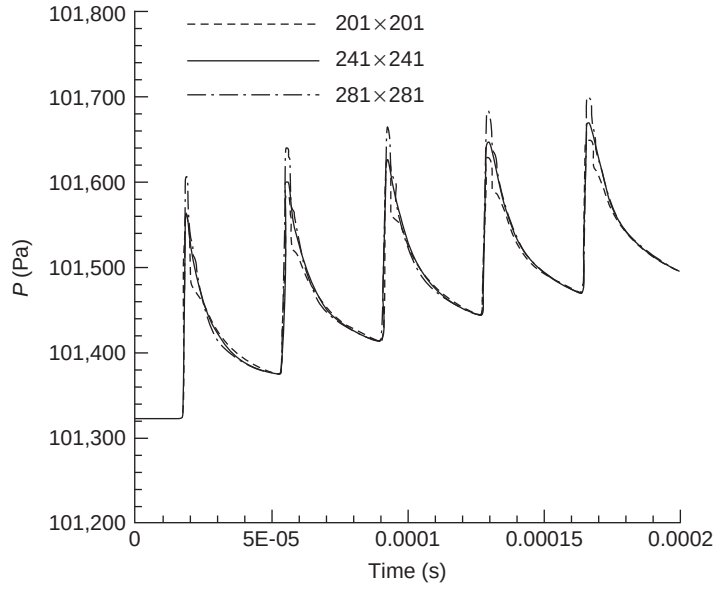

FIG. 63. Variation of pressure at the mid point of the enclosure for three grid sizes, under spatially uniform impulsive heating, zero gravity [82].

from both sidewalls as seen by the multiple peaks. We have shown earlier that the strength of the pressure wave is strongly correlated to the overheat ratio and that the pressure oscillations damp out with increasing time. Computational cells were nonuniformly distributed with fine grids near the boundary, and the ratio of the maximum to minimum grid size was 5.0. The results for a resolution study using three mesh sizes, 201×201, 241×241 and 281×281, are also shown in Fig. 64; the initial time step was, however, the same for all three mesh sizes to represent identical impulsive heating for all cases. From this figure, a mesh size of 241×241 was found to be adequate for the present computations. The time variation of the pressure and the x-component of the velocity at the mid point of the enclosure are shown in Fig. 65 a short time after the impulsive heating. The x-component of the velocity fluctuates between positive and negative values, depending on the direction of the oncoming pressure wave.

The velocity vectors in Fig. 65 show the flow field that developed from the wave motion created by impulsive heating at two different instants (25.78 and 100 ms). Due to spatially uniform heating and zero-gravity conditions, the flow field is essentially symmetric along the horizontal mid plane. Flow structures develop along the top and bottom left corners due to viscous

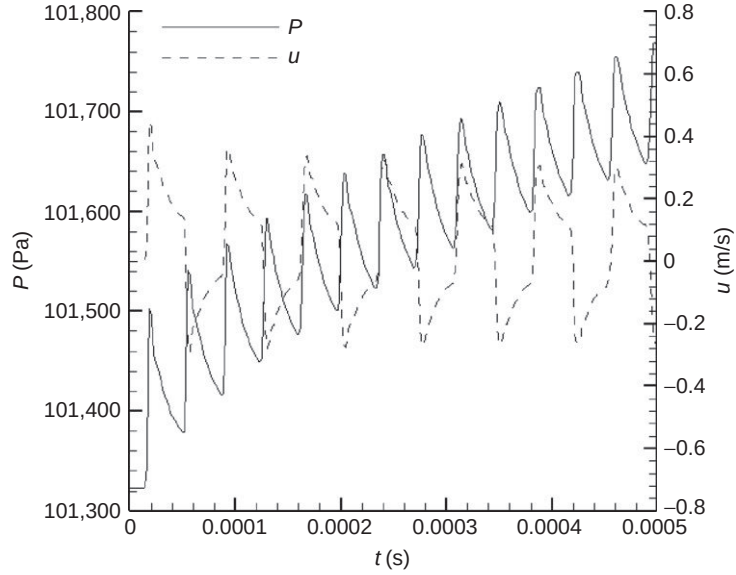

FIG. 64. Variation of pressure and the x-component of velocity at the mid point of the enclosure for early times, under spatially uniform impulsive heating, zero gravity.

interactions between the solid surfaces and bulk fluid. The strength of the flow field decreases considerably at 100 ms compared to its value at 25.78 ms. In Fig. 66, we show the temporal variation of the x-component of the velocity at the mid point for 100 ms. The thermally induced acoustic wave undergoes many reflections from the sidewalls during this period. The dark regions reflect the highly oscillatory nature of the flow field. The x-velocity component decays with every reflection and by 100 ms, the value becomes quite small; however, a flow field still exists within the enclosure as shown earlier in Fig. 65(b).

b. Spatially Uniform Gradual Heating under Zero Gravity. The thermal inertia of walls and heating systems as well as unavoidable heat losses to the environment make it difficult in practice to generate a step change (impulsive heating) in the wall temperature. Here we study the effect of more gradual heating by using an exponential expression for the wall heating:

$$T_L(t) = T_0\left[1 + A\left(1 - e^{-\frac{t}{\tau_h}}\right)\right] \tag{IV.4}$$

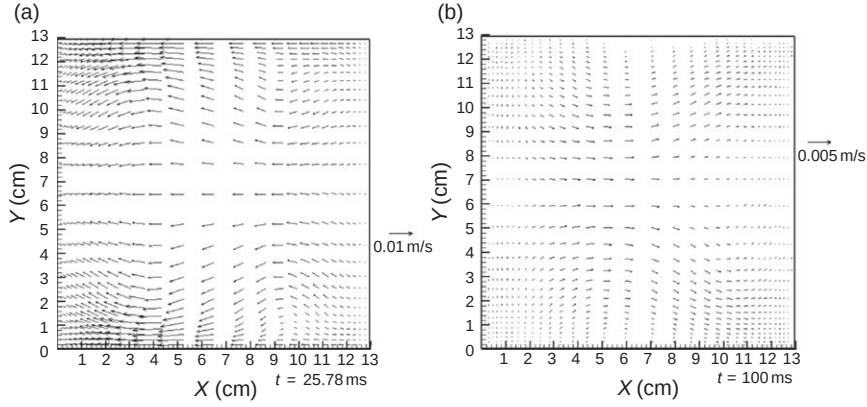

FIG. 65. Velocity vectors at two different times, under spatially uniform impulsive heating, zero gravity [82]: (a) 27.58 ms; (b) 100 ms.

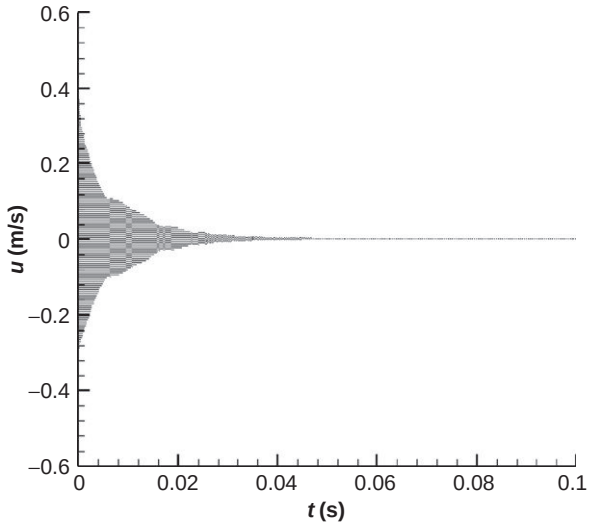

FIG. 66. Variation of the x-component of velocity with time at the mid point of the enclosure, under spatially uniform impulsive heating, zero gravity.

Here, τ_h is a time constant. For impulsive heating, τ_h tends to zero. Figure 67 shows the variation of the pressure and the x-component of the velocity at the mid point for early times with gradual wall heating and a time constant $\tau_h = 5\tau_c$, where τ_c is the travel time of sound waves over the length of the enclosure. In the same figure, the variation of the left wall temperature with

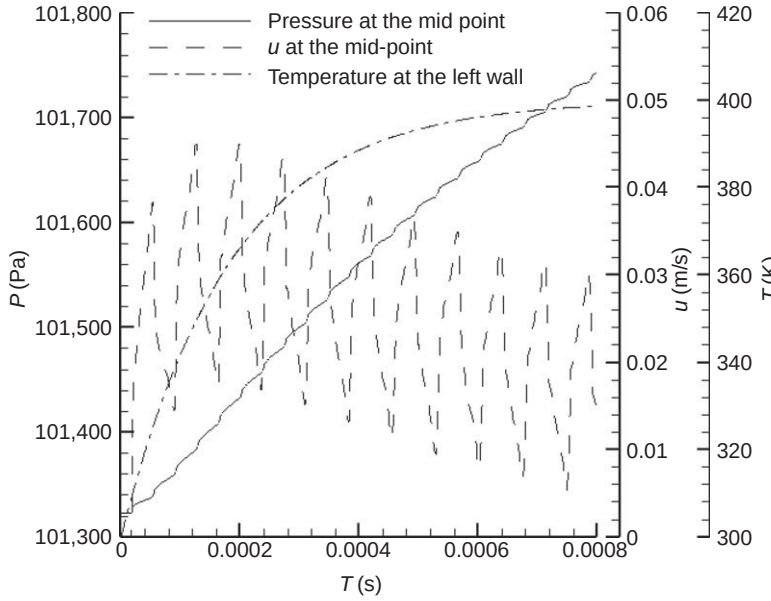

FIG. 67. Variation of pressure and the x-component of velocity at the mid point of the enclosure for early times, under spatially uniform gradual heating with $\tau_h = 5\tau_c$, 0 g.

time is shown. Comparing Fig. 67 with Fig. 62 we note that for gradual wall heating, the thermally induced acoustic wave is much weaker. As shown in Fig. 67, the pressure values at the mid point increase continuously; however, discrete jumps in its value are observed each time the wave crosses the center. The effect of gradual heating on the x-component of the velocity is interesting. The velocity component still fluctuates with time, but does not reverse sign as in Fig. 62, and hence the damping rate is slower in this case.

Figure 68 shows velocity vectors at two different times (25.78 and 100 ms) for the case described above. The velocity field is found to be similar to that for the case of impulsive heating; it is symmetric along the horizontal mid plane, and decays with time.

c. Spatially Nonuniform Gradual Heating at Zero Gravity. For the spatially nonuniform gradual heating situation, the left wall temperature is now given by

$$T_L(t) = T_0\left[1 + 2\bar{A}\frac{L-y}{L}\left(1 - e^{-\frac{t}{\tau_h}}\right)\right] \qquad \text{(IV.5)}$$

where a linear variation of the spatial temperature distribution is considered.

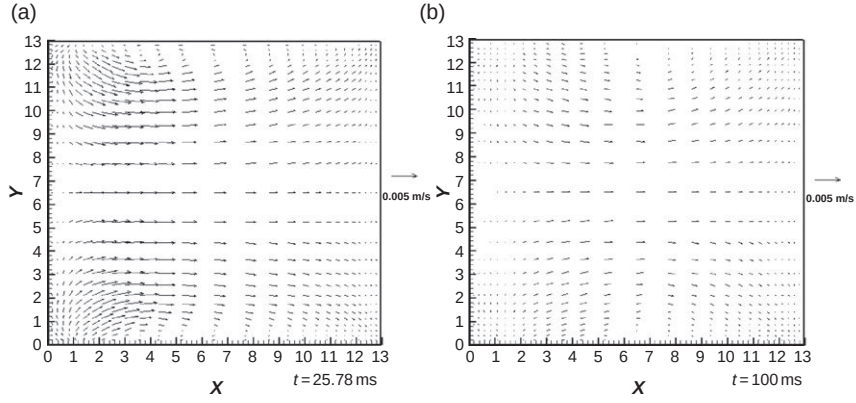

FIG. 68. Velocity vectors at two different times, under spatially uniform gradual heating with $\tau_h = 5\tau_c$, zero gravity: (a) 27.58 ms; (b) 100 ms.

Figures 69 (a)–(d) show the development of velocity vectors from 0.074 ms to 100 ms. At 0.074 ms (Fig. 69 (a)), all fluid flows in the direction nearly normal to the vertical wall because the pressure disturbance is generated in the horizontal direction. Figure 69 (a) also shows that the horizontal velocity in the lower region of the enclosure (with higher wall temperature) is higher than that in the upper region, which demonstrates that the acoustic wave-induced flow is proportional to the temperature increase on the wall. Later, 7.37 ms, there is a recirculating flow pattern at the left top corner, as shown in Fig. 69 (b). With increasing time, this vortical flow field grows and covers the entire enclosure. Even at 100 ms, the flow field is quite strong. We saw earlier that spatially uniform gradual heating can generate a longer lasting flow field than impulsive heating with the same overheat ratio. Here we see that the strength of this flow field can further be enhanced with spatially nonuniform heating.

d. Spatially Nonuniform Gradual Heating under Normal Gravity. Now we consider the effect of gravity on the flows induced by acoustic waves. The conditions considered here are identical to those considered above, albeit at normal gravity conditions. Figures 70 (a)–(d) show the development of velocity vectors in the enclosure from 0.074 ms to 100 ms. At $t = 0.074$ ms, Fig. 70 (a), and $t = 7.37$ ms, Fig. 70 (b), the predicted flow fields are similar to the results shown in Figs. 69 (a) and (b) under zero-gravity conditions. The buoyancy-induced flow takes comparatively larger time to develop than the thermoacoustic wave-induced flows. The flow field shown in Fig. 70 (c) at $t = 25.78$ ms shows the signs of a developing buoyancy-induced flow along the left lower corner of the enclosure. With increasing time ($t = 100$ ms,

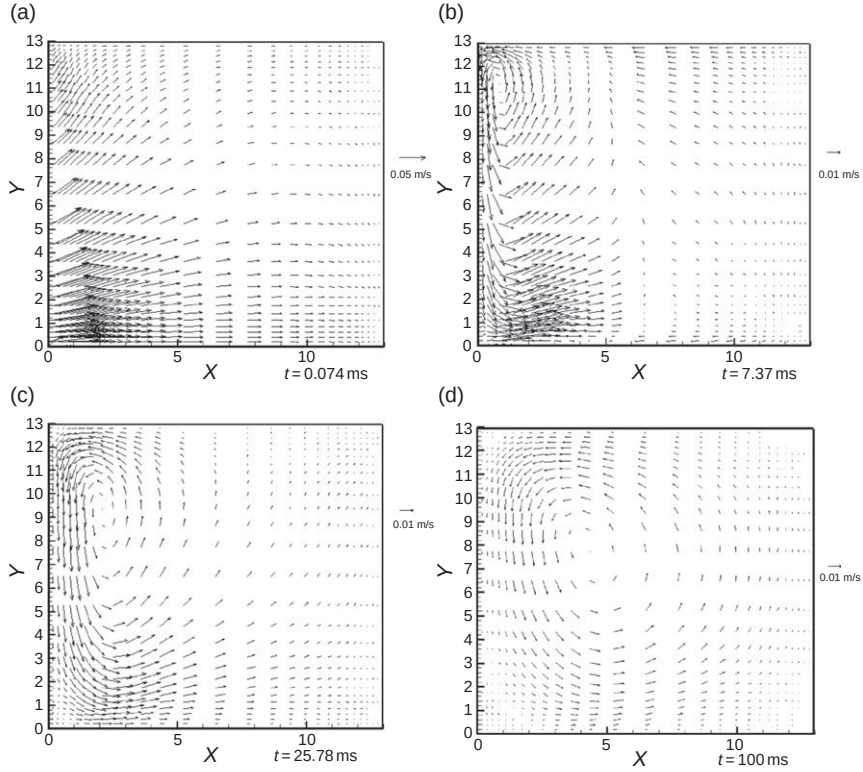

FIG. 69. Velocity vectors at four different times, under spatially non-uniform gradual heating with $\tau_h = 5\tau_c$, zero gravity: (a) 0.074 ms (b) 7.37 ms (c) 25.78 ms (d) 100 ms.

Fig. 70 (d)), this vortical flow field enlarges and covers the entire enclosure. The overall strength of the flow field in the enclosure at $t = 100$ ms under zero-, Fig. 69 (d), and normal-, Fig. 70 (d), gravity conditions are quite similar. The directions of the vertical flows, however, are in opposite directions. With increasing time, the flow field under normal-gravity conditions will represent a purely buoyancy induced flow field, and the flow field under zero-gravity conditions will damp out.

3. *Conclusions*

Table VI summarizes the results for the cases studied. Impulsive heating is found to generate strong thermoacoustic waves; however, the damping rate for the resulting velocity field is high. Gradual heating conditions studied produce

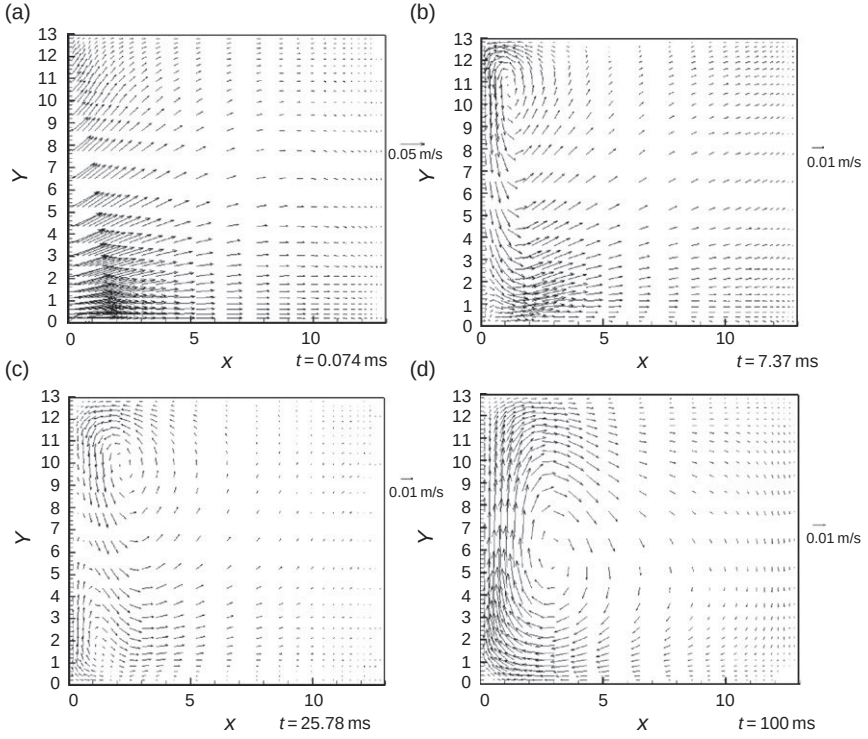

FIG. 70. Velocity vectors at four different times, under spatially non-uniform gradual heating with $\tau_h = 5\tau_c$, normal gravity: (a) 0.074 ms; (b) 7.37 ms; (c) 25.78 ms; and (d) 100 ms.

weaker acoustic waves but they tend to produce flow fields that can sustain for longer periods. Spatially nonuniform heating is found to produce faster flows in the region with higher heating and eventually results in recirculating flow fields in the enclosure. For the conditions studied, the effect of gravity on the flow fields is only evident after about 25 ms from the start of the heating process. Buoyancy induced flow field strength at 100 ms was similar to that obtained by thermally induced acoustic wave-induced flow at zero gravity.

D. Interaction of Thermally Induced Acoustic Waves with Buoyancy Induced Flows: Bottom-Wall Heated Enclosure

1. Problem Statement

In this section, the interactions of thermally induced acoustic waves with the buoyancy induced flow are reported for bottom heated rectangular

TABLE VI
SUMMARY OF THE MAIN OBSERVATIONS [82]

Case	Description	Observations from results for short times	Observations from results at longer times
1	Uniform impulsive heating at zero gravity	1. Strong thermally induced pressure waves	1. Essentially one-dimensional flow field is developed in the enclosure
		2. Horizontal velocity component reverses sign after reflection from a sidewall	2. The damping rate for the flow field is high
2	Spatially uniform gradual heating under zero gravity	1. Weak thermally induced pressure waves	1. Two-dimensional flow field is developed in the enclosure, near the corners of the heated wall
		2. Horizontal velocity component fluctuates in value after reflection from a sidewall but does not reverse sign	2. The damping rate for the flow field is slow and the flow field appears to be quasi-steady
3	Spatially nonuniform gradual heating at zero gravity	1. Pressure waves are insensitive to the variation of the heating rate along the vertical direction	1. Two-dimensional counter-clockwise vortical flow field is established
		2. Horizontal velocity component values are higher at the lower region of the enclosure (higher heating rate)	2. The damping rate for the flow field is low
4	Spatially nonuniform gradual heating under normal gravity	1. Effect of gravity is not observed	1. Effect of gravity (buoyancy) becomes evident
		2. Pressure waves are insensitive to the variation of the heating rate along the vertical direction	2. The counter-clockwise flow field created by spatially nonuniform heating is replaced by a strong clockwise vortical flow
		3. Horizontal velocity component values are higher at the lower region of the enclosure (higher heating rate)	3. Overall strength of the flow field at 100 ms is similar to that observed in Case 3.

enclosures [83]. We consider enclosures with varying aspect ratios: $H/L = 0.5$, 1.0 and 5.0. The vertical walls of the rectangular enclosure are considered to be insulated. Initially the gas and all walls are in thermal

equilibrium ($T = T_0$ everywhere). At $t > 0$, the bottom wall temperature is increased rapidly to a value T_b ($T_b > T_0$) in the following manner:

$$T_b(t) = T_0\left[1 + \frac{T_{max} - T_0}{T_0}\left(1 - e^{-\frac{t}{\tau_h}}\right)\right] \tag{IV.6}$$

Meanwhile, the top wall is held at the initial temperature ($T_t = T_0$). In Eq. (IV.6), T_{max} is the maximum temperature that the heated bottom wall can attain. The rate of increase of the bottom wall temperature can be controlled by varying the time constant τ value in Eq. (IV.6). This is important because the temperature increase rate has a significant effect on the strength of a thermally induced acoustic wave, according to previous studies [53]. For all calculations reported in this paper, the value of $(T_{max} - T_0)/T_0$ is set to 1/3. To study the effect of gravity on the flow field generated by a thermally induced acoustic wave, the computations were carried out for different gravity conditions, viz., +1.0 g, 0 g and –1.0 g.

2. *Results and Discussion*

Numerical simulations of thermally induced waves and buoyancy induced flow were performed in a rectangular enclosure filled with air. The initial pressure of air is 1 atm., and the initial temperature (T_0) is 300 K. The bottom wall is heated to 400 K (T_{max}) at different heating rates (varying τ_h), while the top wall is kept at the initial temperature. Results were obtained for the following seven cases (Table VII) to study the effects of gravity, heating rate, and aspect ratio (H/L) on the flow field and the heat transfer characteristics. For all cases studied, the width of the enclosure was considered to be $L = 0.02$ m.

For a mesh-resolution study, the computational results for the variation of temperature with y at the middle plane of the enclosure at $t = 1.27$ s, using three different mesh sizes, 80×80, 100×100 and 120×120, are shown in Fig. 71 for Case 1 (see Table VII). The time step (2.81×10^{-8} s) was the same for all three mesh sizes. From this figure, a mesh size of 100×100 was found to be adequate for the present computations for cases with $H/L = 1.0$. For cases with non-unity aspect ratios (Table VII), the mesh sizes were adjusted such that the grid density is approximately the same as found in the base case.

a. Effects of Gravity. Simulations were carried out for identical conditions with three different values of ζ, viz., 1.0 g, 0 g, and –1.0 g (Cases 1, 2 and 3, respectively). The aspect ratio of the enclosure is fixed at 1.0 for all of the above three cases, and the time constant of the heating process is also kept at 5.76×10^{-5} s. This value is given by the time for an acoustic wave to

TABLE VII
LIST OF COMPUTATIONAL CASES

	L(m)	H/L	Heating rate τ_h (s)	Gr_H	Gravity ζ (g)
1	0.02	1.0	5.76×10^{-5}	5.27×10^4	+1.0
2	0.02	1.0	5.76×10^{-5}	–	0
3	0.02	1.0	5.76×10^{-5}	5.27×10^4	–1.0
4	0.02	1.0	2.88×10^{-4}	5.27×10^4	+1.0
5	0.02	1.0	1.15×10^{-2}	5.27×10^4	+1.0
6	0.02	0.5	5.76×10^{-5}	6586	+1.0
7	0.02	5.0	5.76×10^{-5}	6.59×10^6	+1.0

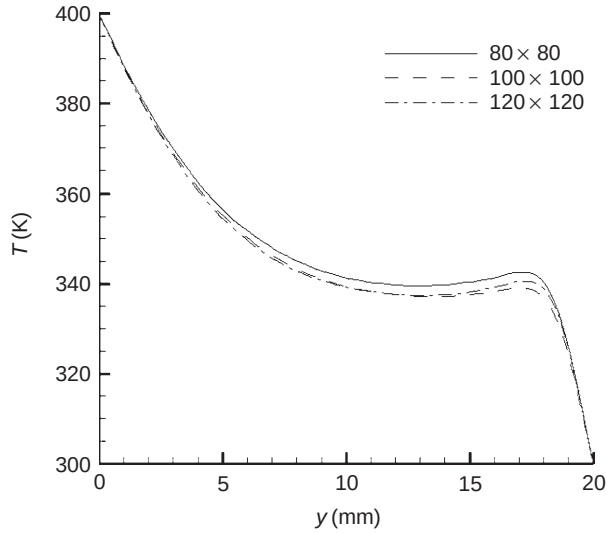

FIG. 71. Variation of temperature with y along the horizontal mid plane of the enclosure at $t = 1.27$ s ($H/L = 1$, $\tau_h = 5.76 \times 10^{-5}$ s, +1.0 g), by different grid sizes.

travel from the bottom of the enclosure to the top under normal atmospheric conditions.

The predicted variations of pressure at the midpoint of the enclosure for all three cases are shown in Figs. 72(a) and (b). A distinctive peak is observed whenever the thermally induced pressure wave crosses the mid point. This wave, traveling at slightly supersonic speed, periodically reflects from both sidewalls as seen by the multiple peaks. The shapes of the pressure waves are also found to be nearly same for the different gravity conditions at early times (Fig. 72 (a)). The pressure variations are plotted over a larger

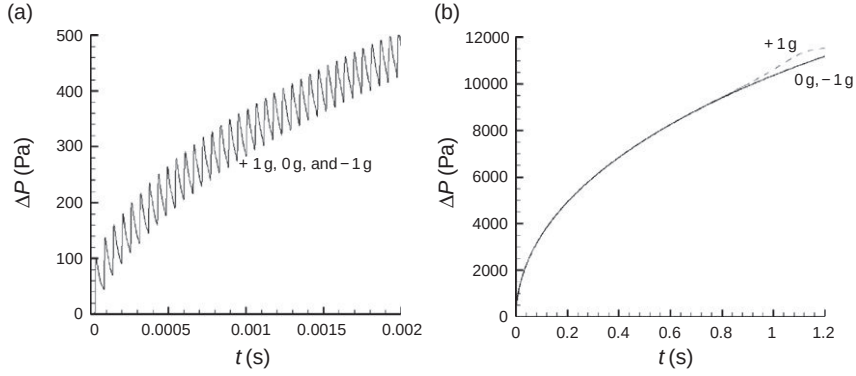

FIG. 72. Variation of pressure ($p - p_i$) with time at the mid point of the enclosure ($H/L = 1$, $\tau_h = 5.76 \times 10^{-5}$ s), under different gravity conditions (+1.0 g, 0 g and −1.0 g).

time-scale in Fig. 72 (b) and the oscillations shown in Fig. 72 (a) are no longer noticeable in the figure due to the change of scale in the pressure axis. For all three cases, the pressure rise behavior is identical. Minor differences only appear when the slower response buoyancy induced flow starts developing at larger times for Case 1 (Fig. 72 (b)). For Case 1, the center point is at the middle of a developing vortical flow, thus causing the incipient pressure rise.

The velocity vectors in Fig. 73 show the flow field developed by the wave motion due to the rapid heating of the bottom wall at an early time ($t = 0.058$ s)

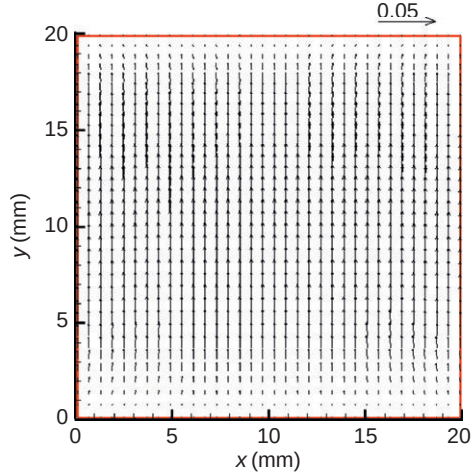

FIG. 73. Velocity vectors at $t = 0.058$ s ($H/L = 1$, $\tau_h = 5.76 \times 10^{-5}$ s), 1.0 g.

for Case 1. Due to spatially uniform heating, the flow field is essentially symmetric along the vertical middle plane. Flow structures develop along the top and bottom corners due to viscous interactions between the solid surfaces and bulk fluid. Results for Cases 2 and 3 (at $t = 0.058$ s) show essentially no difference from those shown in Fig. 73. The flow fields at a larger time ($t = 0.58$ s), however, start to display the distinct effects of gravity on the acoustic wave induced flow field, as shown in Figs. 74(a), (b) and (c) for Cases 1, 2 and 3, respectively. For the case of +1.0 g two characteristic eddies are formed due to the bottom heated buoyancy induced flow. For the cases of 0 g

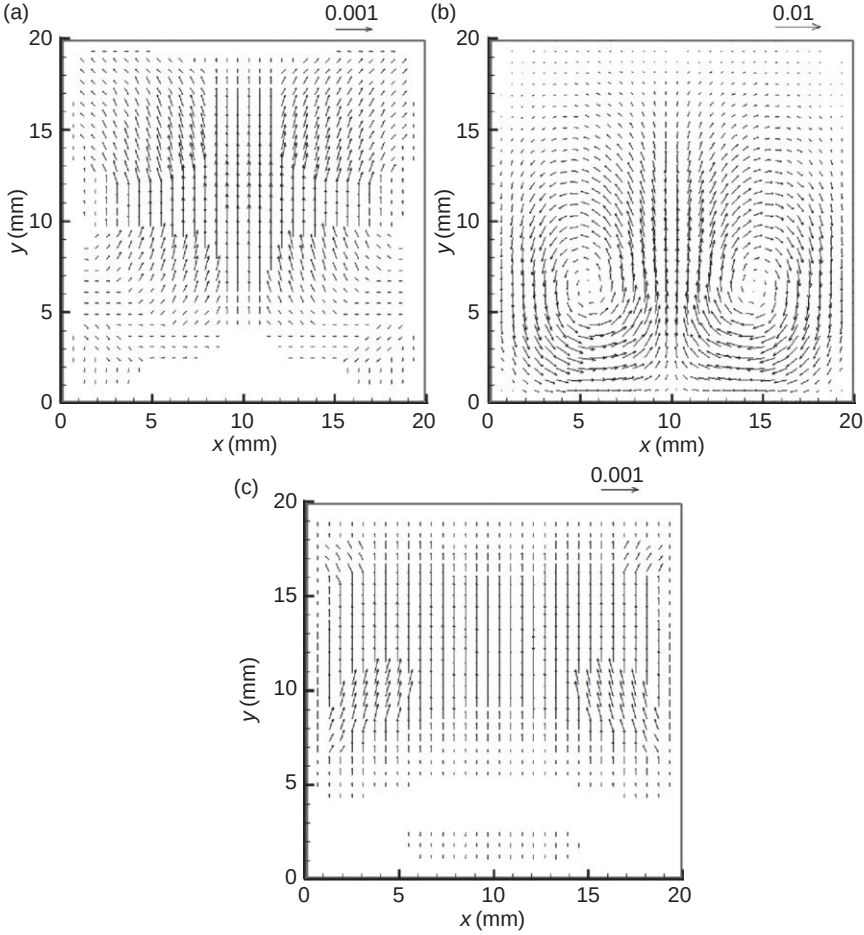

FIG. 74. Velocity vectors at $t = 0.58$ s ($H/L = 1$, $\tau_h = 5.76 \times 10^{-5}$ s): (a) +1.0 g; (b) 0 g (c) –1.0 g.

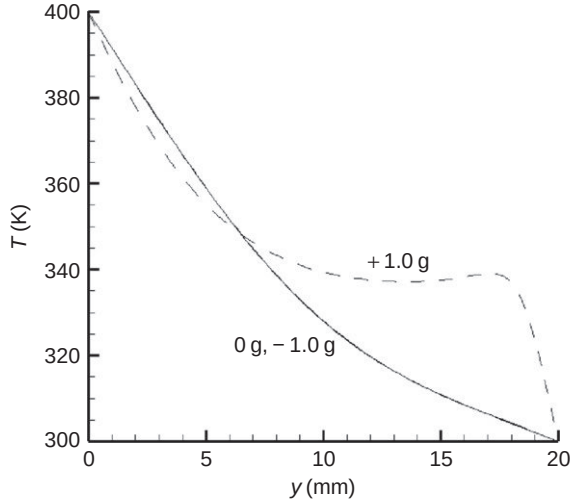

FIG. 75. Variation of temperature with y at the mid point of the enclosure at $t = 1.27$ s ($H/L = 1$, $\tau_h = 5.76 \times 10^{-5}$ s), under different gravity conditions.

(Fig. 74 (b)) and –1.0 g, the flow fields generated by the acoustic waves are considerably damped, due to viscous diffusion. The dampening is further enhanced by the stratified density field that is created in the opposed gravity (-1.0 g) case.

Figure 75 shows the instantaneous temperature profiles along the vertical mid plane for Cases 1, 2 and 3 at $t = 1.27$ s. In the cases of 0 g (Case 2) and -1.0 g (Case 3), the temperature profiles tend to be nearly linear, because heat conduction and acoustic compression and rarefaction influence the temperature distribution (no recirculating flow development). However, for the case of $+1.0$ g (Case 1), sharp temperature gradients are observed near the two horizontal walls and an inversion to the temperature profile occurs near the middle of the enclosure due to a developing vortical flow.

b. Effects of Heating Rate. Next, we studied the effect of heating rate (as characterized by the value of τ in Eq. (IV.12)). Simulations were carried out for varying values of τ_h: 5.76×10^{-5}, 2.88×10^{-4} and 1.15×10^{-2} s as shown in Table VII (Cases 1, 4 and 5, respectively). The aspect ratio of the enclosure is fixed at 1.0 and the value of $\zeta = +1.0$ g for all three cases.

The variation of pressure at the mid point of the enclosure is shown in Fig. 76 for Cases 1, 4 and 5. The strength of the pressure wave and the

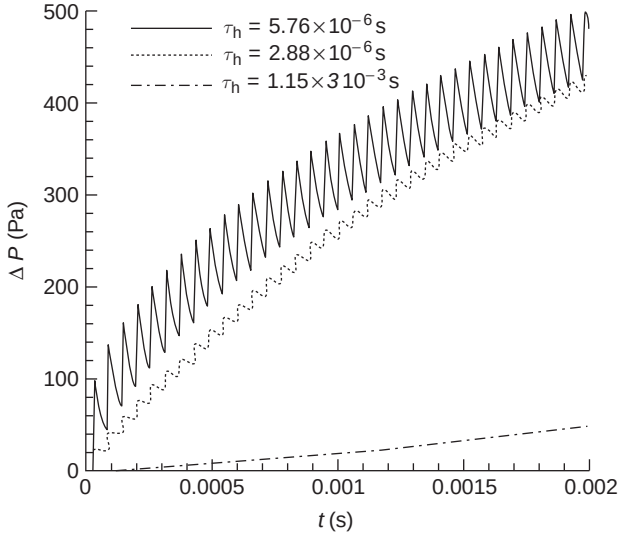

FIG. 76. Variation of pressure with time at the mid point of the enclosure ($H/L = 1.0, +1.0$ g), under different heating rates.

overall rate of pressure increase are found to be strongly correlated to the heating rate. The acoustic waves produced are rather weak when the heating rate is slower, as in Case 5 ($\tau_h = 1.15 \times 10^{-2}$ s).

For $\tau_h = 1.15 \times 10^{-2}$ s, the development of the flow field at $t = 0.058$ s is shown in Fig. 78. At this early time, the fluid motion is limited to the vertical direction as dictated by the acoustic waves. Comparing the results shown in Fig. 77 to those shown in Fig. 73 ($\tau_h = 5.76 \times 10^{-5}$, Case 1), the strength of the flow field is found to decrease considerably when the time constant of the heating rate is increased from 5.76×10^{-5} s (Case 1) to 1.15×10^{-2} s (Case 5). Thus at early times, for both values of τ, the flow field is dominated by the thermally induced pressure field and no buoyancy effects are evident.

Figure 78 shows the development of velocity vectors at $t = 0.58$ s for Case 5. The flow field begins to show the signs of a developing buoyancy induced flow. Two eddies are found to form near the bottom wall. Compared to similar results for Case 1 (Fig. 74 (b)), the velocity values are lower in Case 5 (Fig. 79). The strong acoustically induced flow field in case 1 excites the development of the buoyancy induced flow field in Case 1. The flow fields for Cases 1 and 5 will eventually become identical, as the acoustic waves damp out (as shown in Figs. 81(a) and (b) at $t = 1.27$ s).

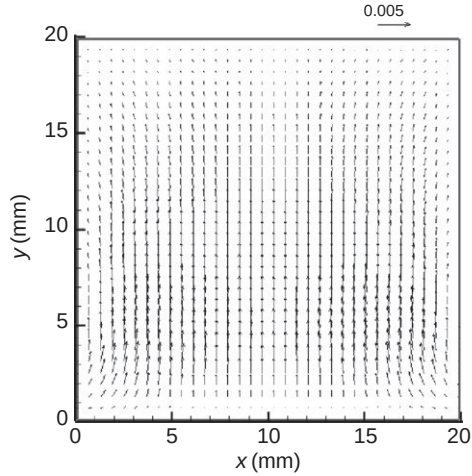

FIG. 77. Velocity vectors at $t = 0.058\,\text{s}$ $(H/L = 1.0, +1.0\,\text{g})$, under heating rate $\tau_h = 1.15 \times 10^{-2}\,\text{s}$.

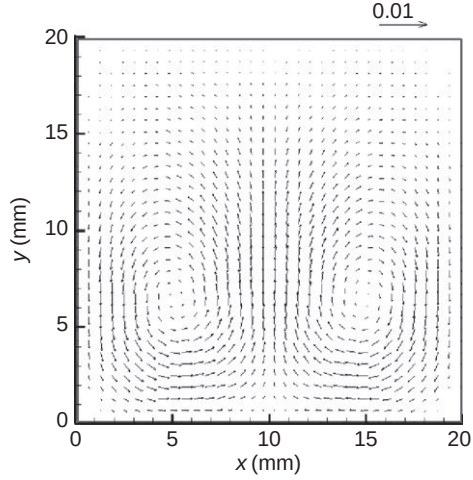

FIG. 78. Velocity vectors at $t = 0.58\,\text{s}$ $(H/L = 1.0, +1.0\,\text{g})$, under heating rate $\tau_h = 1.15 \times 10^{-2}\,\text{s}$.

c. Effects of Aspect Ratio. Simulations were carried out for varying values of aspect ratio $H/L = 1.0$, 0.5 and 5.0 as shown in Table VII (Cases 1, 6 and 7, respectively). The time constant of the heating rate is $\tau_h = 5.76 \times 10^{-5}\,\text{s}$ and the value of $\zeta = +1.0\,\text{g}$ for all three cases. The early time variation of pressure at the mid point of the enclosure is shown in Fig. 80 for Cases 1, 6 and 7.

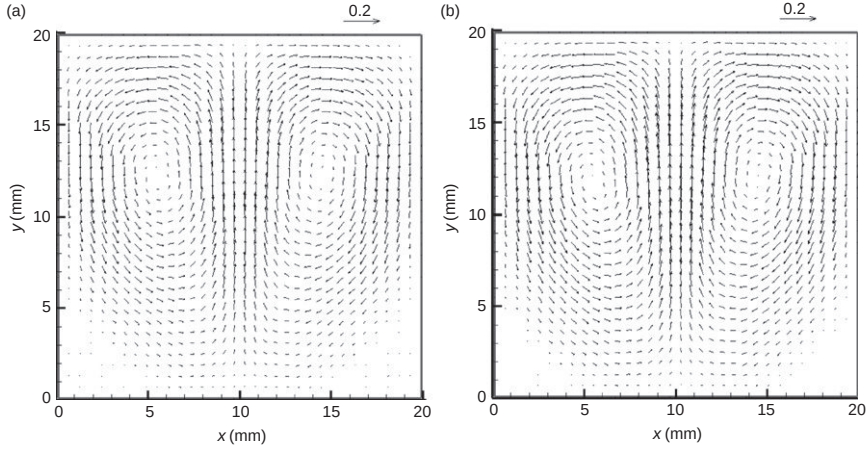

FIG. 79. Velocity vectors at $t = 1.27\,\mathrm{s}$ ($H/L = 1.0$, $+1.0\,\mathrm{g}$), under varying heating rates: (a) $\tau_h = 5.76 \times 10^{-5}\,\mathrm{s}$ (b) $\tau_h = 1.15 \times 10^{-2}\,\mathrm{s}$.

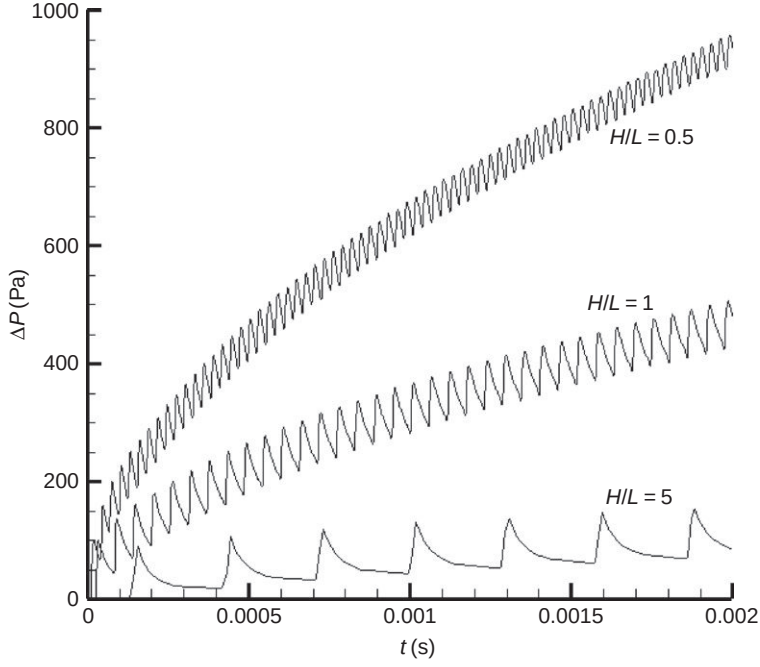

FIG. 80. Variation of pressure with time at the mid point of the enclosure ($\tau_h = 5.76 \times 10^{-5}\,\mathrm{s}$, $+1.0\,\mathrm{g}$), for different aspect ratios.

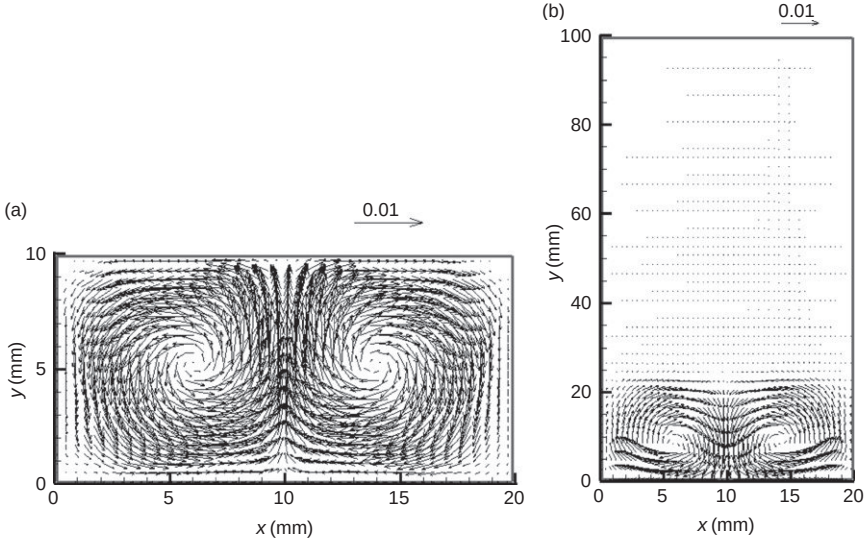

FIG. 81. Velocity vectors at $t = 1.27$ s ($\tau_h = 5.76 \times 10^{-5}$ s, +1.0 g), under different aspect ratios: (a) H/L=0.5 (b) H/L=5.0.

For an enclosure with the smallest aspect ratio ($H/L = 0.5$), the acoustic waves reverberate in the enclosure with a higher frequency and the pressure increase at the mid point is rapid. For larger aspect ratios, the above frequency decreases, as does the rate of increase of pressure at the mid point of the enclosure.

The flow fields at $t = 1.27$ s for Cases 6 and 7 (which have non-unity aspect ratios) are shown in Figs. 81(a) and (b). The corresponding plot for Case 1 was shown earlier in Fig. 81(a). In all cases, two eddies created by the buoyancy induced flow form near the bottom wall. In the case of $H/L = 5.0$ (Case 7) the eddies only affect the lower part of the domain, with the rest of the domain unaffected. For the tall enclosure (Case 7), the flow field was computed for an extended time. The velocity fields at $t = 3.8$ s and 7.02 s are shown in Figs. 82(a) and (b) for Case 7. A multicellular flow field develops for this case.

d. Conclusions. Interaction of the flow fields in an enclosure generated by acoustic waves (created by rapid heating of the bottom wall) and the buoyancy effects were studied by solving the unsteady compressible Navier-Stokes equations. The rapidity of the wall heating process is directly proportional to the strength of the pressure waves induced. The thermally

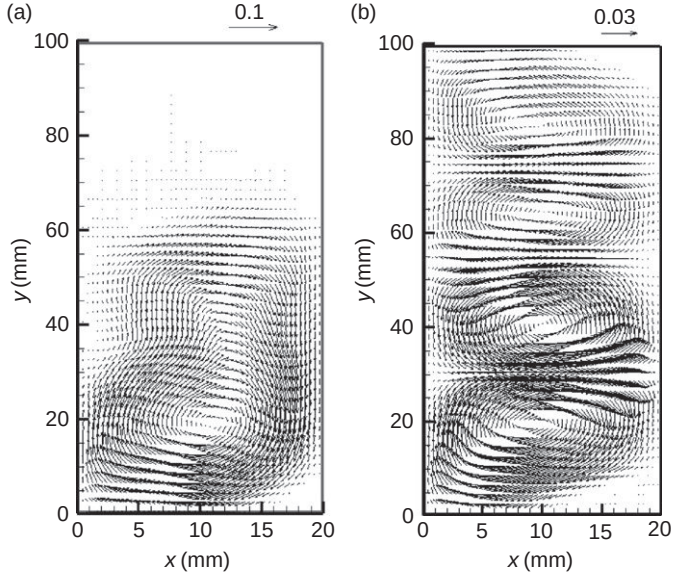

FIG. 82. Velocity vectors for H/L=5.0, $\tau_h = 5.76 \times 10^{-5}$ s, +1.0 g, at (a) $t = 3.8$ s; (b) $t = 7.02$ s.

induced waves create an essentially one-dimensional oscillatory flow in the enclosure, which damps out with time. The buoyancy induced flow is developed slowly compared to the acoustic wave-induced flows. In addition, the strength of the thermally induced waves has significant effects on the temporal development of the buoyancy induced flow. The stronger acoustic wave induced by faster heating will delay the development of buoyancy induced flow. It is also observed that the thermally generated flow field and the buoyancy induced flow field are both affected by the aspect ratio of the enclosure.

Acoustic waves can be generated in an enclosure by rapid heating of a wall for ideal gas, real gas or supercritical fluid. Similar pressure wave shapes are observed for all compressible fluids. However, the strength of pressure wave increases when the initial pressure increases, because of the variation of thermodynamic properties. The rapidity of the wall heating process is directly proportional to the strength of the pressure waves induced. Impulsive heating is found to generate a strong thermally induced acoustic wave; however, the damping rate for the resulting velocity field is high. Immediately after the heating, the thermally induced wave creates an oscillatory flow in the enclosure's flow field, which will then damp out with time. The buoyancy induced flow is developed slowly in comparison with the acoustic wave-induced flows, but it will reach at the steady state eventually.

In addition, the strength of the thermally induced wave has a significant effect on the temporal development of the buoyancy induced flow. It is also observed that the thermally generated flow field and the buoyancy induced flow field are both affected by the aspect ratio of the enclosure.

V. Experimental Study of Thermally Induced Acoustic Waves in Gases

A. Introduction

The behaviors of thermally induced acoustic waves generated by the rapid heating of a bounding solid wall in a closed cylindrical tube are investigated experimentally. In the experiments, a resistance-capacitance (R-C) circuit is used to generate a rapid temperature increase in a thin nickel foil located at one end of the closed cylindrical tube. The thermally generated pressure (acoustic) waves are generated inside the tube, and undergo repeated reflections at the two ends of the tube and gradually decay. The time-dependent gas pressure variation in the tube and the voltage and temperature histories of the foil are recorded by a fast-response measurement system. Finally, the measurement results are compared with the numerical results.

B. Experimental Apparatus and Procedure

The realization of a rapid increase of a wall temperature is of significant interest in the experimental design. The temperature increase rate does not only influence the character of thermally induced acoustic waves, but it also determines whether the wave generated can be detected by a sensor. With the knowledge gained from past work [56], we utilize a direct-current heating of a metal-foil covered end-piece of a plastic tube by means of an R-C circuit. A schematic of the experimental setup is shown in Fig. 83.

A plastic tube with an inside diameter of 38 mm and a length of 201 mm is used for studying the thermally generated acoustic waves. A nickel foil completely covers one end of the tube and is attached with a mica end-piece. A similar mica plate is used at the other end of the tube. These mica plates ensure rigid reflecting surfaces for the pressure waves. In addition, flexible EPDM *(ethylene propylene diene monomer)* rubber plates and thick plastic plates are added at the back of the mica plate and anchored with the tube to ensure a good seal for the tube. The foil is anchored by two long copper bars that serve as connection wires and supports for the foil. The cross-sectional dimensions of the copper bars are $70\,\text{mm} \times 70\,\text{mm}$. This minimizes the voltage drop through the copper bar, and guarantees that the electric current flows through the foil evenly.

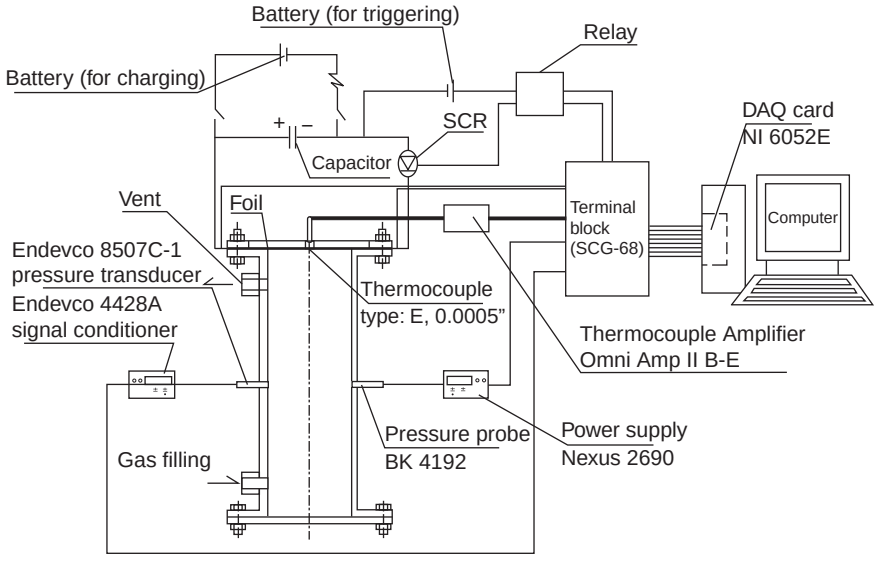

FIG. 83. Schematic of the experimental set up [79].

A very thin nickel foil (thickness is 6.0 μm, electrical resistivity is 6.84×10^{-8} Ω-m) is used in the present study for rapid heating of its surface. A silicon-control-rectifier (SCR), (Littelfuse, model: TO-218X) with a 2.5 μs triggering time is used to fully discharge the capacitor. This arrangement provides a rapid rise of the foil temperature for generating the acoustic waves in the surrounding gas along the tube. Some other advantages of the R-C heating system include good repeatability and easy control of heating rate and maximum temperature increase. The details of the apparatus and circuit elements are listed in Table VIII.

In the experimental setup, the dimensions of the foil (attached around a circular mica end-piece) are 42 mm × 50 mm × 6.0 μm. The electrical resistance of the foil is calculated to be 0.014 Ω. By carefully calculating every component in the R-C circuit, the circuit efficiency $\epsilon = R_{foil}/R_{total}$ is found to be about 53%. Several capacitors rated at 18.0 mF, 27.0 mF and 56.0 mF are used for the measurements. The circuit time constant, $\tau_{RC} = R_{total} \cdot C$ is hence 0.0005 s, 0.00071 s, and 0.0015 s for capacitances of $C = 18.0$ mF, 27.0 mF, and 56.0 mF used in the circuit, respectively.

Two different types of pressure probe (see Fig. 84) are used to measure and monitor the thermally generated acoustic waves in the tube. A condenser microphone (12.7 mm Brüel & Kjær model 4193) and a piezoresistive pressure transducer (Endevco model 8507C-1) are used. The probes are

TABLE VIII
SPECIFICATIONS FOR THE EXPERIMENTAL SYSTEM [79]

No.	Part	Make and model	Specification
1	Capacitors	Sprague Antex A8	18, 27 and 56 mF
2	SCR	Littelfuse TO-218X	Max trigger time: 2.5 μs
3	Foil		Nickel, 0.006 mm thick, 99.95%, resistivity 6.84×10^{-8} Ω-m
4	Thermocouple	Omega Bare-8-E-12	12.7 mm dia. E-type
5	Pressure probes	B&K 4193 with UC0211 adaptor	2 mV/Pa
		Endevco 8507C-1	2.1 mV/KPa
6	Data acquisition board	NI 6052E	333 kHz

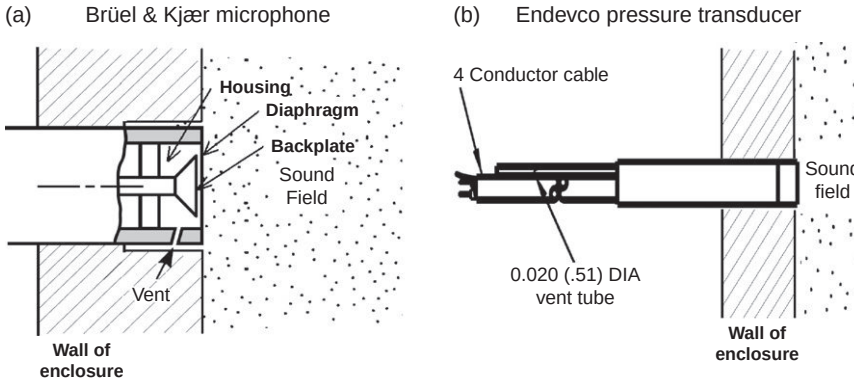

FIG. 84. Details of the pressure probes [79]. (a) Brüel & Kjær microphone. (b) Endevco pressure transducer.

mounted transversely on the plastic tube (see Fig. 93), with the sensing surfaces flush with the tube inner wall. The probes are thus directly exposed to the gas and minimally interfered with the pressure wave propagation. The gaps between the probe boundaries and the holes are sealed by Dow Corning 832 non-corrosive sealant. The Brüel & Kjær condenser microphone was chosen because of its high sensitivity, fast response, and wide frequency-response band. For the Brüel & Kjær condenser microphone, the detection system also included a low-frequency adaptor (UC0211), a microphone preamplifier (model 2669) and a conditioning amplifier (ZN 2690). The piezoresistive pressure transducer, Endevco 8507C-1, is used to measure the variation of the total pressure (sum of the static and dynamic

components) in the tube. The Endevco 8507C-1 piezoresistive pressure transducer is powered and conditioned by a 4428A signal conditioner. The sensitivity of the Endevco transducer is, however, not sufficient to allow the measurement of the small dynamic pressure fluctuations in the tube due to the sudden heating of the foil. Use of these two pressure transducers allow us to probe the thermally induced acoustic waves in greater detail than reported earlier.

The Brüel & Kjær 4193 condenser microphone (see Fig. 84 (a)), consists of a metal housing, inside of which a delicate and highly tensioned diaphragm is placed ahead of a back-plate. The distance between the diaphragm and the back-plate changes if there is any pressure difference between the microphone housing and the tube volume exposed to the diaphragm. The corresponding capacitance variation is converted to pressure signal by the microphone cartridge (not shown). To eliminate the influence of static pressure variation and protect the diaphragm, the microphone housing is connected to the tube medium by a static pressure equalization vent hole (Fig. 84 (a)). The narrow vent hole ensures that the static pressure of the microphone housing follows the pressure variation in the tube. The vent hole was designed [84] to equalize the static pressure variations without suppressing the low-frequency components of the dynamical acoustic pressure which are to be measured. The time constant of the microphone's pressure equalization system is about 0.1 s; therefore, frequencies below 10 Hz are affected by the vent hole. The Brüel & Kjær 4193 microphone is thus suitable for measuring the dynamic pressure variation when the static pressure in the tube remains constant or varies slowly.

The Endevco 8507C-1 piezoresistive pressure transducer, shown in Fig. 84 (b), on the other hand, measures the variation of resistance due to the pressure difference between the two sides of the piezoresistive element. One side is exposed to the gas in the tube and the other side communicates with the outside ambient via a vent tube.

Other than the pressure measurements, the temperature and voltage drop histories of the foil (after the capacitor is discharged) are also recorded in our measurements. Previous numerical studies [54] of thermally generated acoustic waves by a rapidly heated surface show that the early temperature behavior of the heated surface (during the first several micro-seconds) has a significant influence on the behavior of the acoustic wave generated. Hence, we pay special attention to the measurement of the foil temperature at early times after the capacitor is discharged. Chromel-constantan type E thermocouples with a diameter of 12.7 μm are used for their fast response time. The attachment of thermocouple on the foil is also critical. Silver adhesive (503, Electron Microscope Science) was chosen after evaluating many other brands of adhesives, mainly for its high thermal conductivity

and ease of applicability. Due to its heat capacitance, the adhesive slows down the response time of the thermocouple at very early times. The signals from the thermocouple probe are conditioned by an Omega Omni Amp IIB-E conditioning amplifier. The amplifier not only amplifies the weak signal from the thermocouple, but also isolates the high-frequency electrical disturbance by its interior signal conditioning circuit. Although the amplifier eliminates the electrical disturbance at early times, it does not accurately record the peak value of the temperature rise of the foil (due to signal conditioning by the Omega Omni Amp IIB-E amplifier).

The analog temperature, pressure and voltage measurements were recorded, digitized and saved through a National Instrument SCB-68 terminal block and a 6052E data acquisition (DAQ) board. High sample rate (333 kHz) of the 6052E DAQ board guarantees that the signals are recorded with high fidelity. The data acquisition system also provides a voltage output to a relay to control the triggering time of the SCR.

Before each experiment, all devices were powered up and run such that the warm-up time requirements were met. All modules and devices were checked for the reliability of the experiment. The capacitor was charged up to a desired voltage V_0, which was measured by an HP 34401A multi-meter. The LabView 7.0 software was used to record the signals of temperature, voltage and pressure in the experiments, and to provide controlling signals. The SCR was triggered to initiate the experiment. At this point in the experiment, the capacitor is discharged causing rapid heating of the foil. The foil temperature gradually falls after the initial rapid rise. For most experiments, data were collected for about 5.1 s. After one experiment was carried out, the experimental conditions were initialized before the next set of measurements was made. Each experiment was repeated several times in order to confirm the measurements.

C. Experimental Results and Discussion

Approximately one hundred experimental runs were carried out with the test rig using air at ambient conditions ($p_0 = 1$ atm., $T_0 = 299$ K). The nickel foil used for the rapid heating was 6.0 μm thick. Several capacitors rated at 18.0 mF, 27.0 mF and 56.0 mF were used for the measurements. For a given capacitor, a number of different charging voltages V_0 were applied.

Figure 85 exhibits the transient voltage drop across the foil with $C = 27.0$ mF and $V_0 = 30$ V. The response shows a typical R-C circuit discharge behavior. The foil voltage reaches the peak value at about 0.00003 s, and then it gradually decreases to zero by about 0.005 s. The foil voltage is about 37% of the peak value at approximately $t = 0.0011$ s. This is close to the calculated circuit time constant, $\tau_{RC} = R_{total} \cdot C = 0.00071$ s for $C = 27.0$ mF.

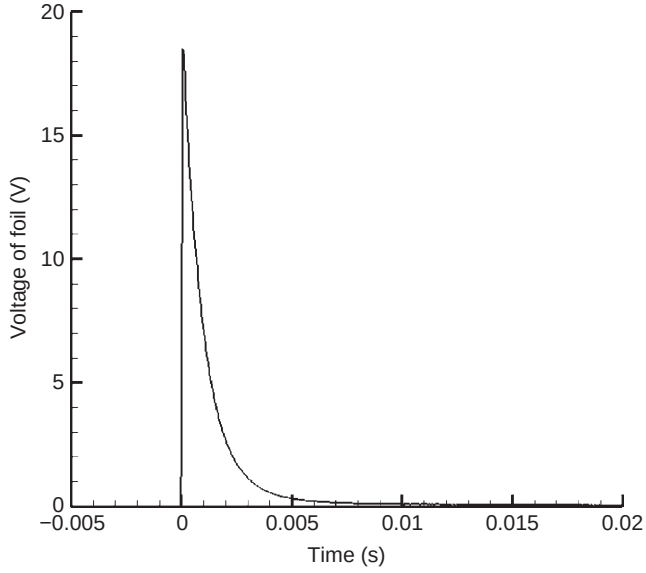

FIG. 85. Transient voltage drop across the foil at $C = 27$ mF and $V_0 = 30$ V.

The corresponding temperatures measured by the thermocouple are shown in Figures 86(a) and (b). At early times (for $t < 0.02$ s) the measured temperature rise rate is found to be much slower than the corresponding voltage discharge rate. The temperature rise in the foil depends on the heat

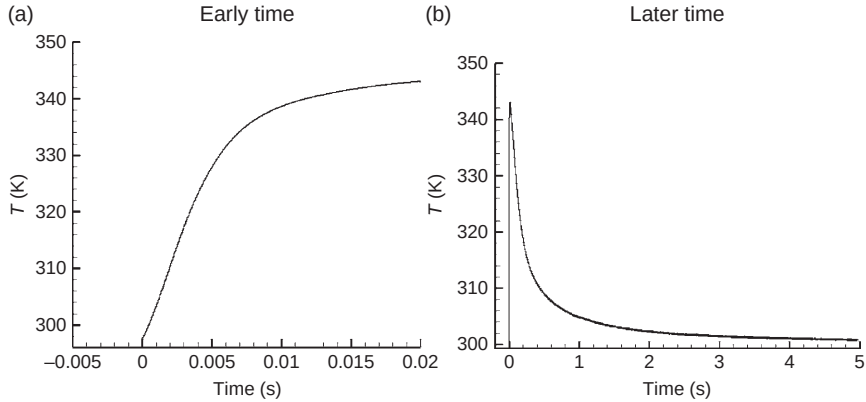

FIG. 86. Transient temperature of the foil at $C = 27$ mF and $V_0 = 30$ V. (a) Early time; (b) Later time.

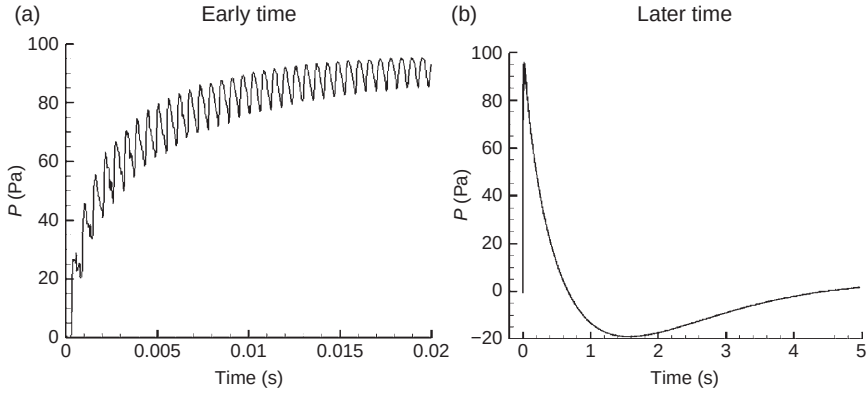

FIG. 87. Experimental trace of pressure ($p - p_{atm}$) wave measured by the B&K microphone, $C = 27$ mF, $V_0 = 30$ V [79]. (a) Early time; (b) Later time.

gain and loss to the air. It is also noted that during the capacitor discharge period, the electromagnetic disturbance is high, and the thermocouple cannot respond during the initial discharge period (for about $t < 0.005$ s).

Figures 87(a) and (b) show the trace of the pressure wave measured by the Brüel & Kjær microphone under the following conditions: $C = 27$ mF, $V_0 = 30$ V. The probe records a peak when the acoustic wave sweeps past the probe diaphragm during its motion from the heated side to the unheated side. The next peak indicates the reflected acoustic wave that now travels from the unheated side to the heated side. During the first several acoustic cycles (Fig. 87(a)) the wave shape shows steep fronts with long tails, which is consistent with the previous studies [53]. Due to viscous dissipation and energy losses, the characteristics of the acoustic wave profile, i.e., sharp peaks and steep fronts, gradually disappear. The measured Mach number of the acoustic wave is about $M = 1.03$. The pressure variation recorded by the Brüel & Kjær 4193 microphone over a longer period of time (about 5.1 s) is presented in Fig. 87(b). It is interesting to observe that the probe records pressure values lower than the ambient value (that is, non-physical values) beginning at about $t = 0.6$ s. The anomalous result is traced to the inherent construction and operational features of the Brüel & Kjær condenser microphone. The existence of the narrow vent hole (see Fig. 84 (a)) causes the non-physical results at longer times. While the Brüel & Kjær microphone is suitable for the measurement of dynamic pressure where static pressure remains constant, it is not designed for the measurement with varying static pressure. When the foil is first heated, it heats the gas inside the tube, so the static pressure increases. Therefore, the

static pressure inside the tube increases to a maximum value, then decreases to the initial value in several seconds as the heat is lost to the outside environment from the wall. As the diameter of the vent hole connecting the microphone housing to the pressure field in the tube is very small, the static pressure inside the microphone housing varies more slowly than that in the enclosed pressure field. Within some time period, the static pressure inside the microphone housing becomes greater than that of the air in the tube, causing the pressure readings to fall below zero (from $t = 0.6$ s to $t = 4.2$ s in Fig. 87 (b)). Finally, the static pressure difference between the microphone housing and the tube is eliminated (due to the cooling of the system), and the pressure measurement will become equal to zero, as displayed in Fig. 87(b) as time approaches $t = 5.0$ s.

As mentioned earlier, a second pressure probe, the Endevco 8507C-1 piezoresistive pressure transducer, was also used in the experiments. In contrast to the Brüel & Kjær 4193 microphone, the vent hole of the Endevco 8507C-1 pressure transducer is exposed to outside the test section (see Fig. 84 (b)), so the variation of static pressure inside the test section does not cause any anomalous results. The unfiltered measurements made by the Endevco probe are shown in Figs. 88(a) and (b), for the same experimental conditions used to produce Figs. 87(a) and (b). At early times, the pressure waves measured by both probes are quite similar, except the noise generated by the Endevco probe is much higher and causes distortion in the signal. More interestingly, the two measured pressure shapes are very different for longer times (compare Figs. 87(b) and 88(b)), for reasons discussed above.

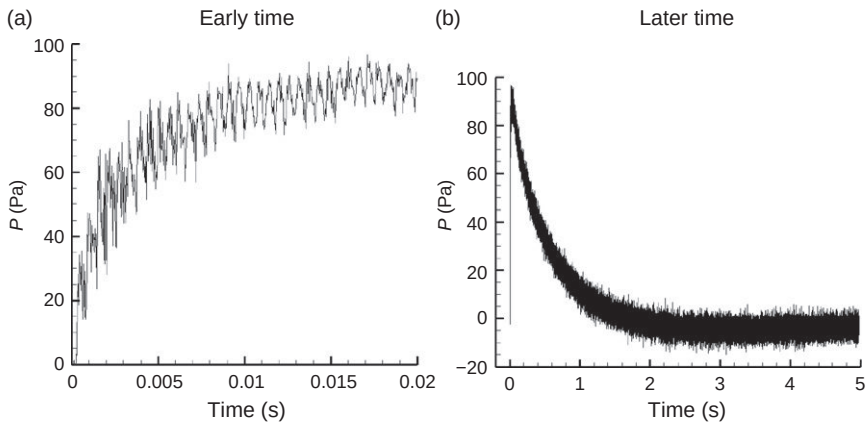

FIG. 88. Experimental trace of pressure wave ($p - p_{atm}$) by the Endevco pressure transducer (unfiltered) at $C = 27$ mF, $V_0 = 30$ V [79]. (a) Early time; (b) Later time.

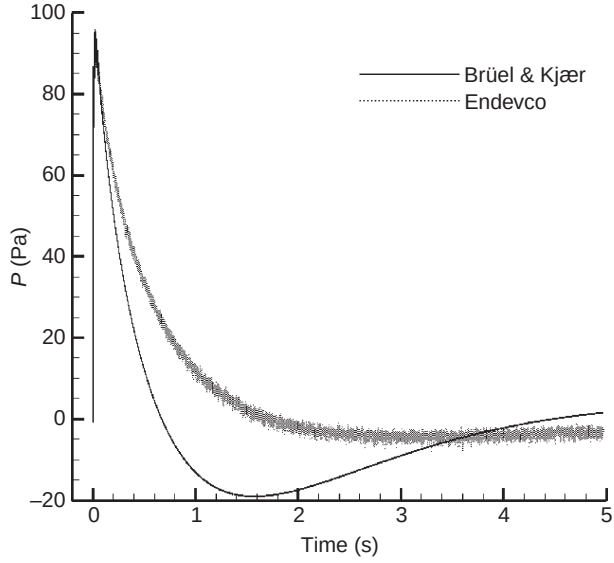

FIG. 89. Comparison of pressure ($p - p_{atm}$) measurement by the Brüel & Kjær microphone (unfiltered) and Endevco pressure transducer (filtered) at $C = 27$ mF, $V_0 = 30$ V.

To decrease the noise in the Endevco probe results, the signal is digitally filtered by using a third-order Butterworth method. The comparison between the measurements by the two pressure probes, using the filtered results for the Endevco probe, is given in Fig. 89. No apparent negative (lower than ambient) pressure signal is found for the Endevco probe, due to its construction and measurement principle. From our experiments, we find the Brüel & Kjær microphone to be useful for the measurements of the dynamic pressure wave (provided that there is no variation in the background static pressure), while the Endevco pressure transducer is useful for the measurement of the overall pressure variations where there is less fluctuation in the pressure field.

A series of measurements were carried out where the capacitor "charge voltage" was varied. Figure 90 shows the effects of the charge voltage on the temporal decay of voltage across the foil where $C = 27$ mF. The corresponding temperature measurements are given in Fig. 91. Any change of the charge voltage of the capacitor only changes the electric energy stored in the capacitor; it does not affect the characteristics of the circuit. The variation of the maximum voltage drop across the foil with charge voltage is shown in Fig. 91 with $C = 27$ mF. The relationship is found to be almost linear (Fig. 92).

Figure 93 exhibits the effects of the charge voltage of the capacitor on the acoustic wave (early time) as measured by the Brüel & Kjær microphone

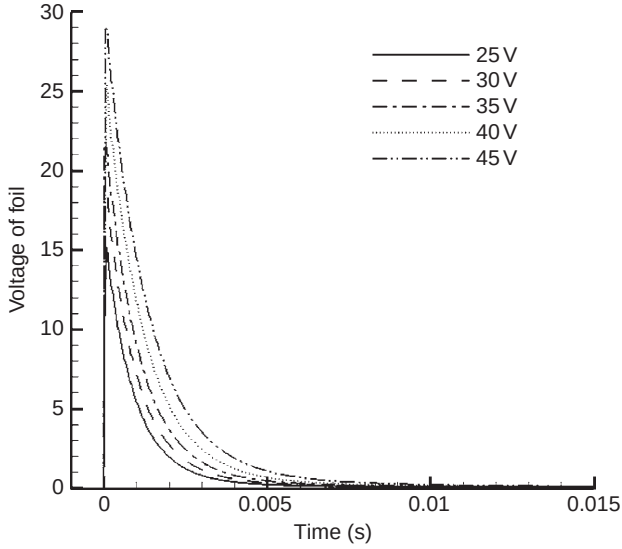

FIG. 90. Effects of the charge voltage on the temporal decay of voltage drop across foil, $C = 27\,\mathrm{mF}$.

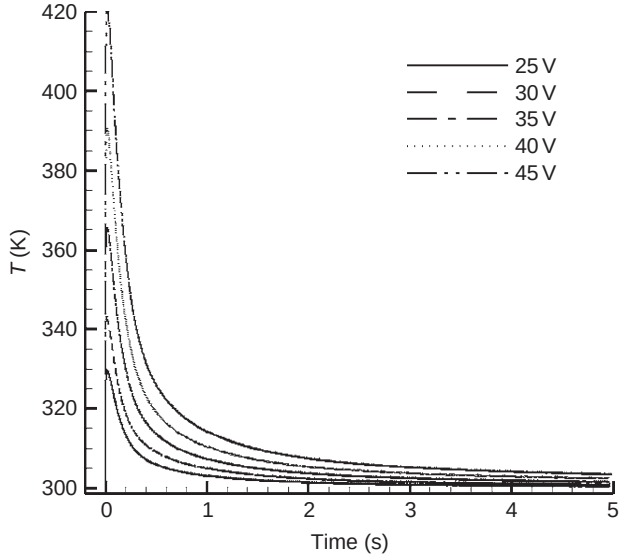

FIG. 91. Effects of the charging voltage on the temperature history of foil (extended time), $C = 27\,\mathrm{mF}$.

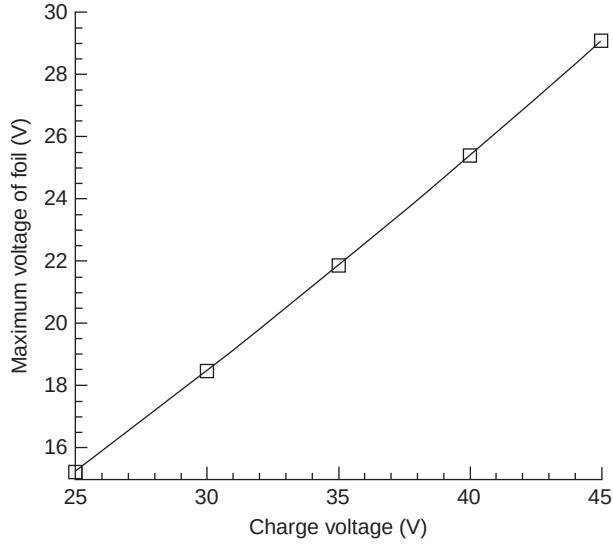

FIG. 92. Variation of the maximum voltage drop across foil with charge voltage, $C = 27\,\text{mF}$.

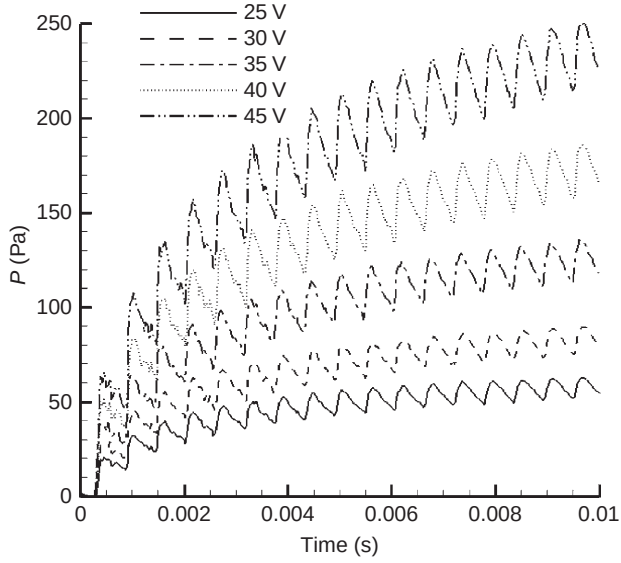

FIG. 93. Effects of charge voltage on the pressure ($p - p_{\text{atm}}$) wave (early time) as measured by the Brüel & Kjær microphone, $C = 27\,\text{mF}$.

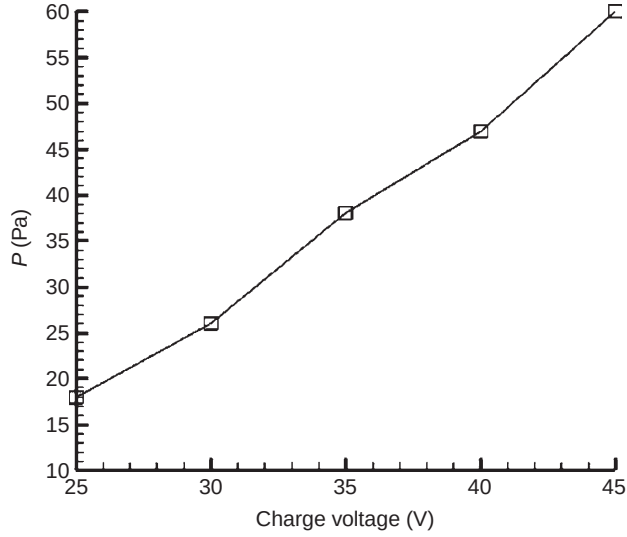

FIG. 94. Variation of the unattenuated amplitude of the acoustic wave with charge voltage, $C = 27\,\mathrm{mF}$.

under similar conditions. Stronger acoustic waves are generated for higher charge voltages, because of the higher temperature increases rate. In addition, the static pressure increase is higher for higher charge voltage. The variation of the unattenuated amplitude of the acoustic wave with charge voltage is given in Fig. 94. The amplitude of the first pressure peak as measured in the middle of tube is plotted. Physically, the acoustic wave originates from the local pressure disturbance near the wall introduced by sudden gas temperature increase. The sudden gas temperature increase is due to the heat conduction from the foil that is rapidly heated. Therefore, the strength of the generated acoustic wave is found to vary almost linearly with the charge voltage.

Figure 95 shows the effects of the capacitor value, or capacitance, on the voltage decay rate across the foil at $V_0 = 30\,\mathrm{V}$ as the capacitor is discharged. The corresponding temperature measurements are given in Fig. 96. The capacitor value not only changes the amount of electric energy stored in the capacitor according to the relationship $Q = CV$, but also changes the discharge character of the circuit.

Figure 97 exhibits the effects of capacitor value on the acoustic wave (early time) as measured by the Brüel & Kjær microphone under similar conditions. The higher capacitor values result in high energy input from the foil, so the acoustic wave generated is stronger, with higher static

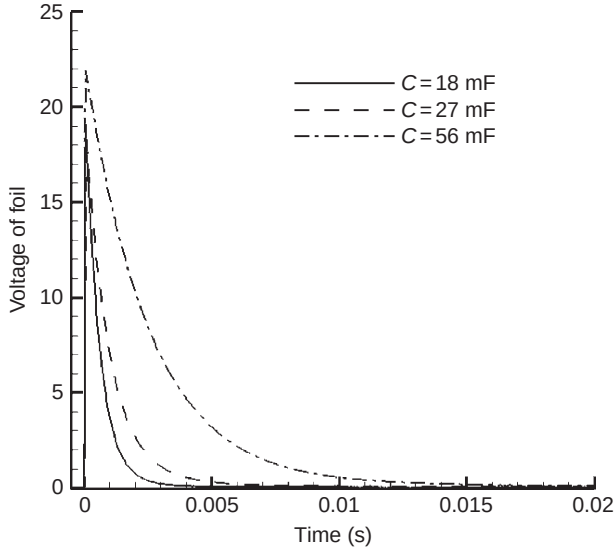

FIG. 95. Effects of capacitance on the voltage drop across foil at early times, $V_0 = 30$ V.

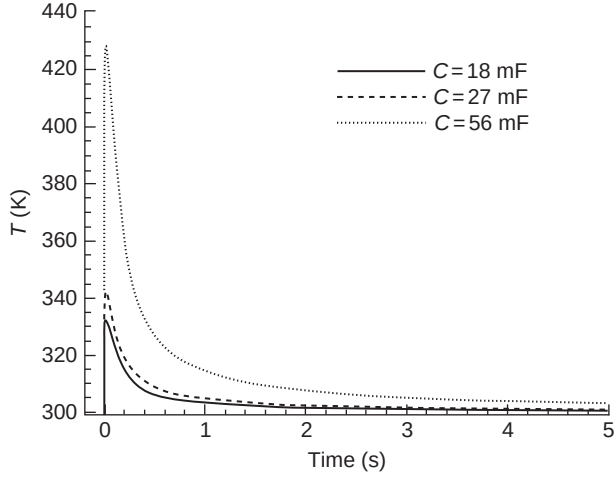

FIG. 96. Effects of the capacitance on the temperature response of the foil, $V_0 = 30$ V.

pressure increases. The variation of the first peak of the acoustic wave with capacitance (as measured at the midpoint of the tube) is given in Fig. 98.

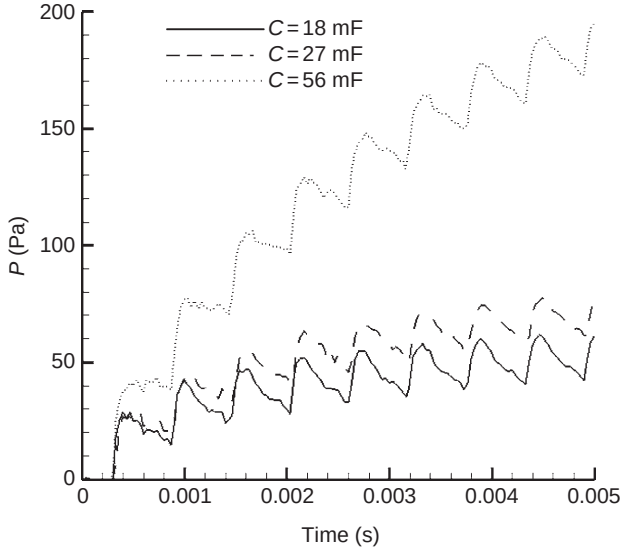

FIG. 97. Effects of the capacitance on the acoustic wave (early time) measured by the Brüel & Kjær microphone at $V_0 = 30$ V.

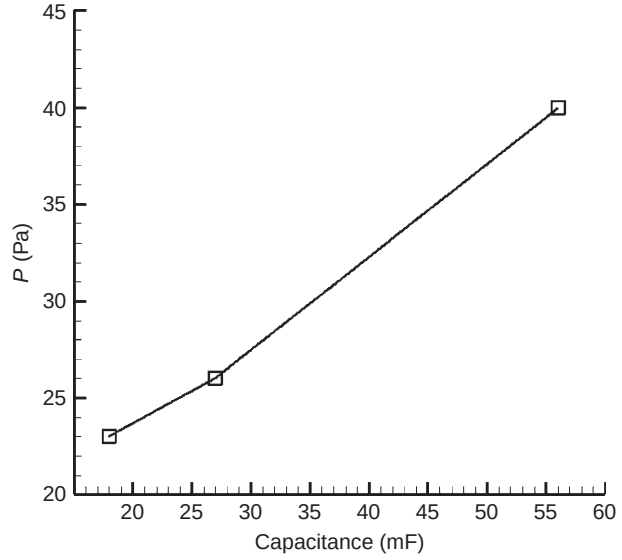

FIG. 98. Variation of the unattenuated amplitude of the pressure ($p - p_{atm}$) wave with capacitance at $V_0 = 30$ V.

1. Estimation of Experimental Uncertainty

Several independent measurements were performed for the completion of the experimental study. These measurements are as follows: gas pressure in the tube (as measured by the Brüel & Kjær 4193 microphone and the Endevco 8507C-1 pressure transducer), foil temperature as measured by the fine thermocouple, and voltage decay across the foil. All measurements are recorded by the NI 6052E DAQ board. The accuracy of the NI 6052E is ± 4.747 mV for the range of voltage measurements made by the 4193 microphone, ± 0.479 mV for the 8507C-1 pressure transducer measurements, and ± 0.242 mV for the thermocouple measurements.

There are two sources of error in the Brüel & Kjær 4193 microphone system: ± 0.2 dB from the 4193 microphone itself and ± 0.1 dB from the 2690 signal conditioner. With the error introduced by the DAQ board, the total maximum error for the pressure measurements made by the Brüel & Kjær 4193 microphone is estimated to be ± 0.15 Pa. There are also two sources of error in the Endevco 8507C-1 pressure transducer system. The uncertainty of the Endevco 8507C-1 pressure transducer is 0.25% of the "full scale output" (6895 Pa); also, the 4428A signal conditioner has an uncertainty of 0.2% of the "full scale output". The total uncertainty of the 8507C-1 pressure transducer system is ± 31.03 Pa.

The errors in the thermocouple measurements include ± 0.045°C error from the cold junction compensation, 0.01%/°C instability from the amplifier, ± 0.02°C error from conversion relation, and ± 0.08°C DAQ board error. Consequently, the total temperature error is 0.145°C plus 0.01% of the reading value. The only error in the voltage measurement is from the DAQ board, which is ± 7.47 mV.

The uncertainty associated with the experimental data is estimated by using the method recommended by Kline [85]. Both the transient pressure measurements by the Brüel & Kjær 4193 microphone and voltage measurements exhibit very high degrees of consistency and very low uncertainties. For the 4193 microphone measurement, the uncertainty, with a 95% confidence level, is 0.75% for the experimental case with the lowest charging voltage and capacitance. The corresponding uncertainty is 0.07% for the voltage measurements. The transient pressure measurements by the Endevco 8507C-1 pressure transducer show significant noise, due to the uncertainty being close to the amplitude of the pressure fluctuation. The maximum uncertainty is ± 1.0% for the temperature measurements.

The ambient temperature for all runs is within ± 0.6% of 299 K, and the ambient pressure is within ± 1% of the standard atmospheric pressure. The error associated with the variation of the ambient conditions is considered to be minor.

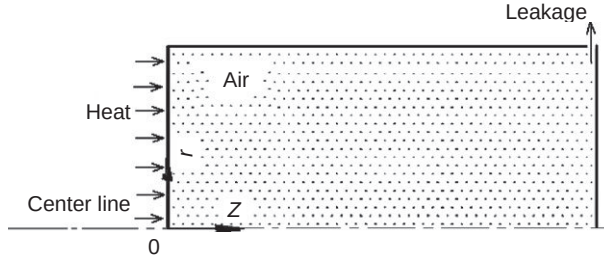

FIG. 99. Computational domain.

2. *Comparison of Numerical and Experimental Results*

To simulate the presence of possible leakage in the experimental tube, part of the side boundary was also considered as being open, as shown in Fig. 99, in some of the calculations. A 50×1000 ($r \times z$) grid size is used for all calculations as the problem is essentially one-dimensional (in the z-direction) for the short time-scale considered. A very fine mesh in the axial direction allows us to capture the characteristics of the thermally induced acoustic waves. In the simulations, we provide the transient temperature history of the foil as the temperature boundary condition for the heated wall. Defining the transient temperature history of the foil is rather challenging. We used the experimental measurements of both voltage and temperature decay to develop the thermal boundary condition for the heated wall for the numerical simulations.

a. Temporal Foil Temperature. The experimental measurements of both voltage and temperature decay were used to develop the thermal boundary condition of the heated wall for the numerical simulations. Limited by the properties of the used thermocouple, its contact with the foil and the electric noise of the discharging circuit, the thermocouple in our experiments can not accurately measure the foil temperature at very early times. The foil voltage measurements and the electric energy input into the foil were used to develop the temperature decay rate at very early times.

Figure 100 gives the foil voltage measurements and the foil temperatures calculated from the foil voltage measurements for the case of $V_0 = 30\,\mathrm{V}$ and $C = 27\,\mathrm{mF}$. In the calculation of temperature (from the voltage measurements), an energy balance equation for the foil is considered:

$$\rho c \delta A \frac{\partial T}{\partial t} = \frac{V(t)^2}{R_{\mathrm{foil}}} + q_{\mathrm{loss}} \tag{V.1}$$

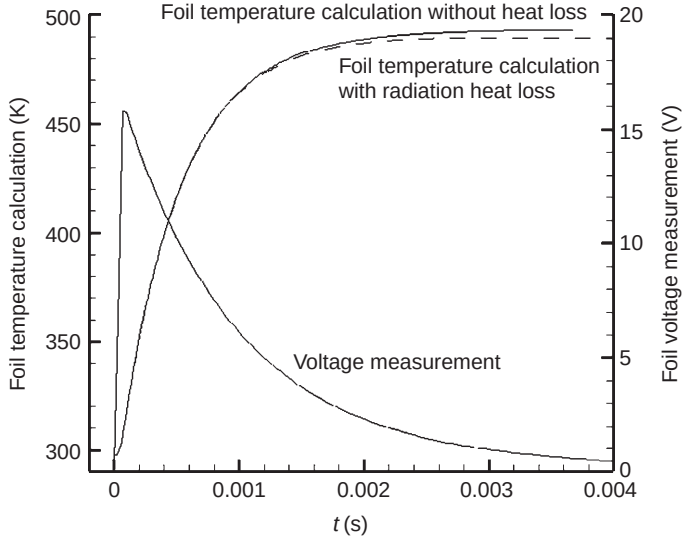

FIG. 100. Measured foil voltage and calculated foil temperature at early times, $C = 27\,\text{mF}$ and $V_0 = 30\,\text{V}$.

Here, c is the specific heat of the foil, A is the foil area, q_{loss} is the total heat loss of the foil to the ambient environment, and $V(t)$ is voltage response of the foil. Here, we consider two cases: (a) no heat loss, $q_{\text{loss}} = 0$, and (b) heat loss by radiation, $q_{loss} = q_{rad} = \alpha\sigma_b(T_{foil} - T_{ambient})$

where α is the absorptivity of the foil (0.36) and σ_b is the Stefan-Boltzmann constant.

The above equation was numerically solved by an explicit scheme. From the calculated temperature profiles (with and without heat loss), we find from Fig. 100 that the heat loss term has only a slight effect on the foil temperature during the temperature rise time (within the initial 0.001 s).

Figure 101 shows the comparison of the calculated foil temperature (with radiation heat loss) from the voltage measurements and the thermocouple temperature measurements. As stated earlier, the thermocouple data were conditioned by an Omega Omni Amp IIB-E conditioning amplifier. The adhesive (silver paint) used also slows down the response of the thermocouple. These effects perhaps cause the measured temperature data at early times to be under-predicted. For larger values of time, somewhat different reasons cause the discrepancy between the measured and predicted values of the temperature. There are several sources of heat loss, such as convective heat loss to air and conduction losses to the

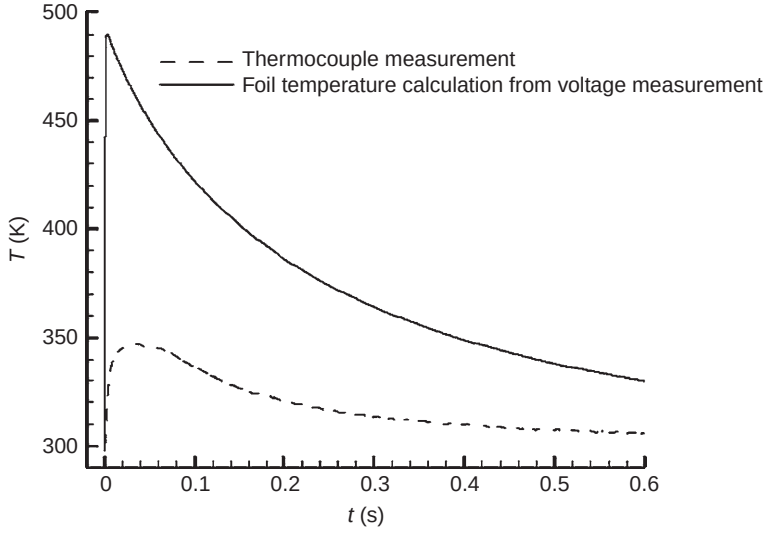

FIG. 101. Calculated foil temperature (with radiation heat loss) and thermocouple measurements, $C = 27\,\text{mF}$ and $V_0 = 30\,\text{V}$.

copper bars and the mica plate, that were not considered in Eq. (V.1). Independent experiments in simple systems confirm that the temperature measurements at larger values of time ($t > 0.1\,\text{s}$) are accurate.

A polynomial fit of the measured data was obtained for $t > 0.1\,\text{s}$. We extend the polynomial fit for the measured temperature decay from $t = 0.1\,\text{s}$ to $t = 0.0001\,\text{s}$, as shown in Fig. 102. We show the temperature profiles shown in Fig. 101 one more time in Fig. 103 albeit for early times ($0 > t > 0.01\,\text{s}$). For the experiments, the foil temperature increases rapidly and then gradually decays. The predicted temperature increase of the foil (from the voltage measurement) meets the extrapolated curve of the temperature decay at about $t = 0.0007\,\text{s}$. This is close to the calculated circuit time constant, $\tau_{RC} = R_{total} \cdot C = 0.00071\,\text{s}$ for $C = 27.0\,\text{mF}$ as discussed earlier.

The constructed temperature profile for the foil is shown in Fig. 104 for $0 > t > 4.4\,\text{s}$. The initial temperature rise for the foil when $0 > t > 0.0007\,\text{s}$ is given as

$$T = a_0 + \sum_{i=1}^{8} \Big(a_i * \cos(i * 1000 * t * w) + b_i * \sin(i * 1000 * t * w) \Big) + 297.636 \tag{V.2}$$

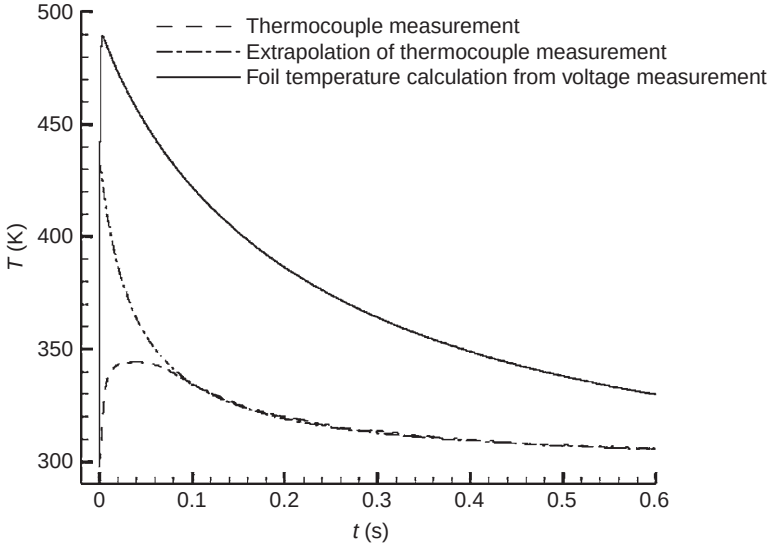

FIG. 102. Extrapolation of measured foil temperature, $C = 27\,\text{mF}$ and $V_0 = 30\,\text{V}$.

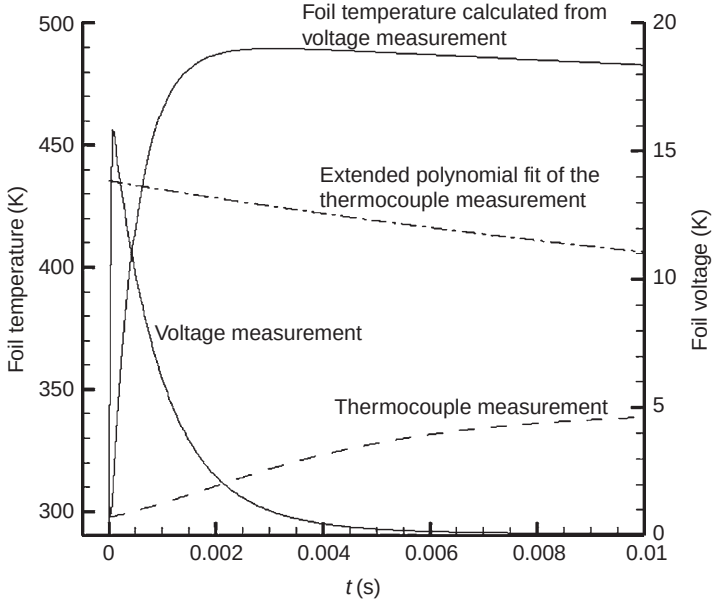

FIG. 103. Extrapolation of measured foil temperature, $C = 27\,\text{mF}$ and $V_0 = 30\,\text{V}$.

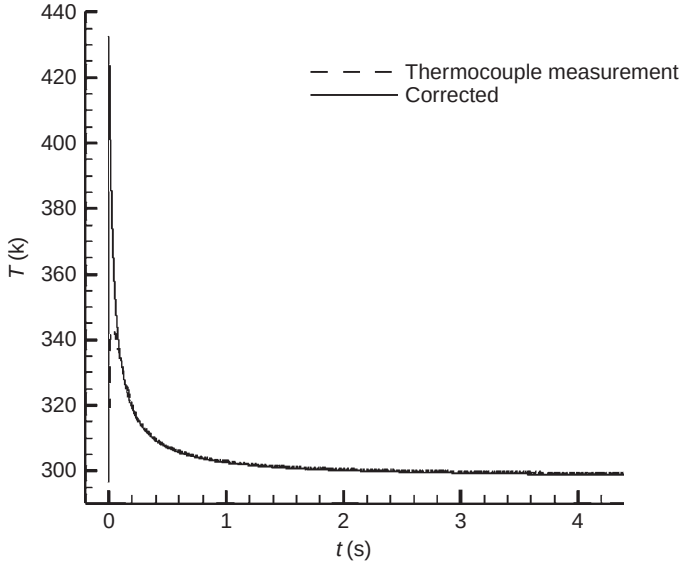

FIG. 104. Measured and calculated foil temperature history $C = 27\,\text{mF}$ and $V_0 = 30\,\text{V}$.

where $a_0 = 140.3$, $a_1 = -60.57$, $a_2 = -34.98$, $a_3 = -22.27$, $a_4 = -13.28$, $a_5 = -6.817$, $a_6 = -2.757$, $a_7 = -0.7334$, $a_8 = -0.05938$, $b_1 = -30.39$, $b_2 = -13.74$, $b_3 = -2.497$, $b_4 = 2.769$, $b_5 = 4.091$, $b_6 = 3.337$, $b_7 = 1.943$, $b_8 = 0.7773$, $w = 2.393$

When $0.0007\,\text{s} > t > 4.2\,\text{s}$,

$$T = \frac{a}{10t + b} + 297.636, \tag{V.3}$$

where $a = 50.92$, $b = 0.3704$

The above corrected temperature history (Eqs. (V.2) and (V.3)) for $0 > t > 4.2\,\text{s}$ was used as the temperature input in our numerical simulations for the experimental case where $V_0 = 30\,\text{V}$ and $C = 27\,\text{mF}$. The method was used to obtain foil temperature histories for other cases with different charge voltages and capacitances.

The numerical model described earlier was used to obtain the predictions of the flow and pressure fields in the tube driven by rapid heating of the foil. For the pressure at the mid point of the tube wall, the comparison of the numerical and experimental results is given in Fig. 105(a), where $V_0 = 30\,\text{V}$ and $C = 27\,\text{mF}$. In the first several acoustic cycles ($t < 0.002\,\text{s}$) the numerical and experimental results have an excellent match. The thermal boundary condition for the foil was switched from Eq.(V.2) to Eq. (V.3) at $t = 0.0007\,\text{s}$.

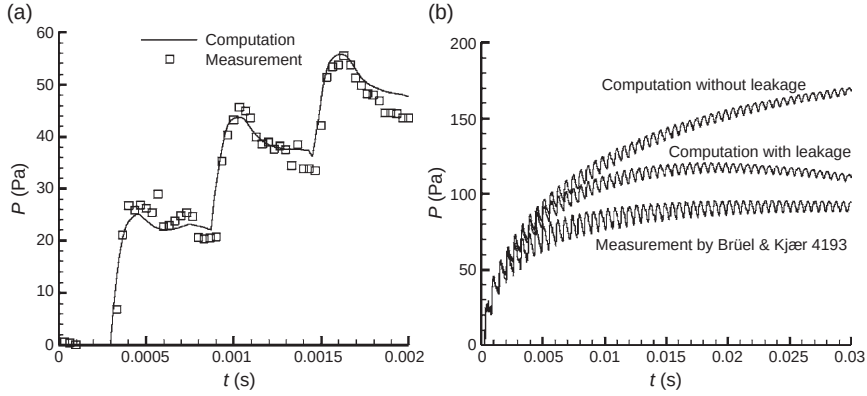

FIG. 105. Comparison of experimental and computational pressure waves, $C = 27\,\text{mF}$ and $V_0 = 30\,\text{V}$. (a) Early time. (b) Later time.

The good agreement between the computational and experimental pressure results demonstrates that the method for considering the transient foil temperature is reasonable.

The comparison for the long time scale is shown in Fig. 105 (b). In the numerical model, all walls are considered smooth and rigid, and also the system is assumed to be sealed perfectly. The numerical results correctly predict the pressure wave speed and amplitude of dynamic pressure fluctuations to be the same as the experimental results. The pressure in the computational study is, however, found to be larger than the experimental measurements. In the experiments, the acoustic energy is partially absorbed by the walls when the wave hits one. There is also the possibility of the existence of leakage in the experimental setup. We repeated the simulations with a small opening at the side boundary (0.1% of the tube length). The computational pressure results considering the leakage are also shown in Fig. 105 (b). Compared to the sealed case, the pressure response in this case is much closer to the experimental results.

Figure 106 shows the comparison of experimental data and numerical predictions for three cases: $C = 27\,\text{mF}$ and $V_0 = 25\,\text{V}$, $C = 27\,\text{mF}$ and $V_0 = 35\,\text{V}$, and $C = 56\,\text{mF}$ and $V_0 = 30\,\text{V}$. The computational and experimental results are found to have the same acoustic speeds and similar wave shapes. The comparisons between the computational and experimental results on the unattenuated amplitude of the acoustic wave (the first peak measured in the middle of the tube) for different charging voltages are given in Fig. 107. In all the different cases, the computational results are found to be close to the experimental results. The maximum deviation between the

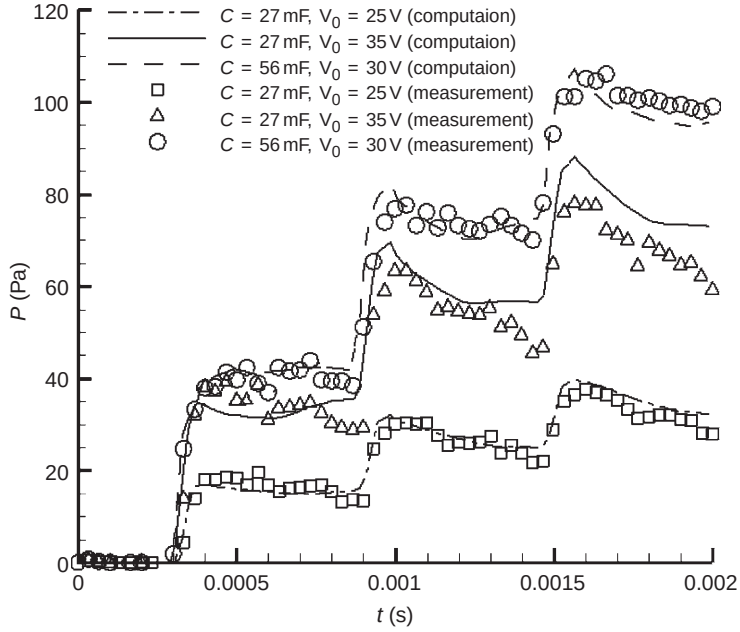

FIG. 106. Comparisons of experimental and computational pressure waves at the middle of the tube for different charging voltages and capacitances.

experimental measurements and numerical predictions is about –7%, for the case of $V_0 = 45\,\mathrm{V}$ and $C = 27\,\mathrm{mF}$. The computational results are always found to slightly under predict the experimental results. The reason the computational results are always a little bit lower than the experimental results may be that the parameters that used in the numerical model are slightly different from the real value. For example, the thickness of the metal foil plays a significant role in the numerical model. However, the value given by manufacturer has $\pm 10\%$ toleration. Therefore, it is possible that the input of our numerical model is not totally same as the experimental setup.

3. *Conclusions*

Experimental measurements were carried out to characterize the generation, development and decay of thermally induced acoustic waves in a cylindrical tube. In the experiments, the development and the decay of pressure waves inside the tube were investigated by two different pressure probes, and the different results are explained by the physics of the probes. The strength of

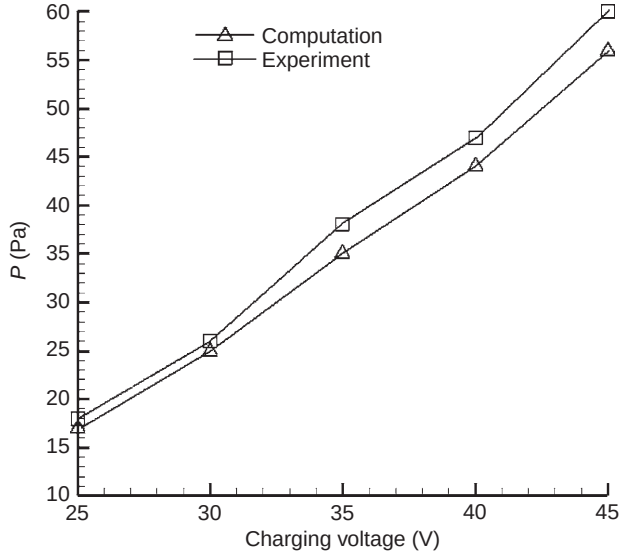

FIG. 107. Comparison of experimental and computational results on the unattenuated amplitude of acoustic wave at the middle of the tube at $C = 27\,\text{mF}$.

the unattenuated amplitude (the first peak) of the acoustic wave produced is found to be linearly dependent on the temperature increase rate of the foil at early times. At early times, the computational and experimental results are an excellent match. The experimental measurements and numerical results for the pressure evolution, however, do not match well at larger times. This is perhaps due to the presence of leaks in the chamber and damping due to the walls (considered rigid in the simulations). However, the physical features of the computational and experimental results are in good agreement.

VI. Thermally Induced Acoustic Waves in Supercritical Fluids

A. Introduction

In general, near-critical fluids have higher thermal conductivities and densities than gases, and the compressibilities are much higher. The use of the van der Waals equation of state for the numerical simulation of the piston effect was recently studied by Wagner *et al.* [86,87] for near-critical fluids by using the SIMPLE algorithm [88]. Unfortunately, the authors do not indicate the heating rate at the left wall. The thermally induced acoustic

wave development, propagation, and reflection etc. were also not explicitly predicted, although they found that the van der Waals equation of state under-predicted the magnitude of the pressure wave significantly, as compared to the predictions using the NIST database 12 [67].

The generation and propagation of thermally induced acoustic waves in supercritical carbon dioxide are investigated [89] via a high-order numerical scheme. The generation, propagation and dissipation of the thermally induced acoustic waves in a supercritical carbon dioxide filled layer are predicted. A one-dimensional problem is considered where supercritical carbon dioxide is contained between two infinite parallel plates. The NIST database 12 was used to obtain the ρ-p-T relations for supercritical carbon dioxide as well as the internal energy $i = f(\rho, T)$ and thermal conductivity, and viscosity relations $k = k(\rho, T)$, $\mu = \mu\ (\rho, T)$

A confined layer (0.01 m) of supercritical carbon dioxide ($p > p_{cr}$; $T > T_{cr}$ where $p_{cr} = 7.377$ MPa and $T_{cr} = 304.1$ K) is considered. The left wall is impulsively heated/cooled to initiate the thermally induced acoustic waves (see Fig. 108). The right wall is held at the initial temperature. The thermally induced acoustic wave generated is studied as a function of space and time.

The one-dimensional continuity and the compressible form of the Navier-Stokes equations are used to describe the generation and propagation of thermally induced acoustic waves in supercritical carbon dioxide:

$$\frac{\partial \rho}{\partial t} + \frac{\partial (\rho u)}{\partial x} = 0 \tag{VI.1}$$

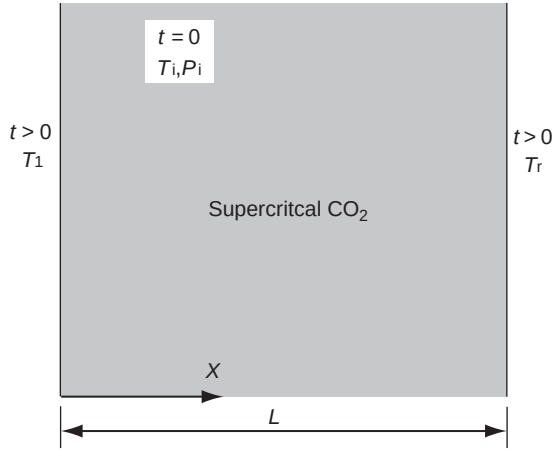

FIG. 108. Schematic of the problem geometry.

$$\frac{\partial(\rho u)}{\partial t}+\frac{\partial(\rho u^2)}{\partial x}+\frac{\partial p}{\partial x}=\frac{\partial \tau}{\partial x} \tag{VI.2}$$

$$\frac{\partial(\rho e)}{\partial t}+\frac{\partial}{\partial x}[(\rho e+p)u]=\frac{\partial}{\partial x}[u\tau]-\frac{\partial q}{\partial x} \tag{VI.3}$$

Where t is time, ρ is density, u is the velocity component, e is the total energy, p is pressure, and q is the heat flux.

Here $e=i+u^2/2$, and i is the internal energy. The equation of state is represented as $p=f(\rho, T)$.

The component of the heat-flux is written as follows, where k is thermal conductivity and T is temperature:

$$q_x=-k\frac{\partial T}{\partial x} \tag{VI.4}$$

The stress component τ is given as:

$$\tau=\lambda\left(\frac{\partial u}{\partial x}\right)+2\mu\frac{\partial u}{\partial x}=\left(\mu'+\frac{4}{3}\mu\right)\frac{\partial u}{\partial x} \tag{VI.5}$$

where μ is the dynamic viscosity, λ is the second coefficient of viscosity and $\mu'=\lambda+(2/3)\mu$ is the bulk viscosity.

B. Equation of State and Thermodynamic Properties of Supercritical Carbon Dioxide

The equation of state describing the p-ρ-T relation of supercritical fluids is complicated. It has been shown earlier [90] that the van der Waals equation do not represent the properties of supercritical carbon dioxide accurately near the critical point. In this study, we used the NIST Standard Reference Database 12 for the $p=f(\rho,T)$ relations and for evaluation of other thermodynamic properties of supercritical carbon dioxide. Variation of pressure for carbon dioxide as a function of temperature and density near the critical point is shown in Fig. 109, where the p-ρ-T relation is strongly nonlinear, especially near the critical point. Polynomial fits were used in the present study to represent, the $p=f(\rho,T)$, $i=f(\rho,T)$, $k=k(\rho,T)$ and $\mu=\mu(\rho,T)$ data provided by the NIST Standard Reference Database 12. The temperature range considered for the developed polynomials is 304.15–312.5 K, and the pressure range is 7.38–8.2 MPa for all the polynomial fits. The pressure deviation for the fitted data form the original NIST data ranges from 0.00002% to 0.01%. The viscosity deviation for the fitted data from the

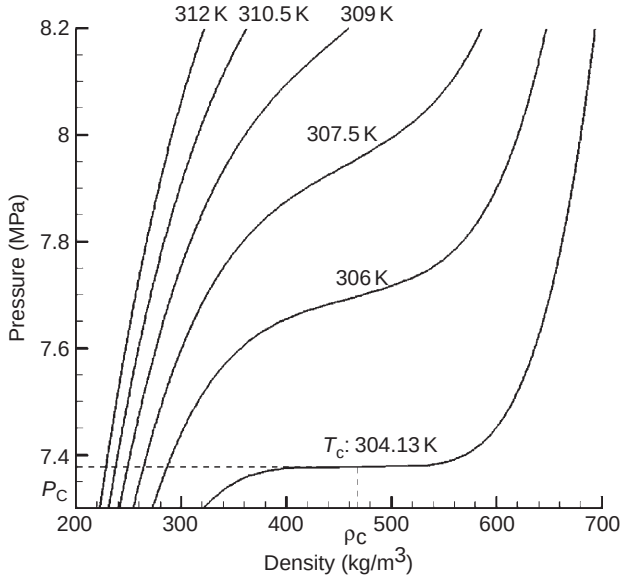

FIG. 109. Variation of pressure for carbon dioxide as a function of temperature and density near the critical point.

original NIST data ranges from 0.00001% to 0.001%, the thermal conductivity deviation ranges from 0.01% to 9%, and the acoustic speed deviation ranges from 0.0004% to 3%. The fitted internal energy deviation from the original NIST data ranges from 0.0001% to 0.6%.

Figure 110 shows the variation of thermal diffusivity of supercritical carbon dioxide as a function of temperature and pressure near the critical point. It is noted that the thermal diffusivity is very low near the critical point. Figure 111 shows the variation of internal energy $i=f(\rho,T)$ and Figure 112 shows the variation of the bulk viscosity of carbon dioxide near the critical point.

C. Numerical Results for Supercritical Carbon Dioxide

Numerical simulations for thermally induced acoustic waves in supercritical carbon dioxide were carried out for 8 cases, which are summarized in Table IX. The supercritical carbon dioxide media confined within two parallel plates is initially considered to be quiescent.

A thermally induced acoustic wave is generated by a step increase/decrease in the temperature at the left wall dictated by the initial time

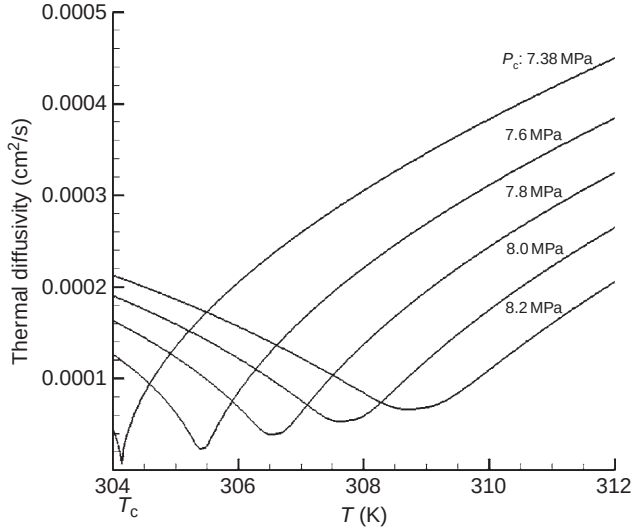

FIG. 110. Variation of thermal diffusivity for carbon dioxide as a function of temperature and pressure near the critical point.

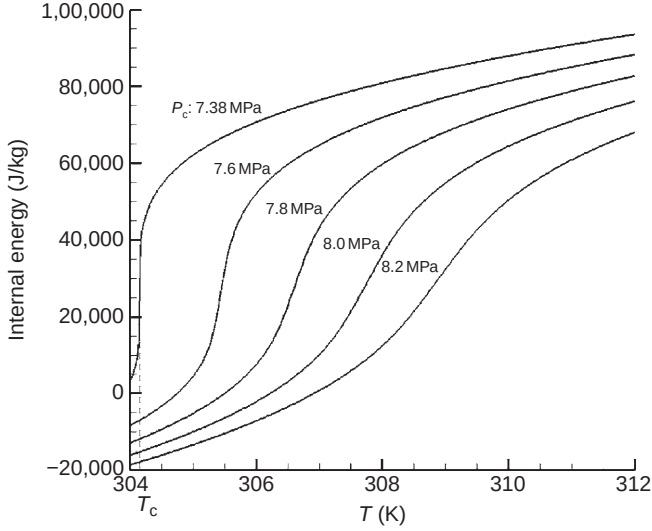

FIG. 111. Variation of internal energy for carbon dioxide as a function of temperature and pressure near the critical point.

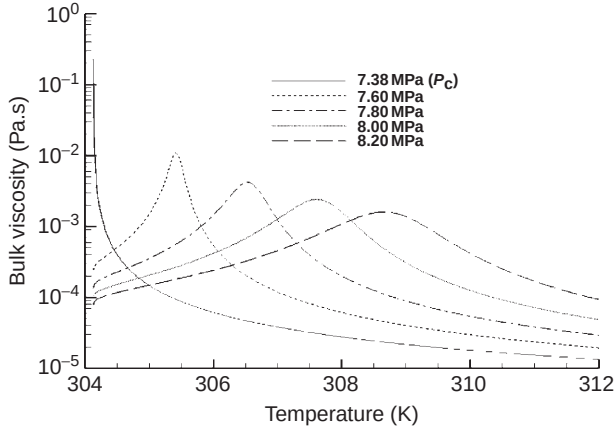

FIG. 112. Variation of the bulk viscosity of carbon dioxide as a function of temperature and pressure near the critical point.

TABLE IX
DESCRIPTION OF CASES

Case	T_i[K]	T_r[K]	T_l[K]	p_i[MPa]	Bulk viscosity
1	310	310	312	7.9	Zero
2	310	310	308	7.9	Zero
3	308	308	309	7.7	Zero
4	308	308	307	7.7	Zero
5	306	306	306.5	7.5	Zero
6	306	306	305.5	7.5	Zero
7	310	310	312	7.9	Non-zero
8	310	310	308	7.9	Non-zero

step of the computations. The temporal variation of the left wall temperature is:

$$T_1(t) = \begin{cases} T_i \text{ for } t = 0 \\ T_1 \text{ for } t > 0 \end{cases}$$

The results presented are for the early behavior of thermally induced acoustic waves in terms of pressure and other variables. The computational domain (1.0 cm) was discretized with 300 grid points. We simulated multiple wave reflections and wave damping within a short computational time.

1. Parametric Results

Figure 113 shows thermally induced acoustic (pressure) wave profiles at four early different times for Cases 1 (sudden heating) and 2 (sudden cooling). The sudden heating causes a pressure peak while the sudden cooling produces a pressure valley. As one gets closer to the critical point, the nonlinearity of p-ρ-T relation is more prominent. So finer meshes and longer computing time are needed for cases closer to critical point. As shown in the figure, the pressure waves were generated along the left heated/cooled wall traveled towards the right wall with a wave speed of about 197 m/s. This predicted wave speed is close to the value obtained from the NIST database 12. Unlike the characteristic "long tails" of the thermally induced acoustic waves in ideal gases, the pressure wave signatures in Fig. 113 show a symmetric profile, due to the high density of the supercritical fluid.

In Fig. 113, the arrows depict the direction in which the waves are moving. The four wave profiles (both for heating and cooling) at 0.1 cycle and 0.2 cycle on the left are traveling towards the right wall. The other four wave profiles at 0.6 cycle and 0.7 cycle traveling left are after reflection from the right wall. As the wave travels within the two walls, the wave shapes become broader due to dissipation.

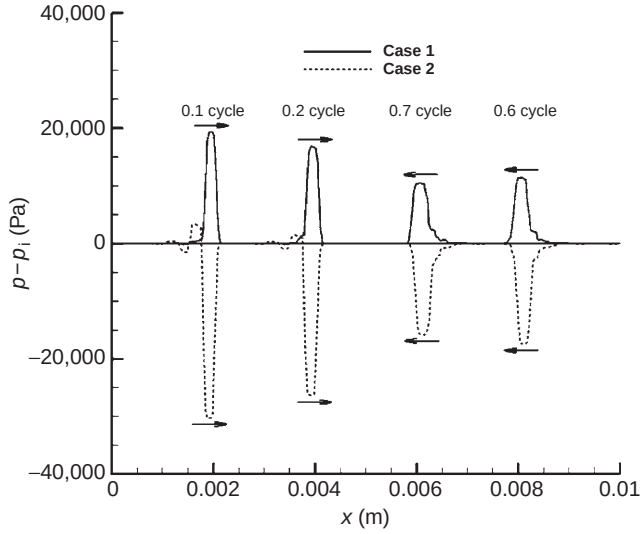

FIG. 113. Thermally induced acoustic (pressure) wave profiles at four early different times within 1 cycle for Cases 1 and 2.

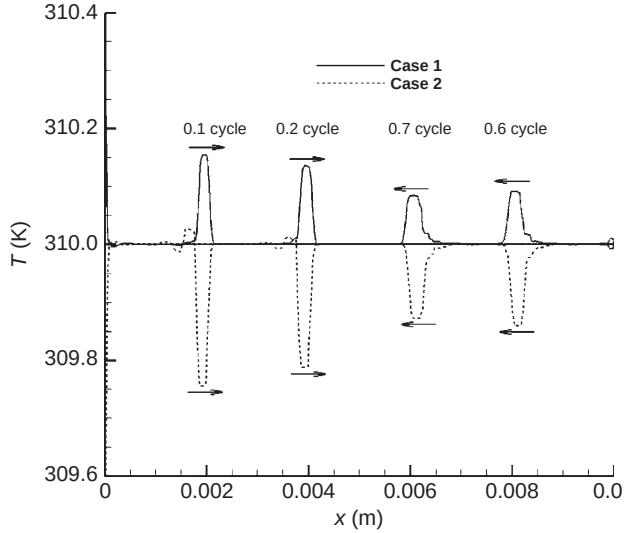

FIG. 114. Spatial variations of temperature waves at four early different times for Cases 1 and 2.

The spatial variation of the "temperature" wave at four early times for Cases 1 and 2 are shown in Fig.114. Comparing Figs. 113 and 114, we see that temperature waves and pressure waves exhibit similar shapes, and travel under the same local sound speed. Thin thermal boundary layers start to form at the left wall, which expand slowly toward the right wall with time.

The temporal variations of pressure at the center point at early time for Cases 1 and 2 are shown in Fig. 115. Rapid temporal variations of the pressure are predicted as the thermally induced acoustic wave arrives at the midpoint after being generated from the left wall and then reflected from both walls. Two observations can be made from this figure. First, the amplitude of the pressure waves are progressively damped as the energy is dissipated in the media. Secondly, the pressure in the bulk fluid gradually increases for Case 1 and decreases for Case 2 as the waves travel back and forth and undergo dissipative losses. These two observations can be more clearly shown in Fig. 116, which shows the temporal variations of pressure at the center point for a longer period (0.1 s) for Cases 1 and 2. Another interesting observation from Fig. 116 is that the temporal variations of pressure at the center for Cases 1 and 2 are not symmetric, although these two cases undergo symmetric temperature changes at the left wall. For the same initial state, a cooling case generates stronger thermally induced acoustic waves than a heating case, as the wave amplitude is determined by the

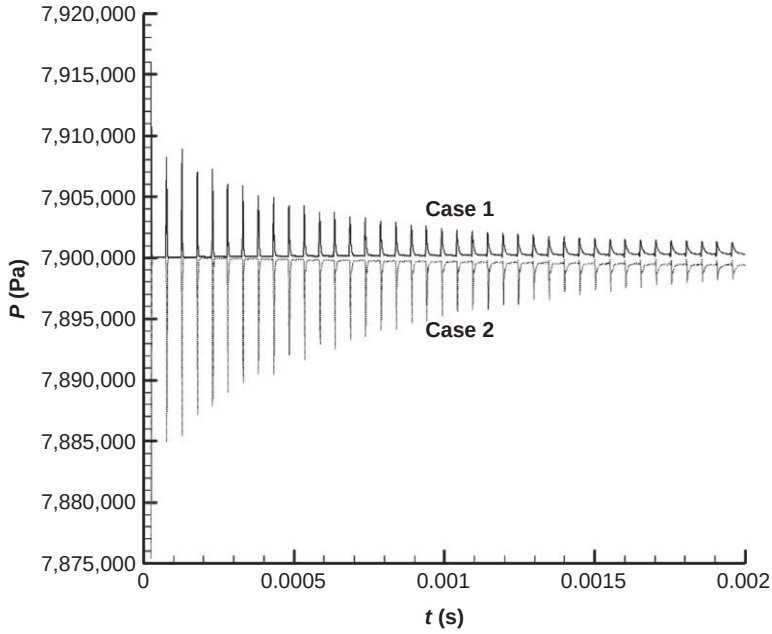

FIG. 115. Temporal variations of pressure at the center point at early time for Cases 1 and 2.

value of $(\partial p \partial T)\big|_\rho$ which decreases with increasing temperature. For the cases studied, a temperature decrease (at constant density) produces a larger change in pressure than a corresponding temperature increase.

The spatial variations of temperature at $t = 0.025$ s, $t = 0.05$ s, $t = 0.075$ s and $t = 0.1$ s for Cases 1 and 2 are shown in Fig. 117. At these times, the thermally induced acoustic waves have reverberated within the domain tens of thousands of times and the wave amplitudes have damped out considerably, heating/cooling the bulk fluid homogeneously. This demonstrates the existence of the so called *piston effect* in supercritical fluid due to rapid heating/cooling. The thermal boundary layers keep expanding as the bulk fluid temperatures increase/decrease. Figure 118 shows the spatial temperature variations for cases 1 and 2, and also for conduction solutions of Cases 1 and 2 at $t = 0.1$ s. The effects of thermally induced acoustic waves in temperature equilibration are evident. For the conduction solutions, the thermal boundary layers expand slowly and the bulk temperatures remain essentially unchanged even after 0.1 s. Comparing between thermally induced acoustic wave results and conduction results after longer times shows the piston effect clearly.

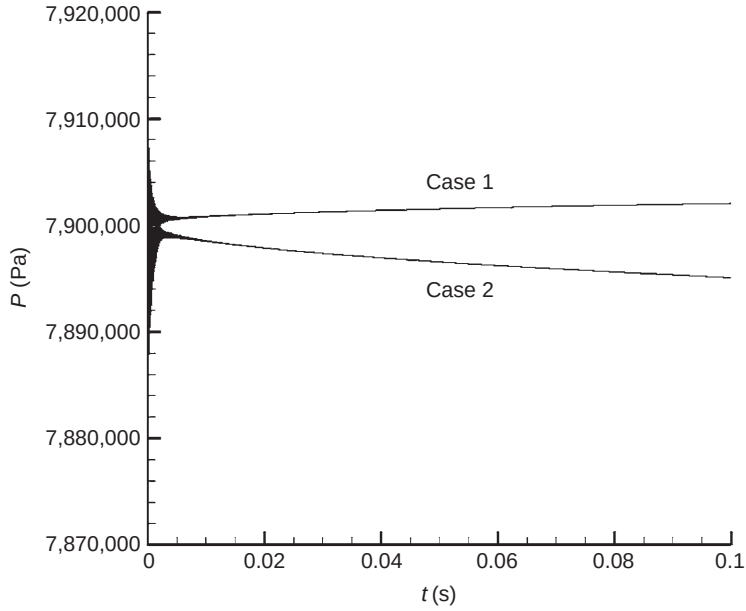

FIG. 116. Temporal variations of pressure at the center point until 0.1 s for Cases 1 and 2.

Simulations for other cases with initial states closer to the critical point ($p_{cr} = 7.377$ MPa and $T_{cr} = 304.1$ K) were also carried out. We show the temporal variations of pressure at the center point until 0.1 s for Cases 3 and 4 ($P_i = 7.7$ MPa and $T_i = 308$ K) in Fig. 119, and for Cases 5 and 6 ($P_i = 7.5$ MPa and $T_i = 306$ K) in Fig. 120. These two figures demonstrate that as the thermally induced acoustic waves progressively damp out, they heat/cool the bulk fluid homogenously. The simulations for the above cases prove the existence of piston effect [91] in the supercritical region.

Temporal variations of pressure at the center at early time for cases 5 and 6 are shown in Fig. 121. Figure 122 shows the spatial variations of temperature at $t = 0.025$ s, $t = 0.05$ s, $t = 0.075$ s and $t = 0.1$ s showing the piston effect for Cases 5 and 6. As the acoustic waves are dissipated, the bulk fluid is heated/cooled homogeneously.

In cases 1–6, simulations were carried out for zero bulk viscosity. Cases for non-zero bulk viscosity were also simulated in this study. The conditions for Cases 7 and 8 are the same as in Cases 1 and 2 respectively, except non-zero bulk viscosity values are considered. Figure 123 shows temporal variations of pressure at the center for Cases 7 and 8. Figure 124 shows spatial variations of temperature at $t = 0.025$ s, $t = 0.05$ s, $t = 0.075$ s and

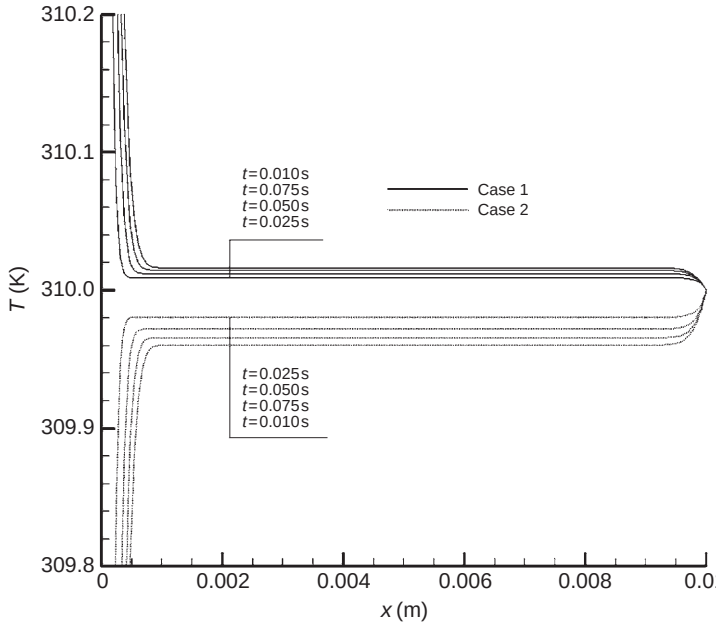

FIG. 117. Spatial variations of temperature at $t = 0.025$ s, $t = 0.05$ s, $t = 0.075$ s and $t = 0.1$ s for Cases 1 and 2.

$t = 0.1$ s for Cases 7 and 8. Through comparing Figs. 123 and 115, Figs. 124 and 116, we see that the effect of non-zero bulk viscosity can be neglected in these two cases. There are two reasons for this. The first is that in this study all cases are one-dimensional. The effect of bulk viscosity may be more evident in a two or three dimensional flow problem. The second reason is that the computed non-zero bulk viscosity value is not very large compared to the molecular viscosity in Cases 7 and 8. The bulk viscosity effects will be stronger as the initial state of the fluid is closer to the critical point.

2. *Conclusions*

The generation and propagation of thermally induced acoustic waves in supercritical carbon dioxide are investigated by numerically solving a fully compressible form of the Navier-Stokes equations. The NIST Standard Reference Database 12 [67] was used to generate the polynomial fits to represent the equation of state and other thermodynamic properties for supercritical carbon dioxide. The numerical algorithm used here based on

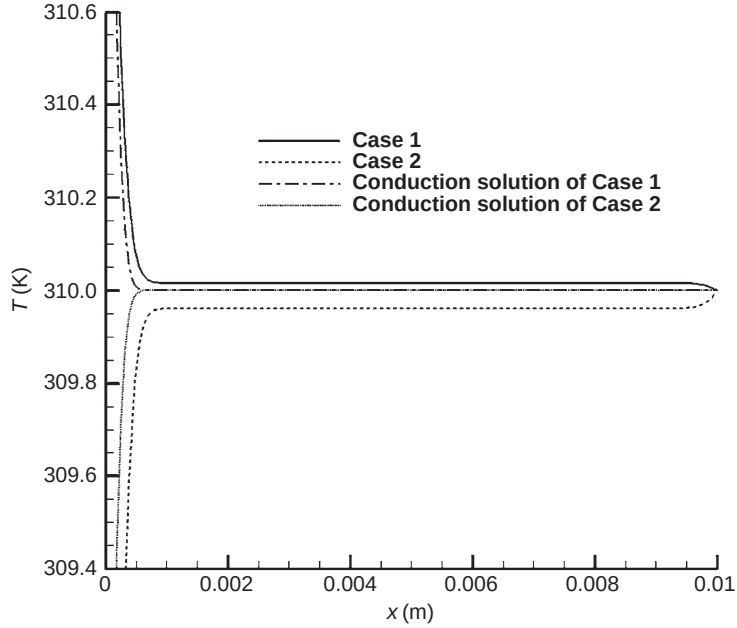

FIG. 118. Spatial temperature variations for Cases 1 and 2, and for conduction solutions of Cases 1 and 2 at $t = 0.1$ s.

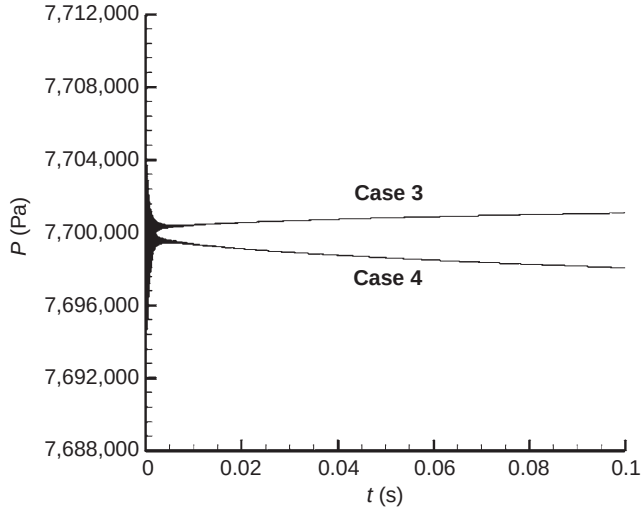

FIG. 119. Temporal variations of pressure at the center point until 0.1 s for Cases 3 and 4.

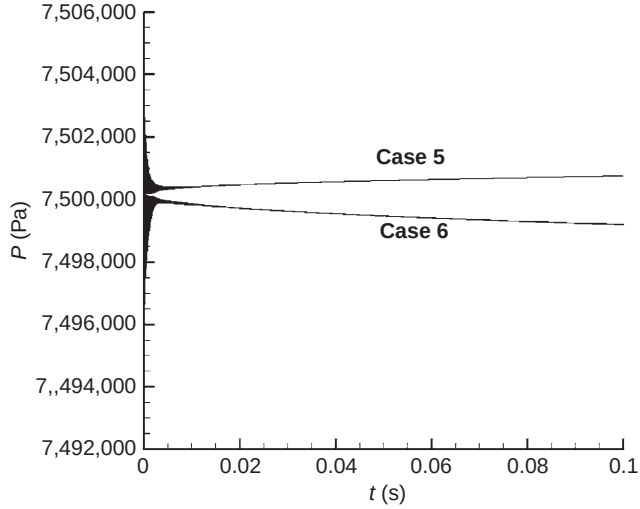

FIG. 120. Temporal variations of pressure at the center point until 0.1 s for Cases 5 and 6.

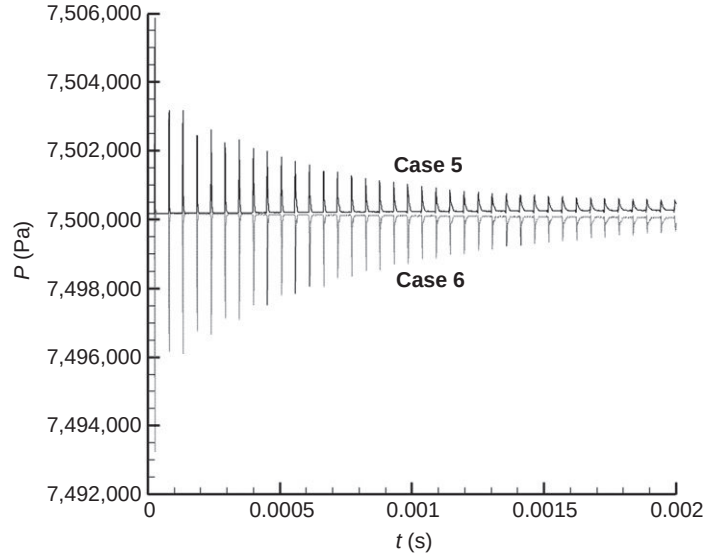

FIG. 121. Temporal variations of pressure at the center point at early time for Cases 5 and 6.

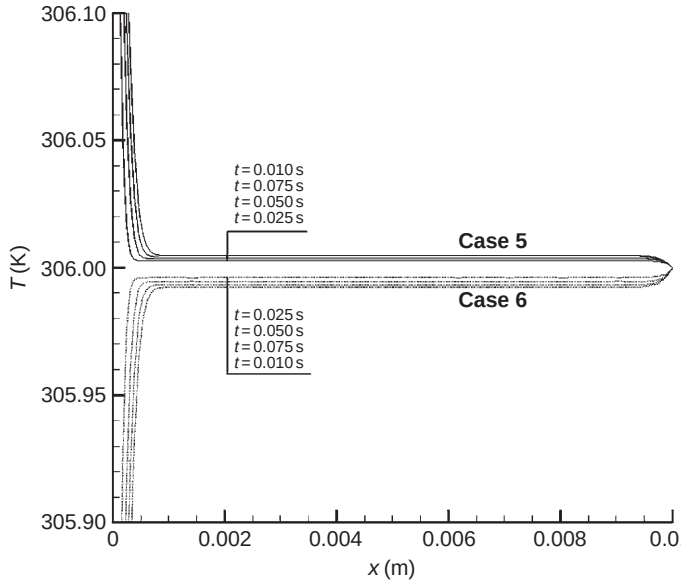

FIG. 122. Spatial variations of temperature at $t = 0.025$ s, $t = 0.05$ s, $t = 0.075$ s and $t = 0.1$ s showing the piston effect for Cases 5 and 6.

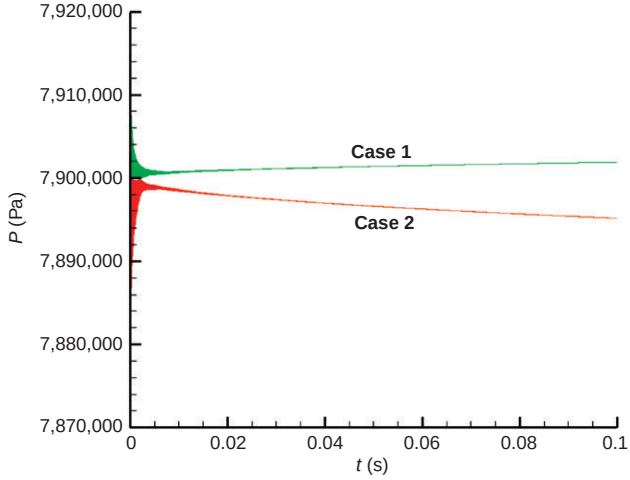

FIG. 123. Temporal variations of pressure at the center point until 0.1 s for Cases 7 and 8.

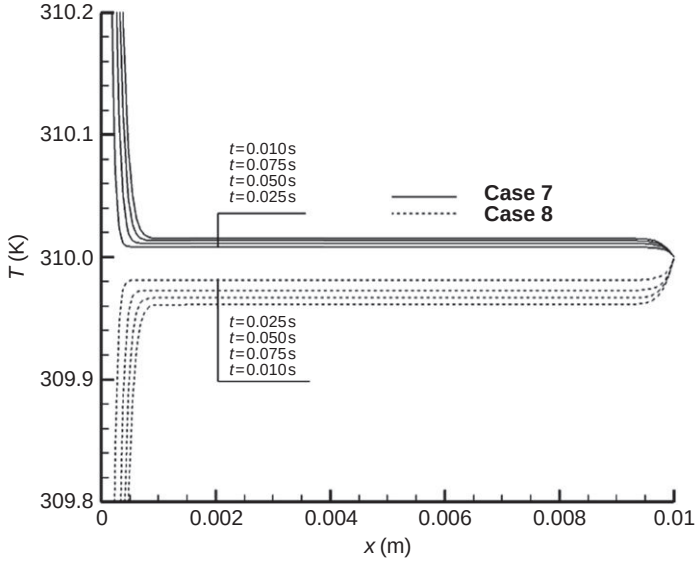

FIG. 124. Spatial variations of temperature at $t = 0.025$ s, $t = 0.05$ s, $t = 0.075$ s and $t = 0.1$ s for Cases 7 and 8.

the FCT algorithm, along with the theory of characteristic-based wall boundary conditions for density, provided the higher-order accuracy needed to resolve the wave.

The details of thermally induced acoustic wave generation, propagation and decay in supercritical fluids were presented. In this study, non-zero bulk viscosity was included in the computational model, however no effect of bulk viscosity was found for the one-dimensional cases considered.

VII. Experimental Study of Thermally Induced Acoustic Waves in Supercritical Fluids

A. Introduction

The behaviors of thermally induced acoustic waves, in high pressure and supercritical carbon dioxide, generated by rapid heating of a bounding solid wall in a closed cylindrical tube were investigated experimentally. In the experiments, a thin aluminum foil attached to one end of the cylinder is heated by a resistance-capacitance (R-C) circuit, which is controlled by a silicon-controlled rectifier (SCR). The rapid heating of the aluminum foil

generates a thermally induced acoustic wave in the closed cylinder, in which the thermally induced acoustic wave keeps traversing between the two ends and undergoes many reflections before it is fully damped out. The time-dependent pressure variations in the cylinder is measured by a microphone located at a specific point on the side of the cylinder, and the temporal temperature variations of the aluminum foil are measured by a thermocouple attached to it, along with a fast-response data acquisition system (DAQ).

B. Experimental Apparatus and Procedures

Carbon dioxide is chosen as the working fluid, due to its good characteristics, such as non-toxicity, non-flammability, inexpensiveness, and benign critical temperature (304.13 K) and critical pressure (7.3773 MPa) [92]. The thermally induced acoustic waves are generated and travels within a cylinder filled with supercritical carbon dioxide, while the DAQ system, the sensor cables and wires must be connected to a data logging system (a personal computer).

Figure 125 shows the schematic of the experimental system used. Carbon dioxide is stored in a tank, and in order to increase the carbon dioxide pressure, a hand pump is employed to pressurize the carbon dioxide in the supercritical chamber until the destination pressure is reached (the destination pressure is above the supercritical pressure). The reason to choose a hand pump is that it is able to compresses a fluid within a small volume to develop high pressure. A hand pump also enables us to accurately regulate the pressure inside the supercritical chamber manually.

1. Generating Thermally Induced Acoustic Waves

Based on the past experimental work [93,94], an R-C circuit is employed to rapidly heat a metal foil attached to a end of the cylinder by means of direct-current heating. The schematic of foil heating is similar to that described in Section V.B earlier. Lin and Farouk [94] used 6.0 μm thick Nickel foils to generate thermally induced acoustic waves, because with a thinner foil, the heating is faster and the maximum temperature of the foil is higher, resulting in stronger thermally induced acoustic waves. In this way, a better measuring accuracy can be achieved.

In the experimental setup, the dimensions of the foil (attached around a circular mica end-piece) are 42 mm × 50 mm × 6.0 mm. The electrical resistance of the foil is calculated to be 0.014 Ω. By carefully calculating every component in the R-C circuit, the circuit efficiency $\varepsilon = R_{\text{foil}}/R_{\text{total}}$ is found to be about 53%. Several capacitors rated at 18.0 mF, 27.0 mF and 56.0 mF are used for the measurements. The circuit time constant, $\tau_{\text{RC}} = R_{\text{total}} \cdot C$ is hence

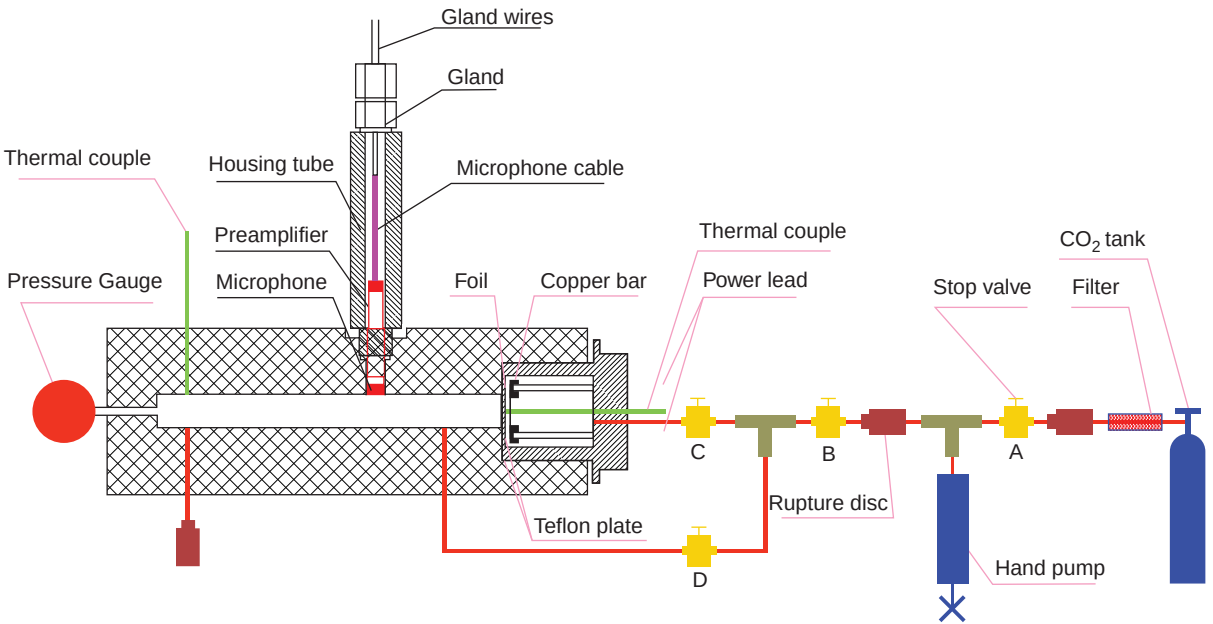

FIG. 125. Schematic of experimental tubing system.

0.0005 s, 0.00071 s, and 0.0015 s for capacitances of $C = 18.0$ mF, 27.0 mF, and 56.0 mF used in the circuit, respectively. Thermally generated acoustic waves are generated and travels within a cylinder of a 1 in diameter. During an experiment, the circuit connecting the capacitor and the foil is switched on by the SCR, which is triggered by the triggering circuit.

The critical temperature and pressure for carbon dioxide are 304.13 K and 7.3773 MPa, respectively. In order to achieving supercritical state, we needed to heat the carbon dioxide from the room temperature (generally 295 K) to supercritical temperature value, and also to pressurize the carbon dioxide form a CO_2 tank to supercritical pressure value. A Thermolyne.$5 \times 4'$ heating tape was used to heat the supercritical chamber from the lab room temperature (generally 295 K) to the destination temperature (above the critical temperature). Rupture discs were employed to make sure that the pressure within the system will never be above a specific value.

For the experiments of thermally induced acoustic waves in supercritical carbon dioxide, the probes are in a high pressure zone, while the data needs to be transmitted to the DAQ card, which is in an atmospheric region. In order to measure the thermally induced acoustic pressure waves in the supercritical chamber, the microphone is connected with the preamplifier through a screw thread on the preamplifier. A cable connects the preamplifier and the amplifier, which is connected with the DAQ card.

C. Experimental Results and Discussion

The experimental initial conditions ($p_i = 7.69$ MPa and $T_i = 307$ K) were in the supercritical region (close to the critical point). At the beginning of an experiment, the supercritical chamber was slowly heated by a heating tape, which is wound round the chamber, to the set value ($T_i = 307$ K). After the desired temperature was reached, the power of the heating tape was adjusted in order to maintain the desired initial temperature. Before the capacitor was discharged to generate thermally induced acoustic waves, the supercritical chamber was maintained at the initial temperature for some time to ensure steady state within it.

Figure 126 shows the temporal variation of the foil temperature ($V_0 = 35$ V). The foil temperature increases rapidly to the maximum value at early times (for less than 0.04 s after the beginning of the capacitor-discharge).

The pressure wave ($V_0 = 35$ V) in the supercritical carbon dioxide is shown in Fig. 127. During the first several acoustic cycles (Fig. 127 (a)) the wave shape shows the same steep fronts followed by some noises as in gases (Section V). The noise in the data is caused by the uneven foil surface and unsmooth internal surface of the cylinder. The measured acoustic speed is in a good match with value predicted by the NIST Standard Reference Database 12 [92].

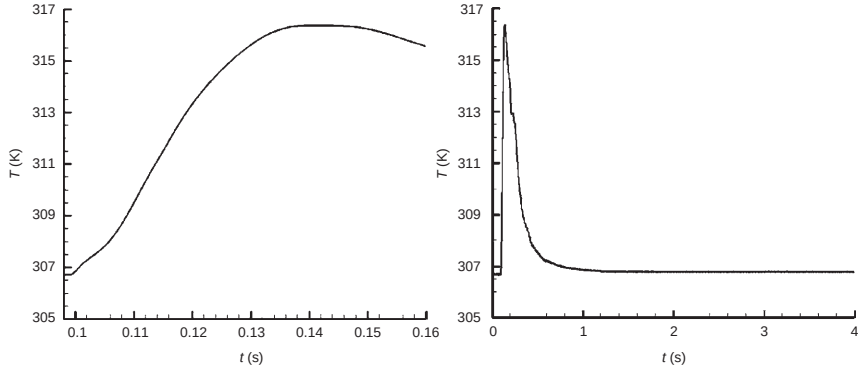

FIG. 126. Temporal variation of the foil temperature ($V_0 = 35$ V). (a) Early time. (b) Longer time scale.

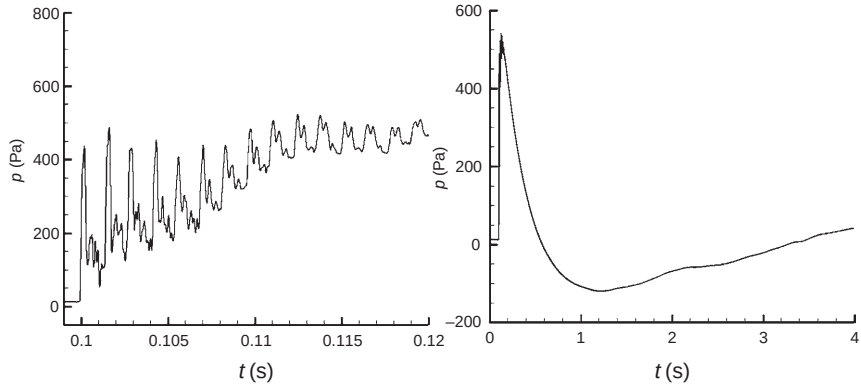

FIG. 127. Temporal variation of pressure ($p - p_i$) wave ($V_0 = 35$ V). (a) Early time; (b) Longer time scale.

The effect of capacitor charging voltage on the foil temperature was studied in the supercritical carbon dioxide experiments ($p_i = 7.69$ MPa and $T_i = 307$ K). Figure 128 shows the temporal variations of pressure ($p - p_i$) wave for different capacitor charging voltages. In Fig. 128 (a), we see that the wave speed and the wave shape are the same for different capacitor charging voltages. At the early time the wave amplitude is found to be dependent on the foil temperature increase rate, which is determined by the capacitor charging voltage.

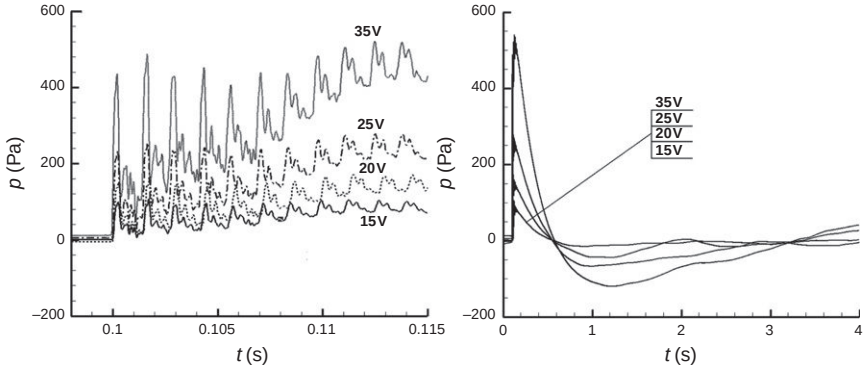

FIG. 128. Temporal variations of pressure ($p - p_i$) wave (showing the effect of the capacitor charging voltage). (a) Early time; (b) Longer time scale.

1. *Comparison of Numerical and Experimental Results*

Comparison of numerical and experimental results for thermally induced acoustic waves in supercritical carbon dioxide at early time was carried out.

A 0.01-m-long one-dimensional problem geometry was employed for the numerical simulation (see Section V), although the length of the cylinder filled with supercritical fluids in experimental is 0.257 m. The problem is essentially one-dimensional at early time. The mesh size was 500 and the Courant number ($(c\Delta t/\Delta x)$) was 0.4 for the numerical simulation. In the numerical model, the temperature boundary condition is determined from the experimental measurements.

Figure 129 compares the experimental and computational pressure waves ($V_0 = 35$ V). The vertical axis is pressure ($p - p_i$) and the horizontal axis is the non-dimensional time tc/L, where t is time, c is acoustic speed and L is length. The pressure wave speed and amplitude predicted in the numerical results compare well with the experimental results. Furthermore, as the wave travels between the left and right walls, the predicted pressure rise of bulk fluid compares well with the measurements. The measurements are a bit noisy due to the uneven foil surface. Each wave peak in the experimental results is wider than that in the numerical results. The B&K microphone actually measures the average pressure within the region covered by the diaphragm, while the numerical results show the pressure right at the center cell of the computational domain.

2. *Conclusions*

Experimental measurements were conducted to characterize the generation, propagation and damping of thermally induced acoustic waves in

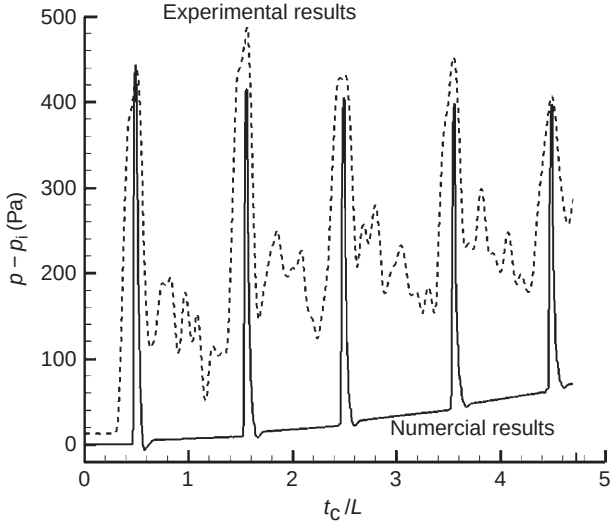

FIG. 129. Comparison of experimental and computational temporal variations of pressure at the center between the left and right walls in supercritical carbon dioxide ($V_0 = 35$ V).

supercritical carbon dioxide ($p_i = 7.69$ MPa and $T_i = 307$ K). In the experiments, the generation, propagation and damping of pressure waves for different capacitor charging voltage were investigated, and the strength of the thermally induced acoustic wave was found to be dependent on the temperature increase rate of the foil at early time. Low frequency disturbances was observed in both early time and longer time pressure profiles, due to the fluid flow within the supercritical chamber induced by the non-uniform temperature field caused by the heating tape. At early times, the computational and experimental results are in good agreement.

VIII. Summary and Conclusions

Acoustic waves in compressible media are generated by two kinds of sources: rapid heating of the media, and mechanical vibration along a bounding/immersed solid wall. The chapter reviews the recent computational and experimental work on interactions of acoustic waves with viscous and conducting fluids. The flow field, and heat transfer associated with both types of generation method are characterized by measurements and simulations. The effect of gravity on the propagation and decay of the acoustic waves are also reviewed.

For high-intensity standing waves driven by wall vibration, the second-order steady acoustic streaming due to acoustic-boundary layer interactions are investigated both experimentally and numerically. The convection induced by acoustic streaming is found to have a marked effect on heat transfer. In turn, the wall temperature variation also change both the structure of acoustic streaming and streaming velocity due to the nonuniform fluid properties.

An experimental setup is described that allowed us to characterize acoustic waves and visualize the flow field produced. The developed computational models provide dynamic simulations of the transport phenomena driven by the interactions of acoustic waves with viscous flows and heat transfer. The models have been verified by the experimental data, and various simulation results in both Cartesian and cylindrical coordinates are presented in the chapter. The models developed can be used as flexible design tools in industrial applications.

The generation, propagation and damping of thermally induced acoustic waves in an enclosure (filled with a gas or with supercritical carbon dioxide) were studied by experimental and numerical methods. In both experimental and numerical investigations, thermally induced acoustic waves were generated by rapidly increasing the wall temperature of the enclosure, and the strength of the pressure waves was found to be directly proportional to the temperature increase rate. The computational and experimental results are in good agreement with each other.

The numerical model developed for thermally induced acoustic waves was applied for a high pressure carbon dioxide. Simulations of thermoacoustic waves were obtained in enclosures with initial pressure values varying from 0.1 MPa to 8 MPa and an initial temperature of 310 K. The pressure and temperature values considered include ideal, real gas and supercritical states of carbon dioxide. The pressure wave shapes observed in both real gas and supercritical states are quite similar to those observed for an ideal gas. However, the strength of the pressure waves increase with increasing initial pressure, which is explained by the variations of fluid properties with pressure.

The effects of the thermally induced acoustic phenomena on the transient natural convection process in an enclosure were studied by solving the unsteady compressible Navier-Stokes equations. The effect of gravitational acceleration was found negligible for early times. As the acoustic waves lose their strength, buoyancy induced natural convection currents dominate the flow field. The development of buoyancy induced flow is however, strongly affected by the strength of the thermally induced acoustic wave. It is also observed that the thermally generated flow field and the buoyancy induced flow field are both affected by the aspect ratio of the enclosure.

The generation, propagation and decay of thermally induced acoustic waves in supercritical carbon dioxide gas are also reported. A numerical study was carried out to investigate the characteristics of these waves in near-critical (super) carbon dioxide gas. The equation of state and property variations of the fluid were obtained via NIST Reference Database 12. Experimental measurements of thermoacoustic waves in supercritical carbon dioxide are also reported.

References

1. Trilling, L. (1955). On thermally induced sound fields. *J. Acoust. Soc. Am.* **27**, 425–431.
2. Zappoli, B., Amiroudine, S., Carles, P., and Ouazzani, J. (1996). Thermoacoustic and Buoyancy-driven transport in a square side-heated cavity filled with a near-critical fluid. *J. Fluid Mech.* **316**, 53–72.
3. Swift, G. W. (1995). Thermoacoustic engines and refrigerators. *Phys. Today* **48**, 22.
4. Boluriaan, S. and Morris, P. J. (2003). Acoustic streaming: from Rayleigh to today. *Int. J. Aeroacoust.* **2**, 255–292.
5. Schlichting, H. (1932). Calculation of plane periodic boundary-layer streaming. *Physik Zeitschr.* **33**, 327–335.
6. Andres, J. M. and Ingard, U. (1953). Acoustic streaming at low Reynolds numbers. *J. Acoust. Soc. Am.* **25**, 932–938.
7. Andres, J. M. and Ingard, U. (1953). Acoustic streaming at high Reynolds numbers. *J. Acoust. Soc. Am.* **25**, 928–932.
8. Lee, C. P. and Wang, T. G. (1990). Outer acoustic streaming. *J. Acoust. Soc. Am.* **88**, 2367–2375.
9. Qi, Q. (1993). The effect of compressibility on acoustic streaming near a rigid boundary for a plane traveling wave. *J. Acoust. Soc. Am.* **94**, 1090–1098.
10. Qi, Q., Johnson, R. E., and Harris, J. G. (1995). Boundary layer attenuation and acoustic streaming accompanying plane-wave propagation in a tube. *J. Acoust. Soc. Am.* **97**, 1499–1509.
11. Vainshtein, P. (1995). Rayleigh streaming at large Reynolds number and its effect on shear flow. *J. Fluid Mech.* **285**, 249–264.
12. Menguy, L. and Gilbert, J. (2000). Non-linear acoustic streaming accompanying a plane stationary wave in a guide. *Acoustica* **86**, 249–259.
13. Andrade, E. N. (1931). On the circulations caused by the vibration of air in a tube. *Proc. R. Soc. Lon. A* **134**, 445–470.
14. West, G. D. (1951). Circulations occurring in acoustic phenomena. *Proc. Phys. Soc. B* **64**, 483–487.
15. Holtsmark, J., Johnsen, I., Sikkeland, T., and Skavlem, S. (1954). Boundary layer flow near a cylindrical obstacle in an oscillating incompressible fluid. *J. Acoust. Soc. Am.* **26**, 26–39.
16. Raney, W. P., Corelli, J. C., and Westervelt, P. J. (1954). Acoustic streaming in the vicinity of a cylinder. *J. Acoust. Soc. Am.* **26**, 1006–1014.
17. Coppens, A. B. and Sanders, J. V. (1968). Finite-amplitude standing waves in rigid-walled tubes. *J. Acoust. Soc. Am.* **43**, 516–529.

18. Cruikshank, D. B. (1972). Experimental investigation of finite-amplitude acoustic oscillations in closed tubes. *J. Acoust. Soc. Am.* **52**, 1024–1034.
19. Trinh, E. H. and Robey, J. L. (1994). Experimental study of streaming flows associated with ultrasonic levitators. *Phys. Fluids* **6**, 3567–3579.
20. Kempton, A. J. (1976). Heat diffusion as a source of aerodynamic sound. *J. Fluid Mech.* **78**, 1–31.
21. Morfey, C. L. (1976). Sound radiation due to unsteady dissipation in turbulent flow. *J. Sound Vib.* **48**, 95–111.
22. Fand, R. M. and Haye, J. (1960). Acoustic streaming near a heated cylinder. *J. Acoust. Soc. Am.* **32**, 579–584.
23. Richardson, P. D. (1967). Heat transfer from a circular cylinder by acoustic streaming. *J. Fluid Mech.* **30**, 337–355.
24. Richardson, P. D. (1969). Local effect of horizontal and vertical sound fields on natural convection from a horizontal cylinder. *J. Sound Vib.* **10**, 32–41.
25. Engelbrecht, H. and Pretorius, L. (1992). The effect of sound on natural convection from a vertical flat plate. *J. Sound Vib.* **158**, 213–218.
26. Gopinath, A. and Mills, A. F. (1993). Convective heat transfer from a sphere due to acoustic streaming. *J. Heat Transf.* **115**, 332–341.
27. Gopinath, A. and Mills, A. F. (1994). Convective heat transfer due to acoustic streaming across the ends of a Kundt tube. *J. Heat Transf.* **116**, 47–53.
28. Vainshtein, P., Fichman, M., and Gutfinger, C. (1995). Acoustic enhancement of heat transfer between two parallel plates. *Int. J. Heat Mass Transf.* **38**, 1893–1899.
29. Mozurkewich, G. (1995). Heat transfer from a cylinder in an acoustic standing wave. *J. Acoust. Soc. Am.* **98**, 2209–2216.
30. Gopinath, A. and Harder, D. R. (2000). An experimental study of heat transfer from a cylinder in low-amplitude zero-mean oscillatory flows. *Int. J. Heat Mass Transf.* **43**, 505–520.
31. Kawahashi, M. and Arakawa, M. (1996). Nonlinear phenomena induced by finite-amplitude oscillation of air column in closed duct. *JSME Int. J.* **39**, 280–286.
32. Kawahashi, M., Tanahashi, M., Arakawa, M., and Hirahara, H. (1995). *Visualization and measurement of acoustic streaming coupling with natural convection*. Presented at "ASME/JSME Fluids Engineering and Laser Anemometry Conference and Exhibition," Hilton Head, SC, USA.
33. Loh, B., Hyun, S., Ro, P. I., and Kleinstreuer, C. (2002). Acoustic streaming induced by ultrasonic flexural vibrations and associated enhancement of convective heat transfer. *J. Acoust. Soc. Am.* **111**, 875–883.
34. Loh, B. and Lee, D. (2004). Heat transfer characteristics of acoustic streaming by longitudinal ultrasonic vibration. *J. Thermophys. Heat Transf.* **18**, 94–99.
35. Mozurkewich, G. (2002). Heat transport by acoustic streaming within a cylindrical resonator. *Appl. Acoust.* **63**, 713–735.
36. Wan, Q. and Kuznetsov, A. V. (2003). Numerical study of the efficiency of acoustic streaming for enhancing heat transfer between two parallel beams. *Flow Turbul. Combust.* **70**, 89–114.
37. Wan, Q., Wu, T., Chastain, J., Roberts, W. L., Kuznetsov, A. V., and Ro, P. I. (2005). Forced convective cooling via acoustic streaming in a narrow channel established by a vibrating piezoelectric bimorph. *Flow Turbul. Combust.* **74**, 195–206.
38. Hamilton, M. F., Ilinskii, Y. A., and Zabolotskaya, E. A. (2003). Acoustic streaming generated by standing waves in two-dimensional channels of arbitrary width. *J. Acoust. Soc. Am.* **113**, 153–160.
39. Hamilton, M. F., Ilinskii, Y. A., and Zabolotskaya, E. A. (2003). Thermal effects on acoustic streaming in standing waves. *J. Acoust. Soc. Am.* **114**, 3092–3101.

40. Wan, Q. and Kuznetsov, A. V. (2005). Investigation of Hysteresis in acoustically driven channel flow at ultrasonic frequency. *Numer. Heat Transf. A* **47**, 137–146.
41. Yano, T. (1999). Turbulent acoustic streaming excited by resonant gas oscillation with periodic shock waves in a closed tube. *J. Acoust. Soc. Am.* **106**, L7–L12.
42. Aktas, M. K. and Farouk, B. (2004). Numerical simulation of acoustic streaming generated by finite-amplitude resonant oscillation in an enclosure. *J. Acoust. Soc. Am.* **116**, 2822–2831.
43. Aktas, M. K., Farouk, B., and Lin, Y. (2005). Heat transfer enhancement by acoustic streaming in an enclosure. *ASME J. Heat Transf.* **127**, 1313–1321.
44. Larkin, B. K. (1967). Heat flow to a confined fluid in zero gravity. *In* "Progress in Astronautic and Aeronautics Thermophysics of Spacecraft and Planetary Bodies" (G. B. Heller, ed.), pp. 819–832. Academic, New York, NY.
45. Kassoy, D. R. (1979). The response of a confined gas to a thermal disturbance: slow transients. *SIAM J. Appl. Math.* **36**, 624–634.
46. Radhwan, A. M. and Kassoy, D. R. (1984). The response of a confined gas to a thermal disturbance: rapid boundary heating. *J. Eng. Math.* **18**, 133–156.
47. Ozoe, H., Sato, N., and Churchill, S. W. (1980). The effect of various parameters on thermoacoustic convection. *Chem. Eng. Commun.* **5**, 203–221.
48. Ozoe, H., Sato, N., and Churchill, S. W. (1990). Numerical analyses of two and three dimensional thermoacoustic convection generated by a transient step in the temperature of one wall. *Numer. Heat Transf. A* **18**, 1–15.
49. Churchill, S. W. and Brown, M. A. (1987). Thermoacoustic convection and the hyperbolic equation of conduction. *Int. Commun. Heat Mass Transf.* **14**, 647–655.
50. Brown, M. A. and Churchill, S. W. (1999). Finite-difference computation of the wave motion generated in a gas by a rapid increase in the bounding temperature. *Comput. Chem. Eng.* **23**, 357–376.
51. Huang, Y. and Bau, H. H. (1995). Thermoacoustic waves in a semi-infinite medium. *Int. J. Heat Mass Transf.* **38**, 1329–1345.
52. Huang, Y. and Bau, H. H. (1997). Thermoacoustic waves in a confined medium. *Int. J. Heat Mass Transf.* **40**, 407–419.
53. Farouk, B., Oran, E. S., and Fusegi, T. (2000). Numerical study of thermoacoustic waves in an enclosure. *Phys. Fluids* **12**, 1052–1061.
54. Aktas, M. K. and Farouk, B. (2003). Numerical simulation of developing natural convection in an enclosure due to rapid heating. *Int. J. Heat Mass Transf.* **46**, 2253–2261.
55. Parang, M. and Salah-Eddine, A. (1984). Thermoacoustic convection heat-transfer phenomenon. *AIAA J.* **22**, 1020–1022.
56. Brown, M. A. and Churchill, S. W. (1995). Experimental measurements of pressure waves generated by impulsive heating of a surface. *AIChE J.* **41**, 205–213.
57. Nitsche, K. and Straub, J. (1986). *Naturewissenschaften* **73**, 370–376.
58. Nitsche, K. and Straub, J. (1986). The critical "hump" of Cv under microgravity result from the D-1 spacelab experiment. Presented at "Proceedings of the Sixth European Symposium on Materials Sciences under Microgravity Conditions," ESA SP-256, Bordeaux, France.
59. Zappoli, B., Bailly, D., Garrabos, Y., Le Neindre, B., Guenoun, P., and Beysens, D. (1990). Anomalous heat transport by the piston effect in supercritical fluids under zero gravity. *Phys. Rev. A* **41**, 2224–2267.
60. Onuki, A., Hao, H., and Ferrell, R. A. (1990). Fast adiabatic equilibrium in a single component fluid near the liquid-vapor critical point. *Phys. Rev. A* **41**, 2256–2279.
61. Boukari, H., Shumeyer, J. N., Briggs, M. E., and Gammon, R. W. (1990). Critical speeding up in pure fluids. *Phys. Rev. A* **41**, 2260–22263.

62. Bonetti, M., Perrot, F., Beysens, D., and Garrabos, Y. (1994). Fast thermalization in supercritical fluids. *Phys. Rev. E* **49**, 4779–4782.
63. Straub, J., Eicher, L., and Haupt, A. (1995). Dynamic temperature propagation in a pure fluid near its critical point observed under microgravity during the German Spacelab Mission D-2. *Phys. Rev. E* **51**, 5556–5563.
64. Guenoun, P., Khalil, B., Beysens, D., Garrabos, Y., Kammoun, P., and Le Neindre, B. (1993). Thermal cycle around the critical point of carbon dioxide under reduced gravity. *Phys. Rev. E* **47**, 1531–1540.
65. Berg, R. F. and Moldover, M. R. (1999). Frequency-dependent viscosity of Xenon near the critical point. *Phys. Rev. E* **60**, 4079–4087.
66. Berg, R. F., Moldover, M. R., and Zimmereli, G. A. (1999). Viscoelasticity of Xenon near the critical point. *Phys. Rev. Lett.* **82**, 920–923.
67. Lemmon, E. W., Peskin, A. P., McLinden, M. O., and Friend, D. G. (2000). "NIST Thermodynamic and Transport Properties of Pure Fluids." National Institute of Standard and Technology, Gaithersburg, MD, Standard Reference Data Program.
68. Oran, E. S. and Boris, J. P. (2000). "Numerical Simulation of Reactive Flows." Cambridge University Press, Cambridge, UK.
69. Poinsot, T. J. and Lele, S. K. (1992). Boundary conditions for direct simulations of compressible viscous flows. *J. Comput. Phys.* **101**, 104–129.
70. Saint-Martin-Tillet, X. N. and Oran, E. S. (1997). "Boundary Conditions for FCT Based Solutions of the Navier-Stokes Equations." Naval Research Laboratory, Washington, DC.
71. Nyborg, W. L. (1998). Acoustic streaming. *In* "Nonlinear Acoustics" (M. F. Hamilton and D. T. Blackstock, eds.), pp. 207–231, Academic Press, New York, NY.
72. Rayleigh., L. (1884). On the circulation of air observed in Kundt's tubes. *Philos. Trans. A* **175**, 1–21.
73. Westervelt, P. J. (1953). The theory of steady rotational flow generated by a sound field. *J. Acoust. Soc. Am.* **25**, 60–67.
74. Nyborg, W. L. (1958). Acoustic streaming near a boundary. *J. Acoust. Soc. Am.* **30**, 329–339.
75. Aktas, M. and Farouk, B. (2004). Numerical simulation of acoustic streaming generated by finite amplitude standing waves in an enclosure. *J. Acoust. Soc. Am.* **116**, 2822–2831.
76. Chester, W. (1964). Resonant oscillations in closed tubes. *J. Fluid Mech.* **18**, 44–64.
77. Alexeev, A. and Gutfinger, C. (2003). Resonance gas oscillations in closed tubes: numerical study and experiments. *Phys. Fluids* **15**, 3397–3408.
78. Lin, Y. (2007). Acoustic wave induced convection and transport in gases under normal and micro-gravity conditions, Ph.D. thesis, Drexel University, Philadelphia, PA.
79. Lin, Y. and Farouk, B. (2008). Experimental and numerical studies of thermally induced acoustic wave in a closed enclosure. *AIAA J. Thermophys. Heat Transf.* **22**, 105–114.
80. Lin, Y. and Farouk, B. (2008). Heat transfer in a rectangular chamber with differentially heated horizontal walls: effects of a vibrating sidewall. *Int. J. Heat Mass Transf.* **51**, 3179–3189.
81. Lemmon, E. W., Peskin, A. P., McLinden, M. O., and Friend, D. G. (2000). NIST Standard Reference Database 12: Thermodynamic and Transport Properties of Pure Fluids, version 5. National Institute of Standards and Technology, Standard Reference Data program, Gaithersburg, MD.
82. Lin, Y., Farouk, B., and Oran, E. S. (2006). Flows induced by thermoacoustic waves in an enclosure: effects of gravity. *J. Thermophys. Heat Transf.* **20**, 376–383.
83. Lin, Y., Farouk, B., and Oran, E. S. (2008). Interactions of thermally induced acoustic waves with buoyancy induced flows in rectangular enclosures. *Int. J. Heat Mass Transf.* **51**, 1665–1674.
84. Brüel & Kjær (2006). Acoustic Transducers: Pressure-Field Microphones. http://www.bkhome.com

85. Kline, S. J. and McClintock, F. A. (1953). Describing uncertainties in single-sample experiments. *Mech. Eng*. **75**, 3–8.
86. Wagner, H. and Bayazitoglu, Y. (2002). Thermal disturbances in near critical fluids. *J. Thermophys. Heat Transf*. **16**, 273–279.
87. Wagner, H., Hos, P., and Bayazitoglu, Y. (2001). Variable property piston effect. *J. Thermophys. Heat Transf*. **15**, 497–503.
88. Patankar, S. V. (1980). "Numerical Heat Transfer and Fluid Flow". Hemisphere, Washington, DC.
89. Lei, Z. and Farouk, B. (2007). Generation and propagation of thermally induced acoustic waves in supercritical carbon dioxide. *In* "ASME International Mechanical Engineering Congress and Exposition." pp. 1–8, Seattle, Washington, DC.
90. Gillis, K. A., Shinder, I. I., and Moldover, M. R. (2004). Thermoacoustic boundary layers near the liquid-vapor critical point. *Phys. Rev. E* **70**, 1–19.
91. Zappoli, B., Amiroudine, S., Carles, P., and Ouazzani, J. (1996). Thermoacoustic and Buoyancy-driven transport in a square side-heated cavity filled with a near-critical fluid. *J. Fluid Mech*. **316**, 53–72.
92. Lemmon, E. W., Peskin, A. P., McLinden, M. O., and Friend, D. G. (2000). NIST Standard Reference Database 12: Thermodynamic and Transport Properties of Pure Fluids, Version 5.0. National Institute of Standards and Technology.
93. Brown, M. A. and Churchill, S. W. (1995). Experimental measurements of pressure waves generated by impulsive heating of a surface. *AIChE J*. **41**, 205–213.
94. Lin, Y. and Farouk, B. (2008). Experimental and numerical studies of thermally induced acoustic waves in a closed enclosure. *AIAA J. Thermophys. Heat Transf*. **22**, 105–114.

Characterization Methods of High-Intensity Focused Ultrasound-Induced Thermal Field

RUPAK K. BANERJEE[1,2,*] and SUBHASHISH DASGUPTA[1]

[1]*Department of Mechanical Engineering, University of Cincinnati, Cincinnati, OH 45221*

[2]*Department of Biomedical Engineering, University of Cincinnati, Cincinnati, OH 45221*

I. Introduction

High-intensity focused ultrasound (HIFU) is a minimally invasive medical procedure which has shown considerable potential for a variety of therapeutic applications. Some of the medical applications of HIFU include thermal ablation of tumors and uterine fibroids, vessel cauterization, thrombolysis, drug delivery, and gene activation (Curra and Crum [1]). HIFU ablation, unlike other minimally invasive hyperthermia techniques, is completely noninvasive with minimum patient recovery time (ter Haar [2]).

Tissue damage via ultrasound is achieved by the conversion of the mechanical energy of acoustic waves to thermal energy as the ultrasound propagates through the tissue (Fig. 1(a)). Temperature rise of the order of 40–60°C is achieved within a few seconds, causing immediate cell death or necrosis in the targeted region (ter Haar [2]). Since the size of the single lesion is small (few centimeters in length × few millimeters in width) in comparison to the tumor (Fig. 1), multiple sonications are typically required to completely destroy the tumor (Fig. 1 (b)).

Unlike other hyperthermia techniques such as radio frequency (RF) and laser ablation procedures, during a typical HIFU procedure, a large amount of energy is deposited in a short duration causing sudden, drastic, and localized rise in tissue temperature. Cell necrosis time for a typical HIFU procedure is a few seconds, while it is of the order of several minutes for other hyperthermia techniques (Hariharan *et al.* [3]). Consequently, to prevent excessive or collateral tissue damage, the HIFU beam should

* Current address: Department of Mechanical, Industrial and Nuclear Engineering, University of Cincinnati, 593 Rhodes Hall, ML 0072, Cincinnati, OH 45221

Advances in Heat Transfer
Volume 42 ISSN 0065-2717
DOI: 10.1016/S0065-2717(10)42002-X

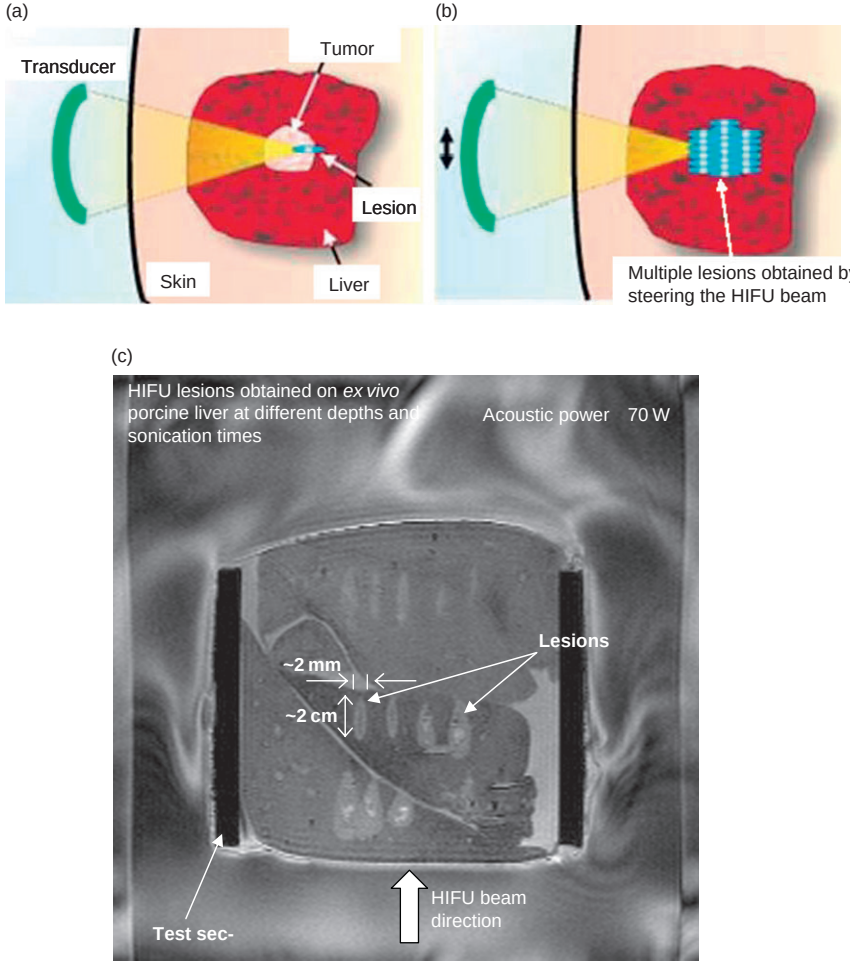

FIG. 1. Schematic of the HIFU tumor ablation procedure describing the formation of (a) single and (b) multiple lesions [2]. (c) HIFU lesions: MRI image showing different shapes of necrosed tissue volumes obtained using HIFU in an *ex vivo* porcine liver. A typical lesion is ellipsoidal in shape with more tissue ablated along the axis of the HIFU beam than in the lateral direction.

be focused at the exact location with correct dosage level. Application of the correct dosage level is critical to avoid damage to sensitive tissues and organ systems anterior or posterior to the ultrasound focal region [4–6]. Several instances of nerve, skin, and bone damage have been reported by previous studies during HIFU treatments. Ren *et al.* [4] reported damage of sciatic nerve due to elevated temperature in the pelvic bone located in the

far field of the HIFU beam while treating uterine fibroids. Nell and Myers [5] showed that temperature rise at the bone surface can exceed the threshold for necrosis even when the HIFU beam focus is more than 4 cm (~10 times the beam width; Fig. 1 (c)) from the bone. Civale *et al*. [6] noted that when the targeted organ in the HIFU procedure is the liver or kidneys, ultrasound absorption in the ribs can produce damage to the skin. Several studies have also shown that presence of structures such as blood vessels near the vicinity of the HIFU ablation zone can act as a heat sink and minimize the efficacy of the ablation procedure [7–9]. Consequently, preclinical evaluations of the thermal and acoustic field generated by the HIFU transducers, using computational, bench-top, *in vitro*, and *in vivo* animal experiments, are critical and necessary to ensure safety and efficacy of this new treatment modality.

Pre-clinical testing of HIFU devices typically include the following elements: (1) measurement of ultrasonic power and focusing characteristics in a liquid medium and (2) measurement or prediction of tissue temperature distribution in a tissue or tissue-mimicking material by *in vitro* and *in vivo* measurements or by using computational modeling [10]. Temperature rise measurements made in tissue-mimicking materials or by using computational modeling are useful to demonstrate that the device is capable of producing enough heat to destroy tumor cells at the intended locations. This test is also essential to demonstrate that the temperature rise in nontargeted tissues, both proximal and distal to the targeted region, is below the prescribed safety limits.

A majority of the commonly used pre-clinical testing methods for HIFU were derived from the standardized techniques developed for diagnostic and imaging ultrasound devices. The acoustic power and focal intensities at the highest HIFU levels (power ~200 W, acoustic intensity $> 1000\,W/cm^2$) are several orders of magnitude more than the intensities (power < 3 W, intensity $< 100\,W/cm^2$) used for diagnostic purposes [2,11]. Similarly, temperature rise obtained at HIFU energy levels is severalfold higher than the safety limit imposed for the diagnostic devices. Consequently, use of the diagnostic ultrasound testing methods for HIFU devices introduces complex issues such as sensor interference and damage due to cavitation and heating, sensor bandwidth limitations, and acoustic nonlinear effects. To address these issues, several HIFU-specific test methods are currently under development.

The goal of this chapter is to present some of the promising new preclinical testing methods developed for acoustic intensity and temperature measurements at HIFU energy levels. This chapter is broadly divided into two sections with the first section focusing on the free field characterization in the liquid medium and the second section on the thermal field

characterization methods in tissue-mimicking materials and *ex vivo* tissues. In the initial sections, the commonly used methods for measuring acoustic power, intensity, and thermal fields are presented with their limitations at HIFU power levels outlined. Subsequently, two new optimization-based preclinical testing methods, one for free field and the other for thermal field, to characterize HIFU devices in clinically relevant power levels are presented and discussed in detail.

A. HIFU Free-Field Characterization in Liquid Medium

A preliminary step in the analysis of new medical devices involving high-intensity ultrasound is the determination of the acoustic intensity field in a liquid medium (mainly in water). There are several national and international standards available [12–15] to streamline the characterization of an ultrasound field generated by diagnostic and imaging ultrasound devices in the liquid medium. However, there are no such standards available for measuring HIFU fields (Harris *et al.* [16]). Currently, the majority of HIFU devices are characterized using standards written for low power diagnostic and imaging applications.

1. Established Characterization Methods

Medical ultrasound fields generated by focused transducers are usually characterized in water using (1) calorimetry methods, (2) hydrophones, and (3) radiation force balance techniques [11].

Calorimetry method. A method to measure the HIFU acoustic power in the liquid medium is the calorimetry method (Hallez *et al.* [17]). The method works on the principle that acoustic power dissipated in liquid is linked to increase in temperature of the bulk of the liquid, due to conversion of acoustic energy to heat. The temperature rise, dT, of the liquid as a result of HIFU sonication is measured using thermocouples. The power P_{cal} is given as $P_{\text{cal}} = mc_{\text{p}}(dT/dt)$, where m is mass of the liquid, c_{p} is specific heat capacity and t is time.

Hydrophones. Polyvinylidene fluoride (PVDF) hydrophones are used as a gold standard for measuring acoustic pressure fields generated by diagnostic and HIFU transducers. In this technique, a membrane or a needle PVDF hydrophone (Fig. 2(a) and (b)) with tip diameter ranging between 0.05 and 1 mm is scanned across the focal region using a tri-axis positioning system. A scanning step size varying between 0.05 and 1 mm is used and the scanning motion is usually controlled by a stepper motor. Data obtained from hydrophone scans can be used to determine focal position, peak pressure, and width of the HIFU beam. The hydrophone measurements are typically made

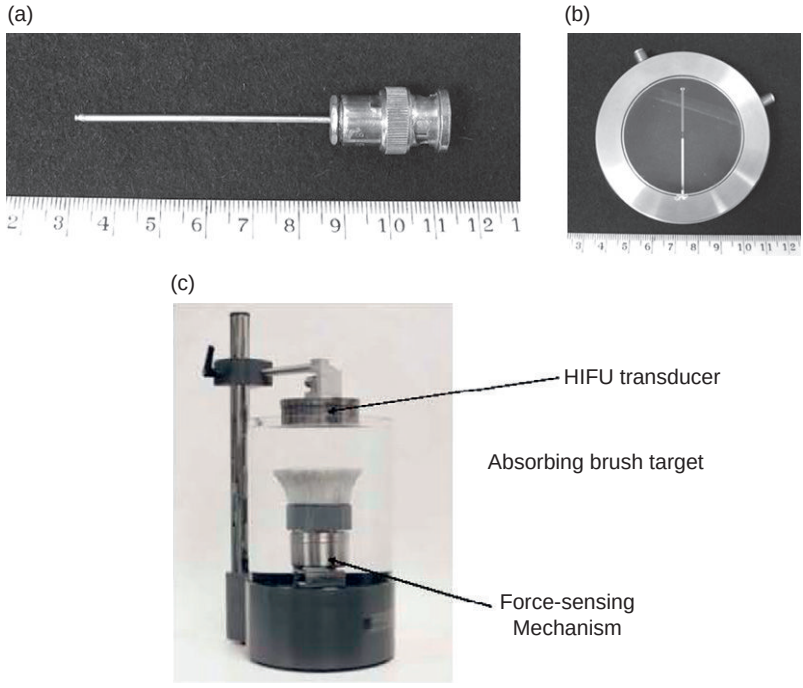

FIG. 2. (a) Piezoelectric ceramic hydrophone used to characterize physiotherapy equipment [16]: tip diameter = 1.6 mm. (b) PVDF membrane hydrophones [16]: membrane thickness = 25 μm, spot size = 0.3 mm. (c) Radiation force balance.

at lower transducer power levels than the output levels used in clinical therapy in order to avoid sensor damage. From the acoustic pressure (or intensity) field, total ultrasound power can be calculated indirectly by integrating the measured intensity over any plane perpendicular to the ultrasound beam.

Radiation Force Balance. Direct measurement of total time-averaged acoustic power can be made using a radiation force balance (Fig. 2 (c) [18]). This instrument is essentially a weighing balance and consists of a highly absorbing or reflecting target suspended in a water bath. The transducer to be calibrated is mounted directly above the target. When the ultrasound is turned on, the target experiences a net force arising due to the momentum associated with the ultrasound wave. The target is connected to a sensitive balance, which measures the force acting on it. From the measured force, acoustic power is obtained by multiplying it with the sound speed. However, radiation force balance can only measure the total acoustic power contained

in the beam and is not capable of obtaining the complete acoustic pressure or intensity field.

Limitations. The calorimetric method discussed above assumes that (1) no ultrasonic energy leaves the container, (2) the amount of energy absorbed by the container walls is negligible, (3) heat transmission between the solution and the walls is negligible, and (4) the energy loss due to acoustic streaming is negligible. These assumptions make the reliability and accuracy of the power measurement method questionable.

Though the radiation force balance and hydrophones techniques are well established and widely used, there are some well-known limitations in both these methods. As mentioned earlier, most of these methods are developed primarily for diagnostic ultrasound applications. Acoustic focal intensities at the highest HIFU levels ($>1000\,W/cm^2$) are several orders of magnitude greater than the intensities used for diagnostic ultrasound [2]. These high intensities introduce limitations which are summarized below.

When the acoustic pressure near the focus exceeds the cavitation threshold of the medium (water), two main problems arise. The first is that dissolved gases are drawn out of solution producing bubbles. These bubbles can shield the sensor from the HIFU beam, thereby preventing accurate measurement of the acoustic pressure and intensity field. The second problem is that the collapse of these bubbles can ultimately damage the sensor itself. Sensor damage can also occur due to direct mechanical effects caused by large compressional and tensional forces.

In addition, the energy absorbed by the sensor can add heat that may cause thermal damage to the sensor. Moreover, the sensitivity of the hydrophone can change significantly when heated close to its Curie temperature. As a result, at high output levels, i.e., at clinically relevant power levels, the intensity and the pressure fields obtained from this technique become unreliable.

Another limitation of using hydrophones is that they can measure only the pressure field and the actual acoustic intensity is calculated based on the plane wave assumption. However, for strongly focused beams, the acoustic intensity is not proportional to the square of pressure field as the acoustic pressure and velocity are no longer in phase with each other. This will introduce significant errors in the calculation of intensity field.

As mentioned earlier, hydrophone scan data are only obtained at low transducer output levels to prevent sensor damage. At these power levels, acoustic waves usually travel undistorted in water and the acoustic spectrum at the focus does not contain significant spread of frequencies. However, at clinically relevant power levels, pressure amplitudes of the acoustic pulses become very high and sound waves begin to propagate nonlinearly in water. This results in the distortion of sinusoidal waves and generation of higher

harmonics. Since the acoustic absorption coefficient of water is proportional to the square of the frequency of the sound wave, the higher harmonic components are absorbed faster than the fundamental frequency resulting in nonlinear losses. As a result, extrapolating the low-power hydrophone data to clinically relevant high power levels will not provide an accurate estimation of the ultrasound field.

In addition, when the acoustic spectrum contains a lot of higher harmonics, the frequency response of the hydrophone is no longer smooth and the output signal from the hydrophone becomes very different from the actual pressure waveform [11]. Several alternative measurement methods are being developed to overcome the existing limitations and characterize the ultrasound fields at high power levels.

2. *Alternate Characterization Methods*

Robust Hydrophones. One possible alternative being researched is development of more robust sensors and hydrophones that can withstand high-intensity sound fields emitted by HIFU beams. Shaw *et al*. [18] designed a novel minimally perturbing pyroelectric sensor to measure acoustic power emitted from HIFU transducers during the actual treatment procedure. The sensor, made from PVDF, is placed in the path of the beam and operates on the pyroelectric principle. A small fraction of the power in the ultrasound beam is absorbed by the sensor resulting in a temperature increase. Due to the pyroelectric properties of the membrane, there is a separation of electrical charge which, when connected to an appropriate electrical circuit, can be measured.

Instead of directly measuring the pressure field, Schafer *et al*. [19] scattered the ultrasound main field using a fused silica optical fiber with polyamide-protecting coating. The scattered signal was then measured using a PVDF detector. Zanelli and Howard [20] developed a metal-coated hydrophone to minimize the risk of cavitation damage. The thin metallic coating over the piezoelectric sensing element provides a smooth outer surface which minimizes nucleation sites for cavitation. Shaw *et al*. [21] developed a device that measured acoustic power by estimating buoyancy forces induced in castor oil placed in the path of the HIFU beam. Ultrasound was focused on a thin container filled with castor oil and sealed with acoustically transparent plastic membrane. The device measured change in the buoyancy of the castor oil when heated by the absorption of ultrasound from which total acoustic power was estimated.

Currently, fiber-optic hydrophones are being developed and are commercially available (RP acoustics, Leutenbach, Germany; Onda Corp., Sunnyvale, CA, USA) as a viable alternative for traditional hydrophones

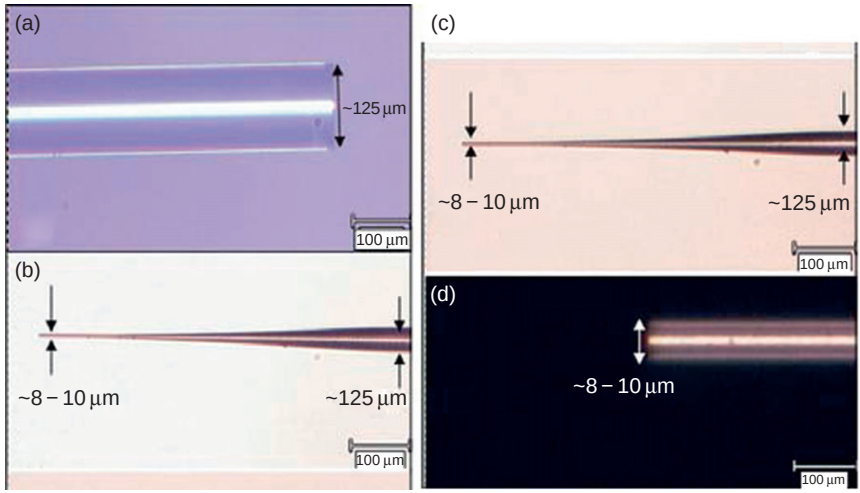

FIG. 3. Raman spectroscopy images of fiber-optic hydrophones with different tip diameters [25].

[22–25]. The sensitive element for measuring pressure in this device is an optic glass fiber with tip diameter varying between 7 and 100 μm (Fig. 3 [25]). This device measures the Fresnel reflectance at the glass fiber tip caused by change in optical refractive index of the medium in the presence of sound waves. The laser light is coupled into the optical fiber which is placed in the path of ultrasound. With the ultrasound turned on, the acoustic pressure waves change the density and the optical refractive index of the medium surrounding the fiber tip. This causes modulation of the laser light signal reflected by the fiber tip and is picked up by the photodetector and converted to acoustic pressure data. Advantages of this device are small tip diameter ($\sim$7 μm [23,25]), large bandwidth (up to 150 MHz), and low cost of optic fiber which can be easily repaired, if damaged, by recleaving. In addition, Morris *et al.* [24] developed a technique that can simultaneously measure both acoustic pressure and temperature using these hydrophones.

Nonintrusive Alternate Characterization Methods. Measurement techniques discussed above involved developing sensors which are more robust and accurate than the conventional hydrophones and radiation force balances. An alternative approach to overcome the sensor-induced inaccuracies would be to eliminate the use of sensors in the beam and nonintrusively measure the acoustic power and intensity field. One such commercially available noninvasive method is the schlieren imaging technique [26,27] which utilizes

changes in the optical index of refraction to qualitatively define the ultrasound field. Unlike hydrophones, which capture pressure information only at one point, the schlieren system can image the entire focal region of the ultrasound beam instantaneously. Consequently, the visual display of HIFU field provides a quick and comprehensive overview of the transducer performance. However, for quantitative evaluation, the pressure field must be reconstructed tomographically.

3. *Acoustic Streaming-Based Method*

To obtain quantitative estimation of the ultrasound field nonintrusively, the present authors developed a new noninvasive method which is capable of determining the acoustic power and intensity field at drive levels where conventional hydrophones become unreliable [28,29]. This new method is based on a phenomenon called acoustic streaming, which is the bulk fluid movement generated when an acoustic wave propagates through a viscous fluid medium. As the ultrasound propagates through the medium, it gets attenuated due to the viscous dissipation of energy in the medium. The momentum lost by the ultrasound wave is gained by the streaming fluid.

The first step in the method involved measuring the streaming velocity. As depicted in Fig. 4(a), the streaming velocity was measured using digital particle image velocimetry (DPIV). An iterative numerical algorithm (Fig. 5) was employed to back calculate the acoustic intensity field giving rise to the measured streaming field (Fig. 4 (b)). The algorithm is briefly outlined below.

The power output for the transducer to be characterized was assumed to be unknown. For the first iteration, a guess was made for the acoustic power, enabling the Khokhlov–Zabolotskaya–Kuznetsov (KZK) acoustic wave equation to be solved. From the KZK equation, the axial component of the driving force F_z was calculated from the equation:

$$F_z = \frac{2\alpha}{(\rho_0 c_0)^2}\bar{p^2} = \frac{2\alpha}{\rho_0 c_0} I \quad \text{where} \quad I = \frac{\bar{p^2}}{\rho_0 c_0} = \frac{p^2}{2\rho_0 c_0}, \tag{1}$$

where α is the absorption coefficient of the medium, I is time-averaged acoustic intensity, p is acoustic pressure, and "$-$" indicates average value. The continuity and momentum equation incorporating F_z were then solved to obtain the first iterate of the velocity field. Streaming velocity fields obtained from both experiment and computation were then used as inputs to a Nelder–Mead multidimensional optimization algorithm (Matlab 2002). The objective function in this algorithm is:

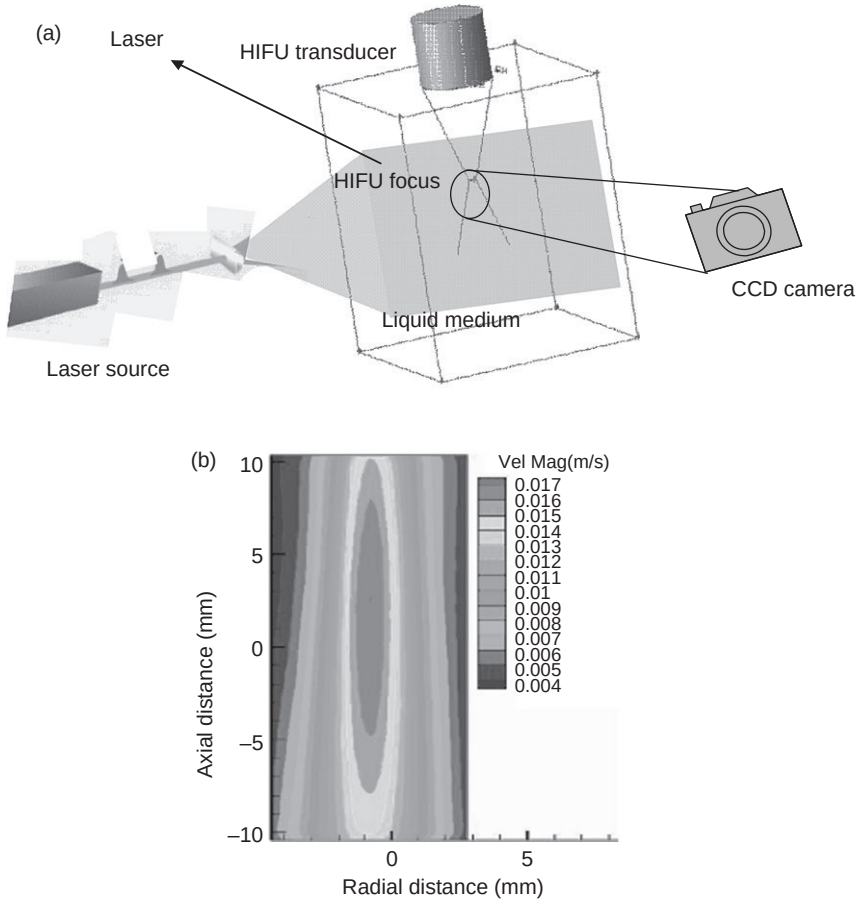

FIG. 4. (a) Schematic of acoustic streaming experiment. (b) Streaming velocity contour.

$$\text{Error}_{\text{RMS}} = \sqrt{\sum_{i=1}^{n} (u_{i,\text{exp}} - u_{i,\text{num}})^2}, \tag{2}$$

where n is the number of velocity nodes in the camera's field of view. $\text{Error}_{\text{RMS}}$ measures the deviation of numerical velocity profile from the experimental values. The optimization routine then updated the power value and recomputed the acoustic field and fluid velocity field. An updated measure of the error was then computed. The entire procedure was repeated until the $\text{Error}_{\text{RMS}}$ was minimized. The power value of the last iteration was taken to be the transducer power.

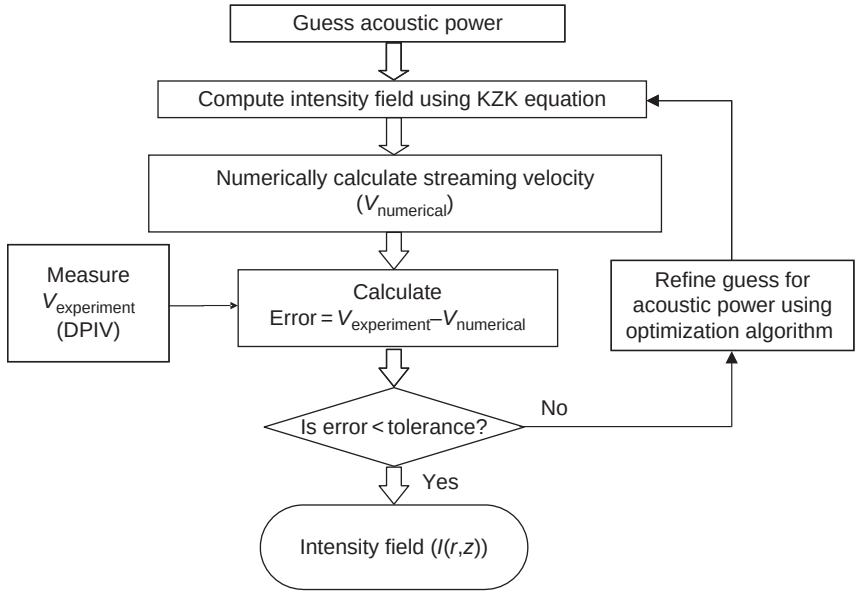

FIG. 5. Flowchart summarizing the inverse methodology used to determine acoustic power and intensity from streaming velocity field.

A HIFU beam axial intensity profile determined by the streaming technique is compared with results from hydrophone scanning in Fig. 6(a). The streaming method matches the hydrophone within 10% at this low power, in terms of both the maximum intensity and the location of the secondary maxima. The total power predicted by the streaming method also matched the power predictions based upon radiation force balance (Fig. 6 (b)). Though this noninvasive acoustic streaming technique allows characterization of HIFU transducers to be performed in an intensity range that may be harmful to conventional hydrophones, it can only be used to characterize the HIFU transducer in a liquid medium. Since the properties of tissue can vary significantly relative to water, especially the absorption and the absorption frequency dependence, noninvasive techniques for characterizing transducers in tissue-mimicking materials or in tissues are needed for improved characterization of HIFU transducers.

The streaming technique as presented in this chapter was able to characterize HIFU transducers when the acoustic power was less than about 30 W, and the corresponding intensity less than around 1400 W/cm^2. These intensities, though below the levels encountered in some HIFU procedures, nonetheless represent an important clinical range [9] and are above

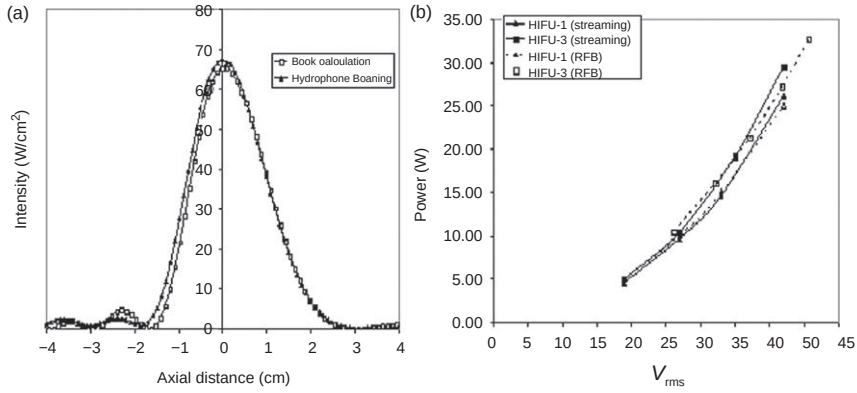

FIG. 6. (a) Intensity vs axial distance along beam measured by back calculation using streaming and hydrophone scanning. (b) Acoustic power vs voltage measured by streaming and radiation force balance (RFB).

intensities which may be damaging to conventional hydrophones. Hariharan *et al*. [9] label this intensity range as being just below the cavitation threshold, the "moderate" intensity regime.

The streaming method provides only the intensity distribution data measured in a free field. It does not give any information about the temperature field or the corresponding bio-effects which are the parameters of interest during the actual clinical procedures. Consequently, the temperature rise and the bio-effects have to be estimated computationally, using the measured intensity data, by solving bio-heat or energy equations [3,9].

The characterization methods discussed so far are applicable to liquid media which have significantly lower acoustic absorption than solid tissue media. In a tissue medium, acoustic energy is converted to heat, a phenomenon which is used for noninvasive therapeutic procedures. Hence, reliable and accurate methods are required to characterize the HIFU-induced thermal field in solid tissue media.

B. HIFU Thermal Field Characterization in Tissue Medium

Characterization of the HIFU thermal field involves multiple assessments, including prescription of the intensity field, quantification of temperature rise (in spatial and temporal coordinates), and lesion volume in a tissue-mimicking material or excised animal organ, determination of the location of the beam focus relative to the desired target and especially for phased arrays, and the angular orientation of the beam. Several methods for

assessing the HIFU-induced thermal effect in tissues or tissue phantoms are available. A popular cost-effective method to measure temperature rise is to use thermocouples embedded in excised tissues or tissue-mimicking materials (Chen *et al*. [31], Huang *et al*. [32]) subject to direct HIFU sonication at selected intensity levels. However, the use of thermocouples is an invasive procedure and highly inconvenient in clinical practice. Besides, thermocouple *artifacts* generated by interference of the thermocouples with the beam (Fry and Fry [33,34], Huang *et al*. [32], Morris *et al*. [35]) and manual errors in positioning the beam on the thermocouple junctions (O'Neill *et al*.[36]) affect the accuracy of the measured data.

In view of inaccuracies associated with direct sonication of thermocouples by the beam, *nonperturbing* methods have been developed to assess the thermal field. The thermal field is measured without having to focus the beam directly on the thermocouple junctions to prevent artifacts (O'Neill *et al*. [36]). The temperature rise measured by thermocouples that are remote from the beam is used to back calculate important characterization parameters such as the beam location and angular orientation. Determination of the beam location and orientation enables prediction of temperature rise at desired locations within the tissue phantom including the temperature at the focus.

A *noninvasive* method, avoiding the use of thermocouples, is to assess the temperature rise and lesion size by the MR thermometry and MR imaging methods (Dasgupta *et al*. [37], Qian *et al*. [38], Melodelima *et al*. [39], Anzai *et al*. [40]). HIFU ablations are performed on tissue samples positioned in the MRI scanner. In contrast to the method using thermocouples, the MRI thermometry method is used to noninvasively measure the spatial and temporal temperature rise and size of the HIFU lesion.

The following section discusses the existing and improved methods to characterize the HIFU thermal field in greater details.

II. HIFU Thermal Field Characterization

A. Invasive Method

1. Use of Thermocouples: Direct Sonication of Thermocouple Junction

Thin wire thermocouples embedded in tissue-mimicking materials or excised tissues have been popularly used as a cost-effective method for measuring the HIFU-induced transient temperature rise. For temperature measurement the HIFU beam is focused on the thermocouple junctions at selected power levels. Using tissue-mimicking materials with thermocouples,

bench-top HIFU experiments have been performed. Huang *et al.* [8] used a tissue-mimicking material provided with an artificial blood vessel to determine the effect of blood flow on HIFU procedures and also studied the effect of acoustic streaming. The HIFU beam was focused on a thermocouple placed within the vessel. Temperature rise was recorded at varying flow rate to estimate the effect of flow on temperature rise. King *et al.* [41] developed a gelrite-based tissue-mimicking phantom which could accurately mimic the thermal and acoustic properties of the actual tissue. The material was embedded with thermocouples to study cavitation thresholds for HIFU procedures (Maruvada *et al.* [42]). More recently, Chen *et al.* [31] used a tissue-mimicking phantom with embedded thermocouples to study acoustic cavitation in HIFU ablation. The present authors measured temperature rise in a tissue phantom (King *et al.* [41]), modified to include an artificial blood vessel (Fig. 7 (a), with thermocouples embedded in the material close to the vessel (Fig. 7 (b)). The purpose of the study was to investigate the effect of blood flow on HIFU-induced thermal effects by comparison of temperature measured with and without simulated blood flow through the vessel. The beam was focused on thermocouple T1, 2 mm away from the vessel, at selected power levels 5, 10.3, 17.3, and 24.8 W. At each power level, sonications were performed at flow rates 0, 400, and 600 ml/min. Temperature rise was also recorded at thermocouples T2 and T3, which are 4 and 6 mm away from the vessel, respectively. However, the method of temperature measurement using thermocouples suffers several limitations which are discussed below.

2. *Limitations in Use of Thermocouples*

The following limitations encountered in using thermocouples for HIFU studies have been reported by the present as well as previous researchers:

Invasive Process. The insertion of thermocouples in real tissues is an invasive process and hence inconvenient in a clinical setting. For HIFU studies, thin wire thermocouples (of diameter 20–75 μm) are used. These are fragile thermocouples and vulnerable to breakage due to mishandling. Such technical difficulties associated with the use of thermocouples limit their use.

Beam Positioning Error. For temperature measurement, the HIFU beam needs to be placed atop the thermocouple junction. A common method for positioning the beam is to move the beam until the position of maximum temperature rise during a brief sonication period is located. However, there exists a possibility of the beam to be displaced from the thermocouple junction during the manual positioning process. As noted by O'Neill *et al.* [36], this can lead to significant underestimates of temperature in HIFU

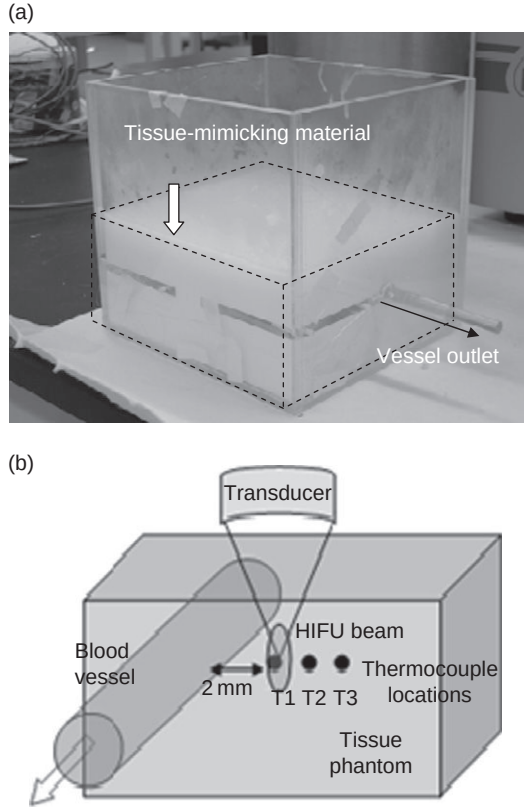

FIG. 7. (a) Photograph of fabricated tissue phantom. (b) Diagram of tissue phantom with artificial blood vessel and embedded thermocouples.

applications, due to the small widths of the HIFU beams across which temperature profiles are steep. The present authors used the manual positioning procedure to place the beam on the thermocouple junction (7B). The beam was focused on thermocouple 2 mm from the vessel. Due to the beam positioning error, which varied from day to day, there was a wide variation of temperature rise under a similar setting of power level and flow rate conditions. Figure 8(a) shows the transient temperature profiles at flow rates 0 and 400 ml/min at power level 17.3 W, in order to quantify the effect of blood flow on temperature rise. There is a rise in temperature during the 30-s heating period followed by temperature decay when the transducer is powered off. As seen in Fig. 8 (a), there is a significant standard deviation of the data (~11%) about the average of 3 days, depicted in the form of error

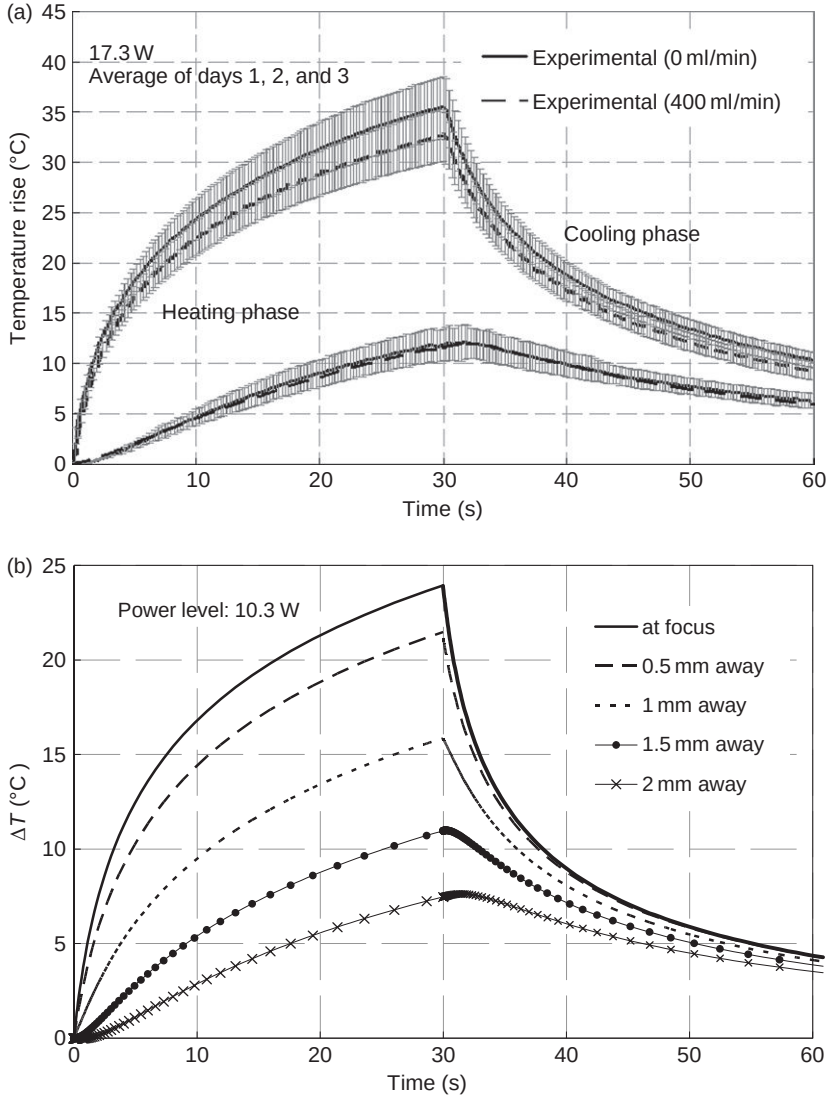

FIG. 8. (a) Experimental transient temperature profiles at 2 and 4 mm thermocouples at power 17.3 W (blood flow rates: 0 and 400 ml/min). Data averaged over days 1, 2, and 3 (three trials per day). Standard deviation about average is shown by error bars. (b) Computed transient temperature profile as a function of beam-thermocouple displacement at power level 10.3 W. Indicates sensitivity of temperature rise to beam-thermocouple displacement.

bars. Furthermore, the error bars of the no flow (0 ml/min) and flow profiles (400 ml/min) overlap each other, making it impossible to quantify the decrease in temperature rise due to blood flow cooling effect, the goal of the investigation. The sensitivity of measured temperature rise to beam positioning error was confirmed by a numerical investigation. In Fig. 8 (b) transient temperature profiles computed at various beam-thermocouple displacements show that a displacement of just 0.5 mm causes a 13% [$(24-21)/24°C \times 100$] decrease in measured temperature rise. The numerical study, in conjunction with experimental data, leads to the conclusion that beam positioning error in the use of thermocouples results in significant inaccuracy in temperature measurements.

Thermocouple Artifacts. Several studies have revealed that temperature rise measured using thermocouples can be inaccurate because of thermocouple artifacts which impose an additional temperature rise over the temperature rise of the tissue material caused by pure absorption of acoustic energy. Thermocouple artifacts are primarily due to *viscous heating*, a phenomenon which was initially reported in the studies by Fry and Fry [33,34]. Hynynen *et al*. [43] performed experimental investigations to determine inaccuracies due to artifacts in HIFU-induced temperature measurements. When the temperature measurement errors were studied, even the smallest thermocouples showed some self-heating artifact and its magnitude depended on the probe size, material, structure, orientation, and the operating frequency. The experimental studies by Huang *et al*. [32] employed thermocouples to measure the temperature rise. Additionally, heating due to artifacts was measured by focusing the HIFU beam on a thermocouple in a low-absorbing medium. Figure 9(a), obtained from the studies by Huang *et al*. [32], shows that the measured profile (profile A) is higher than the calculated temperature profile (profile C) by almost three times, due to additional heating by artifacts. The calculated profile (profile C) and measured thermocouple artifact profile (profile D) were added to yield profile B, which was in close agreement with the measured temperature profile. More recently, Morris *et al*. [35] evaluated the proportion of thermocouple artifacts in temperature rise measured using thermocouples. A novel thin film thermocouple (TFT) was employed which could measure temperature rise without artifacts. The temperature rise measured using the TFT was subtracted from temperature measured using conventional thin wire thermocouples to estimate the artifacts.

The present authors also found the experimental temperature rise to be higher than the computed temperature rise (Fig. 9 (b)) because of artifacts. During the cooling phase, the effect of artifacts no longer exist because of the absence of the beam on the junction, and there is a close agreement between

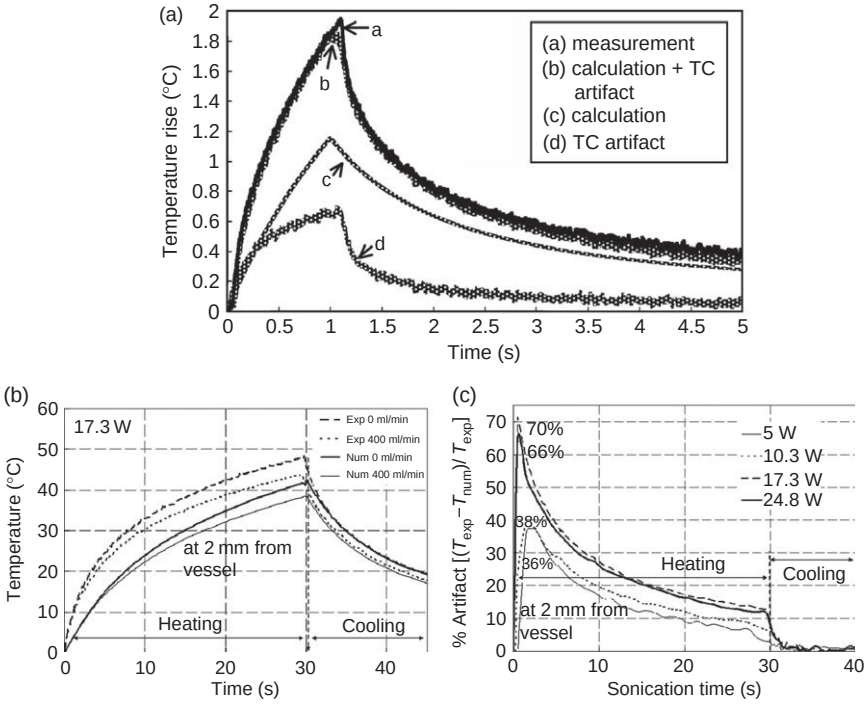

FIG. 9. (a) Measured temperature profile (using thermocouple) and calculated profile (Huang *et al.* [8]). (b) Experimental and computational transient temperature profiles at 0 and 400 ml/min flow rates. Power level is 17.3 W. (c) Percent artifact vs sonication time.

the numerical and experimental temperature decay profiles. Figure 9 (c) shows percentage artifact as a function of sonication time. Percentage artifact, given as % Artifact = {[(experimental temperature rise – numerical temperature rise)/experimental temperature rise] × 100%}, shows a sharp increase in the initial few seconds of sonication (66–70%) and is comparatively lower at the end of sonications (5–12%) which is still a significant amount of inaccuracy. It is also seen that the maximum percentage artifacts, within the initial few seconds, increase with power level. A similar relation between the proportion of artifacts and sonication time was observed by Morris *et al.* [35], though a lower range of power levels was considered. Overall it can be concluded that direct sonication of thermocouples by the HIFU beam leads to significant inaccuracies in the measured temperature data due to artifacts.

The other source of thermocouple artifacts is mismatch of thermal conductivity between the thermocouple junction and the surrounding tissue

material (Nell *et al*. [5]). The thermocouple junction is made of metals such as copper, constantine, and cromega which have higher conductivity than the surrounding tissue material. This causes a distortion of the induced thermal field. However, conductivity artifacts can be reduced by using thermocouples with smaller junction diameters.

Localized Temperature Measurement. Thermocouples can measure temperature rise only at specific points where they are embedded or inserted and are not capable of measuring the temperature rise over the entire ablation zone. In order to determine the *lesion* size or to estimate the extent of tissue damage, it is required to record the spatial temperature rise at the HIFU focal zone, which necessitates an array of thermocouples to be inserted in the tissue. It is inconvenient to insert too many thermocouples in *ex vivo* or *in vivo* animal tissues to measure the spatial temperature rise.

The above limitations in the use of thermocouples call for improved methods to measure HIFU-induced thermal effects for field characterization. Improved and alternative methods to characterize the HIFU thermal field are discussed in Sections II and III.

B. Nonperturbing Method

An improvement in HIFU characterization studies is the development of nonperturbing methods, to assess the thermal field in a tissue medium. In this method direct sonication of thermocouple junctions is avoided to prevent artifacts in the temperature data. The beam is focused at locations off the thermocouple junctions and the temperature rise at the remote junctions is measured. O'Neill *et al*. [36] performed HIFU sonications within an array of six thermocouples in the same plane. The artifact-free temperature rise measured by the thermocouples was used in a curve-fitting technique to extrapolate the temperature rise at the focus. As a result, temperature rise at the focus was more accurately estimated.

1. Inverse Method: Application in Heat Transfer Analysis

The present authors employed the inverse heat transfer method, a nonperturbing iterative method, to predict the temperature rise within a tissue-mimicking material (King *et al*. [41]). The method has been successfully applied outside ultrasound applications. For example, Farhanieh *et al*. [44] back calculated the heat transfer coefficient in a partially filled rotating cylinder, on the basis of the error between the measured and estimated temperatures on the shell. More recently, Paredes *et al*. [45] used a feedback strategy to solve an inverse heat transfer problem to back calculate the

unperturbed formation temperature (UFT) in well bores. The feedback system used the error between the measured and estimated temperatures during the well shut-in process to obtain the UFT.

2. *Inverse Method: Application Specific to HIFU Studies*

A few researchers have applied the inverse method specifically to HIFU studies. As discussed above, Hariharan *et al.* [28] employed an inverse algorithm to back calculate the acoustic intensity on the basis of the HIFU-induced streaming velocities measured in a liquid medium. More recently, an inverse heat transfer method to predict the temperature rise in a tissue phantom was developed by the present authors. Details of the method are discussed below.

Thermocouples Remote from Beam. In the inverse method, HIFU sonications were targeted at selected locations within a 3D array of eight thermocouples embedded in a solid medium or the tissue phantom. Direct sonication of the thermocouple junctions was avoided to overcome the possibility of artifacts corrupting temperature measurements.

Figure 10(a) shows the tissue-mimicking material (King *et al.* [41]) held in a cylindrical test section. An array of eight thermocouples (T1–T8) was embedded in the material (Fig. 10 (b)), forming a 3D array. Thermocouples were arranged in four layers with two thermocouples in each layer separated by a distance of 4 mm. Each layer is 2 mm from the adjacent layer. The HIFU beam was positioned at selected targets within the array while avoiding direct sonication of thermocouples. The transducer was operated at selected power levels, 5, 17.3, and 24.8 W, at each target; the temperature rise at the thermocouples T1–T8 was recorded.

The location of the HIFU beam in a tissue medium is an important parameter in assessment of the thermal field as it influences the temperature rise in the tissue. The inverse method, discussed next, uses the temperature rise measured at the remote thermocouples to back calculate the location of the beam with respect to the thermocouple array using an iterative approach.

Derivation of Beam Location and Angular Orientation. Figure 11 depicts the inverse heat transfer optimization algorithm in the form of a flowchart. As a first step, the beam location, which is an unknown parameter, was assumed and is supplied to the algorithm as an initial prediction. Based on the initial beam location temperature rise, T_{num} was numerically calculated at selected thermocouples such as T3, T6, and T7, forming a subarray. The following method was employed to calculate the temperature rise at T3, T6, and T7.

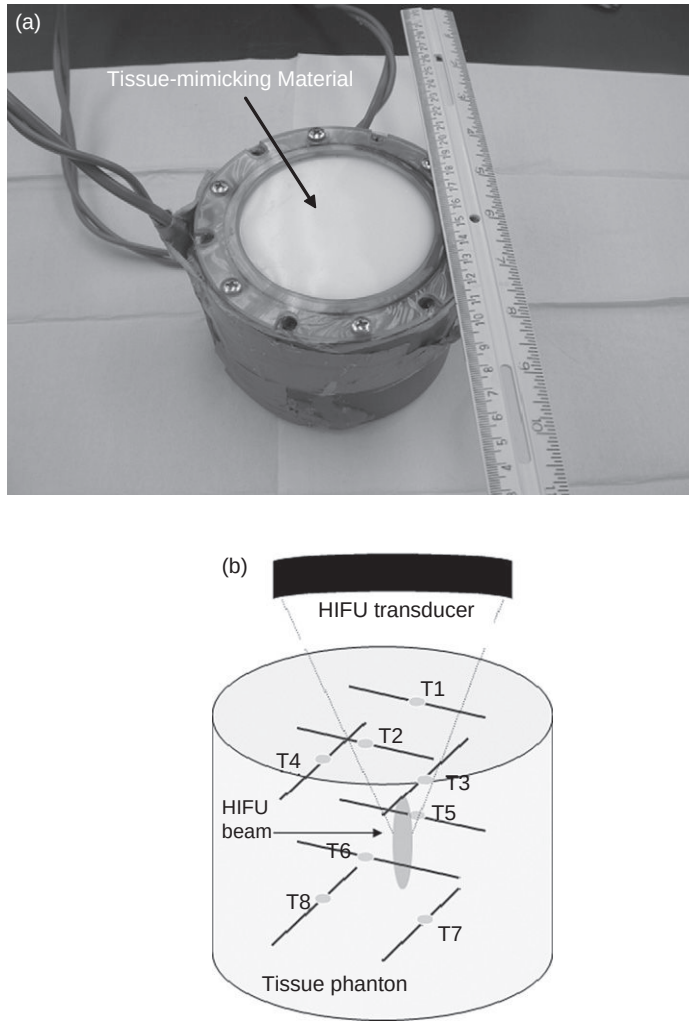

FIG.10. (a) Tissue-mimicking material or tissue phantom held in test section. (b) Schematic of thermocouples embedded in tissue phantom.

a. Calculation of HIFU Heat Source. Sound propagation was modeled using the linearized KZK parabolic wave equation:

$$\frac{\partial}{\partial t}\left[\frac{\partial p}{\partial z} - \frac{D}{2c_0{}^3}\frac{\partial^2 p}{\partial t^2}\right] = \frac{c_0}{2}\left(\frac{\partial^2 p}{\partial r^2} + \frac{1}{r}\frac{\partial p}{\partial r}\right). \tag{3}$$

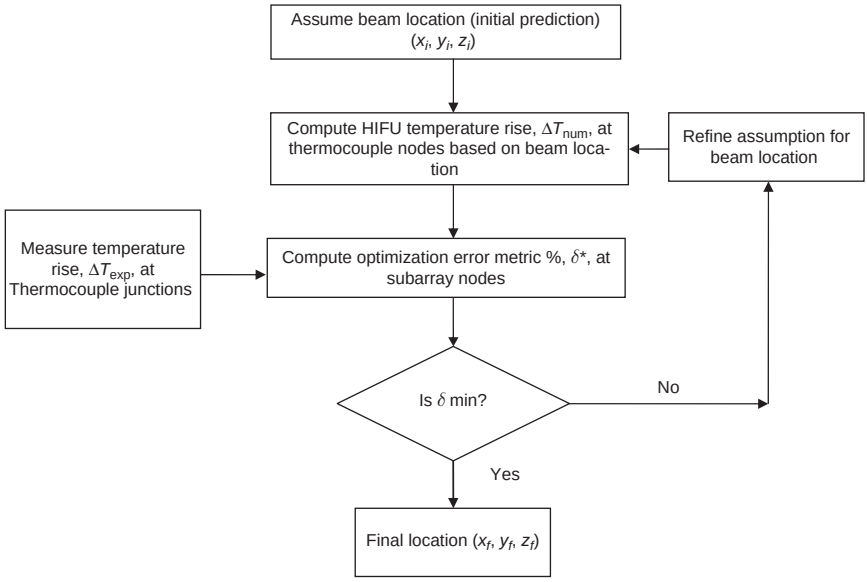

FIG. 11. Flowchart depicting inverse heat transfer algorithm.

Here, p is the acoustic pressure, t is the retarded time, c_0 is the speed of sound in tissue, r is the radial distance from the center of the beam, and D is the sound diffusivity of tissue. Equation (3) was solved using the KZK Texas finite-difference code (Lee *et al.* [46]) to obtain the pressure field, $p\ (r, z)$.

The time-averaged acoustic intensity $I(r, z)$ was calculated from the pressure field using the relation $I(r,z) =< p^2 > /\rho_0 c_0$, ρ_0 being the mean density. The HIFU-induced power deposition rate, Q, was then calculated from the relation:

$$Q = 2.\alpha.I, \tag{4}$$

where α is absorption coefficient of tissue.

b. Calculation of Tissue Temperature Rise. To determine the tissue temperature rise $T(x, y, z, t)$, the heat equation was solved:

$$(\rho_0 c_p)\frac{\partial T}{\partial t} = \frac{\partial}{\partial x_j}\left(k\frac{\partial T}{\partial x_j}\right) + Q, \tag{5}$$

where c_p is the specific heat and Q is the absorbed energy obtained from Eq. (4). Equation 5 was solved using the Galerkin finite-element (FE) method as implemented in the FIDAP software (Fluent Inc., 10 Cavendish Court Lebanon, NH 03766 U.S.A).

The optimization error metric, δ, between the measured temperature rise, T_{exp}, and the computed temperature rise, T_{num}, corresponding to the assumed beam location was calculated. δ is given as:

$$\delta = \frac{1}{n}\sum_{1}^{n}\frac{1}{150}\sqrt{\sum_{t=1\text{s}}^{t=150\text{s}}\frac{(T(n,t)_{\text{exp}} - T(n,t)_{\text{num}})^2}{T(n,t)_{\text{num}}^2}}, \tag{6}$$

where n is the number of thermocouples used to derive beam position. δ is calculated over 100 s of heating and 50 s of the cooling profiles.

Next, the optimization algorithm refined the beam location, using the Nelder–Mead scheme (Nelder and Mead [47]), to reduce δ. In this way a series of iterations were performed until δ dropped to a minimum value. The location corresponding to minimum δ value was taken to be the converged or derived location of the beam. In both the inverse methods (Hariharan *et al.* [28] and present study), the Nelder–Mead multidimensional optimization algorithm (Lagarias *et al.* [48], Matlab 2008) was used. Besides determining the location of the beam in three dimensions, the algorithm was also employed to calculate the angular orientation of the beam. The algorithm was modified to include the beam angle as an additional parameter, which was optimized in a series of iterations in order to minimize the error metric, δ.

Results. The results of applying the inverse method is depicted in Fig. 12. Figure 12 (a) is a schematic showing the position of the thermocouples in the tissue phantom. The focal locations derived by the inverse method (black diamonds) are compared with the targeted coordinates (unfilled diamonds), in Fig. 12 (b) (z-coordinate) and Fig. 12 (c) (x,y coordinates). For example in case 1, the target location is (0,0,0) which is in between T5 and T6 thermocouples and in the plane containing these thermocouples. The derived location is shifted to (0.25,0,3). In addition to plotting convenience, the axial (z) and transverse (x,y) positions are separated due to the fact that the transverse coordinates have a much stronger influence on the temperature field than the axial coordinate, given the small transverse beam dimension relative to the axial size. (For the HIFU transducer used in the experiments, the –6 dB beam width is 1.7 mm in the radial direction compared to 24 mm in the axial direction.) The difference between the targeted axial coordinates and the derived axial coordinates is approximately 3 mm for all three cases (Fig. 12 (b)). The radial [$=(x^2+y^2)^{0.5}$] difference varies between about 0.25 and 0.5 mm (Fig. 12 (c)). The inverse method is also extended to enhance its capability to derive the angular orientation of the beam. This is important in the characterization of transducers with phased arrays.

With knowledge of the beam location, the artifact-free temperature rise at desired locations within the phantom is predicted. In the calculations,

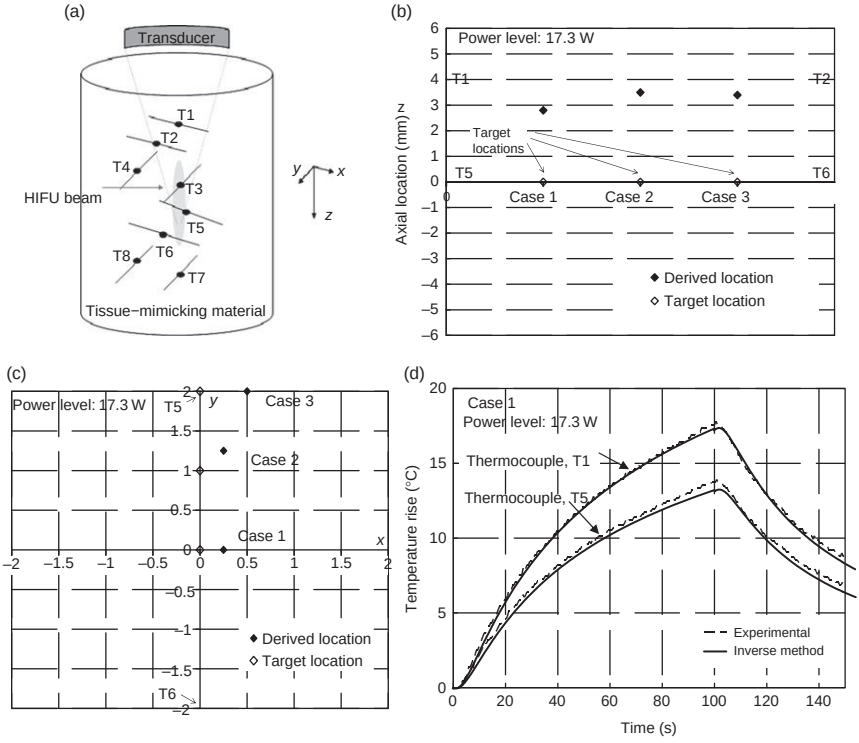

FIG. 12. (a) Schematic diagram of HIFU ablation procedure with thermocouple array. (b) Targeted and derived axial (z) beam location for cases 1, 2, and 3. (c) Targeted and derived radial (x,y) beam location for cases 1, 2, and 3. (d) Measured and predicted (inverse method) temperature profiles at thermocouples T1 and T5.

a subarray of $n = 3$ thermocouples, T3, T6, and T7, was used to derive the 3D beam location. The measured and predicted transient temperature profiles at thermocouples T1 and T5, not used in the calculations, are shown in Fig. 12 (d), for the case where the targeted focal location is midway between T5 and T6 (case 1). The temperature prediction error metric, ε, at thermocouples T1 and T5 is approximately 4%, indicating the efficiency of the inverse method in predicting temperature rise in the tissue phantom.

C. Noninvasive Method

This section describes the imaging-based thermal field characterization methods that are suitable for measuring temperature during *in vivo* animal experiments or during actual clinical procedures.

1. *Diagnostic Ultrasound*

Diagnostic ultrasound can also be used for monitoring HIFU treatment procedures. HIFU and conventional diagnostic ultrasound imaging can be synchronized to develop a system for real-time visualization of HIFU treatment. The system was tested *in vivo* in pig liver by Vaezy *et al.* [49]. The HIFU application resulted in the appearance of a hyperechoic spot at the focus that faded gradually after cessation of HIFU exposure. The duration of HIFU exposure needed for a hyperechoic spot to appear was inversely related to the HIFU intensity.

Figure 13 shows an image-guided 256-element phased-array ultrasound surgery system (Lu *et al.* [50]). The system employs an extracorporeal therapy transducer, a 256-element phased-array applicator, for noninvasive focused ultrasound surgery. A diagnostic ultrasound device is introduced in the system for image guidance in surgery. The therapeutic phased arrays combined with the diagnostic probe are mounted in a water bag of degassed water, below the center of the therapeutic bed. The ultrasound is directed upward, and the degassed water provides acoustic coupling between the transducer and the patient. The integration of the therapeutic transducer and the image probe mounted on the 3D robotic positioner can move in three dimensions to target and identify tumors precisely. The surgeon can perform the ultrasound surgery conveniently on the current diagnostic image in the main control computer through the surgery procedures of 3D navigation, targeting, and monitoring. The main control computer with the main

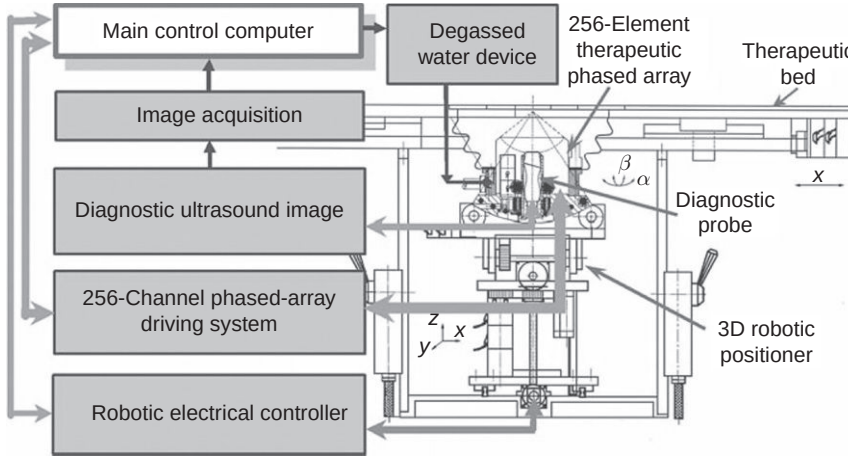

FIG. 13. The schematic block diagram of an image-guided 256-element phased-array focused ultrasound surgery system.

operative program controls the main subsystems: the 256-channel phased-array driving system that drives the 256-element phased array, the robotic electrical controller that controls the 3D robotic positioner's movement, the image acquisition that acquires the image from the diagnostic ultrasound image system, and the degassed water device.

2. *Thermography Method*

Thermal imaging can be used to investigate the localized heating effect of HIFU, to monitor temperature rise in real time. In order to visualize thermally induced protein coagulation, a phantom of polyacrylamide (PAA) gel containing fresh egg albumin was used by Song *et al.* [51] as a tissue-mimicking material. A high-resolution thermal camera was positioned directly over the samples to record thermal fluctuations. Two modes of ultrasound were investigated, i.e., continuous wave and pulsed wave. Through imaging processing and thermal analysis, the temperature profile of the phantoms during HIFU heating was obtained, and the optimized parameters for protein coagulation were identified. The experiments have shown that thermal imaging is an effective way to measure the bioheating effect of HIFU.

The experimental setup used by Song *et al.* [51] is illustrated in Fig. 14. A Merlin thermal camera with high resolution of 320×256 pixels focal plane arrays and 25 mm lens (FLIR Systems Inc., Boston, MA, U.S.A) was positioned directly over the phantoms to record the HIFU heating. The camera was able to measure the temperature difference as small as 0.018°C. A specially constructed HIFU tank was devised to quickly obtain the exact focal point on the phantom sample. This development dispenses with the

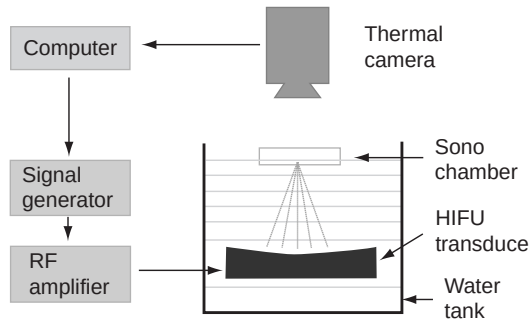

FIG. 14. The schematic block diagram of an image-guided 256-element phased-array focused ultrasound surgery system.

need to search, locate, and position with the membrane hydrophone. A specially constructed sono – chamber was devised to hold the gel phantoms, and acoustic energy could pass through the chamber without attenuation. The water temperature was 37°C.

Two modes of ultrasound waves, i.e., continuous and pulse waves, were compared to investigate the HIFU heating effect in term of temperature difference measured by the thermal camera. The continuous wave was at a frequency of 1.0 MHz, with different amplitudes. The pulsed wave was at the same frequency of 1 MHz, with 0.5, 1.0, 2.0, and 3.0 V amplitude, but only 1000 pulses within 1 s.

When PAA gel containing egg white was subjected HIFU irradiation, the focal lesion of the phantom was heated and finally coagulated. It was easy to confirm the development of a white color of the coagulated lesion under direct observation, with the increase of electrical power, the diameter of the coagulated area increased from 0 to 5.33 mm There were no temperature changes for samples 1 and 2 under continuous wave, and no temperature change was recorded for any sample under pulsed wave. But there was dramatic heating effect starting from sample 3, the most powerful heating was observed with sample 8, the maximum temperature reached nearly 60°C at 60 s (Fig. 15 (a) and (b)), and then temperature dropped slightly after that. Under visual observation, the hot spot turned white and some of the gel was even blown off by the intensive heat generated by HIFU.

The high-resolution thermal camera was used in the experiments of HIFU heating, to monitor the phantom temperature in real-time, noncontact, and noninvasive way. Different parameters for HIFU irradiation were evaluated, and it was of interest to note that HIFU continuous wave of 0.5 V amplitude, or below, demonstrated no significant heating, therefore no protein

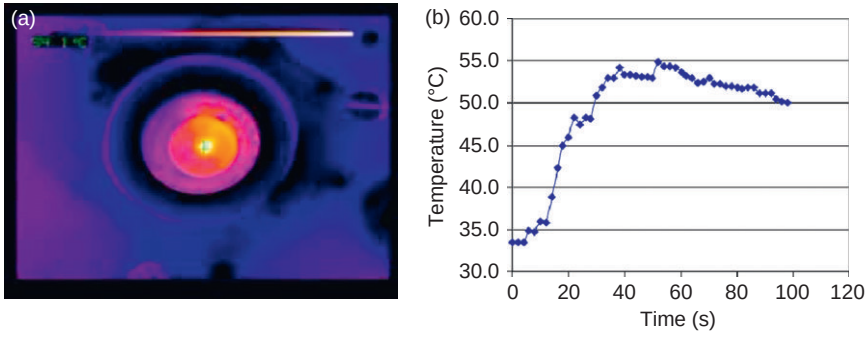

FIG. 15. (a) Thermographic results of HIFU heating of continuous wave. (b) Heating effect of continuous wave ultrasound.

coagulation, while the highest temperature was recorded nearly 60°C in a confined coagulation area by continuous wave of 2 V amplitude.

3. *Magnetic Resonance Imaging Method*

A relatively recent and *noninvasive* method to monitor thermal therapeutic procedures such as radio-frequency (RF) and HIFU therapy is use of the magnetic resonance imaging (MRI) technique (Fig. 16(a)), for both thermometry and imaging (Qian *et al*. [38]). In the investigations led by Anzai *et al*. [40], the feasibility of MRI-guided RF ablations was evaluated for the

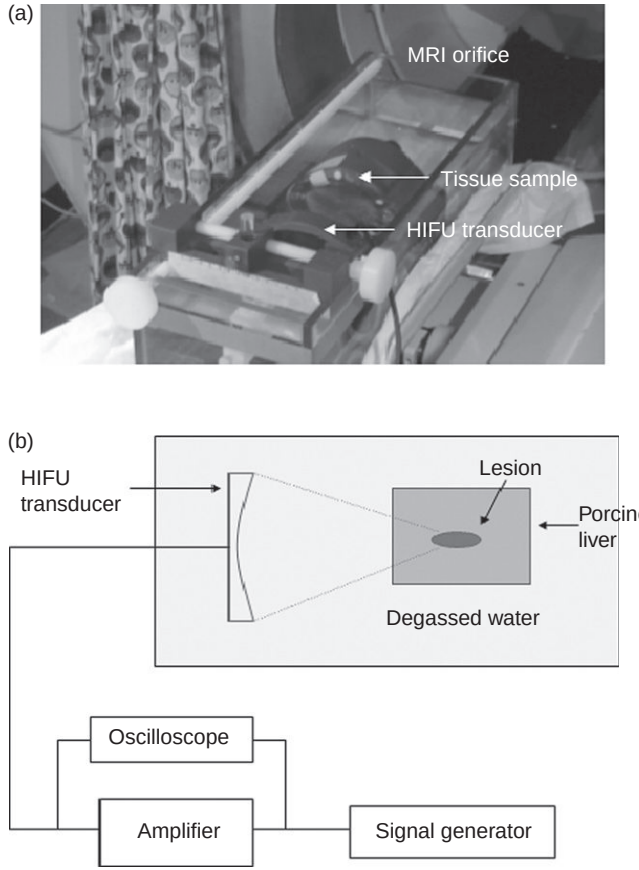

FIG. 16. (a) Photograph of experimental setup showing HIFU transducer aligned with tissue sample in the MRI machine. (b) Schematic of experimental setup.

treatment of brain tumors. Bohris *et al.* [52] employed the MRI method in HIFU ablation studies and validated the results by comparing the temperature maps with fiber-optic measurements in heated muscle tissue. The accuracy of the MR method for temperature measurements was found to be better than 1°C. Hynynen *et al.* [53] tested the feasibility of MRI-guided HIFU ablation of benign fibroadenomas in the breast. HIFU ablation under MRI guidance was performed with 64 transducers at 4.6 MHz to create lesions on 47 *porcine* liver samples in experiments performed by Melodelima *et al.* [39]. There was an 11% agreement between the HIFU-induced lesion sizes measured visually and using MR thermal dose maps.

Ultrasound imaging does not provide the high-resolution images, real-time temperature monitoring, and adequate post treatment lesion assessment required for fast and effective therapy. In contrast to ultrasound, MRI offers excellent soft tissue contrast, noninvasive temperature measurement techniques, and 3D imaging capabilities. In a separate study, the present authors validated the temperature measured by the MR thermometry method by comparing with the histology data and the numerical calculations. The MRI-monitored HIFU experimental setup used in our validation study is depicted in Fig. 16. The signal generator (Agilent technologies 33220A) generates a signal of required frequency. The signal is magnified by the amplifier (Amplifier Research 100A200B) which powers the transducer. The power input to the transducer is monitored by the oscilloscope (Model 54615B, Agilent). Freshly excised tissue samples are held in a Plexi glass tank containing degassed water and subject to HIFU ablations at selected power levels and sonication times. Experiments are performed in the 3T MRI SIEMENS scanner. The induced temperature rise and lesion size are measured by the scanner as described in the following sections:

Noninvasive Temperature Measurement. In the present study, MRI-monitored HIFU ablations were performed at varying sonication times, 20, 30 and 40 s, at a constant acoustic power level of 70 W. Prior to each sonication, three-plane localization imaging was performed to determine the position of the tissue with respect to the HIFU transducer center. Temperature measurement was performed based on the proton resonance frequency (PRF) shift thermometry (Ishihara *et al.* [54], De Poorter *et al.* [55], Rieke *et al.* [56]).

Prior to the execution of the HIFU ablation experiments, the MR procedure required calibration for temperature measurement. The PRF method uses changes in the phase of gradient echo images to estimate the relative temperature change ΔT, as given by:

$$\Delta T = \frac{\varphi - \varphi_{\text{baseline}}}{\gamma \alpha B_0 \text{TE}}, \tag{7}$$

where α is the PRF change coefficient for aqueous tissue, γ is the gyromagnetic ratio, B_0 is the main magnetic field (= 3.0 Tesla), TE is the echo time, and ϕ_{baseline} is the initial phase before heating. ϕ_{baseline} was the phase angle of a pixel outside the heated area which corresponded to the base temperature of 22°C.

Figure 17(a) shows schematic of the experimental setup used to calibrate the scanner. The aim of the experiment was to determine the constant of proportionality relating magnetic phase change to temperature rise.

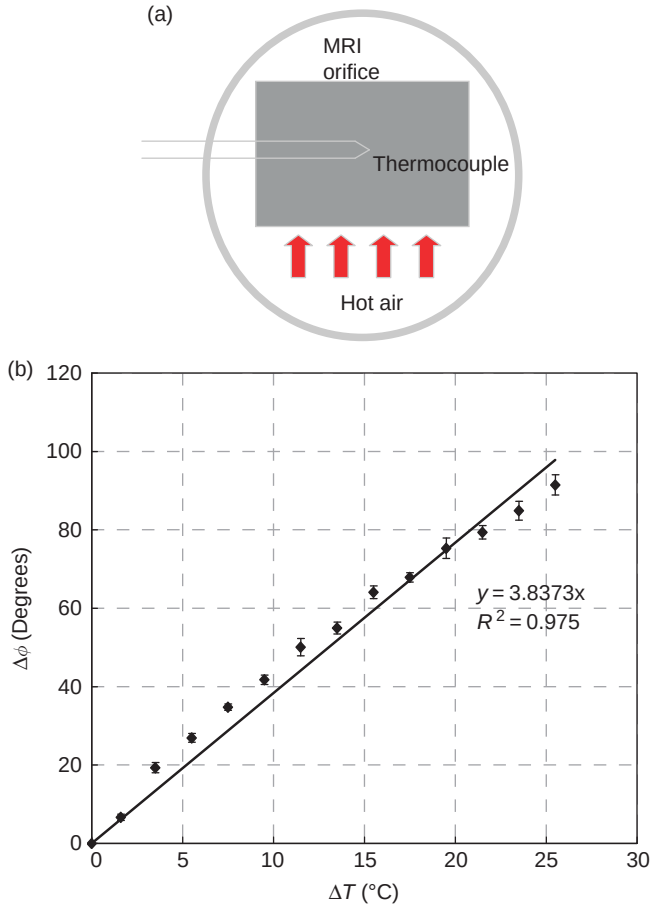

FIG. 17. (a) Experimental setup used in caliberation of MRI scanner for temperature measurement. (b) MRI calibration curve showing linear relationship between magnetic phase angle ($\Delta\phi$) and temperature rise (ΔT) ($R^2 = 0.975$).

This constant is the product of γ, α, B_0, and TE in Eq. (7). To record temperature of an insulated copper–constantine fine wire, thermocouple (diameter 0.075 mm) was inserted in the tissue. The tissue was held in an MRI compatible test section and heated by hot air through a duct at the base. The temperature rise of the tissue was recorded by the thermocouple and the corresponding phase shift was recorded by the scanner every 2 s. The phase shift at each time point was obtained by averaging the phase shifts over pixels around the thermocouple junction and not on the junction, to avoid junction artifacts in the signal. The pixels chosen were very close to the junction to ensure that they experienced the same temperature rise as the junction. In this way it was ensured that a reliable MR signal was obtained at each time point. Figure 17 (b) shows the calibration curve relating phase change and temperature rise. The linear relationship $y = 3.8373 \times (R^2 = 0.975)$ was found between the magnetic phase change and the temperature rise. The calibration experiment was repeated three times to ensure repeatability of the results. The standard deviation of the data was within 6% of the average.

Figure 18(a) and (b) shows the HIFU-induced transient temperature profiles in the liver sample at sonication times 20 and 40 s, respectively. When the transducer is powered on during the ablation procedure, there is a rise in temperature. This is followed by decay in temperature when the transducer is powered off. The calculated profiles (shown as solid lines) are compared to the experimental profiles (shown as black symbols). The error bars seen in the experimental data represent the standard deviation of the data about the mean of three measurements and is within ± 5°C. The measured average temperature rise after 20 s ablation is 62°C and that after 40 s is 72°C. The measured and the computed temperature rise at the end of the heating phase are within 11% $[(70-62)/70 \times 100]$ agreement at sonication time 20 s (Fig. 18 (a)) which indicates the capability of the MRI scanner to assess the HIFU-induced temperature field within acceptable accuracy. At the highest sonication time of 40 s, the measured temperature rise is limited to ~72°C (above a room temperature of 20°C), whereas the computed temperature rise is 83°C, indicating a 13% agreement. This is attributed to boiling of the tissue at higher energy levels, studied by Khokhlova *et al.* [57], which is not accounted for in the computations. In this study, noise filtering was achieved by using a low-pass filter, as recommended in the studies by Oshiro *et al.* [58]. Noise is caused by RF sources such as the RF amplifier used in the study. However, due to the filter used in the study, the temperature rise could be recorded even when the electronic components were powered on, which was not possible in the initial experiments without adequate filtering.

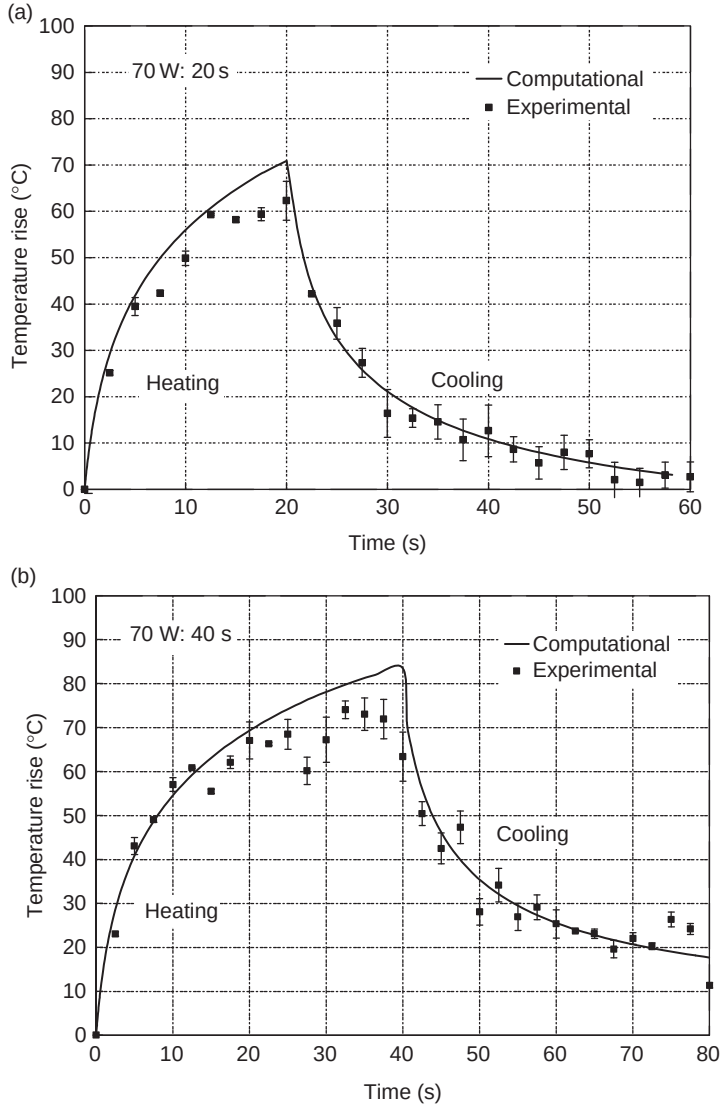

FIG. 18. Temperature rise as a function of time for (a) 20 s and (b) 40 s ablations at 70 W power. Numerical and experimental (MR) temperature data compared.

Lesion Size Measurement. MRI was used for imaging the HIFU-induced lesions at selected depths within the tissue. Figure 19 shows MRI-recorded lesions in the liver sample at sonication times 20, 30, and 40 s at three

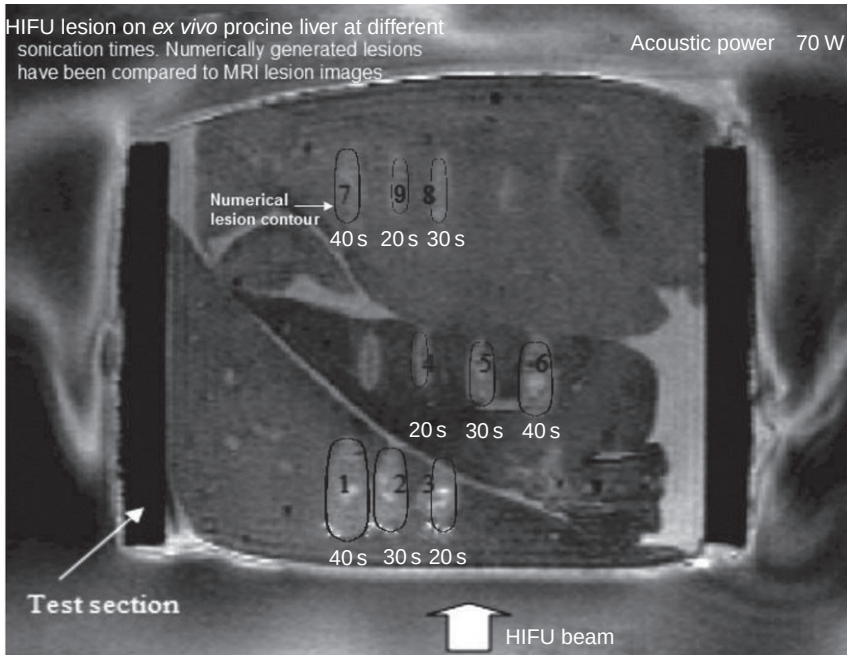

FIG. 19. MRI images of lesions (in white) and numerically generated lesions (black outline) are superimposed for 20, 30, and 40 s sonications at three depths.

different depths (rows 1, 2, and 3) within the tissue. Rows 1, 2, and 3 correspond to intensity levels: 1704, 1220, and 817 W/cm^2. The MRI lesions are compared to the calculated lesion contours (shown as black outlines). It is seen that at a given depth, the size of the lesion increases with sonication time. Also lesion size at a given sonication time decreases with depth from the tissue surface. This is because with increasing depth there is an increase in the attenuation of HIFU energy by the intervening medium between the focus and the tissue surface. It is also seen that the lesions at high-intensity levels (row 1) possess a tadpole shape instead of the typical cigar shape. This is attributed to the redistribution of HIFU energy by bubbles formed as a result of tissue boiling, a phenomenon observed by Khokhlova *et al.* [57].

After the ablation experiments, the liver samples were subjected to histology examination of the exposed tissue zones. Figure 20(a) shows the magnified view of the lesion boundary. The tissue region subjected to HIFU exposure appears as a continuous smudge of cells indicative of coagulative necrosis and is clearly demarcated from the surrounding undamaged tissue which appears as a collection of discrete cells. Thus, the examination

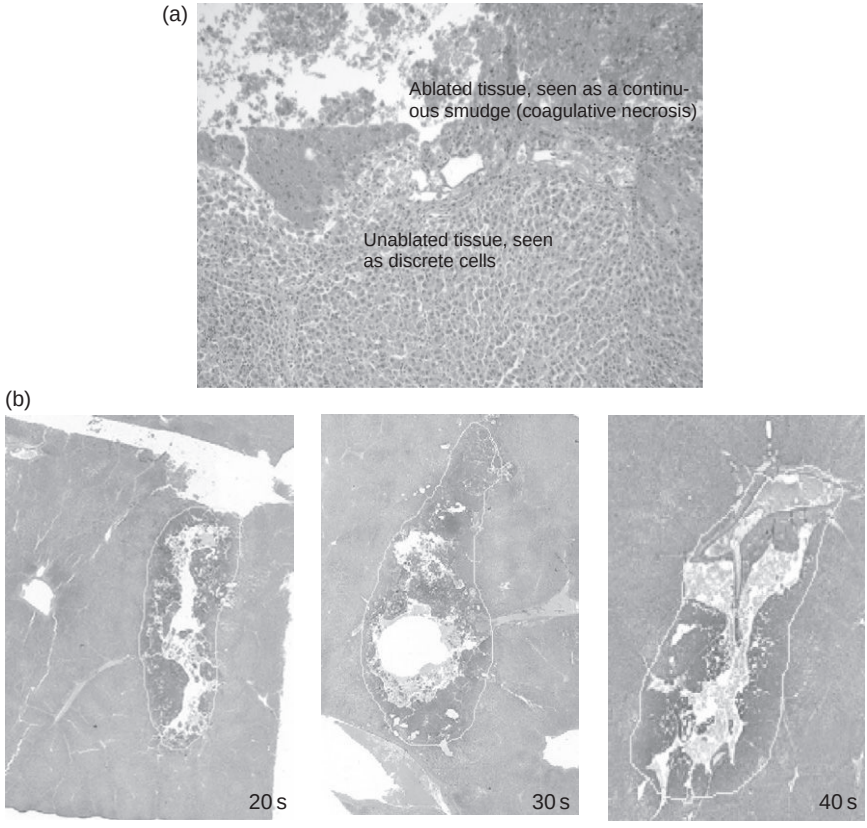

FIG. 20. (a) Magnified view of lesion boundary. (b) Histology image of lesions at sonication times 20, 30, and 40 s.

confirmed the occurrence of coagulative necrosis within the ablated zones. Figure 20 (b) shows lesion images obtained from the histology study at sonication times 20, 30, and 40 s. These images were used to measure lesion size as a function of sonication time. Hence, besides MRI lesion size was also determined from the histology study.

The MRI-monitored HIFU studies were useful in quantification of the lesion size as a function of sonication time. Figure 21(a) shows the computed and imaged lesion size as a function of sonication time. In row 2 (intensity 1220 W/cm3), lesion size increases from 0.22 cm^3 at 20 s to 0.58 cm^3 at 40 s sonication time, which indicates a nonlinear dependence of lesion size on sonication time. It is also seen that with increasing depth from the surface, lesion size decreases at a constant sonication time. Thus, row 1 lesions are

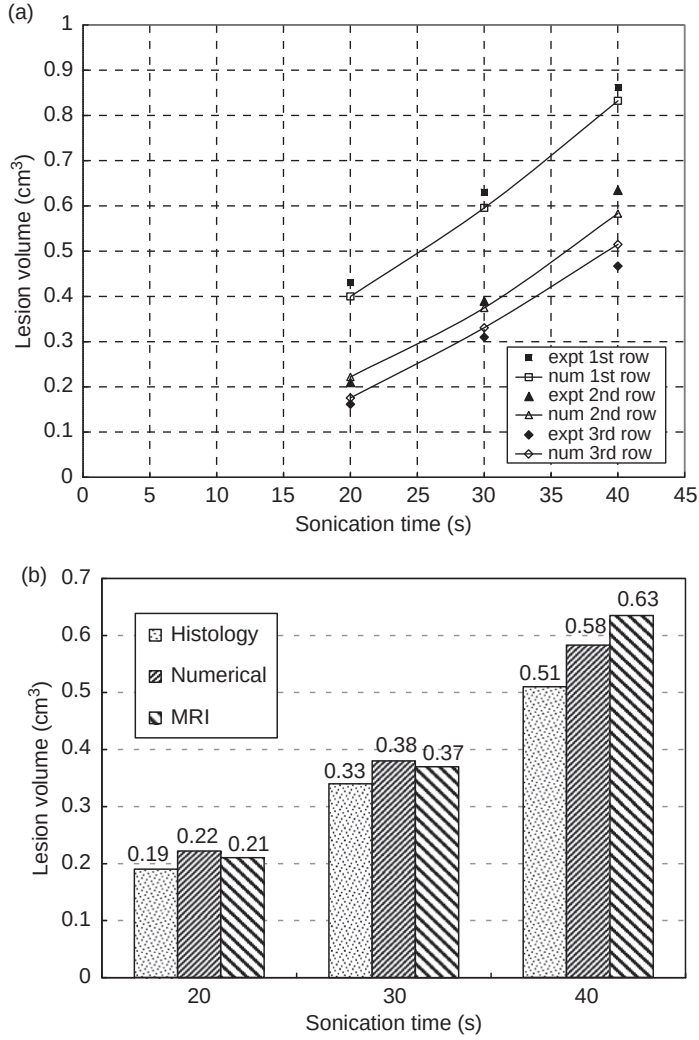

FIG. 21. (a) HIFU lesion volume vs sonication time for numerical and MR methods. (b) Lesion volume for different sonication times, as determined by histology, numerical simulation, and MR imaging.

larger than the lesions in rows 2 and 3. This is because of decrease of focal intensity with depth.

In Fig. 21 (b), lesion size obtained from three methods, histology, numerical, and MRI, are compared at sonication times 20, 30, and 40 s in row 2.

It is seen that there is a 13% agreement among the lesion size obtained by using all the three methods. Hence, this is for the first time that all the three methods were used to determine the HIFU lesion size as a function of operating parameters like sonication time and acoustic intensity.

Validation of Computational Models. Computational modeling is an important tool in HIFU studies for predicting the induced thermal effects. Several studies have used numerical models to calculate the HIFU-induced temperature rise and lesion size (Hariharan *et al*. [9]). For reliable prediction of the thermal effects, it is necessary to validate the models. Subsequent to the MRI-monitored HIFU studies, computations were performed to calculate the temperature rise and lesion size in the excised liver, at the selected sonication times 20, 30, and 40 s. Equations 3–5, as described before, are solved to obtain the transient temperature rise in the tissue medium. The transient temperature field was used in thermal-dose and lesion-volume calculations. Thermal dose, used for calculation of lesion size, was computed throughout the tissue medium, using the method developed by Sapareto and Dewey [59]. They showed that an exponential relation exists between the tissue temperature and the exposure time required to coagulate the tumor cells. The thermal-dose parameter is expressed as:

$$t_{43}(x,y,z) = \int_{t=0}^{t=t_{\text{final}}} R^{43-T(t)}\,dt, \tag{8}$$

where t_{43} is the thermal dose at the reference temperature of 43°C, and t_{final} is the treatment time.

$T(t)$ is the temperature (in degree Celsius) as a function of time obtained experimentally, and,

$$R = \left\{ \begin{array}{ll} 0.5 & \text{if } T(t) \geq 43^{\circ}\text{C} \\ 0.25 & \text{otherwise} \end{array} \right\}.$$

According to this relation, thermal dose resulting from heating the tissue to 43°C for 240 min is equivalent to that achieved by heating to 56°C for 1.76 s. The bounding surface of the HIFU lesion was taken to be the surface where the thermal dose attained a value of 240 equivalent minutes at 43°C. The lesion volume is the amount of tissue within the surface. He *et al*. [60] found that the thermal-dose threshold values and the R values are different for different urological systems. In principle, the threshold established for the particular organ and species should be used in thermal-dose calculations. As these values are often not available, a value of 240 equivalent minutes is usually used. For example, in the HIFU ablation studies by Righetti *et al*.

[61] involving excised livers, a thermal dose of 243 min (~240 min) was used as the threshold for cell necrosis.

The temperature rise and lesion volume obtained from the calculations were compared with results of MRI thermometry and a 13% agreement was found (Figs. 18 and 21). Thus, besides measuring the temperature rise and lesion volume noninvasively, the MRI and histology methods were also useful in validating results of computational methods.

III. Future Direction

In order to ensure safety of patients during HIFU therapy and to enhance effectiveness of the procedure, proper characterization of HIFU devices, for accurate prediction of the induced thermal field, is necessary. The MRI thermometry method and the inverse heat transfer method have both been found useful in the characterization of the HIFU thermal field. Such methods will be useful to device manufacturers as well as regulatory bodies like the FDA, to better evaluate the performance of HIFU devices. However, the present studies can be extended or modified for enhancing the accuracy of thermal field characterization.

A. Improvement in Calculations: Accounting for Boiling, Cavitation, and Nonlinearity

The computational method to calculate temperature rise and lesion size, under a given set of operating parameters, is usually limited by the assumption of linearity and the inability to treat cavitation or boiling. The computational method employed by the present authors has the capability to calculate the HIFU-induced temperature rise and lesion volumes within acceptable accuracy especially at low or moderate energy levels. The authors feel that for a greater accuracy in predicting temperature rise and lesion size at high energy levels, in future HIFU studies, the computational method should account for boiling, cavitation, and nonlinearity. The HIFU heat source can be modified to account for the redistribution of energy due to the bubbles.

B. Extension of Inverse Heat Transfer Method: Calculation of Intensity and Acoustic Absorptivity

The inverse method developed in the study derives the location of the HIFU beam. The method can also be applied to derive other variables, such

as the acoustic power. In this instance, it is essential that a nonlinear propagation model be used by the optimization scheme. The propagation model, used in recent studies, is the linearized KZK algorithm, but any appropriate propagation model can be incorporated into the inverse procedure. In the iterative procedure, the acoustic power would be combined with the focal coordinates as a fourth parameter. Alternatively, a subsequent optimization based upon power can be performed once the focal coordinates have been determined, though any influence of the power on the focal position would not be captured adequately.

Disclaimer: The mention of commercial products, their sources, or their use in connection with material reported herein is not to be construed as either an actual or an implied endorsement of such products by the US Department of Health and Human Services.

References

1. Curra, F. P. and Crum, L. A. (2003). Therapeutic ultrasound: surgery and drug delivery. *Acoust. Sci. Technol.* **24**(6), 343–348.
2. ter Haar, G. R. (2001). Acoustic surgery. *Phys. Today* **54**(12), 29–34.
3. Hariharan, P., Chang, I., Banerjee, R. K., and Myers, M. R. (2007). Radio frequency (RF) ablation in a realistic reconstructed hepatic tissue. *J. Biomech. Eng.* **129**, 354–364.
4. Ren, X. L., Zhou, X. D., Yan, R. L., Liu, D., Zhang, J., He, G. B., Han, Z. H., Zheng, M. J., and Yu, M. (2009). Sonographically guided extracorporeal ablation of uterine fibroids with high -intensity focused ultrasound: midterm results. *J. Ultrasound Med. [Letters to the Editor]*. **28**, 95–103.
5. Nell, D. M. and Myers, M. R. (2010). Thermal effects generated by high-intensity focused ultrasound beams at normal incidence to a bone surface. *J. Acoust. Soc. Am.* **127**(1), 549–559.
6. Civale, J., Clarke, R., Rivens, I., and ter Haar, G. (2006). The use of a segmented transducer for rib sparing in HIFU treatments. *Ultrasound Med. Biol.* **32**(11), 1753–1761.
7. Kolios, M. C., Sherar, M. D., and Hunt, J. W. (1996). Blood flow cooling and ultrasonic lesion formation. *Med. Phys.* **23**, 287–1298.
8. Huang, J., Holt, R. G., Cleveland, R. O., and Roy, R. A. (2004). Experimental validation of a tractable numerical model for focused ultrasound heating in flow-through tissue phantoms. *J. Acoust. Soc. Am.* **116**, 2451–2458.
9. Hariharan, P., Banerjee, R. K., and Myers, M. R. (2007). HIFU procedures at moderate intensities—effect of large blood vessels. *Phys. Med. Biol.* **52**, 3493–3513.
10. Harris, G. R. (2010). FDA regulation of clinical high intensity focused ultrasound (HIFU) devices. *In* "2009 Proceedings of IEEE Ultrasonic Symposium." Rome, Italy pp. 145–148.
11. Shaw, A. ter Haar, G. R. (2006). "Requirements for Measurement Standards in High Intensity Focused (HIFU) Ultrasound Fields." National Physical Laboratory (NPL) report. ISSN 1744–0599.
12. IEC 61157. (1992). Requirements for the declaration of the acoustic output of medical diagnostic ultrasonic equipment. *International Electrotechnical Commission*. Geneva, Switzerland.

13. IEC 61161. (1992). Ultrasonic power measurements in liquids in the frequency range 0.5 MHz to 25 MHz. *International Electrotechnical Commission*. Geneva, Switzerland.
14. Preston, R. C. (2000). Standards for measurement. *Ultrasound Med. Biol.* **26**(Suppl. I), S63–S67.
15. Zeqiri, B. and Hodenett, M. (2010). Measurements, phantoms, and standardization. *J. Eng. Med.* **224**, 375–391.
16. Harris, G. R. (2005). Progress in medical ultrasound exposimetry. *IEEE Trans. Ultrason. Ferroelectr. Freq. Control* **52**(5), 717–736.
17. Hallez, L., Touyeras, F., Hihn, J. Y., and Klima, J. (2007). Energetic balance in an ultrasonic reactor using focused or flat high frequency transducers. *Ultrasonics* **14**, 739–749.
18. Shaw, A. (2004). Delivering the right dose, advanced metrology for ultrasound in medicine. *J. Phys. Conf. Ser.* **1**, 174–179.
19. Schafer, M. E., Gessert, J. E., and Moore, W. (2006). Development of a High Intensity Focused Ulrasound (HIFU) Hydrophone System. *Proc. Int. Symp. Ther. Ultrasound 2005*. **829**, 609–613.
20. Zanelli, C. I. and Howard, S. M. (2006). A robust hydrophone for HIFU metrology. *Proc. Int. Symp. Ther. Ultrasound 2006* **829**, 618–622.
21. Shaw, A. (2006). How to measure HIFU output properly. *Proc. Int. Symp. Ther. Ultrasound 2005* **829**, 628–632.
22. Wang, Z. Q., Lauxmann, P., Wurster, C., Kohler, M., Gompf, B., and Eisenmenger, W. (1999). Impulse response of a fiber optic hydrophone determined with shock waves in water. *J. Appl. Phys.* **85**(5), 2514–2516.
23. Lewin, P. A., Mu, C., Umchid, S., Daryoush, A., and El-Sherif, M. (2005). Acousto-optic, point receiver hydrophone probe for operation up to 100 MHz. *Ultrasonics* **43**, 815–821.
24. Morris, P., Hurrell, A., Shaw, A., Zhang, E., and Beard, P. (2009). A Fabry-Perot fiber-optic ultrasonic hydrophone for the simultaneous measurement of temperature and acoustic pressure. *J. Acoust. Soc. Am.* **125**(6), 3611–3622.
25. Gopinath, R., Arora, P., Gandhi, G., Daryoush, A. S., El-Sherif, M., and Lewin, P. A. (2009). Thin film metal coated fiber optic hydrophone probe. *Appl. Opt.* **48**(31), G77–G82.
26. Harland, A. R., Petzing, J. N., and Tyrer, J. R. (2002). Non-invasive measurements of underwater pressure fields using laser Doppler velocimetry. *J. Sound Vib.* **252**(1), 169–177.
27 27. Theobald, P., Thompson, A., Robinson, S., Preston, R., Lepper, P., Swift, C., Yuebing, W., and Tyrer, J. (2004). "Fundamental Standards for Acoustics Based on Opticalo Methods—Phase Three Report for Sound in Water." National Physical Laboratory (NPL) report 2004. CAIR9 ISSN 1740-0953.
28. Hariharan, P., Myers, M. R., and Banerjee, R. K. (2008). Characterizing medical ultrasound fields using acoustic streaming. *J. Acoust. Soc. Am.* **123**(3), 1706–1719.
29. Myers, M. R., Hariharan, P., and Banerjee, R. K. (2008). Direct methods for characterizing high-intensity focused ultrasound transducers using acoustic streaming. *J. Acoust. Soc. Am.* **124**(3), 1790–1802.
30. MATLAB 2008, Mathworks INC.
31. Chen, D., Fan, T., Zhang, D., and Wu, J. (2009). A feasibility study of temperature rise measurement in a tissue phantom as an alternative way for characterization of the therapeutic high intensity focused ultrasonic field. *Ultrasonics* **49**(8), 733–742.
32. Huang, J., Holt, R. G., Cleveland, R. O., and Roy, R. A. (2004). Experimental validation of a tractable numerical model for focused ultrasound heating in flow-through tissue phantoms. *J. Acoust. Soc. Am.* **116**, 2451–2458.
33. Fry, W. J. and Fry, R. B. (1954). Determination of absolute sound levels and acoustic absorption coefficients by thermocouple probes-theory. *J. Acoust. Soc. Am.* **26**, 294–310.

34. Fry, W. J. and Fry, R. B. (1954). Determination of absolute sound levels and acoustic absorption coefficients by thermocouple probes-experiments. *J. Acoust. Soc. Am.* **26**, 311–317.
35. Morris, H., Rivens, I., Shaw, A., and ter Haar, G. (2008). Investigation of the viscous heating artifact arising from the use of thermocouples in a focused ultrasound field. *Phys. Med. Biol.* **53**, 4759.
36. O'Neill, B., Vo, H., Angstadt, M., Li, K. P.C., Quinn, T., and Frenkel, V. (2009). Pulsed high intensity focused ultrasound mediated nanoparticle delivery: mechanisms and efficacy in murine muscle. *Ultrasound Med. Biol.* **35**, 416–424.
37. Dasgupta, S., Wansapura, J., Hariharan, P., Pratt, R., Witte, D., Myers, M. R., and Banerjee, R. K. (2010). HIFU lesion volume as a function of sonication time, as determined by MRI, histology, and computations. *J. Biomech. Eng.* Aug; **132**(8).
38. Qian, Z. W., Xiong, L., Yu, J., Shao, D., Zhu, H., and Wu, X. (2006). Non-invasive thermometer for HIFU and its scaling. *Ultrasonics* **44**, 31–35.
39. Melodelima, D., Salomir, R., Mougenot, C., Moonen, C., and Cathignol, D. (2006). 64-element intraluminal ultrasound cylindrical phased array for transesophageal thermal ablation under fast MR temperature mapping: an *ex vivo* study. *Med. Phys.* **33**, 2926–2934.
40. Anzai, Y., Luftkin, R., DeSalles, A., Hamilton, D. R., Farahani, K., and Black, K. L. (2005). Preliminary experience with MR-guided thermal ablation of brain tumors. *Am. J. Neuroradiol.* **16**, 39–48.
41. King, R. L., Herman, B. A., Maruvada, S., Wear, K. A., and Harris, G. R. (2006). Development of a HIFU phantom. *Proc. 6th Int. Symp. Ther. Ultrasound* **911**, 351–356.
42. Maruvada, S., Liu, Y., Herman, B., Pritchard, W. F., and Harris, G. R. (2008). Temperature measurements and determination of cavitation thresholds during High Intensity Focused Ultrasound (HIFU) exposures in *ex-vivo* porcine muscle. *J. Acoust. Soc. Am.* **123**, 2995.
43. Hynynen, K. and Edwards, D. K. (1989). Temperature measurements during ultrasound hyperthermia. *Med. Phys.* **16**, 618–626.
44. Farhanieh, B. and Heydari, M. M. (2008). An inverse problem method for overall heat transfer coefficient estimation in a partially filled rotating cylinder. *Heat Transf. Eng.* **29**, 272–283.
45. Paredes, G. E. and Martinez, E. G. E. (2009). A feedback-based inverse heat transfer method to estimate unperturbed temperatures in wellbores. *Energy Convers. Manageme.* **50**, 140–148.
46. Lee, Y. S. (1993). Numerical solution of the KZK equation for pulsed finite amplitude sound beams in thermoviscous fluids, PhD dissertation University of Texas at Austin.
47. Nelder, J. A. and Mead, R. (1965). A simplex method for function minimization. *Comput. J.* **7**, 308–313.
48. Lagarias, J. C., Reeds, J. A., Wright, M. H., and Wright, P. E. (1995). "Convergence Properties of the Nelder-Mead Algorithm in Low Dimensions." AT&T Bell Laboratories, Tech. Rep. Murray Hill, NJ.
49. Vaezy, S., Shi, X., Martin, R. W., Chi, E., Nelson, P. I., Bailey, M. R., and Crum, L. A. (2001). Real-time visualization of high-intensity focused ultrasound treatment using ultrasound imaging. *Ultrasound Med. Biol.* **27**(1), 33–42.
50. Mingzhu, Lu., Wan, M., Xu, F., Wang, X., and Chang, X. (2006). Design and experiment of 256-element ultrasound phased array for noninvasive focused ultrasound surgery. *Ultrasonics* **44**(1), e325–e330.
51. Song, C., Marshall, B., McLean, D., Frank, T., Cuschieri, A., Campbell, P., and Sibbet, W. (2005). Thermo graphic investigation of the heating effect of high intensity focused ultrasound. *Conf. Proc. IEEE. Eng. Med. Biol. Soc.* **4**, 3456–3458.

52. Bohris, C., Schreiber, W. G., and Jenne, J. (1995). Quantitative MR temperature monitoring of high intensity focused ultrasound therapy. *Magn. Reson. Imaging* **17**, 603–610.
53. Hynynen, K., Pomeroy, O., Smith, D. N., Huber, P. E., McDannold, N. J., Kettenbach, J., Baum, J., Singer, S., and Jolesz, F. A. (2001). MR imaging-guided focused ultrasound surgery of fibroadenomas in the breast: a feasibility study. *Radiology* **219**, 176–185.
54. Ishihara, Y., Calderon, A., Watanabe, H., Okamoto, K., Suzuki, Y., Kuroda, K., and Suzuki, Y. (1995). A precise fast temperature mapping using water proton chemical shift. *Magn. Reson. Med.* **34**, 814–823.
55. De Poorter, J., Wagter, C. D., Deene, Y. D., Thomsen, C., Ståhlberg, F., Achten, E., and Noninvasive MR, I. (2005). Thermometry with the proton resonance frequency (PRF) method: *in vivo* results in human muscle. *Magn. Reson. Med.* **33**, 74–81.
56. Rieke, V., Vigen, K., Sommer, G., Daniel, B. L., Pauly, J. M., and Butts, K. (2004). Referenceless PRF shift thermometry. *Magn. Reson. Med.* **51**(6), 1223–1231.
57. Khokhlova, V. A., Bailey, M. R., Reed, J. A., Cunitz, B. W., and Kaczkowski, P. J. (2006). Effects of nonlinear propagation, cavitation, and boiling in lesion formation by high intensity focused ultrasound in a gel phantom. *J. Acoust. Soc. Am.* **119**(3), 1834–1848.
58. Oshiro, T., Sinha, U., Lu, D., and Sinha, S. (2002). Reduction of electronic noise from radiofrequency generator during radiofrequency ablation in interventional MRI. *J. Comput. Assist. Tomogr.* **26**(2), 308–316.
59. Saperato, S. and Dewey, W. C. (1984). Thermal dose determination in cancer therapy. *Int. J. Radiat. Oncol. Biol. Phys.* **10**(6), 787–800.
60. He, X., Bhowmick, S., and Bischof, J. C. (2009). Thermal therapy in urologic systems: a comparison of Arrhenius and thermal isoeffective dose models in predicting hyperthermia injury. *J. Biomech. Eng.* **131**(7), 74507.
61. Righetti, R., Kallel, F., Stafford, R. J., Price, R. E., Krouskop, T. A., Hazle, J. D., and Ophir, J. (1999). Elastographic characterization of HIFU-induced lesions in canine livers. *Ultrasound Med. Biol.* **25**(7), 1099–1113.

Plasma Discharge in Water

YONG YANG, ALEXANDER FRIDMAN, and YOUNG I. CHO*

Department of Mechanical Engineering and Mechanics, Drexel University, Philadelphia, PA 19104, USA

I. Introduction

A. Needs for Plasma Water Treatment

1. Cooling Water Management

Water is used as a cooling medium in large centralized air-conditioning systems as well as in thermoelectric power plants. In both cases, the cooling water plays an essential role in removing heat from condensers. Since the evaporation of pure water is the basic means to remove heat from the condensers, the concentration of mineral ions in circulating cooling water increases with time, resulting in hard water within a week even if soft water is used as makeup water. Hence, a part of the circulating water is periodically or continuously discharged in order to maintain the proper concentration of the mineral ions in circulating cooling water in the form of blowdown.

Thermoelectric power plants produce about half of the nation's electricity. According to the US Geological Survey's (USGS) water use survey data [1], thermoelectric generation accounted for 39% (136 billion gallons per day [BGD]) of all freshwater withdrawals in the nation in 2000, second only to irrigation (see Fig. 1) [1]. Furthermore, the average daily national freshwater consumption for thermoelectric power generation is predicted to increase from the current 4 BGD for the production of approximately 720 GW electricity to 8 BGD for 840 GW in 2030 (see Fig. 2) [2].

In the cooling water management, it is important to distinguish between water withdrawal and water consumption. Water withdrawal represents the total water taken from a source, while water consumption represents the amount of water withdrawal that is not returned to the source. Freshwater consumption for the year 1995 (the most recent year for which these data are available) is presented in Fig. 3. Freshwater consumption for thermoelectric

* Current address: Department of Mechanical Engineering and Mechanics, Drexel University, Philadelphia, PA 19104, USA

Advances in Heat Transfer
Volume 42 ISSN 0065-2717
DOI: 10.1016/S0065-2717(10)42003-1

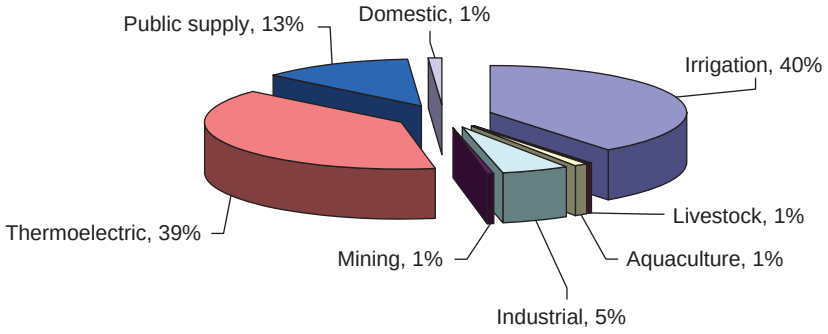

FIG. 1. U.S. freshwater withdrawal (2000). Source: USGS, Estimated use of water in the United States in 2000, USGS Circular 1268, March 2004. Add-up may not be equal to 100% due to rounding.

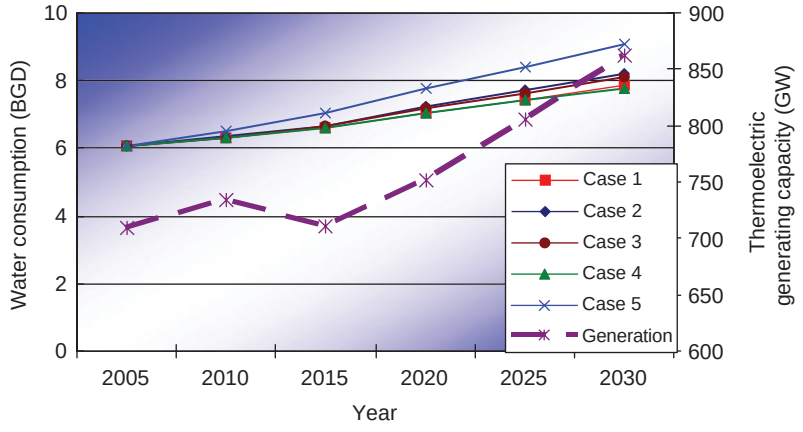

FIG. 2. Average daily national freshwater consumption for thermoelectric power generation 2005–2030 (predicted). Source: DOE/Office of Fossil Energy's Energy & Water R&D Program, 2008.

uses appears low (only 3%) when compared with other use categories (irrigation was responsible for 81% of water consumed). However, even at 3% consumption, thermoelectric power plants consumed more than 4 BGD [1].

A modern 1000-MW thermoelectric power plant with 40% efficiency would reject 1500 MW of heat at full load. This is roughly equivalent to 512×10^6 Btu/h and uses about 760,000 gal/min of circulating water based on 18°F temperature difference in condenser [3]. As heat is removed via the evaporation of pure water at a cooling tower, the need for the makeup water is about 7500 gal/min for the typical fossil plant, which results in 10 million gallons a day [3].

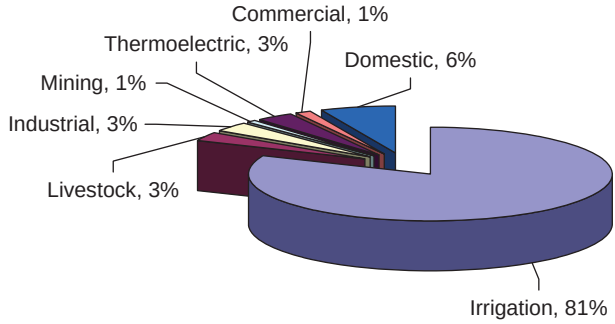

FIG. 3. U.S. freshwater consumption (1995). Source: USGS, Estimated use of water in the United States in 1995, USGS Circular 1220, 1998. Add-up may not be equal to 100% due to rounding.

One of the critical issues in the cooling water management is the condenser tube fouling by mineral ions such as calcium and magnesium. Since calcium-carbonate ($CaCO_3$) problem is most common in cooling water, one can use the term "calcium scale" to refer all scales caused by mineral ions. In order to prevent or minimize the condenser tube fouling, the cycle of concentration (COC) in wet recirculation cooling systems is often kept at 3.5. Since increasing the COC can reduce the amount of makeup water, the water consumption can be reduced with the increased COC. For example, if one can increase the COC to 8, the freshwater consumption can be reduced by approximately 25%, meaning that the makeup water can be reduced by 2.5 million gallons a day in a 1000-MW thermoelectric power plant.

Since the amounts of mineral ions in circulating cooling water primarily depend on the COC, the condenser tube fouling also depends on the COC. Hence, the issue in the cooling water management is to increase the COC without the condenser fouling problem. The present review deals with an innovative water treatment technology utilizing plasma discharges in water, with which one can increase the COC without the fouling problem in condenser tubes. The key issue is how to precipitate and remove mineral ions such as calcium and magnesium from circulating cooling water so that the $CaCO_3$ scales can be prevented at the condenser tubes and at the same time the COC can be increased.

2. *Water Sterilization*

The availability of clean water is an issue that has paralleled the continual increase in water consumption due to both global population growth and the economic development in a number of developing countries. From a global

perspective, an estimated 1.1 billion people are unable to acquire clean safe water [4]. As estimated by the Environmental Protection Agency (EPA), nearly 35% of all deaths in developing countries are directly related to contaminated water [5]. The need for improved water treatment exists on both political and humanitarian dimensions. Contaminated water can be attributed to a number of factors, including chemical fouling, inadequate treatment, deficient or failing water treatment, and poor distribution system. An additional cause of contamination is the presence of untreated bacteria and viruses within the water. Even in the United States, the increased presence of *Escherichia coli* (*E. coli*), along with various other bacteria, has been a cause for concern.

In an effort to inactivate bacteria, there are several commercially available methods such as chemical treatments, ultraviolet (UV) radiation, and ozone injection technologies. The experimental success and commercialization of these water treatment methods are not, however, without deficiencies. With regard to human consumption, chemical treatments such as chlorination could render potable water toxic. Although both UV radiation and ozone injection have been proven to be practical methods for the decontamination of water, the effectiveness of such methods largely depends upon adherence to regimented maintenance schedules. It is because of these deficiencies that the importance of research and development of new and improved water treatment methods continues to grow.

B. Previous Studies on the Plasma Water Treatment

In recent years, there is an increasing interest in the study of pulsed electric breakdown in water and other liquids as it finds more applications in both industry and academic researches. A large number of papers and conference contributions were published during the last few years. High-voltage (HV) electrical discharges in water have been shown to be able to induce various reactions including the degradation of organic compounds [6–13], the destruction of bacteria and viruses [14–19], the oxidation of inorganic ions [20–25], and the synthesis of nanomaterials and polymers [26–29]. The reactions are usually thought to be initiated by various reactive species, UV radiation, shockwaves, high electric field, or intense heat produced by pulsed electric discharge. The concentration of the reactive species and the intensity of the physical effects largely depend on the discharge type and solution properties.

Locke [27] published a comprehensive review on the application of strong electric fields in water and organic liquids with 410 references in 2006. They explained in detail the types of discharges used for water treatment, physics of the discharge, and chemical reactions involved in the discharge in water.

More recently, Bruggeman and Leys [29] published another review paper on non-thermal plasma in contact with water. They discussed three different types of plasmas: direct liquid discharges, discharges in gas phase with a liquid electrode, and discharges in bubbles in liquids. A different excitation method for each type was discussed individually. In addition, plasma characteristics of the different types of plasma in liquids were discussed. Currently several research groups around the world actively study plasma discharges for water treatment, which will be briefly discussed next.

Schoenbach and his colleagues at Old Dominion University have studied the electrical breakdown in water with submillimeter gaps between pin and plane electrodes by using optical and electrical diagnostics with a temporal resolution on the order of 1 ns [30–34]. By using a Mach–Zehnder interferometer, the electric field distribution in the pre-breakdown phase was determined by means of the Kerr effect, which indicates a change in the refractive index of a material. Values of electric fields in excess of computed electric fields, which reached over 4 MV/cm for applied electrical pulses of 20 ns duration, were recorded at the tip of the pin electrode. The results of this research have found bioelectric applications in the construction of compact pulse power generators.

Locke and his colleagues at Florida State University have qualitatively studied the production of reductive species by pulsed plasma discharge in water using different chemical probes [35–37]. They showed that the formation of primary radicals from water decomposition occurred in the discharge zone. The immediate region surrounding the discharge zone was responsible for radical recombination to form products that diffused into bulk water where the radicals participated in bulk phase reactions. The rate of the formation of reductive species in the pulsed streamer discharge increased as the input power to the system increased, offering a possibility that in a mixture of aqueous contaminants some pollutants or a component of certain pollutants could degrade by reductive mechanisms, thereby increasing the degradation efficiency of the process.

Graves and his colleagues at the University of California, Berkeley, presented a unique method to inactivate microorganisms in 0.9% NaCl solution (i.e., normal saline solution) by means of microplasmas [17]. They employed *E. coli* bacteria to investigate the disinfection efficiency of the device. The device consisted of a thin titanium wire covered by a glass tube for insulation except for the tip of the wire and ground electrode. Microbubbles could be formed at both electrodes from the application of an asymmetric high-frequency, high voltage. Repetitive light emission was observed in the vicinity of the powered electrode. More than 99.5% of *E. coli* was deactivated in 180 s.

Sato and his colleagues at Gunma University, Japan, studied the environmental and biotechnological applications of HV pulsed discharges in water.

A pulsed discharge was formed in water by applying a HV pulse in point-to-plane electrode systems [38–42]. They found that bubbling through a hollow needle electrode made it possible to raise the energy efficiency in the decomposition of organic materials by reducing the initial voltage of the discharge. Oxygen gas bubbling was found to be effective for the decomposition because of the forming of active species originating from oxygen gas.

Sunka and other researchers from the Institute of Plasma Physics, Academy of Sciences of the Czech Republic, developed a pulsed corona discharge generator in water using porous ceramic-coated rod electrodes (shown in Fig. 9) [43–45]. They studied the properties of the ceramic layer and its interaction with the electrolyte and reported that surface chemistry at the electrolyte/ceramic surface interface was an important factor in generating electrical discharges in water using porous ceramic-coated electrodes. Initiation of the discharge in water using these types of electrodes depended on the surface charge of the ceramic layer in addition to the permittivity and porosity of the ceramic layer. The surface charge could be determined by the polarity of applied voltage, and pH and the chemical composition of aqueous solution. By applying bipolar HV pulses to eliminate possible build-up of an electrical charge on the ceramic surface, large-volume plasma could be produced in water in the range of kilowatts.

Recently, Yang and his colleagues from Drexel Plasma Institute, Drexel University, reported the formation of liquid-phase non-equilibrium plasma in water. Since plasmas were only considered to exist through the ionization of gases, people had believed that plasmas in liquids must have been generated inside gas-phase bubbles produced through intense local heating or via cavitation and could be sustained within those bubbles. For the generation of non-equilibrium plasma in liquids, a pulsed power system was often used with 32–112 kV pulse amplitude, 0.5–12 ns pulse duration, and 150 ps rise time. The measurements were performed with a 4Picos ICCD camera with a minimum gate time of 200 ps. It was found that discharge in liquid water formed in a picosecond time scale, and the propagation velocity of the streamers was about 5000 km/s. The reduced electric field E/n_0 at the tip of the streamer was about 200 Td. Both the propagation velocity and the reduced electric field in the test were similar to the streamer propagation in gas phase, indicating that the plasma could be formed in liquid phase without phase change. The details of the experiment will be discussed later.

C. Process of Conventional Electrical Breakdown in Water

Although a large number of studies were conducted on electric discharges in gases, studies on the electric breakdown in liquids have been limited by the high density of liquids and a short mean free path of electrons, therefore

requiring a very high electric field E/n_0. The critical breakdown condition for gas can be described by the Paschen curve, from which one can calculate the breakdown voltage. A value of 30 kV/cm is a well-accepted breakdown voltage of air at 1 atm. When one attempts to produce direct plasma discharge in water, a much higher breakdown voltage on the order of 30 MV/cm is needed based on the Paschen curve due to the density difference between air and water. A large number of experimental data on the breakdown voltage in water showed, however, that the breakdown voltage in water was of the same magnitude as for gases. In other words, the breakdown of liquids can be performed not at the extremely high electric fields required by the Paschen curve but at those that only slightly exceed the breakdown electric fields in atmospheric-pressure molecular gases. This interesting and practically important effect can be explained by taking into account the fast formation of gas channels in the body of water under the influence of an applied high voltage. When formed, the gas channels give the space necessary for the gas breakdown inside water, explaining why the voltage required for the breakdown in water is of the same magnitude as that in gases.

To generate electrical discharges in water, usually one needs to have a pulsed HV power supply. Water is a polar liquid with a relative permittivity of $\varepsilon_r = 80$. The electrical conductivity of water ranges from about 1 μS/cm for distilled water to several thousand μS/cm for cooling water, depending on the amount of dissolved ions in water. Given that a specific water is exposed to an electric pulse with a duration of Δt, when $\Delta t >> \varepsilon_r \varepsilon_0/\sigma$, where ε_0 is vacuum permittivity and σ is the conductivity of water, the aqueous solution can be considered as a resistive medium [28]. For such a long electric pulse, the electrolysis of water takes place with the production of hydrogen and oxygen. For the case of a much shorter pulse duration, i.e., when $\Delta t << \varepsilon_r \varepsilon_0/\sigma$, water behaves as a dielectric medium [28], and a high applied voltage will lead to the breakdown of the solution.

High electric field strength can usually be achieved by using needle electrodes with sharp tips, from which electric discharges in water usually start. If the discharge does not reach the second electrode, it is called a partial discharge (also called pulsed corona discharge, in analogy with the discharges in gases), and branches of such a discharge are called streamers (see Fig. 4 (a)). However, the nature of the discharges in liquids and the mechanism of streamer formation are much less understood, and may be completely different from those for discharges in gases. If a streamer reaches the opposite electrode, it makes a conductive channel between the two electrodes. Furthermore, if the current through the discharge is very high (above 1 kA), it is usually called an arc discharge. While an arc discharge is usually continuous, the transient phase of the arc discharge is referred to as a pulsed spark discharge.

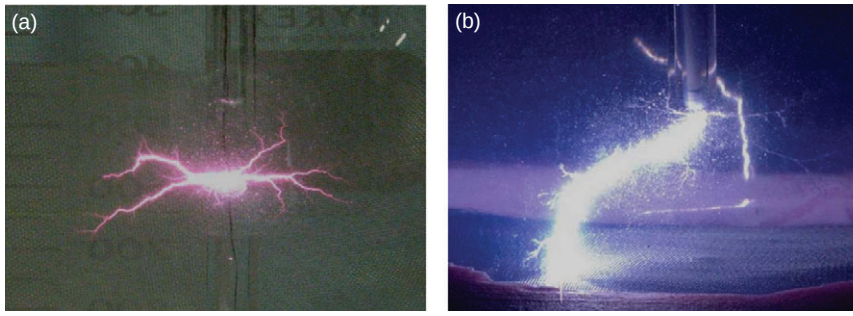

FIG. 4. Images of plasma discharge in water: (a) pulsed corona; (b) pulsed arc, produced at Drexel Plasma Institute.

TABLE I

SUMMARY OF THE CHARACTERISTICS OF PULSED CORONA, PULSED ARC, AND PULSED SPARK DISCHARGE IN WATER [26,27,46–55]

Pulsed corona	Pulsed arc	Pulsed spark
Non-thermal discharge.	Thermal discharge.	Similar to pulsed arc, except for short pulse duration and low temperature.
High operating frequency (100–1000 Hz).	Low operating frequency (<1 Hz).	Pulsed spark is faster than pulsed arc, i.e., strong shockwaves are produced.
Current transferred by slow ions.	Current transferred by electrons.	Plasma temperature in the spark is around a few thousand K.
Streamer filaments do not propagate across electrode gap.	Streamer filaments bridge electrode gap.	
A few joules or less per pulse.	Usually greater than 1 kJ per pulse.	
Weak to moderate UV generation.	Strong UV emission.	
Weak to moderate shockwave.	Strong shockwave.	
Relatively low current, i.e., peak current less than 100 A.	Large current with peak value greater than 100 A.	

The characteristics of pulsed corona and pulsed arc are summarized in Table I. In the partial discharge the current is transferred by slow ions, producing corona-like non-thermal discharges. In case of water with a high electrical conductivity, a large discharge current flows, resulting in a

shortening of the streamer length due to the faster compensation of the space charge electric fields on the head of streamers. Subsequently, a higher power density, i.e., a higher plasma density, in the channel can be obtained, resulting in a higher plasma temperature, a higher UV radiation, and the generation of acoustic waves.

In the arc or spark discharges, the current is transferred by electrons. The high current heats a small volume of plasma in the gap between two electrodes, generating quasi-thermal plasma, where the temperatures of electrons and heavy particles are almost equal. When a HV, high-current discharge takes place between two submerged electrodes, a large part of the energy is consumed in the formation of a thermal plasma channel. This channel emits UV radiation, and its expansion against the surrounding water generates intense shockwaves. The shockwave can directly interact with the microorganisms in water. Of note is that the pressure waves can scatter microorganism colonies within the liquid, thus increasing their exposure to inactivation factors. For the corona discharge in water, the shockwaves are weak or moderate, whereas for the pulsed arc or spark the shockwaves are generally very strong.

When the plasma discharge is initiated between two electrodes, the medium between the two electrodes is ionized creating a plasma channel. The plasma discharge generates UV radiation and converts surrounding water molecules into active radical species due to the high energy level produced by the discharge. The microorganisms could be effectively inactivated, while the organic contaminants could be oxidized through contact with active radicals. The chemical kinetics of these reactions remains an area of significant research [27,29]. Various active species can be considered as the byproducts of plasma discharge in water. The production of these species by plasma discharge is affected by a number of parameters such as applied voltage, rise time, pulse duration, total energy, polarity, the electric conductivity of water, etc. Among the active species, hydroxyl radical, atomic oxygen, ozone and hydrogen peroxide are the most important ones for the sterilization and removal of unwanted organic compounds in water. Table II summarizes the oxidation potentials of various active species produced by plasma in water, which ranges from 1.78 V (hydrogen peroxide) to 2.8 V

TABLE II

Oxidation Potential of Active Species Produced by Plasma in Water [56]

Active species	Hydroxyl radical (OH)	Atomic oxygen (O)	Ozone (O_3)	Hydrogen peroxide (H_2O_2)
Oxidation potential	2.8 V	2.42 V	2.07 V	1.78 V

(hydroxyl radical). Note that fluorine has the highest oxidation potential of 3.03 V, whereas chlorine, which is one of the most commonly used chemicals for water decontamination, has an oxidation potential of only 1.36 V.

In addition to the aforementioned active species, the electrical breakdown in water produces UV radiation (both VUV and UV). VUV (i.e., vacuum UV), as the name indicates, can only propagate in vacuum because it is strongly absorbed by air or water. For pulsed arc discharge, the high-temperature plasma channel can function as a blackbody radiation source. The maximum emittance is in the UVa to UVc range of the spectrum (200–400 nm) [28,55], as determined by the Stephen–Boltzmann law. Water is relatively transparent to UV radiation in this wavelength range. The energy per photon ranges from 3.1 eV to 6.2 eV. UV radiation has proven to be effective for decontamination processes and is gaining popularity as a means for sterilization because chlorination leaves undesirable byproducts in water. The radiation in the wavelength range of 240–280 nm may cause an irreparable damage to the nucleic acid of microorganisms, preventing proper cellular reproduction, and thus effectively inactivating the microorganisms.

Alternatively, the photons can provide the necessary energy to ionize or dissociate water molecules, generating active chemical species. Recently, it is suggested that the UV system may produce charged particles in water such that charge accumulation occurs on the outer surface of the membrane of bacterial cell. Subsequently, the electrostatic force on the membrane overcomes the tensile strength of the cell membrane, causing its rupture at a point of small local curvature as the electrostatic force is inversely proportional to the local radius squared [57–59].

Since one of the major applications of the plasma discharge in water is in the development of a self-cleaning filter to be discussed later in this review article, the ability for the discharge to generate shockwaves will be briefly summarized next. When a HV, high-current discharge takes place between two electrodes submerged in water, a large part of the energy is consumed on the formation of a thermal plasma channel. The expansion of the channel against the surrounding water generates a shockwave. For the corona discharge in water the shockwaves are often weak or moderate, whereas for the pulsed arc the shockwaves are strong. The difference arises from the fact that the energy input in the arc or spark discharge is much higher than that in the corona.

Similarly, between the arc and spark, the arc produces much greater shockwaves due to its higher energy input. The water surrounding the electrodes becomes rapidly heated, producing bubbles, which help the formation of a plasma channel between the two electrodes. The plasma channel may reach a very high temperature of 14,000–50,000 K, consisting of a highly ionized, high-pressure, and high-temperature gas. Thus, once formed,

the plasma channel tends to expand. The energy stored in the plasma channel is dissipated via both radiation and conduction to the surrounding cool liquid water and mechanical work. At the liquid–gas phase boundary, the high-pressure build-up in the plasma is transmitted into the water interface and an intense compression wave (i.e., shockwave) is formed, traveling at a much greater speed than the speed of sound. Note that the shockwaves have another benefit in the sterilization process through a good mixing of water to be treated, significantly enhancing the plasma treatment efficiency as in the aforementioned self-cleaning filter performance.

However, the plasma discharge for water treatment is not without deficiencies. One of the concerns in the use of a sharp needle as a HV electrode is the adverse effect associated with the needle tip erosion. In a point-to-plane geometry, a large electric field can be achieved due to the sharp tip of the needle with a minimum applied voltage V. For a sharp parabolic tip of the needle electrode, the theoretical electric field at the needle tip becomes $E \propto V/r$, where r is the radius of curvature of the needle tip. As indicated by the above equation, the electric field at the tip of the electrode is inversely proportional to the radius of curvature of the needle tip. Hence, the maximum electric field could be obtained by simply reducing the radius of curvature r, which is much easier than increasing the voltage as the maximum value of the voltage is usually restricted by the electric circuit as well as insulation materials used around electrodes.

Sunka [60] pointed out that the very sharp tip anode would be quickly eroded by the discharge, and one had to find some compromise between the optimum sharp anode construction and its lifetime for extended operation. Also it was demonstrated recently that the erosion of electrodes at pulse electric discharge in water would result in the production of metal and oxide nanoparticles in water. These particles are very difficult to remove once they enter the drinking water system due to their nanometer sizes, and potential danger to human body is not clearly known.

Another concern in the application of pulsed electric discharges in water is the limitation posed by the electrical conductivity of water on the production of such discharges [60]. In the case of a low electric conductivity below 10 μS/cm, the range of the applied voltage that can produce a corona discharge without sparking is very narrow. On the other hand, in the case of a high electric conductivity above 400 μS/cm, which is the typical conductivity of tap water, streamers become short and the efficiency of radical production decreases. In general, the production of hydroxyl radicals and atomic oxygen is more efficient at water conductivity below 100 μS/cm. Thus, this is one of the major challenges in the application of plasma discharges for cooling water management as the electric conductivity of most cooling water is at the range of 2000–2500 μS/cm.

II. Underwater Plasma Sources

A. Direct Discharges in Liquid

Various electrode geometries have been studied for the generation of plasma discharges in liquid. Figure 5 shows some of the typical electrode configurations. Note that only the cases where both the HV electrode and ground electrode are placed in liquid are shown here. Among them, the point-to-plane geometry has been the most commonly used configuration (shown in Fig. 5 (a)). Also a point-to-plane geometry with multiple points was used to generate a large-volume corona discharge in water (Fig. 5 (b)). For pulsed arc discharges, a point-to-point electrode geometry was often used (Fig. 5 (c)).

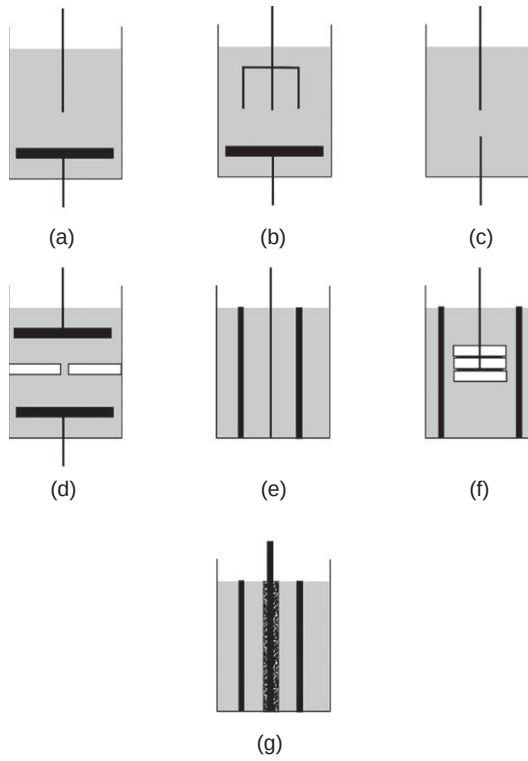

Fig. 5. Schematics of electrode geometries used for plasma discharges in liquid: (a) single point-to-plane; (b) multiple points-to-plane; (c) point-to-point; (d) pin hole; (e) wire-to-cylinder; (f) disk electrode; (g) composite electrode with porous ceramic layer.

As mentioned in the previous section, one of the concerns in the use of a sharp needle as the HV electrode is the tip erosion due to the intense local heating at the tip. To overcome the limitation of the needle-plate configuration, "pinhole" electrodes (also called a diaphragm discharge, as shown in Fig. 5 (d)) with large surface areas were developed, where the HV and ground electrodes are separated by a dielectric sheet with a small hole [61–64]. When high voltage is applied on the electrodes, an intense electric field could be formed around the pinhole. Subsequently, a pre-discharge current could be concentrated in the small hole, leading to strong thermal effects, resulting in the formation of bubbles. Pulsed corona discharge occurs inside the bubbles at the pinhole because of the high electric field. The length of the streamers generated is decided by the parameters such as water conductivity, the size of the pinhole, flow velocity through the pinhole, and voltage polarity. Similar to the corona discharge in the point-to-plane geometry, a pulsed arc discharge could be formed once the streamer bridges the two electrodes. Figure 6 shows (a) pulsed corona and (b) arc discharges through a pinhole produced at Drexel Plasma Institute.

Another critical issue that researchers are facing is to increase the volume of an active plasma discharge region, for industrial applications with a large water flow rate. Clearly the point-to-plane electrode geometry would be difficult to scale up for such an industrial application. Also it is difficult to discharge uniformly at multiple pinholes. In order to effectively treat a large volume of water with plasma discharges, different approaches could be used including a wire–cylinder geometry (Figs. 5 (e) and 7), a disk geometry (Fig. 5 (f)), and a concentric cylinder geometry with a HV center composite electrode coated with a thin layer of porous ceramic (Figs. 5 (g) and 9).

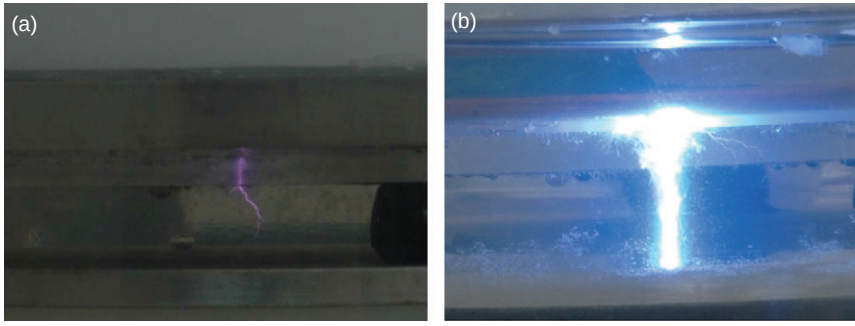

FIG. 6. Images of plasma discharges through a pinhole: (a) pulsed corona; (b) pulsed arc, produced at Drexel Plasma Institute.

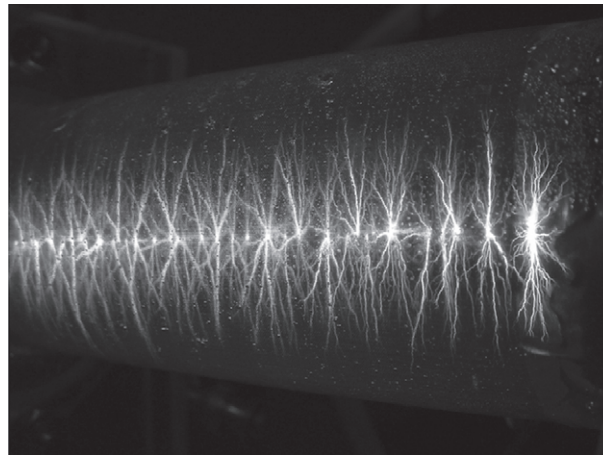

FIG. 7. Time-integrated image of discharges generated using a wire–cylinder geometry in water, where tungsten wire and stainless steel mesh cylinder were used. Chamber dimensions: 44-mm ID, 100-mm length [65].

The geometry using multiple disks shown in Fig. 5 (f) utilized a number of thin circular stainless steel disk electrodes separated by dielectric layers to produce pulsed multichannel discharges in water [66]. The thickness of the disk electrodes was about 80 μm. The diameter of the acryl disk was slightly greater than that of the stainless steel disk so that pre-breakdown current was limited to a small area enclosed by a pair of the acrylic disks and the circumferential edge of the stainless steel disk. Such a confinement of the current allowed water to be heated and evaporated in this small area, promoting the initiation of plasma discharges. The edge of the stainless steel disk was rounded such that the radius of curvature of the edge was about half of the disk thickness d. Hence, the maximum electric field at the edge was estimated to be $E \sim 2U/d$, staying relatively constant with a high-level value comparable to a point-to-plane geometry throughout the discharge process. Furthermore, a large-volume plasma could be produced by stacking multiple disks together. Figure 8 shows photographs of pulsed multichannel discharge arrays generated with two stainless steel disks.

As mentioned previously, Sunka and his coworkers developed a HV composite electrode coated with a thin layer of porous ceramic [28,43]. Such an electrode can be used in a wide variety of geometrical configurations, including wire–cylinder and planar geometry. The role of the ceramic layer is to enhance the electric field on the anode surface by the concentration of the

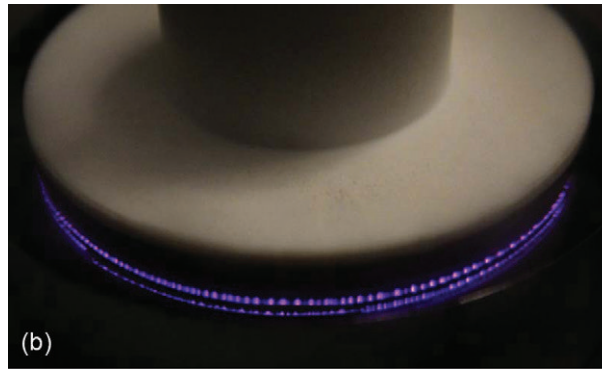

FIG. 8. Pulsed multichannel discharge array in water generated by two stainless steel disk electrodes separated by a dielectric layer [66].

pre-discharge current in small open pores so that a large number of discharge channels could be distributed uniformly and homogeneously on the electrode surface. The composite electrodes can be made in various dimensions, enabling the construction of reactors that can operate at average power in the range of kW. Figure 9 shows images of multichannel pulsed electrical discharges in water generated using porous-ceramic-coated metallic electrodes.

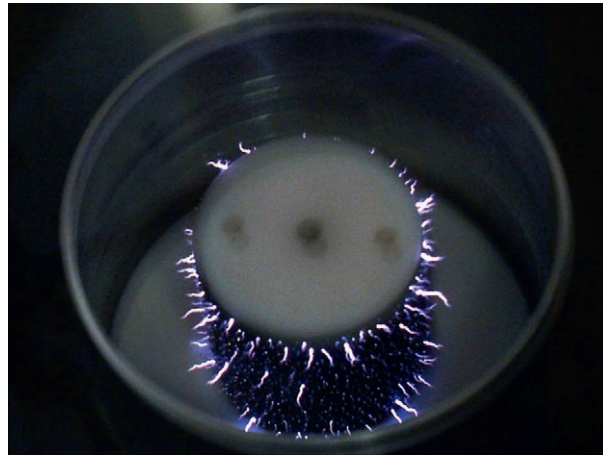

FIG. 9. Multichannel pulsed electrical discharge in water generated using porous-ceramic-coated metallic electrodes [43].

B. Bubble Discharges in Liquid

In engineering applications of plasma discharges in liquids, high-voltage, high-power discharges are often needed for the generation of breakdown in liquids as well as for desired processing. For example, high electrical current and/or high liquid temperature can sterilize water. In this case, the high energy supplied by a power source is first used to evaporate the liquid adjacent to the HV electrode, generating gas bubbles that are subsequently ionized by large electric fields caused by the high voltage. Liquid temperatures in such applications are usually high, at least locally near the breakdown locations, due to the excess power dissipated in the liquid. However, in some circumstances high temperature is not desired. For such applications, a non-thermal plasma system that can generate gas-phase plasmas in contact with liquids is often used. Since the gas-phase plasma can only interact with the liquid through the gas–liquid interface, a maximization of the interface area is usually desired, which can be achieved by using bubble plasmas, i.e., plasmas generated in small bubbles suspended in liquid. Note that the ratio of the area of gas–liquid interface to the total gas volume is inversely proportional to the radius of the gas bubbles. Many different configurations have been used as shown in Fig. 10 (a)–(e).

Similar to direct discharges in water, the most commonly used configuration is the point-to-plane configuration, where the point electrode was made of a small-diameter hollow tube to inject gas into water [67–70]. Different types of gas were used depending on applications. For example, oxygen gas was often used to promote the formation of oxygen radicals.

Alternatively, gas was bubbled between two metal electrodes (Fig. 10 (b)). The discharge occurred between the electrodes by applying the HV, producing OH radical that was detected by a spectroscopic technique [71,72].

Another interesting discharge in liquid was to use a gas channel, inside which two metal electrodes were placed to generate plasma discharge (Fig. 10 (c)) [73,74]. The gas is continuously supplied through the hollow tube, flowing around the electrodes from both sides and exiting from the open ends at the middle of the reactor (see Fig. 10 (c)). The gases coming from the top and bottom merge into one where two point electrodes were closely positioned, forming a stable gas channel between the two metal electrodes. Subsequently, the generated discharge was an arc discharge which was cooled and stabilized by the surrounding water.

Aoki and his coworkers [75] studied radio frequency (RF)-excited discharges in argon bubbles in a dielectric covered metal rod and wire reactor (Fig. 10 (d)). First, bubbles were formed in front of the slot antenna (see black area in the figure) by microwave heating of water where water in an

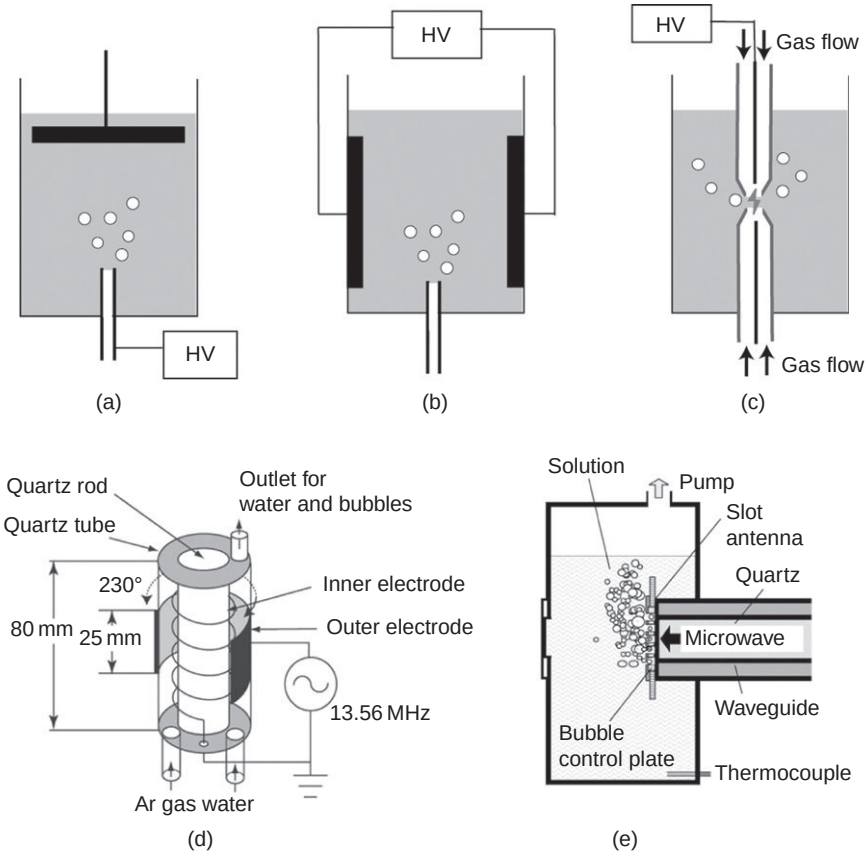

FIG. 10. Schematics of electrode geometries for bubble discharge: (a) point-to-plane; (b) parallel plate; (c) gas channel with liquid wall; (d) RF bubble discharge [75]; (e) microwave bubble discharge [77].

evacuated vessel at a vapor pressure of 5 kPa was evaporated by a slight increase in the temperature above the boiling point (room temperature). In the second step, microwave breakdown took place inside bubbles filled with water vapor. In the third step, the bubbles containing the plasma moved up due to the upward force by buoyancy. After that, new water filled the vacant space in front of the slot antenna. These steps were successively repeated forming a large number of bubble plasmas. Microwave-excited plasma in water with or without externally introduced bubbles was studied by Ishijama (Fig. 10 (e)) [76,77] and Nomura [78–80].

III. Dynamics of Non-Equilibrium Plasma in Liquid Water

A. Experiment Setup

Typically, the electric breakdown of liquids is initiated by the application of high electric field on the electrode, followed by rapid propagation and branching of plasma channels. Usually plasmas are only considered to exist through the ionization of gases, and for all cases described above, the production of plasmas in liquids was believed to first generate bubbles through heating or via cavitation and sustain the plasmas within those bubbles. The question is, is it possible to ionize the liquid without cracking and void formation?

To answer this question, Yang and his coworkers [81] used two different pulsed power systems. The first pulsed power system generated pulses with 27 kV pulse amplitude, 12 ns pulse duration, and 300 ps rise time. The voltage waveform is shown in Fig. 11. The second system generated maximum 112 kV pulses with 150 ps rise time and duration on the half-height about 500 ps. The voltage waveform is shown in Fig. 12. Discharge cell had a point-to-plate geometry with the point electrode diameter of 100 μm. The distance between the point and plate electrodes was 3 mm. The measurements were performed with the help of 4 Picos ICCD camera with a minimum gate time of 200 ps and spectral response of 220–750 nm. Figure 13 shows the schematic diagram of the experiment setup.

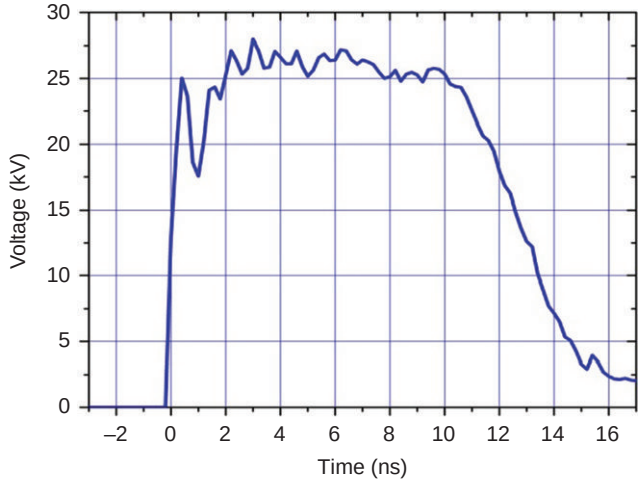

Fig. 11. Voltage waveform produced from the nanosecond-duration power supply used by Yang *et al.* [81].

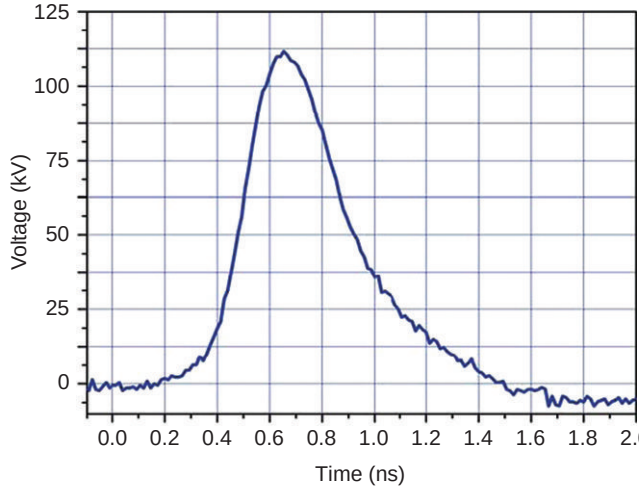

FIG. 12. Voltage waveform produced from the subnanosecond-duration power supply used by Yang *et al.* [81].

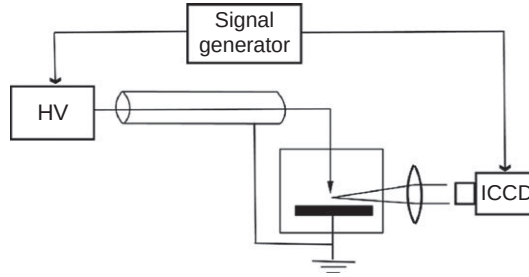

FIG. 13. Schematic diagram of the experiment setup used by Yang *et al.* [81].

B. Results and Discussions

It was found that discharge in liquid water developed in nanosecond time scale. The diameter of the excited region near the tip of the HV electrode was about 1 mm. The discharge demonstrated a typical streamer-type structure, as shown in Fig. 14. No bubbling or void formation was observed. Thus, the discharge observed had a nature completely different from that of the discharges initiated by electrical pulses with a longer rise time [82]. Ishijima [77] reported that the pulses with 40 ns rise time and 18 kV amplitude produced the velocity of discharge propagation about 2.5 km/s during

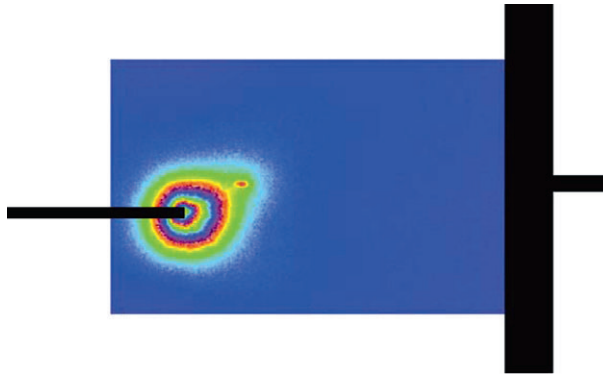

FIG. 14. Image of a nanosecond-duration discharge in water taken at a camera gate of 100 μs by Yang *et al.* [81].

the initial phase of the discharge. Both the shadowgraph and Schlieren images suggested that the branches were of gaseous nature.

In the case of a short rise time, discharge propagation with a velocity of up to 200 km/s was observed during the very initial stage of the discharge, which corresponded to the moment of voltage increase (Fig. 15) [81]. Typical

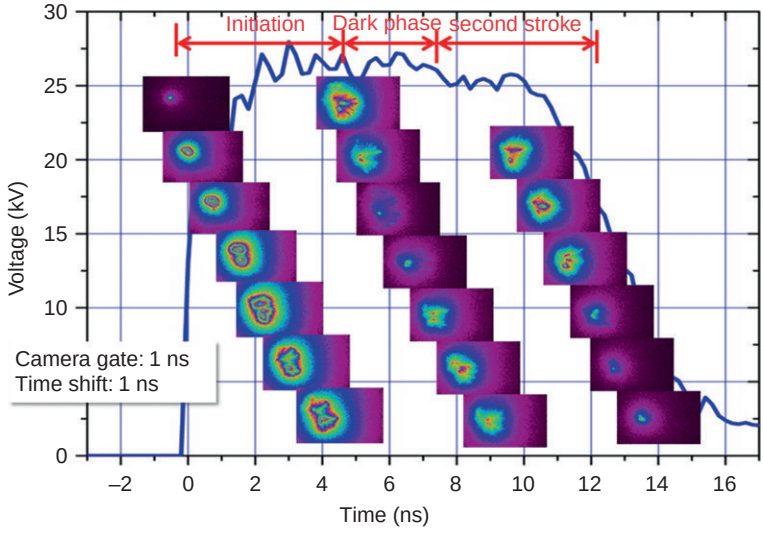

FIG. 15. Images showing the dynamics of nanosecond-duration discharge emission and HV potential on electrode taken at a camera gate of 1 ns [81].

emitting channel diameter was about 50 μm, and propagation length was 0.5–0.6 mm for 27 kV. When voltage reached the maximum, the discharge stopped and the "dark phase" appeared ($t = 6-9$ ns in Fig. 15). During this phase, discharge could not propagate probably because of both space charge formation and electric field decrease. Voltage decrease on the HV electrode led to the reverse stroke formation and second emission region ($t = 10$–14 ns in Fig. 15). This means that the channels lost the conductivity, while the trailing edge of the nanosecond pulse generated a significant electric field and the excitation of the media. This effect can be considered as a proof that there was no void formation or phase transition during the first stage of the discharge.

Discharge development in the case of 110 kV is shown in Fig. 16. It is clear that the plasma channel was generated during voltage increase time, i.e., less than 150 ps. Observed propagation velocity reached 5000 km/s (5 mm/ns) and was almost the same as the typical velocity of streamer propagation in air. Typical channel diameter was estimated as $d = 50$–100 μm, with the radius of curvature at the tip of streamer of about 20 μm. Thus, one could estimate the reduced electric field at the tip of the streamers to be about 200 Td, if equi-potential was assumed between the plasma channel and the electrode. Again, this electric field strength was almost the same as the one at the tip of streamer propagating in air. Figure 17 shows the discharge geometry dependence on the pulsed voltage applied. The length of the channels decreased gradually with increasing voltage, a phenomenon

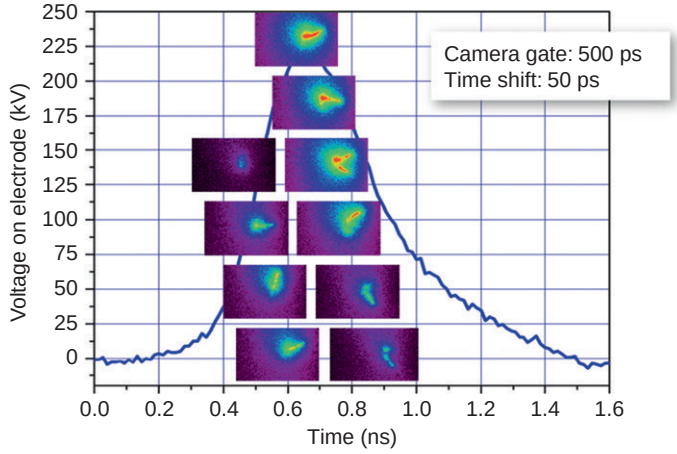

FIG. 16. Images showing the dynamics of nanosecond-duration discharge emission and HV potential on electrode taken at a camera gate of 0.5 ns [81].

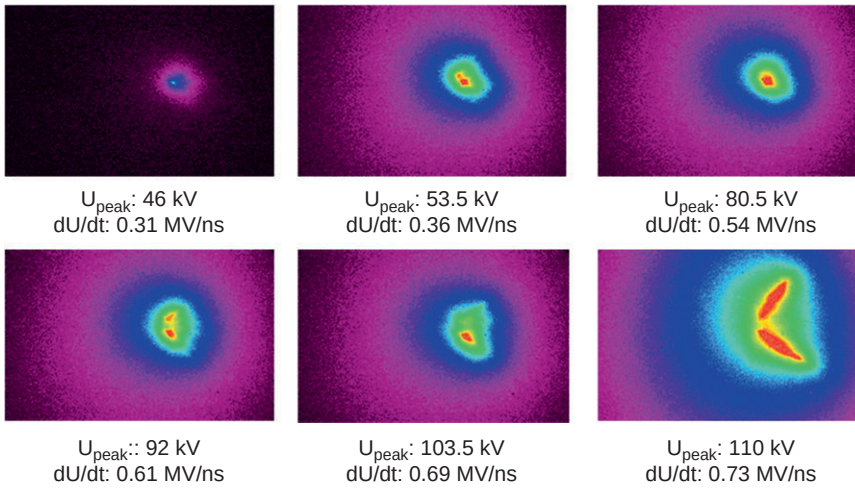

FIG. 17. Subnanosecond-duration discharge development for different voltages [81].

which, for fixed pulsed duration, indicated that the streamer velocity decreased. For voltage below 50 kV, discharges could not start during 500 ps, and subsequently emission was not observed.

In summary, the dynamics of excitation and quenching of non-equilibrium plasma in liquid water were investigated, and the possibility of formation of non-equilibrium plasma in liquid phase was demonstrated. Based on these findings, it was concluded that the mechanism of the streamer development in liquid phase in the picosecond time scale was similar to the ionization wave propagation in gases [81].

IV. Analysis of Microsecond Streamer Propagation

The study of liquid-phase non-equilibrium plasma in liquid water described above opens doors to new potential applications in the areas such as bacterial sterilization, organic compound destruction, and material synthesis. However, for most underwater plasma related applications, the more conventional microsecond-duration pulses could be used. Hence, it is important to get a better understanding of the key physical mechanisms of the breakdown process. In most cases, the electric breakdown of liquids is initiated by the application of a high electric field on the electrode, followed by rapid propagation and branching of streamers. The overall mechanism is complex as it involves different physical processes including field emission,

bubble formation, ionization, heating, vaporization, etc. Thus, it is difficult to include all the effects in a single analytical model. A number of proposed theories for the initiation of the breakdown of dielectric liquids are available in the literature [83–88]. The initial bubble formation could be attributed to pre-existing cavities in water, direct ionization, field assisted emission, or joule heating induced by local field emission. However, the exact mechanism is still unclear.

Despite different mechanisms proposed, most initiation theories lead to the formation of a low-density region where self-sustained electron avalanches take place. Thus, the next question is what the driving force is to sustain and expand the cavity to form complex geometrical structures. Similar to the initiation process, the propagation is complicated because it involves interactions between plasma, gas, and liquid phases of the media. Recent experiments demonstrated the existence of different modes of propagation, where both a primary streamer mode with a slow velocity and a secondary streamer mode with a high velocity were observed [82]. Several models were proposed to correlate electric field with streamer velocity [89–91]. Different effects, including liquid viscosity, trapping of positive and negative carriers in the conducting channel, and local electric charge at streamer head, were taken into account. But again, there is not yet a commonly accepted model.

The objective of the present section is to develop a theoretical framework in order to better understand the propagation of streamers of electric discharge in water subjected to high voltage. The breakdown process is usually characterized by two typical features of breakdown: rapid propagation of discharge streamers and high tendency of branching and formation of random dendritic structures. Therefore, the present study consists of two components: quantitative model for possible mechanisms to produce the driving force needed to sustain and promote the propagation, and stability analysis of a single cylindrical filament with surface charges in an external electric field.

Despite the fact that the mechanism is not fully understood, the propagation of streamers during electric breakdown of water clearly involves the displacement of adjacent liquid along their paths. The process requires a driving force, which is to be discussed in this section. Two quantitative models have been developed: one is based on the electrostatic effect on the streamer–water interface, and the other a more traditional local heating effect. Comparison is made to examine the validities of the two models.

A. Electrostatic Model

A schematic diagram of the present electrostatic model is shown in Fig. 18 (a). A thin needle electrode with a rounded tip is aligned perpendicular to a

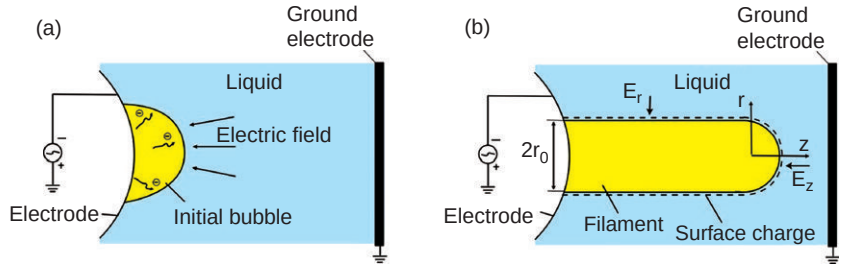

FIG. 18. Initiations of (a) bubble formation and (b) cylindrical filament formation in water [92].

ground plate electrode. High voltage Φ_0 is applied on the needle electrode. According to Kupershtokh, liquids could become phase unstable under a high electric field strength so that gas channels could form along electric field lines [93]. The time required for breakdown ignition in the channels can be estimated as $\tau_b = (k_I\, n_0)^{-1}$, where k_I is the direct ionization rate coefficient and n_0 is the molecule density [18]. Under atmospheric pressure, n_0 is in the order of $10^{19}\,\mathrm{cm}^{-3}$, while k_I is in the order of 10^{-10} to $10^{-9}\,\mathrm{cm}^3/\mathrm{s}$ in the reduced electric field E/n_0 of $10^3\,\mathrm{V\,cm}^2$ [94]. Hence, τ_b is in the order of 0.1–1 ns. For negative discharges, due to the higher momentum transfer collision frequency and thus a low mobility in the liquid phase, electrons tend to deposit on the gas–liquid interface and charge it negatively. For positive discharges, the high mobility of electrons would leave the interface charged positively. Under both circumstances, it is possible that the charged interface would be pushed to displace the liquid under external electric field by electrostatic force.

A simplified calculation can be made to examine whether or not the electrostatic force would be sufficient to overcome the resistance of water at the interface. The pressure due to the surface tension, γ, on a water interface of a spherical bubble with a radius of curvature r, can be approximated by the Young–Laplace equation $p = 2\gamma/r$. With $r \sim 1\,\mu\mathrm{m}$ and $\gamma = 72.8 \times 10^{-4}\,\mathrm{N/m}$, the surface tension pressure is $\sim$15 kPa. The ultimate strength of water of approximately 30 MPa must be exceeded for rupturing the liquid [95]. Considering forces due to charged particles only and ignoring those due to field gradients and material property gradients, the electric force at the interface becomes simply the electrostatic force, L, which is the product of charge density per unit area σ and the electric field E, i.e., $L = e\sigma E$, where e is the charge per electron. For $E = 10^8\,\mathrm{V/cm}$, σ should have a value of $10^{12}\,\mathrm{charges/cm}^2$. For electrons with an average energy of 1 eV, the electron thermal velocity can be estimated as $6 \times 10^7\,\mathrm{cm/s}$. So a modest electron density of $10^{13}\,\mathrm{cm}^{-3}$ will provide the flux necessary to charge the surface to the breaking point within 1 ns. Although these estimations for water rupturing

also neglect both loss mechanisms and the energy requirements to overcome the hydrodynamic resistance, the electrostatic mechanism still seems a likely candidate for streamer propagation, and such forces may dominate at nanosecond time scale.

The growth of a plasma filament is determined by the conservation equations of mass, momentum, and energy. To quantify the breakdown process described above, the equations for the formation and propagation of the plasma-filled filaments are defined as [96]

$$\frac{\partial \rho}{\partial t} + \nabla \cdot (\rho u) = \frac{2\lambda(T)T}{\Delta_v H r_0^2} \tag{1}$$

$$\frac{\partial u}{\partial t} + u \cdot \nabla u + \frac{1}{\rho}\nabla P = 0 \tag{2}$$

$$\frac{\partial}{\partial t}(\rho(Z + u^2)) + \nabla \cdot \left(\rho u\left(Z + \frac{P}{\rho} + \frac{u^2}{2}\right)\right) = \kappa(T)E^2 \tag{3}$$

where t is time; ρ and P are the radial density and pressure inside streamer, respectively; u is the velocity of streamer; T is the temperature; λ is the thermal conductivity; $\Delta_v H$ is the evaporation heat of water; r_0 is the radius of streamer; Z is the internal energy of ionized gas; E is the electric field strength; and κ is the electric conductivity. It is usually difficult to directly solve Eqs. (1)–(3) because of the high non-linearity of the equations.

For simplification, the streamer is assumed to be a cylinder with a hemispherical tip as shown in Fig. 18 (b). The reference frame is fixed on the tip. The radius of the filament is r_0. Although it appears from photographic evidences that the filament is usually of a conical shape, the cylindrical approach is still a good approximation when the length of the filament is much greater than the radius. The electric conductivity κ inside the filament could be described as

$$\kappa = \frac{n_e e^2}{m v_{en}} \tag{4}$$

where m is the mass of electron and v_{en} is the frequency of electron-neutral collisions. Note that v_{en} is proportional to the gas number density and the value of v_{en}/p is usually in the order of $10^9\,s^{-1}Torr^{-1}$ [94]. Sunka measured the broadening of the $H\alpha$ line profile, which is commonly used to characterize the density of plasma, reporting the electron density inside streamers during the initial phase of water breakdown, to be in the order of $10^{18}\,cm^{-3}$ [60].

With water vapor pressure of 20 Torr saturated at the room temperature, the electric conductivity inside the filament can be estimated to be in the order of 10^7 S/m, a value which is comparable to those for metals. So the filament could be regarded as equi-potential with the electrode, and thus could be treated as an extension of the electrode throughout the expansion. The external fluid provides drag force and constant external pressure for the development of the filament. Gravity is neglected here because the body force induced by gravity is much smaller than electric forces.

The electric field outside a slender jet can be described as if it were due to an effective linear charge density (incorporating effects of both free charge and polarization charge) of charge density σ on the surface. Since the charge density in liquid can be ignored comparing with that on the filament surface, one can have the following equation for the space outside the filament by applying Laplace equation in the radial direction:

$$\frac{1}{r}\frac{\partial}{\partial r}\left(r\frac{\partial \Phi}{\partial r}\right) = 0 \tag{5}$$

with boundary condition $\Phi|_{r=r_0} = \Phi_0$ and $\Phi|_{r=R} = 0$. R is the distance between anode and cathode. Since the filament could be regarded as an extension of the electrode, R decreases as the streamer propagates through the gap.

Solving the above equation with an assumption of negative discharge, the radial electric field E_r and local surface charge density σ_r can be written as

$$E_r = \frac{\partial \Phi}{\partial r} = -\frac{\Phi_0}{r_0 \ln(R/r_0)} \tag{6}$$

$$\sigma_r = \varepsilon E_{r_0} = -\varepsilon_r \varepsilon_0 \frac{\Phi_0}{r_0 \ln(R/r_0)} \tag{7}$$

There is no analytical solution for the electric field at the hemispherical tip of the filament. A frequently used approximation is $E_z \approx \phi_0/r_0$. Here the equation for the electric field at the tip of a needle in a needle-to-plane geometry developed by Lama and Gallo was used [97]:

$$E_z = -\frac{2\Phi_0}{r_0 \ln(4R/r_0)} \tag{8}$$

Similarly, the local charge density at the tip is

$$\sigma_z = \varepsilon E_z = -\varepsilon_r \varepsilon_0 \frac{2\Phi_0}{r_0 \ln(4R/r_0)} \tag{9}$$

From Eqs. (6)–(9), one can conclude that the radial direction electrostatic pressure $E\sigma$ exerted on the side wall of the streamer is weaker than the axial direction electrostatic pressure on the tip. Note that both electrostatic pressures are roughly inversely proportional to r_0^2, meaning that at the initial stage of the filament growth when r_0 is small, the electrostatic forces on both directions are strong and the filament will grow both axially and radially. A direct consequence of both the axial and radial expansions of the streamer channel is the launching of compression waves into adjacent liquids [82]. At some critical point, the electrostatic force reaches a balance with hydrodynamic resistance acting on the surface in the radial direction first, while the filament continues to grow in the axial direction.

Experimentally recorded propagation speeds of the filaments varied depending on the measurement techniques, ranging from a few km/s to 100 km/s [82,98,99]. In spite of the discrepancy observed by different groups, the propagation was clearly in the supersonic regime. Thus, the formation of shockwaves should be taken into consideration (see Fig. 19). The drag force on the tip of the streamer, which is a stagnation point, equals the force produced by the total hydrodynamic pressure:

$$P_{\mathrm{hd}} = P_1\left(\frac{2\alpha}{\alpha+1}M_1^2 - \frac{\alpha-1}{\alpha+1}\right) + \frac{1}{2}\rho(CM_2)^2 \tag{10}$$

where P_1 is ambient pressure; $P_1((2\alpha/\alpha+1)M_1^2 - (\alpha-1/\alpha+1))$ is the pressure behind shock front; α is the specific heat ratio of water; M_1 is the Mach number of streamer; M_2 is the Mach number after the shock front; and C is

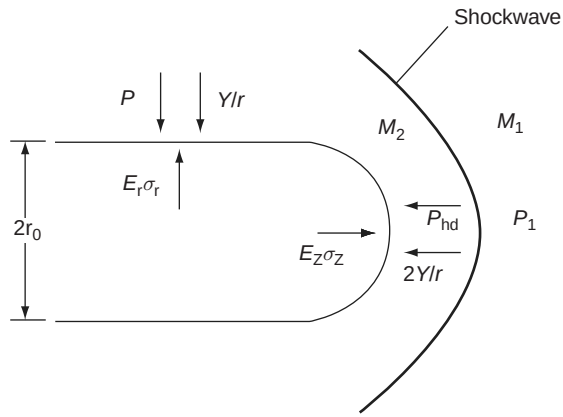

FIG. 19. Force balance for the electrostatic model proposed by Yang *et al.* [92].

the speed of sound in liquid. The relationship between M_1 and M_2 can be written as [100]

$$M_2^2 = \frac{(\alpha-1)M_1^2+2}{2\alpha M_1^2+1-\alpha} \tag{11}$$

Equating the hydrodynamic pressure to the sum of the electrostatic pressure and the pressure produced by surface tension at the tip can give the following equation for streamer propagation:

$$4\varepsilon_r\varepsilon_0\frac{\Phi_0^2}{r_0^2\ln^2(4R/r_0)} = P_1\left(\frac{2\alpha}{\alpha+1}M_1^2-\frac{\alpha-1}{\alpha+1}\right)+\frac{1}{2}\rho(CM_2)^2+\frac{2\gamma}{r_0} \tag{12}$$

The balance between the electrostatic force and the force produced by the total hydrodynamic pressure in the radial direction can be given as

$$\varepsilon_r\varepsilon_0\frac{\Phi_0^2}{r_0^2\ln^2(R/r_0)} = P_1+\frac{1}{2}\rho(CM_2)^2+\frac{\gamma}{r_0} \tag{13}$$

Note that there are three unknowns, M_1, M_2, and r_0, in the above equations. So it is possible to solve Eqs. (11)–(13) simultaneously, when the applied voltage Φ_0 and the inter-electrode distance R are specified.

To demonstrate the validity of the present model, the filament radius predicted by the model is shown in Fig. 20. For a typical inter-electrode

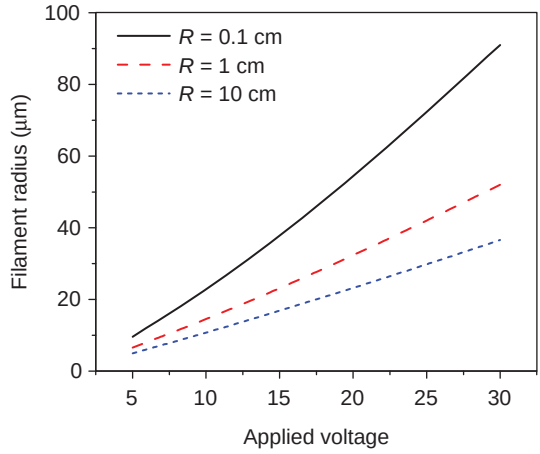

FIG. 20. Variations of filament radius as a function of applied voltage and inter-electrode distance [92].

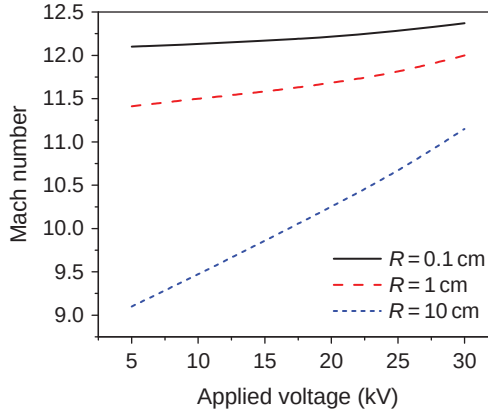

FIG. 21. Variations of Mach number of streamer as a function of applied voltage and inter-electrode distance [92].

distance of 1 cm, the filament radius increases from 3 μm to 50 μm as the applied voltage rises from 5 kV to 30 kV. The value is comparable to typical experimental values. For example, An reported that the light emission from the discharge was restricted to a channel of 100 μm diameter, indicating the interaction of charged particles in the region [82].

Figure 21 shows the filament propagation speed as a function of Φ_0 and R. The calculated propagation speed from the present model is around 15 km/s, which is higher than the primary streamer speed but lower than the secondary streamer speed reported by An and his coworkers [82]. The Mach number increases moderately with the applied voltage, a phenomenon which is understandable from the point of view of energy conservation. The streamer propagation velocity is relatively independent of the inter-electrode distance. For an applied voltage of 30 kV, the Mach number increases from 11.2 to 12.3 when inter-electrode distance decreased from 10 cm to 0.1 cm. This is consistent with the known property of negative streamers as the previous experiment showed that for a given voltage the propagation velocity was relatively constant as the streamer crossed the gap, and while it increased as the streamer approached the plane electrode [91]. This phenomenon can be understood by Eq. (6): the inter-electrode distance R is decreased with the propagation of the streamers; as a result the electric field at the tip of the streamer was increased, leading to a higher propagation speed. However, the amount of the increase in the electric field will not be significant because of the natural logarithm in the equation.

B. Thermal Mechanism

In the electrostatic model described above, it is assumed that the translational temperature inside the streamer was low, and the electrostatic force is the only driving force for the growth of the filament. The assumption is valid only at the initial stage of the filament development, as the temperature will keep rising as the molecules gain more energy through electron-neutral collisions. The heating time, τ, is approximately $\tau = \tau_{en} + \tau_{vt}$, where τ_{en} is the time for electron-neutral excitation and τ_{vt} is the time for vibrational-translational (v-t) relaxation. For electron-neutral excitation, $\tau_{en} = 1/\nu_{en} = 1/(n_e \cdot k_{en})$, where ν_{en} is the electron-neutral non-elastic collision frequency, n_e is the electron density, and k_{en} is the rate constant for electron-neutral collisions. k_{en} can be expressed as $k_{en} = \sigma_{en} v_{te}$, where σ_{en} is the cross section for vibrational excitation of H_2O molecules by electron impact and v_{te} is the electron thermal velocity.

For electrons with an average energy of 1 eV, the cross section for vibrational excitation is about $\sigma = 10^{-17}\,cm^2$ [101]. k_{en} is thus about $10^{-8}\,cm^3/s$ as is typical ($v_{te} = 6 \times 10^7\,cm/s$). Spectroscopic measurements indicated that the stark broadening of $H\alpha$ line corresponded to an electron density of about $10^{18}\,cm^{-3}$ at a quasi-equilibrium state [60]. Thus, the typical electron-neutral excitation time can be estimated to be in the order of a few nanoseconds. For the v-t relaxation, $\tau_{vt} = 1/(n_v \cdot k_{vt})$, where n_v is the density of vibrational excited molecules and k_{vt} is the v-t relaxation rate coefficient. For water molecules at the room temperature, k_{vt} is about $3 \times 10^{-12}\,cm^3/s$ [94]. Assuming that n_v is in the same order with electron density, τ_{vt} could be estimated to be in the order of several hundred nanoseconds, suggesting that heating can take place inside the filaments under sub-microsecond time scale due to the energy transfer from the electrons to the translational energy of the water molecules, and furthermore the propagation of the streamers can be caused by the continuous evaporation of water molecules at the tip. Here the energy dissipation is not considered, and the actual heating time might be longer, but still the local heating mechanism under the sub-microsecond time regime seems possible.

To quantify the process described above, it is assumed that a small cylindrical portion of water (i.e., see shaded portion in Fig. 22) evaporates at the tip of the streamer during time Δt so that the length of the streamer grows from L to $L + \delta L$, as shown in Fig. 22. The diameter of the evaporated water cylinder is assumed to be $2r_e$. There is no definitive value for pressure P_e inside the small vaporized portion given the extremely high temperature. However, P_e can be estimated to be in the order of 1000 atm because of the density difference between liquid water and vapor. Such a high pressure could provide the driving force needed for the growth of the filament.

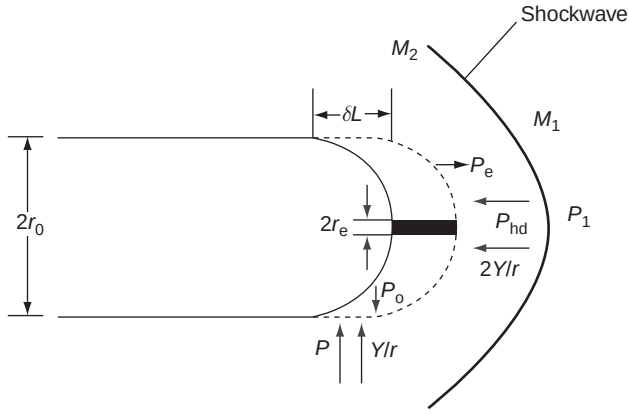

FIG. 22. Force balance for the thermal model proposed by Yang *et al.* [92].

As in the previous section, one can get the force balance along the axial direction at the tip of the filament assuming a steady state condition as

$$P_1\left(\frac{2k}{k+1}M_1^2-\frac{k-1}{k+1}\right)+\frac{1}{2}\rho(CM_2)^2+\frac{2\gamma}{r_e}=P_e \tag{14}$$

The energy required for the evaporation of water can be calculated as

$$E_e=\rho V_e(c_p\Delta\ T+\Delta_v H) \tag{15}$$

where ρ and c_p are the density and specific heat of water, respectively, and V_e is the volume of evaporated water. V_e can be written as

$$V_e=\pi r_e^2\cdot\delta L \tag{16}$$

After evaporation, the overheated and over-pressured water vapor will expand radially, while satisfying the force balance along the axial direction, until it reaches an equilibrium with the outside hydrodynamic pressure. The process can be regarded as adiabatic under a sub-microsecond time scale, and thus one can have the following equations:

$$P_eV_e^{\alpha_s}=P_0V_0^{\alpha_s} \tag{17}$$

$$\frac{P_0}{P_e}=\left[\frac{\varepsilon_r\varepsilon_0\Phi_0^2}{\rho r_0(c_p\Delta T+\Delta H_{l-g})\ln(R/r_0)}\right]^{\alpha_s} \tag{18}$$

where P_0 and V_0 are the pressure and volume, respectively, of the water vapor after the expansion; r_0 is the radius of the filament after expansion; and α_s is the specific heat ratio of the water vapor. The force produced by P_0 should be in balance with the forces created by both surface tension and total environmental hydrodynamic pressure as given below:

$$P_0 = P_1 + \frac{1}{2}\rho(CM_2)^2 + \frac{\lambda}{r_0} \tag{19}$$

Another set of equations can be obtained through the consideration of energy conservation. The energy required to vaporize water is the electric energy provided by the power supply. If the entire filament is viewed as a capacitor with capacitance C, the required energy can be calculated as

$$E = \frac{C\Phi_0^2}{2} \tag{20}$$

The capacitance of the cylindrical filament is

$$C = \frac{2\pi\varepsilon\varepsilon_0 L}{\ln(R/r_0)} \tag{21}$$

So the energy change required to extend the length by δL becomes

$$\delta E = \frac{\pi\varepsilon\varepsilon_0\delta L\Phi_0^2}{\ln(R/r_0)} \tag{22}$$

By equating δE to E_s, one has

$$r_e = \sqrt{\frac{\varepsilon\varepsilon_0\Phi_0^2}{\rho(c_p\Delta T + \Delta H_{l-g})\ln(R/r_0)}} \tag{23}$$

Assuming $\alpha \approx 1$ due to the low compressibility of water, and rearranging Eqs. (11), (14), (18), (19), and (23) to eliminate M_2, r_e, and P_g, one can get a set of equations about M_1 and r_0 as follows:

$$P_1M_1^2 + \frac{\rho C^2}{2M_1^2} - P_e + 2\gamma\sqrt{\frac{\rho(c_p\Delta T + \Delta H_{l-g})\ln(R/r_0)}{\varepsilon_r\varepsilon_0 r_0\Phi_0^2}} = 0 \tag{24}$$

$$P_e\left[\frac{\varepsilon_r\varepsilon_0\Phi_0^2}{\rho r_0(c_p\Delta T + \Delta H_{l-g})\ln(R/r_0)}\right]^{k_s} - P_1 - \frac{\rho C^2}{2M_1^2} - \gamma\sqrt{\frac{\rho(c_p\Delta T + \Delta H_{l-g})\ln(R/r_0)}{\varepsilon_r\varepsilon_0 r_0\Phi_0^2}} = 0 \tag{25}$$

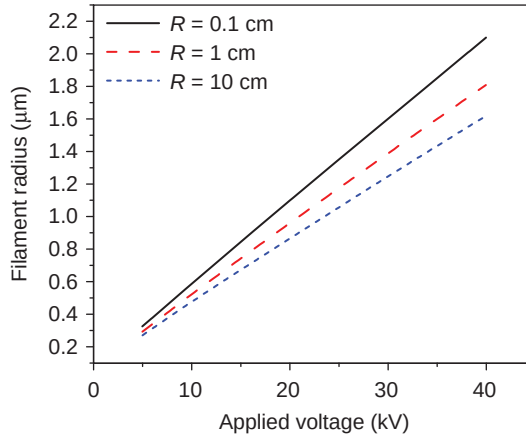

FIG. 23. Variations of filament radius as a function of applied voltage and inter-electrode distance [92].

For water vapor, α_s can be assumed to be 1.3 [102]. For high-temperature underwater discharges, the translational plasma temperature was measured to be between 4000 and 6500 K [103]. An average value of 5000 K is used for ΔT in the present study. Figure 23 shows the Mach number of filament propagation, M_1, as a function of Φ_0 and R. The propagation velocity is about 50 km/s, which is higher than the secondary streamer velocity of 25 km/s reported by An [82], but lower than the value of 200 km/s reported by Woodworth and his coworkers [99]. The discrepancy in the two measurements probably comes from the different techniques used for the velocity measurements. The value of M_1 remains constant for various values of Φ_0 and R, indicating that the propagation velocity of the streamers is independent of either the applied voltage or inter-electrode distance. Similar phenomenon was observed previously [82,99], where the propagation velocity of secondary streamers was constant over a wide voltage range. Figure 24 shows the filament radius as a function of Φ_0 and R. The radius increases slightly as the streamers approach the other electrode, while it decreases almost linearly as the applied voltage drops. The absolute value of r_0 is about one order smaller than that obtained from the electrostatic model. This can be understood if one considers the energy requirements for the two mechanisms. For the evaporation of water, the energy needed to break the hydrogen bonds between water molecules should be much greater than that required to displace the same volume of water.

The different models based on the electrostatic force and evaporation of water give different results of the streamer propagation speed and filament radius. The electrostatic model shows streamers with a larger radius and a

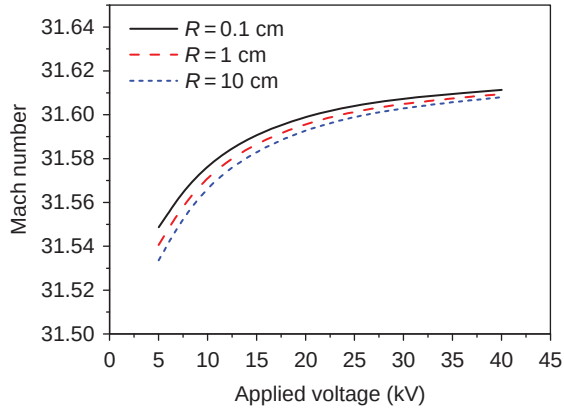

FIG. 24. Variations of the Mach number of streamer as a function of applied voltage and inter-electrode distance [92].

lower Mach number, while the thermal model demonstrates that the streamers can move much faster but are thinner than those determined from the electrostatic model. The different findings from the two models suggest that different mechanisms might be associated with the different modes of the streamer propagation. At the initial primary streamer mode before any significant heat is generated, the electrostatic force might have played a major role. The appearance of the secondary streamer requires more time, during which the electron energy can be transferred to translational energy of water molecules and subsequently evaporation becomes the dominant force to drive the filament to move forward. The transition time between the primary and secondary streamers is in the order of 100 ns [82], a value which is in accordance with the heating time as estimated above.

C. Stability Analysis

The breakdown process is usually characterized by two features: an initial development of thin discharge channels and a subsequent branching of these channels into complicated "bush-like" patterns. Apparently, the branching process is associated with the instability of the filament. In this section, the linear stability analysis of axisymmetric perturbation of a filament surface with a certain electric charge density is presented. As long as the wavelength of the perturbation is much smaller than the length of the filament, the stability characteristics can be approximated by considering perturbations to a charged cylinder of constant radius as shown in Fig. 25. H is the depth of wave influence, and u is the velocity of liquid relative to the disturbance.

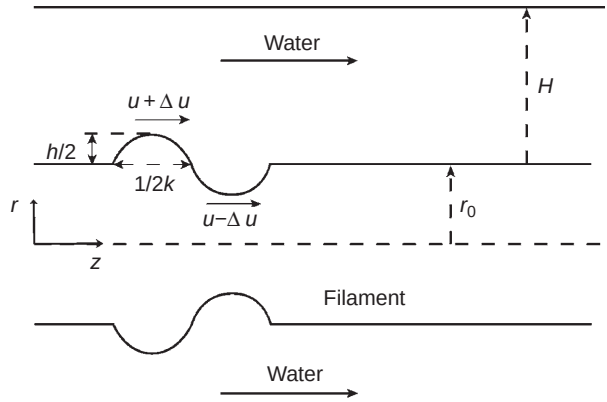

FIG. 25. Schematic diagram of disturbance at the surface of filament [92].

The peak-to-peak amplitude and wave number of the disturbance are h and k, respectively. Then the surface of the perturbation can be represented by the following equation:

$$r = r_0 + \frac{h}{2}\exp(ikz + \omega t) \tag{26}$$

where ω is the oscillation frequency of the instability. To analyze the linear stability, the disturbance of the local electrostatic force, surface tension, and hydrodynamic pressure are considered following a geometrical perturbation. Generally, the surface tension tends to minimize the surface area and subsequently stabilizes the disturbance, while the local enhancement of the electrostatic force tends to push the disturbance to grow. In the reference frame that moves together with the tip of filament, the effects of these three forces are considered separately for the pressure balance between the crest and trough along the stream line (see Fig. 19).

1. *Electrostatic Pressure*

According to Eqs. (6)–(9), the electrostatic pressure which can be described by the product of electric field and surface charge density is proportional to the square of the local curvature of the interface, which is different at the crest and trough of the perturbation. Thus, the electrostatic pressures at the crest and trough, $P_{\mathrm{E,c}}$ and $P_{\mathrm{E,t}}$ become

$$P_{\mathrm{E,c}} = \varepsilon_r \varepsilon_0 \Phi_0^2 \frac{\chi_c^2}{4} \tag{27}$$

$$P_{\mathrm{E,t}} = \varepsilon_r \varepsilon_0 \Phi_0^2 \frac{\chi_{\mathrm{t}}^2}{4} \tag{28}$$

where ε_r is the relative permittivity of water and χ_{c} and χ_{t} are the mean curvatures at the crest and trough, respectively. The expression for the mean curvature can be written as [104]

$$\chi = \frac{1}{r\sqrt{1+(\partial_z r)^2}} - \frac{\partial_z(\partial_z r)}{(1+(\partial_z r)^2)^{3/2}} = \frac{1}{r} - \partial_z(\partial_z r) \tag{29}$$

Substituting Eq. (26) into Eq. (29), one can get expressions for M_{c} and M_{t}:

$$\chi_{\mathrm{c}} = \frac{1}{r_0 + h/2} + \frac{h}{2}k^2 \tag{30}$$

$$\chi_{\mathrm{t}} = \frac{1}{r_0 + h/2} - \frac{h}{2}k^2 \tag{31}$$

Subsequently, $P_{\mathrm{E,c}}$ and $P_{\mathrm{E,t}}$ can be written as

$$P_{\mathrm{E,c}} = \varepsilon_r \varepsilon_0 \Phi_0^2 \frac{\chi_{\mathrm{c}}^2}{4} = \varepsilon_r \varepsilon_0 \Phi_0^2 \left(\frac{1}{(2r_0 + h)^2} + \frac{hk^2}{2(2r_0 + h)} \right) \tag{32}$$

$$P_{\mathrm{E,t}} = \varepsilon_r \varepsilon_0 \Phi_0^2 \frac{\chi_{\mathrm{c}}^2}{4} = \varepsilon_r \varepsilon_0 \Phi_0^2 \left(\frac{1}{(2r_0 - h)^2} - \frac{hk^2}{2(2r_0 - h)} \right) \tag{33}$$

Thus, the electrostatic pressure difference between the crest and trough becomes

$$\Delta P_{\mathrm{E}} = P_{\mathrm{E,c}} - P_{\mathrm{E,t}} = -\frac{\varepsilon_r \varepsilon_0 \Phi_0^2 h}{2r_0^3} + \frac{\varepsilon_r \varepsilon_0 \Phi_0^2 h k^2}{2r_0} \tag{34}$$

2. *Surface Tension*

The pressures due to the surface tension across the interface at the crest and trough can be written as

$$P_{\mathrm{T,c}} = \gamma \chi_{\mathrm{c}} = \gamma \left(\frac{1}{r_0 + h/2} + \frac{h}{2}k^2 \right) \tag{35}$$

$$P_{\mathrm{T,t}} = \gamma\chi_{\mathrm{t}} = \gamma\left(\frac{1}{r_0 - h/2} - \frac{h}{2}k^2\right) \tag{36}$$

Thus the pressure difference due to surface tension between the cress and trough becomes

$$\Delta P_{\mathrm{T}} = P_{\mathrm{T,c}} - P_{\mathrm{T,t}} = -\frac{\gamma h}{r_0^2 - h^2/4} + \gamma h k^2 \tag{37}$$

Since $r_0 >> h$, the above equation can be simplified as

$$\Delta P_{\mathrm{T}} = -\frac{\gamma h}{r_0^2} + \gamma h k^2 \tag{38}$$

3. Hydrodynamic Pressure

When there is a disturbance on the interface of the filament, the flow speed of liquid will be perturbed in the depth of wave influence, inducing a hydrodynamic pressure difference ΔP_{H} between the crest and trough:

$$\Delta P_{\mathrm{HD}} = \frac{1}{2}\rho\left(u + \frac{\Delta u}{2}\right)^2 - \frac{1}{2}\rho\left(u - \frac{\Delta u}{2}\right)^2 = \rho u \Delta u \tag{39}$$

where $\Delta u/2$ is the perturbation in the flow speed caused by the shape of the wave. The dynamic pressure is related to the flow speed through Bernoulli's equation. The pressure difference from the electrostatic force and dynamic effect of the flow has the sign opposite to that of the pressure difference due to the surface tension. For a balance between two kinds of oppositely directed pressure differences, one has

$$\rho u \Delta u + \frac{\gamma h}{r_0^2} - \gamma h k^2 - \frac{\varepsilon_r \varepsilon_0 \Phi_0^2 h}{2r_0^3} + \frac{\varepsilon_r \varepsilon_0 \Phi_0^2 h k^2}{2r_0} = 0 \tag{40}$$

In order to solve Eq. (40), the perturbed flow speed Δu must be expressed in terms of experimentally measurable quantities. The following derivation is inspired by Kenyon [105].

Assuming that the perturbed flow speed is constant over the depth of wave influence, the mass conservation equation through vertical cross sections between the crest and trough becomes

$$\left(u + \frac{\Delta u}{2}\right)\left(H - \frac{h}{2}\right) = \left(u - \frac{\Delta u}{2}\right)\left(H + \frac{h}{2}\right) \tag{41}$$

where H is the depth of wave influence. The above equation can be reduced to

$$u \cdot h = \Delta u \cdot H \tag{42}$$

The theoretical expression for H was given by Kenyon [106] as

$$H = \frac{1}{2\pi k} \tag{43}$$

Using Eqs. (42) and (43) to eliminate H and Δu, Eq. (40) becomes

$$\rho\omega^2 = k\left(\gamma k^2 + \frac{\varepsilon_r\varepsilon_0\Phi_0^2}{2r_0^3} - \frac{\gamma}{r_0^2} - \frac{\varepsilon_r\varepsilon_0\Phi_0^2 k^2}{2r_0}\right) \tag{44}$$

Since this is a quadratic equation, there will be two different branches of the dispersion relation, and an instability occurs if $\mathrm{Re}(\omega) > 0$. The first thing to note in Eq. (44) is that when the applied voltage Φ_0 is equal to zero and the surface is flat, in other words, when the radius of the filament r_0 goes to infinity, the above equation reduces to $\rho u^2 = \gamma k$, which is the equation for the classic two-dimensional Rayleigh instability.

Figure 26 shows the instability growth rate ω at a low applied voltage, where the process is in Rayleigh mode. The dashed line represents the classic Rayleigh instability for $\Phi_0 = 0$ and $r_0 \to \infty$. For $\Phi_0 \neq 0$ and r_0 is finite, instability only happens at high wave numbers. When the voltage increases under this mode, the growth rate is decreased until fully suppressed at a

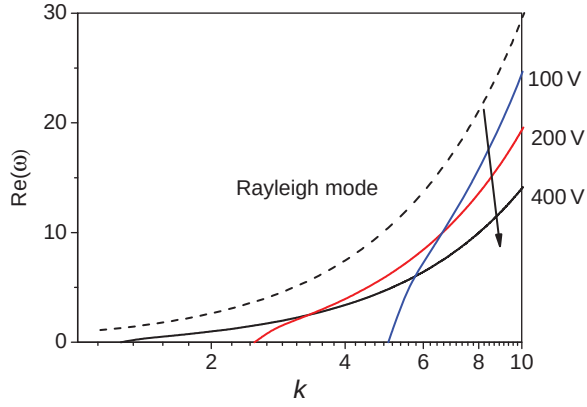

FIG. 26. Instability growth rate ω at low applied voltages. k and ω are nondimensionalized using streamer radius r_0 and time scale $t = (\rho r_0^3/\gamma)^{1/2}$ [92].

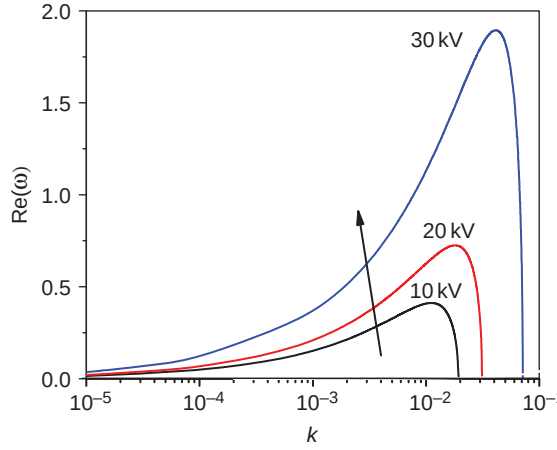

FIG. 27. Instability growth rate ω at high applied voltages. k and ω are nondimensionalized as in Fig. 26 [92].

certain critical value. The physical explanation to this can be as follows: the Rayleigh instability occurs due to surface tension, a phenomenon which always acts to break a cylindrical jet into a stream of droplets; on the other hand, the electrostatic force, which is proportional to the square of the applied voltage, always acts on the opposite direction of the surface tension. When the applied voltage increases, the Rayleigh instability will be suppressed when the two forces are balanced.

As the voltage continues to increase, the instability is dictated by the electrostatic mode, where the electrostatic force exceeds the force created by the surface tension and becomes the dominant force. Figure 27 shows the instability growth rate ω at a high voltage. Both the growth rate and the range of wave number increase as the voltage rises. The physics of this mode is a consequence of the interaction of the electric field with the surface charge on the interface; surface tension is a parameter of less importance for this mode. The mechanism for the instability is that a perturbation in the radius of the filament induces a perturbation in the surface charge density and therefore a perturbation in the electrostatic pressure. At a high voltage, the perturbation is amplified by the fact that the electrostatic pressure P_E is proportional to Φ^2, causing the instability. In contrast to the Rayleigh mode, the instability in the electrostatic mode is unavoidable at low wave numbers (long wavelength). This may explain why the filament always tends to branch into bush-like structures.

In conclusion, the electric breakdown of water involves both the generation and propagation of low-density channels through liquid. Different

physical processes and interactions between different phases of the media should contribute to the complexity of the problem. In the current section, different modes of the streamer propagation have been considered into simplified steps, with each step characterized by a driving force and the corresponding hydrodynamic drag. The effects of the electrostatic force and local heating on the streamer propagation have been analyzed using simplified assumptions. It is shown that both of them are dominant for the streamer propagation, but at different time scales. Furthermore, a linear instability analysis has been performed on a charged cylindrical streamer in an external electric field to understand the bush-like growth pattern of breakdown in liquid. It is shown that the stability may be caused by the competition between perturbations in the electrostatic pressure and surface tension caused by the disturbance of the streamer geometry. With increasing applied voltage, the electrostatic instability is found to grow whereas the classic Rayleigh instability is found to be suppressed.

V. Application of Spark Discharge for Scale Removal on Filter Membranes

In the next few sections, new developments of underwater plasma treatment at Drexel Plasma Institute for various applications will be reported. First, the application of spark discharge for scale removal on filter membranes is studied. In modern wastewater treatment, filters are routinely used for removing unwanted particles from water. Conventionally, microfiltration methods are used to remove suspended particles from water. Whenever a filter is used in a water system, the pressure drop across the filter gradually increases with time and/or the flow rate gradually decreases with time. This reduced performance of a filter is due to the accumulation of impurities on the filter surface, and the clogged area becomes sites for bacterial growth for further reducing the opening in the filter surface, increasing the pumping cost. Therefore, in order to continuously remove suspended particles from water, the filter must be replaced frequently, a process which is prohibitively expensive in most industrial water applications. To overcome the drawbacks of frequent filter replacement, self-cleaning filters are commonly used in industry. Although there are a number of self-cleaning filter technologies available on the market, most self-cleaning filters use a complicated backwash method, which reverses the direction of flow during the cleaning phase. Furthermore, the water used in the backwash must be clean filtered water, which reduces the filter capacity. Aforementioned drawbacks of the conventional filter technologies motivated the authors to develop a new self-cleaning filter using spark-generated shockwaves.

As illustrated in previous sections, strong shockwaves can be formed during the process of pulsed arc or spark discharge. The energy transferred to the acoustic energy can be calculated as [107]

$$E_{\text{acoustic}} = \frac{4\pi r^2}{\rho_0 C_0} \int (P(r,t) - P_0)dt \tag{45}$$

where r is the distance from the spark source to the pressure transducer; ρ_0 is the density of water; C_0 is the speed of sound in water; and P_0 is the ambient pressure. One can conclude that the pressure created by the spark discharge is much higher than ambient pressure at positions close to the source. Traditionally, the high-pressure shockwave is studied for HV insulation and rock fragmentation, while recently it has found more applications in other areas including extracorporeal lithotripsy and metal recovery from slag waste [108–110].

In order to validate the concept to use spark discharge for filter cleaning, an experimental setup was built where discharges could be produced in water, and pressure drop across a filter surface was measured over time at various spark frequencies and flow conditions. It was hypothesized that the energy deposited by the spark shockwave onto water–filter interface was enough to remove the contaminants having Van der Waals bonds with filter surface. The objective of the study was to examine the feasibility of a self-cleaning water filtration concept using spark discharges in water.

A. Experiment Setup

An experimental system was designed to test the effectiveness of the self-cleaning filter concept using spark discharges in water under various flow conditions. The system consisted of two parts: a flow loop with a filter to simulate a cooling-tower water system and a pulsed power system to produce spark discharges in water. A schematic diagram of the test loop is shown in Fig. 28. To simulate deposits on filter surfaces, artificially hardened water with hardness of 1000 mg/L of $CaCO_3$ was made by adding calcium chloride ($CaCl_2$) and sodium carbonate (Na_2CO_3) in proper proportions to tap water. To minimize the abrasion of mechanical parts by $CaCO_3$ particles, a peristaltic pump (FPU259, Omega Inc., Stamford, CT) was used to circulate the hard water in the test loop. The flow rate in the test system was varied from 50 mL/min to 400 mL/min using a valve in a flow meter. In all experiments 5% of the untreated water was bypassed for the purpose of the creation of the tangential flow along the filter surface. It is of note that some tangential flow was believed to be necessary for the successful removal of the unwanted deposits from the filter surface using the spark-generated shockwaves.

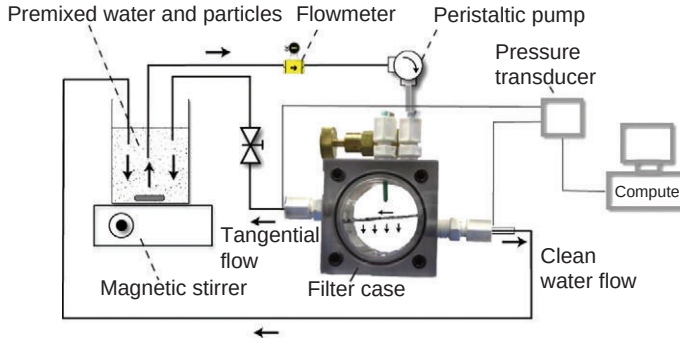

FIG. 28. Schematic diagram of the testing loop used by Yang *et al.* [111].

Usually filters have to be cleaned or replaced when excessive amounts of foreign materials are accumulated on the filter surface. The decision to clean or replace a filter is often based on the changes in flow rate or pressure drop across the filter. When the pressure drop increases to a pre-determined value or the flow rate reduces to a pre-determined value, the filter is cleaned or replaced. In the present experiment, the pressure drop across the filter with a filter surface area of 25 cm^2 was measured using a differential pressure transducer (PX137-015AV, Omega Inc., Stamford, CT). The analog signal from the pressure transducer was collected and digitized by a data acquisition system (DI-148U, Dataq Instruments, Akron, OH) and processed by a computer.

A pulsed power system in the present study consisted of three components: a high-voltage power supply with a capacitive energy storage, a spark-gap based switch, and a discharge source immersed in water. A schematic diagram of the pulsed power system is shown in Fig. 29. The HV pulses were provided by a pulsed power supply. The power supply charged an 8.5-nF capacitor bank and the pulse was triggered by an air-filled spark-gap switch. Arc discharge was initiated in the switch from the overvoltage produced by the power supply and capacitor, and the spark gap made use of a very low impedance of arc to transfer high-power energy within nanoseconds. Power deposited into water was analyzed by measuring the current passing through the discharge gap and the voltage drop in the gap. For measurements of the current, a magnetic-core Pearson current probe was utilized (1 V/Amp +1/–0% sensitivity, 10 ns usable rise time, and 35 MHz bandwidth). Voltage was measured using a wide bandwidth 1:1000 voltage probe (PVM-4, North Star Research Corp., Albuquerque, NM). Signals from the current and voltage probes were acquired and recorded by a digital phosphor oscilloscope (DPS) (500 MHz bandwidth, 5×10^9 samples/s, TDS5052B, Tektronix, Beaverton, OR). Acquired data were then integrated using a customized MATLAB code.

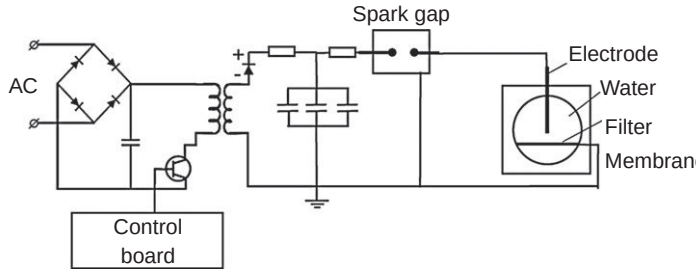

FIG. 29. Schematic diagram of a pulsed power system used in the study by Yang *et al.* [111].

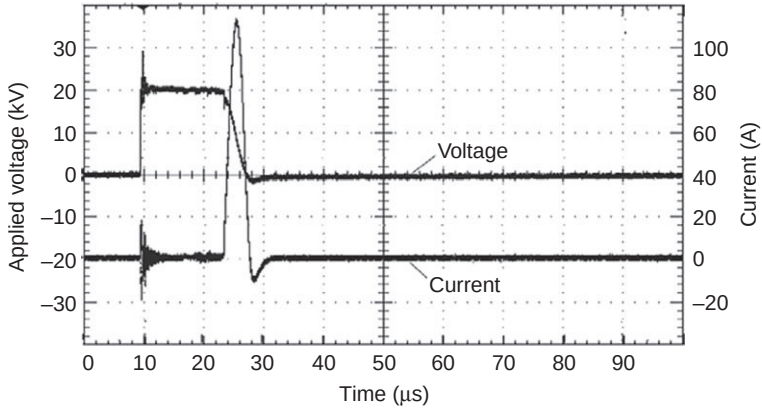

FIG. 30. Typical voltage and current waveforms of a pulsed discharge in water [111].

Typical voltage and current waveforms are shown in Fig. 30. A fast rise time (~8 ns) was obtained with the closure of a spark-gap switch. The peak-to-peak voltage was 29.6 kV. The initial steep rise in the voltage profile indicated the time moment of breakdown in the spark gap, after which the voltage slightly decreased with time over the next 12 μs due to a long delay time while the corona was formed and transferred to a spark. The rate of the voltage drop over time depends on the capacitance used in the test. The current profile shows the corresponding histories which show initially sharp peaks and then very gradual changes over the next 12 μs. At $t \approx 12$ μs, there was a sudden drop in the voltage indicating the onset of a spark or the moment of channel appearance, which was accompanied by sharp changes in both the current and voltage profiles. The duration of the spark was approximately 3 μs, which was much shorter than the duration of the corona. It is worth to mention that the energy dissipated in electrolysis can be

comparable with, or even higher than, the energy deposited in spark, especially at high-conductivity water conditions, because of the conduction current. The pulsed energy stored in the capacitor E_b was about 2.0 J, which was calculated as

$$E_b = 0.5CV_b^2 \tag{46}$$

where C was 8.5 nF and V_b the capacitor voltage was 21.5 kV. The value was much lower than the peak-to-peak electrode voltage because of the oscillation in electric circuit upon the closing of spark gap. By integrating the voltage and current, the energy deposited into spark discharge was calculated as

$$E_p = \int_{t1}^{t2} V(t)I(t)dt \tag{47}$$

where $V(t)$ and $I(t)$ are the voltage and current measured by the oscilloscope, respectively, and t_1 and t_2 are the starting and ending times of the spark, respectively. The result was approximately 1.9 J/pulse, showing most of the energy stored in the capacitor finally went into the spark discharge.

The spark discharge source in water consisted of a stainless steel 316 wire electrode (anode) with a radius of 2 mm and an exposed length of 5 mm, and a stainless steel mesh which acted as both a filter surface and grounded cathode. The tip of the anode electrode was sharpened to 0.2 mm diameter to provide a field enhancement. The distance between the anode electrode and stainless steel mesh was 10 mm. The opening in the stainless steel mesh was 10 μm. The electric conductivity of the tap water (provided by the City of Philadelphia) used in the experiment was approximately 400 μS/cm. The value was maintained at 1000 μS/cm after the introduction of $CaCl_2$ and Na_2CO_3. No significant change was observed in the conductivity after the application of the spark discharge.

B. Results and Discussion

Figure 31 shows the changes in the pressure drop under various flow rates ranging from 200 mL/min to 400 mL/min without spark discharge. The pressure drop for a flow rate of 400 mL/min was approximately 50 Torr at the beginning of the test, which approached to an asymptotic value of about 400 Torr at $t = 3.5$ min, indicating that the filter was fully covered by the particles. In all three cases of different flow rates, the pressure drop slowly increased during the first 30 s. In the following 2–3 min the pressure drop increased rather rapidly, arriving at respective asymptotic values.

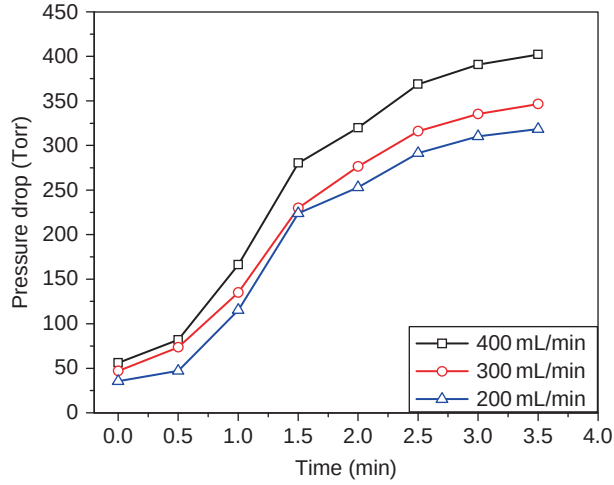

FIG. 31. Changes in pressure drop at three different flow rates with an artificially hardened water [111].

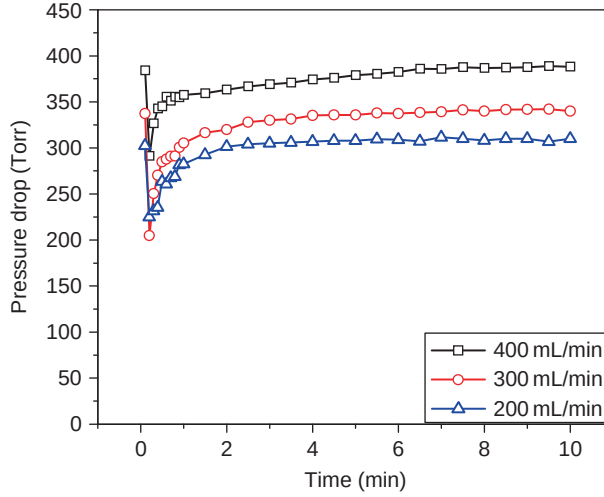

FIG. 32. Variations of pressure drop after one single spark discharge at three different flow rates with an artificially hardened water [111].

Figure 32 shows the long-time response of the pressure drop across the filter surface after one single spark discharge at three different flow rates of 200, 300, and 400 mL/min. One could visually observe that some particles

were dislodged from the filter surface and were pushed away from the filter surface by tangential flow, and a sudden change in the pressure drop immediately following the single spark discharge confirmed the removal of the deposits from the filter surface.

The cleaning effect can be explained by the pressure pulse produced by spark discharge. A number of researchers studied the bubble growth by spark discharge in water [112–115]. One of the most effective models is Kirkwood–Bethe model as given below [107]:

$$\left(1-\frac{\dot{R}}{C}\right)R\ddot{R}+\frac{3}{2}\left(1-\frac{\dot{R}}{3C}\right)\dot{R}^2=\left(1+\frac{\dot{R}}{C}\right)H+\left(1-\frac{\dot{R}}{C}\right)\frac{R}{C}\dot{H} \tag{48}$$

where C and H are the speed of sound of the water and the specific enthalpy at the bubble wall, respectively. R is the radius of the bubble wall. The overdots denote the derivatives with respect to time. By expressing the time derivative of specific enthalpy as a function of derivative of plasma pressure P inside the bubble, Lu showed that it was possible to solve P as [107]

$$P(r,\,t_r)=A\left[\frac{2}{n+1}+\frac{n-1}{n+1}\left(1+\frac{n+1}{rC^2}G\right)^{1/2}\right]^{(2n/(n-1))}-B \tag{49}$$

where A, B, and n are constants ($A=305.0$ MPa, $B=304.9$ MPa, $n=7.15$); r is the distance from the source of the spark to the pressure transducer; and

$$G=R\left(\frac{H+\dot{R}\dot{R}}{2}\right),\quad t_r=t+\frac{(r-R)}{C_0} \tag{50}$$

Using the above equation, Lu simulated that for a spark discharge with energy of 4.1 J/pulse, the maximum pressure at a distance of 0.3 m could be up to 7 atm [107]. The cleaning effect was due to the rapid pressure change produced by a spark discharge.

With a single pulse, it took approximately 3 min for the pressure drop to return to its asymptotic value after the application of the single spark discharge. This suggests that one needs to repeatedly apply spark discharges to effectively remove the particles from the filter surface over an extended period.

Figure 33 shows the changes in the pressure drop over time for three different flow rates. One spark discharge was applied every minute from the supply-water side (i.e., untreated water side) where the accumulation of suspended particles takes place. For the case of 300 mL/min, the pressure drop decreased from the maximum asymptotic value of 350 Torr to 230 Torr after the first spark discharge. Since water with particles was continuously

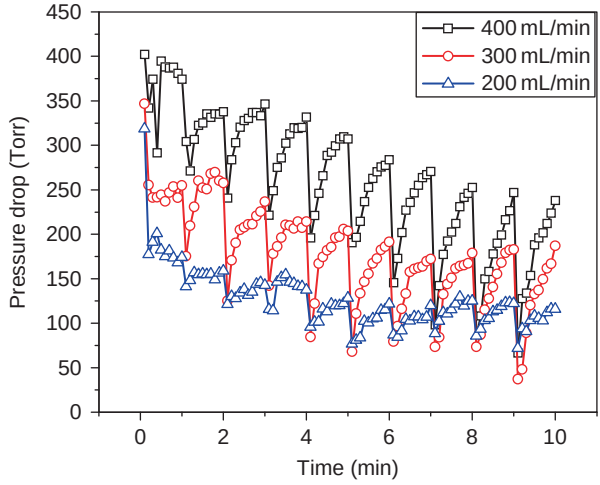

FIG. 33. Changes in pressure drop under repeated pulsed spark discharges with an artificially hardened water [111].

circulated through the filter surface, the pressure drop began to increase immediately after the completion of the first spark discharge as shown in Fig. 32. The second and third spark discharges further reduced the pressure drop to 170 and 125 Torr, respectively. The pressure drop again began to increase immediately after each spark discharge. The sixth spark discharge brought the pressure drop down to a value of approximately 65 Torr, and subsequent spark discharges almost resulted in the minimum value of the pressure drop. For the cases of 200 and 400 mL/min, similar trends of the changes in the pressure drop were observed.

Figure 34 (a) and (b) shows the changes in the pressure drop under repeated pulsed spark discharges with frequencies of 2 and 4 pulses/min, respectively. Three horizontal arrows indicate the original asymptotic values for three different flow rates, which were the maximum pressure drop due to clogged filter surface by $CaCO_3$ deposits. First spark discharge significantly reduced the pressure drop in both cases. After that, the rate of the reduction slowed down. The pressure drop oscillations because of the application of spark pulses reached quasi-steady conditions after about 10 pulses for both cases. In these oscillations, the maximum pressure drop decreased to about 45% of its original asymptotic value, while the minimum pressure drop was close to that of the clean filter. These results demonstrate the validity of the present spark discharge method. Note that the present cleaning method using the spark discharge does not require a backwash to

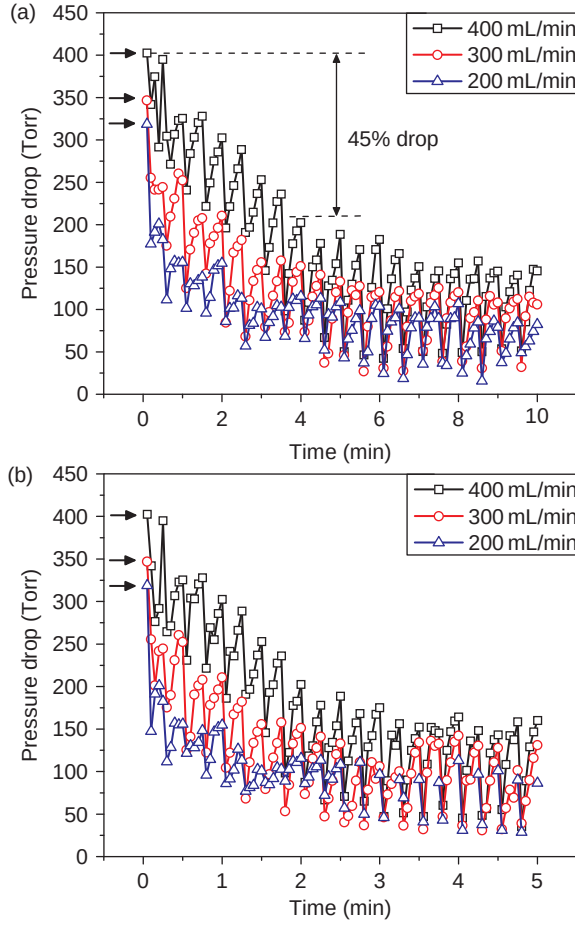

FIG. 34. Changes in pressure drop under repeated pulsed spark discharges with frequencies of (a) 2 pulses/min and (b) 4 pulses/min [111]

remove deposits from the filter surface nor stopping the flow. Furthermore, the present spark discharge method can maintain the pressure drop across the filter at a rather low value (i.e., almost close to the initial clean state), thus providing a means to save not only freshwater but also electrical energy for the operation of pump and required for the backwash in the conventional backwash system.

Figure 35 shows the changes in the pressure drop over time with the anode electrode placed beneath the filter membrane (i.e., plasma discharge was applied from the treated water side). In this case, the momentum transfer

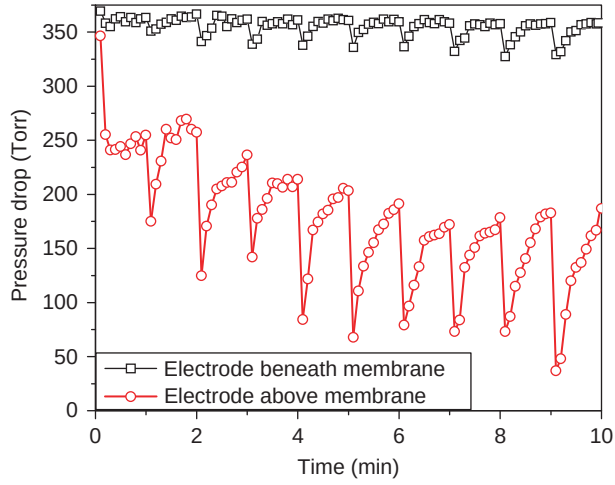

FIG. 35. Pressure drops across filter membrane under repeated pulsed spark discharges in water for the cases of electrode beneath membrane and electrode above membrane [111].

from the shockwave to particles on the filter surface was indirect and had to go through the membrane. Figure 35 clearly shows that the pressure drop did not improve significantly in this case, indicating that the cleaning effect was negligible comparing with the case when the electrode was placed at the untreated water side. The fact that the momentum transfer from the shockwave to the membrane was weak is actually good news. The low energy transfer rate means that the present spark discharge may not deform the membrane significantly and therefore will not damage the membrane, and has the potential to be applied in the cleaning of more delicate membranes such as in a reverse osmosis as well as solid filters over an extended period of time.

VI. Plasma-Assisted $CaCO_3$ Precipitation

As mentioned in the introduction section, thermoelectric generation accounted for 39% (136 BGD) of all freshwater withdrawals in the United States in 2000, second only to irrigation [1]. Each kilowatt-hour (kWh) of thermoelectric generation requires the withdrawal of approximately 25 gallons of water, which is primarily consumed for cooling purposes.

Since heat removal from condenser tubes requires the evaporation of pure water, the concentration of the mineral ions such as calcium and magnesium

in the circulating cooling water increases with time. Even though the makeup water is relatively soft, the continuous circulation eventually increases the hardness of the water due to pure water evaporation. These mineral ions, when transported through piping in ordinary plumbing system, can cause various problems, including the loss of heat transfer efficiencies in condensers and pipe clogging due to scale formation [116,117]. Thus, in order to maintain a certain calcium hardness level in the cooling water, one must discharge a fraction of water through blowdown and replace it with makeup water. In a typical cooling-tower application, the COC in cooling water is often maintained at 3.5. That means if the $CaCO_3$ hardness of the makeup water is 100 mg/L, the hardness in the circulating cooling water is maintained at approximately 350 mg/L. If the COC can be increased through continuous precipitation and removal of calcium ions, one can significantly reduce the amounts of makeup and blowdown water, resulting in the conservation of freshwater.

Various chemical and non-chemical methods are used to prevent scaling and thus increase the COC. Among them the scale-inhibiting chemicals like chlorine and brominated compounds were the best choice for the control of mineral fouling. Although it had a high success rate, there were also many disadvantages and concerns in their use. Aside from the high cost of chemicals, more stringent environmental laws increased the costs associated with their storage, handling, and disposal. These chemicals also pose danger on human health and environment with accidental spills or accumulated chemical residues over a long period of time [116,118]. Thus, there is a need for new approach which is safe and economical from both environmental and cost points of view in cleaning and maintenance of heat exchangers. Physical water treatment (PWT) is a non-chemical method to mitigate mineral fouling with the use of electric or magnetic fields, catalytic surfaces, ultrasounds, or sudden pressure changes. Numerous studies have been reported for the effectiveness of ultrasound [119], solenoid coils [120–122], magnetic fields [123,124], catalytic material [125,126], and electrolysis [127].

Herein the present study reports for the first time the pulsed-spark-discharge-assisted precipitation of dissolved calcium ions in hard water system. By measuring the variations of calcium and bicarbonate ion concentrations, the solution pH, and the size and number of solid particles suspended in water, the effect of the spark discharge treatment on the nucleation precipitation of $CaCO_3$ was studied. The morphology of the precipitates was examined by scanning electron microscopy (SEM), whereas their crystal structure was identified by X-ray diffraction (XRD).

A. Experiment Setup

1. Water Preparation

To simulate the actual situations in the field, a closed-loop laboratory cooling tower was utilized in the study where Philadelphia city tap water was recirculated to produce concentrated hard water. Figure 36 shows the schematic diagram of the cooling tower. The recirculation system consisted of a blower to supply air to the cooling tower, a heater to heat the air, a pump to circulate the water, and the cooling tower itself which was filled with Styrofoam balls used as strainers. As pure water evaporated in the cooling tower, the mineral ions such as calcium and magnesium were left behind and collected in the reservoir. Thus, with the continuous recirculation of hard water in the cooling tower, the concentration of mineral ions was gradually increased until desired $CaCO_3$ hardness of 200–500 mg/L was reached. It usually took several days to obtain the desired concentration. The water pH resulting from this preparation was in the range of 8–10. A total of 100 L of concentrated hard water for each sample was prepared and kept in the reservoir and used for the whole duration of the experiment. The concentrations of cations and anions were analyzed, and Table III summarizes the chemical compositions of different water samples collected from the laboratory cooling tower.

2. Pulsed Spark Discharge Generation System

A pulsed power system was constructed to produce spark discharge directly in water. The system consisted of three components: a HV power supply with a capacitive energy storage, a spark-gap based switch, and a point-to-plain electrode system immersed in water. A schematic diagram of the pulsed power system is shown in Fig. 37. An 8.5-nF capacitor bank was charged by HV pulses provided by a pulsed power supply.

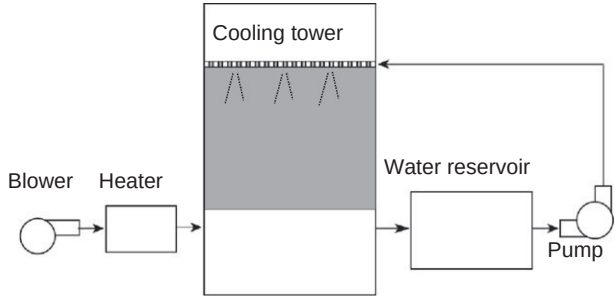

Fig. 36. Schematic diagram of the laboratory cooling tower used by Yang *et al.* [128].

TABLE III
CHEMICAL COMPOSITIONS OF WATER SAMPLES COLLECTED IN THE LABORATORY COOLING TOWER [128]

	Sample 1	Sample 2	Sample 3
Ca^{2+}	96	128	167
Na^{+}	156	230	297
Mg^{2+}	8	13	17
Cl^{-}	98	140	186
SO_4^{2-}	176	269	362
HCO_3^{-}	296	392	498
pH	8.67	9.10	9.62
$CaCO_3$ hardness	279	378	492

All values are in mg/L.

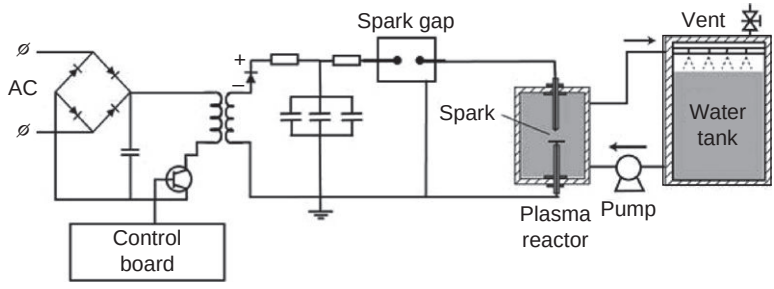

FIG. 37. Schematic diagram of the pulsed power and water circulation system used by Yang *et al.* [128].

When triggered by an air-filled spark-gap switch, spark discharge was initiated between the electrodes from the overvoltage produced by the capacitor. The electrode system included a stainless steel 316 wire electrode as anode and a stainless steel disk as grounded cathode. The radius of the anode and the disk cathode was 2 and 40 mm, respectively. The radius of curvature at the tip of the anode was 0.2 mm. The distance between the anode and the disk cathode was 10 mm.

Power deposited into water was analyzed by measuring the current passing through the discharge gap and the voltage drop in the gap. For measurements of the current, a magnetic-core Pearson current probe was utilized (1 V/Amp +1/–0% sensitivity, 10 ns usable rise time, and 35 MHz bandwidth). Voltage was measured using a wide bandwidth 1:1000 voltage probe (PVM-4, North Star Research Corp.). Signals from the current and voltage probes were acquired and recorded by a DPS (500 MHz

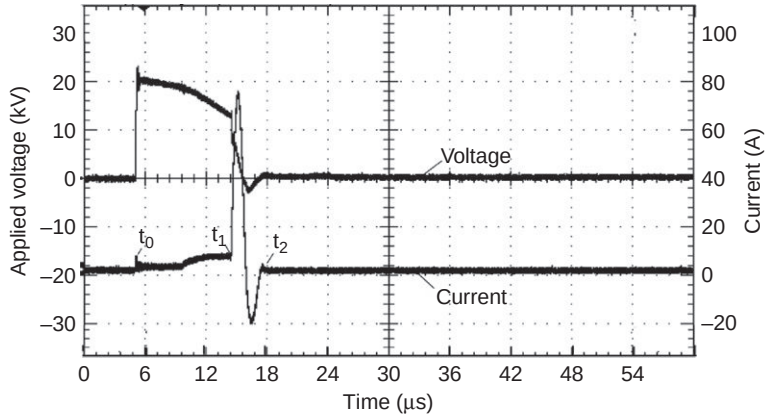

FIG. 38. Typical voltage and current waveform of the spark discharge in water used by Yang *et al*. [128].

bandwidth, 5×10^9 samples/s, TDS5052B, Tektronix). Acquired data were then integrated using a customized MATLAB code.

Typical voltage and current waveforms are shown in Fig. 38. A fast rise time (~9 ns) was obtained with the closure of a spark-gap switch. The peak-to-peak voltage was about 24 kV. The pre-breakdown time, i.e., the time required before the spark formation was about 8.8 μs. During the pre-breakdown time, the energy was mostly consumed by ionic current due to the high conductivity of water samples. After that, the abrupt increase in current was observed. This may possibly indicate that spark was formed as the streamer reached the other electrode and formed the highly conductive channel. The full width at half maximum (FWHM) of the major current pulse during spark discharge was 1.1 μs. The typical peak-to-peak breakdown current was 98 A. It is worth to mention that the energy dissipated in pre-breakdown current can be comparable with, or even higher than, the energy deposited in spark, especially at high-conductivity water conditions. The pulsed energy stored in the capacitor E_b was about 1.7 J, which was calculated by Eq. (46). By integrating the voltage and current, the energy deposited into the spark discharge was calculated as

$$E_S = \int_{t_1}^{t_2} V(t)I(t)dt \tag{51}$$

where $V(t)$ and $I(t)$ are the voltage and current measured by the oscilloscope, respectively, and t_1 and t_2 are the starting and ending point of the spark,

respectively. Similarly, the energy dissipated in the pre-breakdown stage was calculated as

$$E_p = \int_{t_0}^{t_1} V(t)I(t)dt \tag{52}$$

where t_0 is the time when the high voltage was applied. The value of E_s and E_p was approximately 0.69 and 0.81 J/pulse, respectively, indicating that about 88% of the energy stored in the capacitor was deposited in water. The rest of the energy was possibly dissipated in the circuit during the discharge process.

3. *Water Treatment*

Water samples with different initial calcium hardness (i.e., Samples 1, 2, and 3) were treated by spark discharge in a polytetrafluoroethylene (PTFE) cylinder. In each run, 1 L of solution was exposed to the discharge for 20 min. The frequency of the discharge was set as 2 Hz. Hence, the total energy deposited into 1-L water during a 20-min treatment can be calculated as about 3600 J. The temperature difference between before and after treatment was less than 1.5°C, so it can be concluded that no significant bulk heating was caused by the spark discharge. About 10 mL of the sample was extracted every 5 min for pH and ion concentration measurement. A filter with 0.5-μm pore size was used to remove suspended $CaCO_3$ from the sample. After that, calcium-ion concentration was analyzed by standard ethylenediaminetetraacetic acid (EDTA) titration, and concentration of bicarbonate ion was decided by total alkalinity test and phenolphthalein alkalinity test [129]. Untreated samples were collected from the stock solution at the same time intervals in order to evaluate the loss of calcium as a result of the natural precipitation process.

After the 20-min plasma treatment, the water was spray circulated for 12 h to degas the excessive carbon dioxide (CO_2) dissolved in water and to observe the residual effect of the plasma. Then the water sample was treated again by the spark discharge for 20 min. The process was repeated for three times over a 36-h period until the hardness reaches an asymptotic value. The same experiments without plasma exposure were also carried out as reference. All the experiments were replicated three times and the average values were calculated.

Before and at the end of each experiment, a laser particle counter (PC-2200, Spectrex, Redwood City, CA) was used to count the size distribution of particles in suspension. After that, the solids were filtered with a

pressurized filter (0.5-μm pore size) and dried in vacuum. SEM images and XRD analyses were carried out at Drexel SEM and XRD laboratories. SEM (XL30, FEI, Hillsboro, OR) images were obtained to examine the topography of the deposits. Prior to each SEM examination, the deposit samples were coated with platinum through low-vacuum sputter coating in order to prevent the accumulation of static electric charge during the irradiation of electrons. XRD (D500, Siemens, Munich, Germany) analyses were conducted to characterize the crystallographic structure of the scale deposits.

B. Results

1. *Effect of Immediate Plasma Exposure*

Figure 39 presents the variation of pH and calcium-ion concentration as a function of time and input plasma energy, and their comparisons with no-treatment cases. For the case of Sample 1, the calcium-ion concentration dropped from the initial value of 96–71 mg/L after 10 min of plasma treatment. After that, the hardness would reach asymptotic value and not decrease with further input of energy. Accompanying the drop of the calcium-ion concentration, the pH of the treated water sample decreased from 8.67 to 8.51, possibly because of the liberation of H^+ ions according to

$$Ca^{2+} + HCO_3^- \rightarrow CaCO_3 + H^+ \tag{53}$$

Additionally, the ionization of water molecules by high-energy electrons from plasma discharge may also contribute to the decrease of the pH through the following reactions:

$$H_2O + e \rightarrow H_2O^+ + 2e \tag{54}$$

$$H_2O^+ + H_2O \rightarrow H_3O^+ + OH^\bullet \tag{55}$$

Samples 2 and 3, with initial calcium-ion concentration of 128 and 164 mg/L, respectively, showed a similar trend as Sample 1. The hardness was reduced by about 25% after 10-min treatment, with an energy input of approximately 1800 J/L. In comparison to the plasma-treated cases, no significant change was observed for the no-treatment cases.

Figure 40 presents the variations of bicarbonate ion concentration with time determined by total alkalinity test and phenolphthalein alkalinity test. Generally, the concentration of bicarbonate ion decreased during a 10-min stabilization period before reaching an asymptotic value. Similar to the concentration of calcium ions, bicarbonate ion

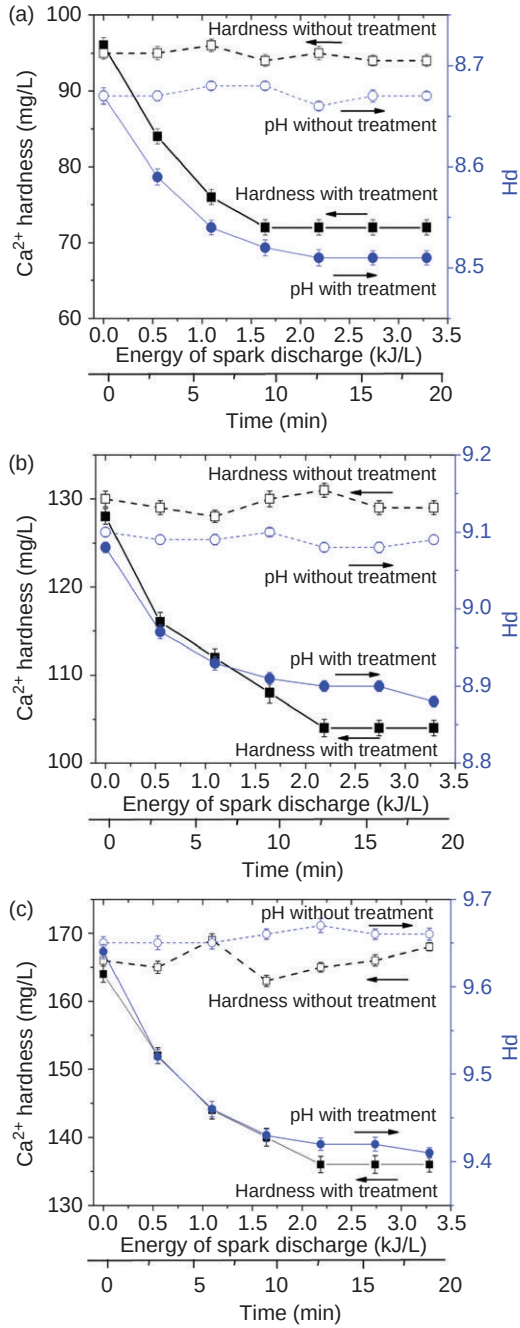

FIG. 39. Variations of pH and Ca^{2+} hardness over time with and without plasma treatment: (a) Sample 1; (b) Sample 2; (c) Sample 3. See Table III for more information on the three samples [128].

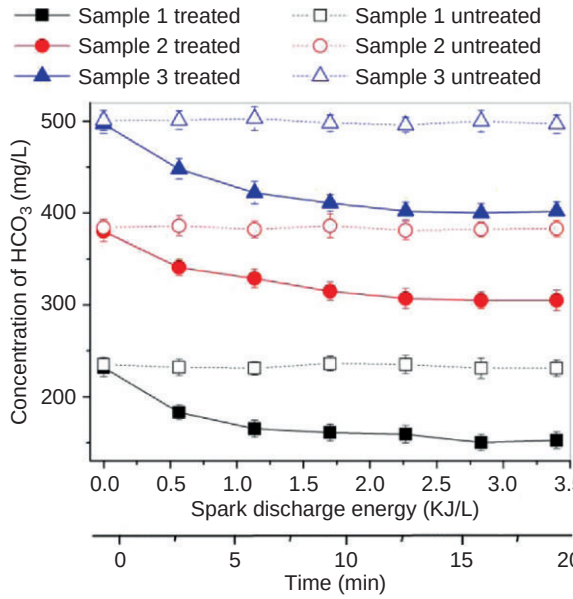

FIG. 40. Variations of HCO_3^- over time for cases with and without plasma treatment [128].

concentration changed very little for energy input greater than 2 kJ/L. It was probably because the rate of precipitation reactions was limited by the diffusion rate of calcium and bicarbonate ions toward the reaction zone due to the high localization of the plasma discharge. In addition, the acidification of the anode vicinity by plasma induced H^+ generation (Eqs. (54) and (55)) could become detrimental to the precipitation process.

Figure 41 shows the number of particles per unit volume of 1 mL as a function of particle size before and after plasma treatment. The results depict in general that before the treatment, the number of particles less than 10 μm was significantly greater than that of larger particles (greater than 10 μm). For example, for Sample 1 (Fig. 41 (a)), the number of particles with size between 1 and 2 μm was 17,048 before treatment as compared to 2445 for particles greater than 10 μm. After treatment, a significant increase in the number of particles was observed for all cases as compared to the no-treatment cases. For Sample 1, the number of particles with size between 1 and 10 μm increased from 39,904 at the initial state to 77,680 at the end of the treatment, while the number of particles with size over 10 μm increased from 2445 to 3529. For Samples 2 and 3 (Figs. 41 (b) and (c)), particles smaller than 10 μm also made up the majority of the suspended

solids in water. The number of small particles (i.e., below 10 μm) after the treatment was significantly increased comparing with that obtained at no-treatment cases.

Assuming that all the particles were in spherical shape for the purpose of mathematical estimation, the total mass of suspended solid contents m was calculated using the following equation:

$$m = \sum_{N_d(d=1\mu m)}^{N_d(d=62\mu m)} \rho \cdot \frac{\pi d^3}{6} \cdot N_d \tag{56}$$

where ρ is the density of the $CaCO_3$ particle; d is the diameter of the particle; and N_d is the number of particles. ρ is taken as 2.7 g/cm^3, which is the density of calcite. For Sample 1, the total mass of solid particles before the treatment was 64 mg/L, which corresponded to 64 mg/L $CaCO_3$ hardness. The value increased to 104 mg/L after the plasma treatment, which means that the difference of a 40 mg/L of ionic content in water was transformed from the dissolved ionic states into solid content during the process. Aforementioned titration results from Fig. 39 (a) showed that the calcium ion hardness in water was reduced by 25 mg/L, equaling 62.5 mg/L of $CaCO_3$ hardness. Considering that the resolution of the laser particle counter was 1 μm, which means that the precipitation of particles with less than 1-μm diameter was not taken into account, the results obtained by titration and laser particle counting was in good agreement, demonstrating that the calcium ions were transformed into $CaCO_3$ solids during the process. For all three cases, the results are summarized in Table IV.

Figure 42 (a) shows the SEM photographs of particles retrieved from Sample 1 without plasma treatment. Chemical composition of the particles was analyzed by energy dispersion spectrometer (EDS). Figure 43 shows that

TABLE IV

RESULTS OBTAINED BY LASER PARTICLE COUNTING [128]

	Sample 1	Sample 2	Sample 3
Total number of particles before treatment, cm^{-3}	42,349	38,587	47,034
Mass of suspended particles before treatment	64	72	53
Total number of particles after treatment, cm^{-3}	81,710	71,340	105,846
Mass of suspended particles after treatment	104	120	108
Increase of solid mass in water	40	48	56
Decrease of ionic $CaCO_3$ hardness in water	62	67	75

All values are in mg/L.

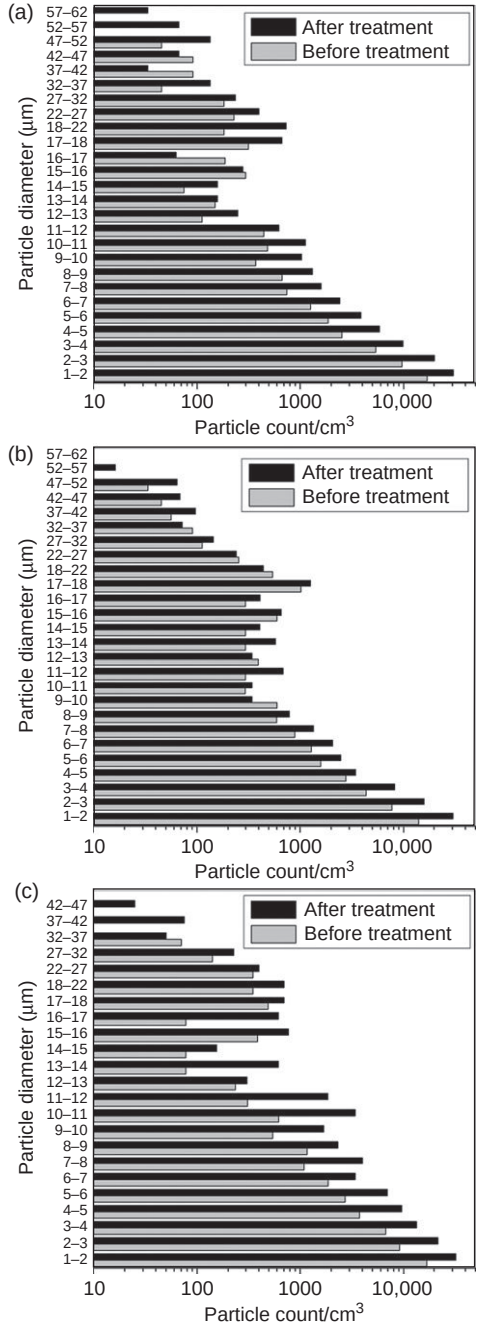

FIG. 41. Particle size distributions before and after plasma treatment for (a) Sample 1; (b) Sample 2; (c) Sample 3 [128].

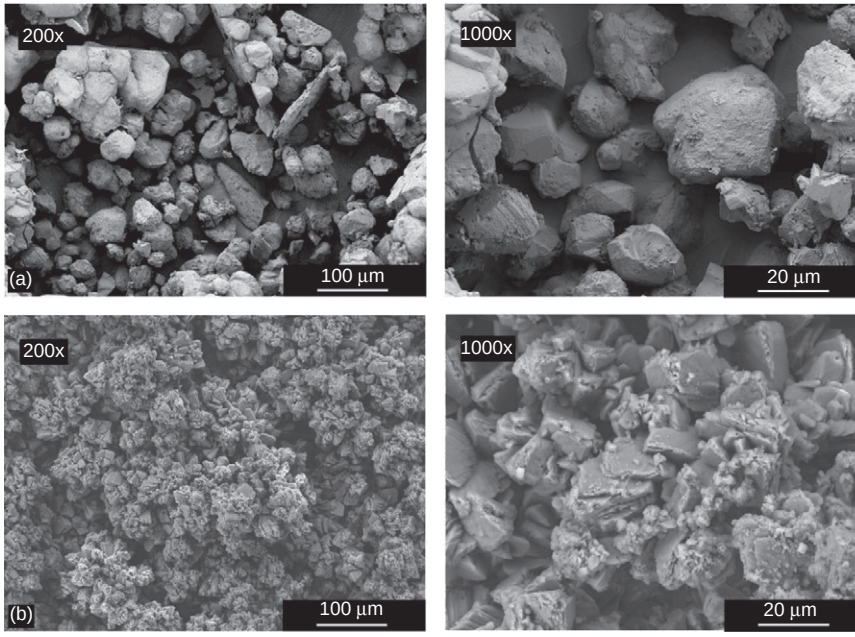

FIG. 42. SEM images of $CaCO_3$ crystals obtained from: (a) untreated water; (b) plasma-treated water [128].

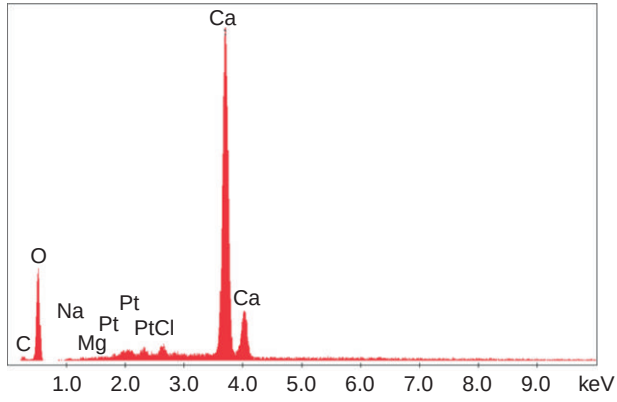

FIG. 43. Elemental composition of the particles shown in Fig. 41(b) obtained by energy dispersion spectrometer (EDS) [128].

TABLE V
THERMO-CHEMICAL DATA OF REACTIONS 1, 2, AND 3 [129]

	Reaction 1	Reaction 2	Reaction 3
H (kJ/mol)	48.26	–41.06	12.36
G (kJ/mol)	43.60	–20.9	–47.70

the particles were mainly composed of $CaCO_3$, with slight amount of sodium and magnesium, as identified in Table V, together with the platinum coated prior to the SEM observation. The crystals exhibited the morphology close to the rounded vaterite form. However, XRD pattern, as shown in Fig. 44 (a), coincided with those of calcite. It was probably because of the

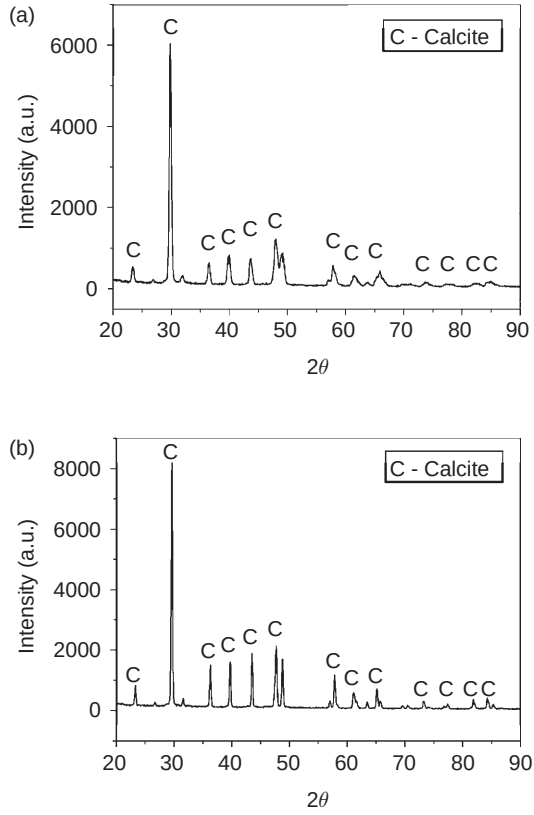

FIG. 44. XRD pattern of the $CaCO_3$ crystals obtained from: (a) untreated water; (b) plasma-treated water [128].

thermodynamically unstable property of the vaterite crystals. The preparation of water samples usually took several days. Possibly during this period, vaterite may have recrystallized into more stable calcite crystals without changing shape.

Figure 42 (b) shows the photographs of the particles collected from the Sample 1 after the plasma treatment. The crystals demonstrated typical rhombohedron morphology of calcite. The formation of the calcite was confirmed by XRD shown in Fig. 44 (b). The mean crystal size of precipitation test was about 5 μm after 20 min of the plasma treatment. For the treated water with high hardness (i.e., Samples 2 and 3), calcite crystals were also observed, and their size remained almost the same as that observed in Sample 1. The fact that the total amount of precipitates was increased as indicated by the laser particle counting suggests that the number of nuclei was significantly increased. That demonstrates that the plasma had induced chemical changes in the calcareous water during the treatment, which was implied later in the nucleation process during the precipitation test.

2. *Effect of Spray Circulation*

To disturb the acidic condition so that a higher level of hardness reduction could be achieved than the aforementioned asymptotic hardness, the treated water sample was spray circulated for 12 h to degas the excessive CO_2 in the plasma-treated water. For Sample 1, the pH value increased from 7.74 to 7.92 during this period, indicating releasing of CO_2 gas from water solution. In the mean time, the hardness decreased from 190 mg/L to 160 mg/L (see two arrows in Fig. 45 (a)). After that, the water sample was treated again by the spark discharge for 20 min, and the hardness dropped from 160 mg/L to 140 mg/L before reaching another equilibrium. At the end of a 36-h test, the hardness reached the final asymptotic value shown in Fig. 45 (a), which indicated an approximate 45% reduction from the initial hardness. Similar results were observed for both Samples 2 and 3 with hardness reductions of 53% and 59%, respectively. For example, for Sample 3 with an initial hardness of 420 ppm, the final hardness was 170 ppm at the end of 36-h circulation with three brief daily plasma treatments. Note that when the 12-h-interval 20-min plasma treatment was not used, the hardness of Sample 3 increased to 440 ppm after 36-h circulation, 5% increase in hardness obviously due to the evaporation of pure water as shown in Fig. 45 (a).

In summary, the hardness of water could be reduced by 45–59% by the combination of plasma discharges and spray circulation. Since the plasma treatment was applied for only 20 min in the 12-h interval, and spray circulation is a standard operation for cooling water in cooling tower, plasma discharge can be regarded as a “catalyst” for precipitation.

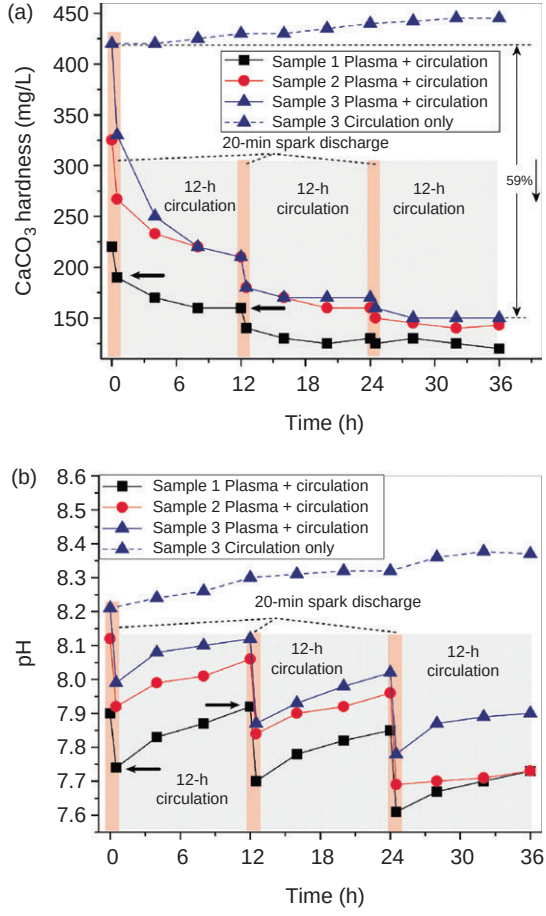

FIG. 45. Variations of (a) $CaCO_3$ hardness; (b) pH value over time with plasma treatment and spray circulation [130].

C. MECHANISM STUDY

1. Discussions of Possible Mechanisms

This is the first time, to the authors' knowledge, that the precipitation of dissolved calcium ions in water by the application of plasma discharge was studied. In this section, the possible mechanism for the plasma-induced $CaCO_3$ precipitation is discussed.

First, the effect of electrolysis, which is another hard water softening technology using electric energy, is examined. Gabrielli and his coworkers

studied the principle of softening process by electrolysis and showed that the precipitation was induced by the local pH increase near the vicinity of the cathode [127]. A model electrolyzer with an electrode area of 560 cm^2 was tested. Under the operating current density of 20 A/m^2, applied voltage of 12 V and flow rate of 6 L/h, the Ca^{2+} hardness of the water sample was reduced from 96 mg/L to about 72 mg/L when a quasi-steady state operation was achieved. Hence, the energy consumption was calculated as 806 J/L.

For the present spark discharge, electrolysis most likely took place during the pre-breakdown stage, as the current would be transferred by the ionized gas after the formation of the conductive channel between the two electrodes. The same level of hardness reduction was achieved as in Gabrielli's experiments after applying spark discharge in Sample 1 for 10 min, as shown in Fig. 39 (a). The energy dissipation in the pre-breakdown stage was calculated as 984 J/L based on the results shown in Fig. 38. However, it was difficult to estimate the exact amount of energy consumed by electrolysis, as multiple physical and chemical processes, including ionization, light emission, cavitation, and shockwave and reactive species formation, were initiated during the same stage. But certainly, only a fraction of 984 J/L energy was dissipated in electrolysis.

Another factor that may subdue the effect of electrolysis is the mixing of the liquid caused by the formation of shockwaves. It may prohibit the formation of local high pH area near vicinity of the cathode. Therefore, the electrolysis-induced precipitation might be suppressed in the present experiment, and it could be concluded that the reduction of water hardness may not be the sole effect of the electrolysis, though it may contribute partially to the precipitation process.

Next the chemistry behind the $CaCO_3$ precipitation is described. The main reactions of precipitation and dissolution of $CaCO_3$ in hard water system are [129]

$$Ca^{2+}_{(aq)} + CO^{2-}_{3\,(aq)} \Leftrightarrow CaCO_{3(S)} \tag{57}$$

and

$$CaCO_{3(S)} + H^{+}_{(aq)} \Leftrightarrow Ca^{2+}_{(aq)} + HCO^{-}_{3}\,(aq) \tag{58}$$

In a saturated condition, the forward reaction of the precipitation of $CaCO_3$ does not take place as both calcium and bicarbonate ions are hydrated. When water is supersaturated and there is sufficient energy supplied, the water molecules are disturbed or become freed from the ions, resulting in the precipitation of $CaCO_3$. Equation (58) shows the dissolution

of solid $CaCO_3$ by acid, a process that takes place during acid cleaning of scaled heat exchangers.

Generally, one needs to concern with the above two reactions. In reality, precipitation and dissociation reactions are much more complicated. The recombination and crystalization rates of calcium and carbonate ions are controlled by three reactions. Reaction 1 relates the dissociation of bicarbonate ions into the hydroxyl ions OH^- and CO_2 [131]:

$$HCO_{3\,(aq)}^{-} \Leftrightarrow OH^{-}_{(aq)} + CO^{2}_{(aq)} \text{ (Reaction 1)} \tag{59}$$

The forward reaction indicates the dissociation of the bicarbonate ions, which is the most critical step from the precipitation process. Of note is that the bicarbonate ions do not cause any harm in terms of scaling as long as they remain as bicarbonate ions. Reaction 1 shows the first step in the conversion of bicarbonate to carbonate ions. The presence of hydroxide ions is best indicated by a local increase in pH, and CO_2 typically evolves from the water as a gas over time.

In Reaction 2 hydroxyl ions produced from Reaction 1 further react with existing bicarbonate ions, producing carbonate ions and water [131]:

$$HCO_{3\,(aq)}^{-} + OH^{-}_{(aq)} \Leftrightarrow H_2O_{(l)} + CO_{3\,(aq)}^{2-} \text{ (Reaction 2)} \tag{60}$$

Reaction 3 is the reaction between calcium and carbonate ions, resulting in the precipitation and crystallization of $CaCO_3$ particles [131]:

$$CO^{2-}_{(aq)} + CO_{3\,(aq)}^{2-} \Leftrightarrow CaCO_{3(S)} \text{ (Reaction 3)} \tag{61}$$

Table V presents the thermo-chemistry of the above three reactions [129]. The values of ΔH and ΔG give some useful insights into the behavior of the system of reactions. The endothermic Reaction 1 is the most rate-limiting, since it needs a relatively large input of energy to continue in the forward direction based on the high enthalpy value. The Gibbs free energy is relatively high; thus, this reaction will tend to form bicarbonate ions, unless this energy restriction is overcome. In order for hydroxide ions to be produced as a result of dissociation of the bicarbonate ions, the energy required for the reaction can be calculated as:

$$\frac{48,260\ \text{J}}{\text{mol}} \frac{1\ \text{mol}}{6.02 \times 10^{23}\text{ions}} = 0.801 \times 10^{-19}\ \text{J} \quad (\text{or} \sim 0.5\ \text{eV}) \tag{62}$$

To overcome the barrier, enough energy needs to be added to water so that the bicarbonate ions can be dissociated, and subsequently precipitating dissolved calcium ions to $CaCO_3$ via Reactions 2 and 3.

Thus, it is clear that dissociation of bicarbonate ions plays an important role in the precipitation process, as observed in the experiments (Fig. 40). From thermodynamics, the reaction rate coefficient k for Reaction 1 is

$$k = A\mathrm{e}^{-\frac{E_a}{T}} \tag{63}$$

where A is a constant; E_a is activation energy for the reaction; and T is the system temperature (in the unit of eV). It is obvious that higher temperature will lead to higher precipitation rate. For example, when hard water is heated (i.e., volume heating) by boiling or microwave, the $CaCO_3$ deposit can be usually observed in bulk solution or heated surface.

For plasma treatment cases, the total input energy was on the level on kJ/L, so that no significant volume heating exists. However, direct pulsed spark discharges in water have been shown to generate a temperature up to 5000–10,000 K (about 0.5–1 eV) inside the plasma channel [60], a phenomenon which is sufficient to induce direct pyrolysis of bicarbonate ions. The high-temperature zone is highly localized around the plasma channel, so that higher efficiency could be achieved over volume heating under same energy input level due to exponentially dependence of the reaction rate on the temperature. The maximum temperature depends on both plasma power and water properties.

Furthermore, the thermal dissociation of bicarbonate ions may be enhanced by emission of UV light from the high-temperature plasma channel, which functions as a blackbody radiation source. Full-spectrum UV radiation was demonstrated to be produced from spark discharge [28]. The VUV ($\lambda = 75-185$ nm) emitted would be absorbed by the water layer immediately surrounding the plasma channel, leading to the expansion of the high-temperature zone [27]. However, the amount of solution that can be treated directly by the thermal process is still limited by the small volume of the high-temperature zone.

Another factor that may contribute to the dissociation of bicarbonate ions is the electric field. There are reports about the increase of nucleation rate of different crystals when subjected to external electric fields [132–134]. Dhanasekaran and Ramasamy [135] studied the free energy required for the formation of a two-dimensional nucleus of any possible shape under electric field. They calculated the critical free energy for nucleation as

$$\Delta G = \frac{\beta^2\sigma^2}{4kT(\ln\alpha + \varphi E^2)} \tag{64}$$

where β is a constant depending on the geometrical shape of the nucleus; σ is the interfacial tension; k is the Boltzmann constant; T is the

temperature; α is the supersaturation ratio; E is the external electric field; and φ is defined as

$$\frac{\varepsilon_0 v\left[\left(\frac{1}{\varepsilon_s}-\frac{1}{\varepsilon_l}\right)\sin^2\theta+(\varepsilon_s-\varepsilon_l)\cos^2\theta\right]}{8\pi kT}$$

where v is the volume of the crystalline nucleus; θ is the angle between the direction of the electric field and the nucleation surface; and ε_s and ε_l are the dielectric constant of the nucleus and solution, respectively. According to Dhanasekaran's theory, the free energy for nucleation decreases as the strength of electric field increases at certain angles, which leads to higher nucleation rate.

The effect of electric field could also be explained by the disruption of electric double layer of hydrated ions. Dissolved calcium and bicarbonate ions do not react at room temperature as both ions are surrounded by water molecules forming electric double layers. A number of researchers postulated that the magnetic or electric field, if strong enough, might disrupt the electric double layer and initiate the precipitation [136–138]. In order for an electric field to directly affect the electric double layer near a negatively charged surface, one needs an electric field that provides force which is able to overcome the force in the electric double layer. Typically, there are approximately two electron volts across an electric double layer, and the Debye length for a dilute solution like water is about 10 nm [139,140]. Thus, the electric field required to directly affect the electric double layer becomes approximately $2\,\text{V}/10\,\text{nm} = 2\times10^8\,\text{V/m}$. To initiate pulsed electric discharges in water using a point-to-plane electrode system, it is necessary to have a high-intensity electric field at the tip of the point electrode, which can be calculated as

$$E \approx \frac{V}{r_e} \tag{65}$$

where V is the applied voltage and r_e is the radius of curvature at the tip of the electrode. For the present system, $V = 24\,\text{kV}$ and $r_e \approx 200\,\mu\text{m}$, leading to an electric field of $1.2\times10^8\,\text{V/m}$, which is comparable to the electric field required to disrupt the hydration shells of the ions, and could possibly accelerate the dehydration process of ionic pair association. Additionally, unlike the highly localized thermal effect, the electric effect is not limited to the vicinity of the electrode tip. After the initiation of pulsed discharge, multichannel streamers with lengths up to several centimeters could be produced when propagating from one electrode to the other electrode. An and his coworkers [82] measured the radius of the streamers and inferred

that the electric field at the tip of the self-propagating streamers was more than 2×10^9 V/m. Subsequently, the bicarbonate ions may be dissociated along the propagation path of the streamers leading to the precipitation of $CaCO_3$ in bulk water as described earlier.

For the different saturation levels in different cases, it was hypothesized that the saturation level could be related to the localization of the beneficial effect of the plasma (electric field, heat, electrolysis), and the acidification of the solution by the plasma as described in Eqs. (54) and (55), which was detrimental to the precipitation. Dynamic equilibrium was possibly reached at different levels between the dissociation of HCO_3^-, the rate of which depended on the property of the solution for different cases, and the production of H^+, which was largely decided by the input energy.

Finally, the anticipated benefits of the current work are discussed from the economic point of view. For a modern 1000-MW fossil-fueled power plant with 40% efficiency, it would reject 1500 MW of heat at full load and uses about 2800 m^3/min of circulating water based on 10°C temperature difference in a condenser [3]. As heat is removed via evaporation of pure water at a cooling tower, the need for makeup water is about 28 m^3/min to compensate the loss through evaporation, wind drift, and blowdown [3]. Assuming that the makeup water is moderately hard with a $CaCO_3$ hardness of 100 mg/L, the total amount of $CaCO_3$ it brings into the cooling tower is

$$\dot{m}_{CaCO_3} = \frac{28\ \mathrm{m}^3}{\mathrm{min}} \times \frac{100\ \mathrm{mg}}{\mathrm{L}} = \frac{2800\ \mathrm{g}}{\mathrm{min}} \tag{66}$$

In a typical cooling-tower application, the COC is usually maintained at 3.5. That means the hardness in the circulating cooling water is maintained at approximately 350 mg/L, and the blowdown rate can be calculated if the wind drift loss is neglected:

$$q_{\text{blow down}} = \frac{q_{\text{makeup}}}{\text{COC}} = 8\frac{\mathrm{m}^3}{\mathrm{min}} \tag{67}$$

It has been demonstrated that the present pulsed plasma technology could continuously precipitate Ca^{2+} from water, and potentially allows a cooling tower to operate at a higher COC than the current standard due to the reduction in blowdown frequency. Ideally, zero blowdown could be achieved, if all the Ca^{2+} brought in by the makeup water is precipitated by the plasma; thus, the constant mineral concentration is maintained in the main cooling loop without blowdown. The energy cost, as shown earlier, is about 1800 J/L to achieve in average 25% reduction in water hardness. Assuming that the cooling water is treated in a side-stream loop, the flow rate needed is

$$q = \frac{\dot{m}\mathrm{CaCO_3}}{\frac{350\ \mathrm{mg}}{\mathrm{L}} \times 25\%} = 32\frac{\mathrm{m}^3}{\mathrm{min}} \tag{68}$$

which is approximately 1.2% of the flow rate of the main loop. The power needed to treat the water in the side-stream loop can be calculated as

$$P = \frac{1800\frac{\mathrm{J}}{\mathrm{L}} \times 32 \times 10^3\frac{\mathrm{L}}{\mathrm{min}}}{60\frac{\mathrm{s}}{\mathrm{min}}} = 960\ \mathrm{kW} \tag{69}$$

which is 0.1% of the full capacity of the 1000-MW power plant. In the mean while, the flow rate of makeup water can be reduced from $28\,\mathrm{m}^3$/min to $20\,\mathrm{m}^3$/min, which equals a saving of approximately $11{,}500\,\mathrm{m}^3$/day, due to the elimination of blowdown.

2. *Effect of UV Radiation*

First, the effect of UV radiation on the precipitation process of calcium ions was studied. For spark discharges, the high-temperature plasma channel can function as a blackbody radiation source. The maximum emittance is in the UVa to UVc range of the spectrum produced by the spark discharge (200–400 nm), as determined by the Stephen–Boltzmann law. Water is relatively transparent to UV radiation in this wavelength range. The energy per photon ranges from 3.1 eV to 6.2 eV, indicating the possibility of HCO_3^- dissociation through UV absorption. Severe mineral fouling was usually observed at the quartz sleeve of commercial UV lamps, where the build-up of the fouling material could be associated with the reactions between dissolved ions and UV radiation, although the mechanism was not fully understood [141,142].

To investigate this mechanism of the reaction between dissolved mineral ions and UV radiation, the present study constructed a special discharge chamber where a point-to-plane electrode system was placed in a quartz sleeve filled with distilled water, as shown in Fig. 46. The diameter of the quartz sleeve was 25.4 mm to avoid possible damages by shockwaves produced by the spark discharge. The quartz sleeve was found to provide a good UV window for the water samples while effectively trapping various chemical reactive species, heat, and other effects. Before each test, the quartz sleeve was cleaned using 0.1 N HCl solution to remove any possible $CaCO_3$ deposit from previous experiments. Test water samples were circulated outside the quartz sleeve and treated by the spark discharge produced inside the quartz sleeve for the same time periods as in the previous experiments. The results were compared to those obtained for the cases without the quartz sleeve, and no hardness reduction was observed for the samples treated by plasma separated by the quartz sleeve. This indicates that the process

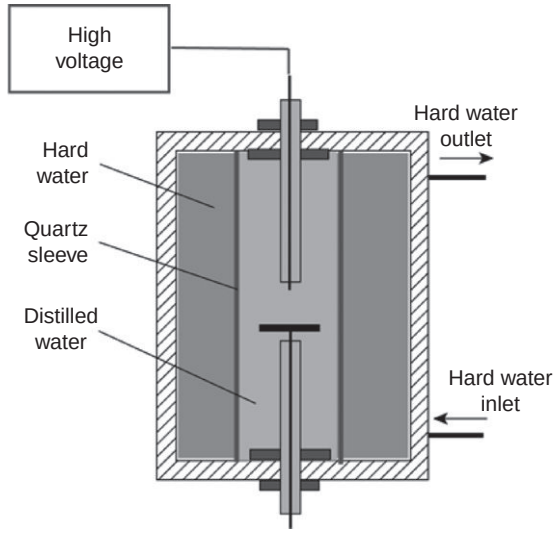

FIG. 46. Modified discharge chamber to test the effect of UV on the precipitation of $CaCO_3$ [130].

of calcium-ion precipitation was not triggered by the transfer of energy to water sample through UV radiation.

3. *Effect of Reactive Species*

From the emission spectrum of the pulsed discharge in distilled water, the formation of hydroxyl radicals and other reactive species by underwater plasma process was reported [60,143,144]. In case of hard water, OH radicals would react with bicarbonate ions to produce carbonate radicals $CO_3^{\bullet -}$, through the following reaction [145,146]:

$$HCO_{3(aq)}^{-} + OH^{\bullet}{}_{(aq)} \Leftrightarrow H_2O + CO_{3(aq)}^{\bullet -} (k = 8.5 \times 10^6\ M^{-1}s^{-1}) \qquad (70)$$

Being a highly oxidizing species, $CO_3^{\bullet -}$ is known to be active in the oxidation of some organic compounds by direct electron transfer to produce the corresponding cation radical and carbonate anion [146]:

$$CO_{3(aq)}^{\bullet -} + R \Leftrightarrow R^{\bullet +} + CO_{3(aq)}^{2-} \qquad (71)$$

Hence, it is hypothesized that the reactive species produced by the spark discharge in hard water may transform the bicarbonate ions into carbonate

ions without going through Eqs. (59) and (60). To test this hypothesis, multiple layers of polyethylene meshes were placed close to the electrodes. Polyethylene is one of the most commonly used materials for active-species scavenger in water. Typical rates of the reaction between the OH radical and organic materials are in the order of 10^9–$10^{10}\,M^{-1}s^{-1}$, about two orders of magnitude higher than that of the reaction between OH radicals and bicarbonate ions. Thus, the polyethylene mesh could serve as an effective scavenger screen to the radicals. The water samples were circulated and treated for the same time period with all the other experimental parameters remaining the same as in the previous experiments. No significant difference was observed in the calcium-ion concentration as compared to the results shown in Fig. 39. Therefore, it was also concluded that the reactive species were not responsible for the plasma-induced $CaCO_3$ precipitation.

4. *Effect of Micro-Heating*

To gain further insight into the structure of the precipitated calcium-carbonate particles, morphological analysis and crystallization examination were performed by SEM and XRD, respectively. Figure 42 shows the particles retrieved from the untreated water sample. The crystals exhibited the morphology similar to round-shaped vaterite, although XRD data showed that the particles were in calcite form (not shown). Figure 5 (b) shows the particles retrieved from the plasma-treated water sample. The crystals demonstrated a typical rhombohedron morphology of calcite, suggesting different mechanisms of precipitation after plasma treatment. Natural $CaCO_3$ precipitation is a complex process that has been studied extensively. It is known that $CaCO_3$ exists in three crystalline polymorphs with different structures: calcite, aragonite, and vaterite. Among them, calcite is the most thermally stable form, and is the dominant polymorph of $CaCO_3$ formed by the loss of CO_2 or evaporation of natural calcium-bicarbonate solutions if temperature is the controlling factor (Siegal and Reams, 1966). The other two crystalline forms are metastable phases of $CaCO_3$, which would transform to calcite spontaneously under normal conditions. The transformation process would be expedited on heating. Therefore, from the fact that calcite with a rhombohedron morphology was formed during the plasma-assisted precipitation process, one may hypothesize that the precipitation may be temperature related.

Direct proof of the validity of this hypothesis is difficult, as it is not easy to produce a local heating zone with temperature up to 5000–10,000 K in water without inducing other effects. In order to test this hypothesis, the

present study utilized a transient hot-wire method. When a thin wire immersed in a sample liquid is heated by electrical current (i.e., joule heating), the wire can play as an electrical heating element and produce an elevated temperature in the surrounding water. The transient hot-wire technique is widely employed today for the measurement of the thermal conductivity of fluids over a wide range of temperatures [148,149]. Although the temperature rise in the conductivity measurement is usually much lower than that in the spark discharge channel, the hot-wire method is still a good approximation as the duration of the high temperature produced by the spark discharge is relatively short (usually in μs) and the intense local heating would quickly be dissipated through the conductive and convective heat transfer in water.

A platinum wire of 80 μm in diameter and 20 mm in length was used in the study. The resistance of the effective length of the wire was about 10 Ω at 25°C. The power for the circuit for heating the wire was provided by a square-wave alternating voltage unit, with the voltage waveform shown in Fig. 47. The wire was heated during a duty cycle and cooled during an off-duty cycle when $V = 0$. The temperature rise of the wire ΔT can be given by the following equation [150]:

$$\Delta T = \left(\frac{q}{4\pi\lambda}\right)\ln\left(\frac{4kt}{a^2 C}\right) \tag{72}$$

where λ and κ are the thermal conductivity and diffusivity of the liquid, respectively; q is the heat generation per unit length of the wire; a is the radius of the wire; $C = e^{y} \approx 1.781$, y is Euler's constant; and t is the time of heating. With $R = 10\,\Omega$ and $l = 20$ mm, q can be calculated as

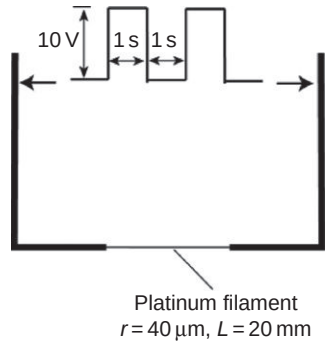

FIG. 47. Schematic diagram and voltage waveform used in the transient hot-wire method used by Yang *et al.* [130].

$$q = \frac{\frac{V^2}{R}}{l} = \frac{2.5 \times 10^4 \text{ W}}{\text{m}} \tag{73}$$

Hence, the temperature rise at the end of heating period was about 825 K. The actual temperature rise would be much lower than the theoretical value due to the boiling of water. During the cooling period, the time constant for cooling was [151]

$$\tau = \frac{\rho V c_p}{hA} \tag{74}$$

where ρ, V, c_p, and A are the density, volume, specific heat, and surface area of the platinum wire, respectively, and h is the convection coefficient of water. Substituting the values for ρ, V, c_p, and A into Eq. (74), one can get

$$\tau \approx \frac{100}{h} \text{ s} \tag{75}$$

For water, the typical convective heat transfer coefficient h is 300–10,000 W/(m^{2}K) [151], which means under normal conditions, the time constant for cooling $\tau << 1$ s, and the wire would be cooled to room temperature during the cooling period.

Figure 48 shows the effect of transient hot wire on the changes in calcium-ion concentration for three different water samples. For all three cases, about 15% hardness decrease was observed for the similar level of energy

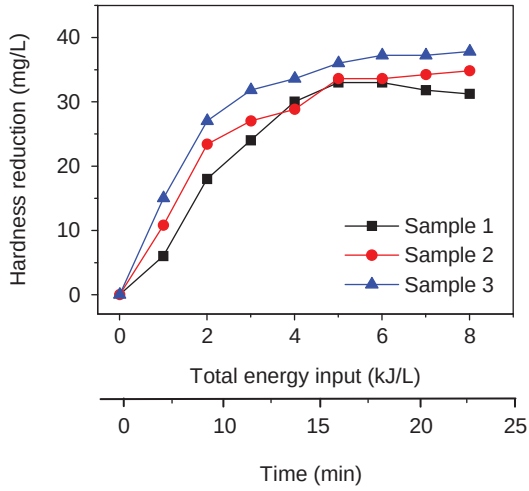

FIG. 48. $CaCO_3$ hardness reduction versus input energy by the transient hot-wire method used by Yang *et al.* [130].

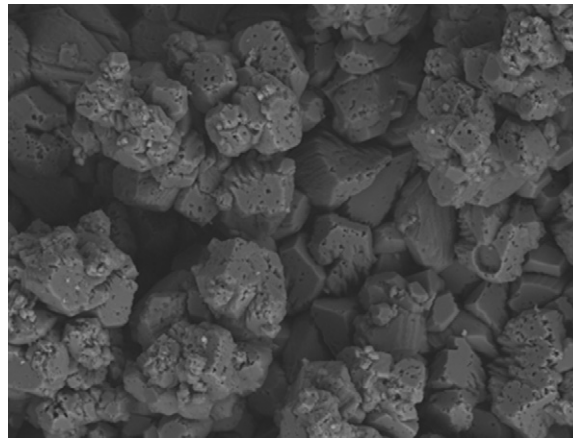

FIG. 49. SEM images of $CaCO_3$ scale obtained from hot-wire surface [130].

input despite the much lower temperature gradient compared to that in the plasma treatment cases. Considering the maximum 25% hardness drop in the case of the pulse spark discharge, one can conclude that the local micro-heating can be one of the major pathways to the precipitation of calcium ions in hard water.

White deposits were observed on the filament immediately after the application of the pulsed voltage. At $t = 15$ min, the filament was fully covered by $CaCO_3$ scale, when hardness reduction reached an asymptotic value. It could be attributed to the fact that the wire could not function as a hot surface in water anymore because of the accumulation of the thermal-insulating $CaCO_3$ scale. The scale on the filament was examined using SEM and XRD as shown in Fig. 49. Rhombohedral shape calcite was observed, which was similar to the shape of $CaCO_3$ particles collected in the plasma treatment cases. Figure 50 shows the number of particles per 1 mL water sample as a function of particle size before and after the hot-wire treatment for Sample 1. No significant increase in the number of particles was observed as compared to the no-treatment cases, possibly due to the fact that most of the $CaCO_3$ precipitated on the hot-wire surface instead of in bulk water.

5. *Non-Thermal Effect of Plasma*

To study the influence of other products produced by plasma discharge and avoid the introduction of any thermal effects, a nanosecond pulsed

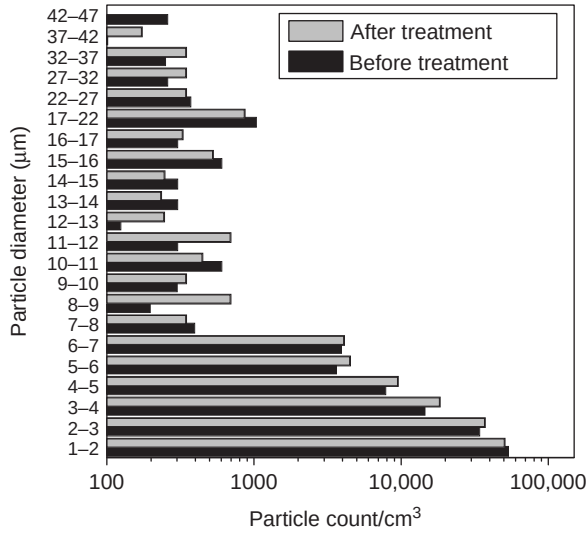

FIG. 50. Particle size distributions before and after transient hot-wire treatment [130].

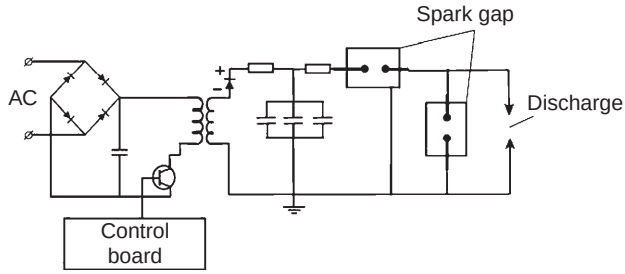

FIG. 51. Schematic diagram of the double spark-gap configuration used by Yang *et al.* [130].

power supply was constructed by adding another spark gap in the circuit as shown in Fig. 51. The second spark gap was built with an adjustable inter-electrode distance to adjust the duration of the pulse so that one could remove the voltage from the load. The typical voltage and current waveforms are shown in Fig. 52. The pulsed source provided 20 kV pulses with about 10 ns in duration at a repetition rate of approximately 38 Hz. Details of the corona discharge produced were reported elsewhere [152]. Spectroscopy measurement through the expansion of $H\alpha$ emission line demonstrated almost non-thermal condition inside the plasma channel,

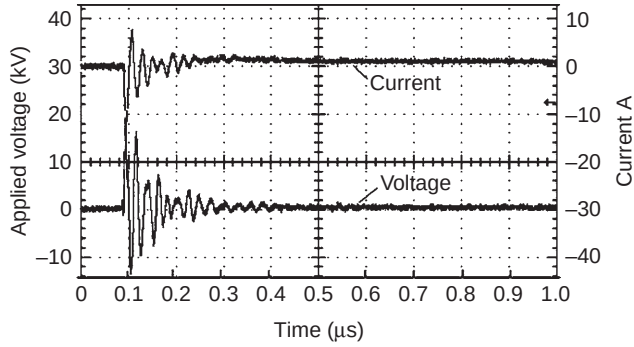

FIG. 52. Typical voltage and current waveform produced by the circuit in the double spark-gap configuration used by Yang *et al.* [130].

confirming that the effect of micro-heating on the precipitation of calcium ions was eliminated.

Figure 53 shows the changes in calcium-ion concentration with the application of the nanosecond corona discharge. Maximum 7% drop in the hardness was observed, demonstrating the possibility to trigger the precipitation process through non-thermal discharges. The precipitation rate

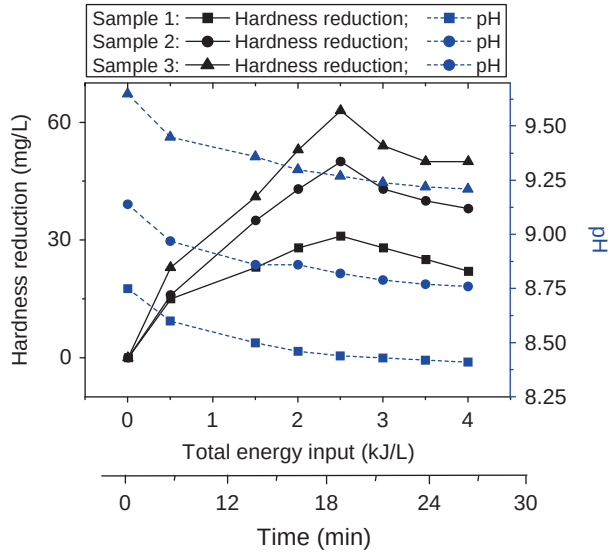

FIG. 53. Variations of $CaCO_3$ hardness and pH over time for different energy inputs by the transient hot-wire method [130].

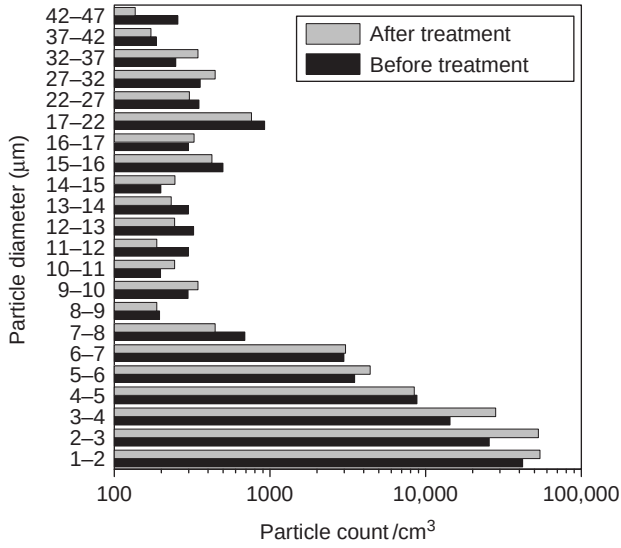

FIG. 54. Particle size distributions before and after pulsed nanosecond discharge treatment [130].

decreased with time, reaching zero at $t = 20$ min. After that, the hardness value began to increase, possibly because precipitated $CaCO_3$ particles began to re-dissolve due to the ionization of water molecules and subsequent acidification of the solution, as illustrated by Eqs. (54)–(55). Drop in pH was observed for all three water samples as shown in Fig. 53.

Figure 54 shows the number of particles per 1 mL water sample as a function of particle size before and after treatment. A significant increase in the number of particles, especially for particles with diameter below 10 μm size, was observed, indicating the occurrence of precipitation in bulk volume. The particles suspended in the bulk volume were collected and examined using both SEM and XRD. Figure 55 shows a mixture of irregular and rhombohedral shaped calcite. The former was probably pre-existing in the water sample before the plasma treatment. The rhombohedral shaped calcite was probably formed during the plasma treatment, which was in similar polymorph with $CaCO_3$ particles collected in the regular spark discharge treatment.

6. *Further Discussion*

The present study proposes that the local micro-heating is the primary mechanism in the calcium hardness reduction by spark discharges. Since

FIG. 55. SEM image of $CaCO_3$ particles obtained from water sample treated by pulsed nanosecond discharge [130].

one can easily precipitate supersaturated calcium ions in hard water by simply increasing water temperature (i.e., volume heating). Technically sound and simple, but it is not a real solution due to high cost. Hence, instead of volume heating, the present study attempted to dissociate the bicarbonate ions using spark discharges in water, which is referred as a *local micro-heating*.

For comparison, one can calculate the numbers of OH^- from both the volume heating and local heating in order to see the benefit of the local heating in the precipitation of calcium ions. The amount of OH^- per unit time which one can produce from the dissociation reaction of bicarbonate ion, Eq. (9), is calculated as [94]

$$n_{OH^-} = n_{HCO_3^-} \times k \tag{76}$$

where is the number of HCO_3^- participating in the reaction and k is the reaction rate coefficient. According to the Arrhenius equation, the reaction rate coefficient k becomes

$$k = Ae^{-E_a/T} \tag{77}$$

where E_a is activation energy and T is the system temperature (in the unit of eV). Due to the exponential curve of the equation, the Arrhenius equation indicates that *the higher the water temperature is, the faster the reaction will be*. The present study utilized spark discharges in water. Hence, one can expect a very intense local heating of a small volume of water around the tip

of the electrode, significantly raising the temperature of the small volume of water near the tip.

The important scientific issue is whether the spark discharge used in the study can dissociate HCO_3^- without spending a large amount of electrical energy. One can examine two cases (i.e., volume heating and local heating) to find out which case produces more OH^- for the exactly same amount of energy spent.

For the volume heating, one can assume to heat the entire volume of water by one degree (e.g., from 300 K to 301 K). Then, the number of OH^- one can produce for $E_a \approx 1$ eV becomes

$$\begin{aligned} n_{OH^-} &= n_{HCO_3^-} \times k = n_{HCO_3^-} \times A e^{-E_a/T} \\ &= A n_{HCO_3^-} e^{-11000/301} = e^{-36.5} A n_{HCO_3^-} \end{aligned} \tag{78}$$

For the local heating using spark discharge, one can assume to heat 1% of the entire water volume by 100 degrees (e.g., from 300 K to 400 K). The number of HCO_3^- participating in the reaction is 1%, i.e., $n'_{HCO_3} = 0.01 \times n_{HCO_3}$, because spark discharge is assumed to heat only 1% of the total water volume. Then, the number of OH^- one can produce for $E_a \approx 1$ eV becomes

$$\begin{aligned} n'_{OH^-} &= n'_{HCO_3} \times k' = n'_{HCO_3} \times A e^{-E_a/T'} = 0.01 A n_{HCO_3} e^{-11{,}000/400} \\ &= 0.01 e^{-27.5} A n_{HCO_3} = e^{-32} A n_{HCO_3} \end{aligned} \tag{79}$$

Comparing the number of the hydroxyl ions produced for the two cases, i.e., n_{OH^-} and n_{OH^-}, one can see that the local heating by spark discharge can produce about 100 times more OH^- and thus 100 times more efficiently precipitate dissolved calcium ions in hard water than the volume heating.

In conclusion, it has been demonstrated earlier that pulsed plasma discharge can trigger the precipitation process of $CaCO_3$ in hard water [128]. Equilibrium of calcium-ion concentration after approximately 10-min plasma treatment was observed in previous experiments. The possibility to shift the equilibrium and enhance the precipitation was demonstrated by degassing the dissolved CO_2 from water through spray circulation. It was hypothesized that the precipitation process was associated with different effects produced by the discharge. Experiments were conducted showing that UV radiation or reactive species produced by the spark discharge was negligible for the precipitation process. The effect of micro-heating was tested using a hot-wire method, while the non-thermal effect of the plasma was investigated by application of a nanosecond pulsed electric discharge in water.

It was observed that both cases showed about 10% drop of calcium-ion concentration, indicating that the precipitation process may be associated with both the thermal and non-thermal effects of plasma in water. The morphology of the $CaCO_3$ particles collected from the two experiments was in agreement with that collected from water samples treated by conventional thermal spark discharge, indicating that the precipitation process may be associated with both the thermal and non-thermal effects of plasma. Further investigations are necessary to determine the detailed pathways of $CaCO_3$ precipitation by pulsed plasma treatment.

VII. Application for Mineral Fouling Mitigation in Heat Exchangers

$CaCO_3$ is the most common scale-forming mineral occurring in industrial water facilities. It is generally the first mineral to precipitate out either by heating or by concentrating water due to its relatively low solubility, although its concentration in source water significantly varies depending on locations. Control of $CaCO_3$ scale is thus often the limiting factor in most industrial cooling water applications, as it decreases the efficiency of heat exchangers because of the insulating effect of the deposits. Furthermore, the formed deposits reduce the opening area in heat exchanger tubes, thus requiring more pumping power if one desires to maintain a constant flow rate [116,117,121,122]. A 0.8-mm layer of $CaCO_3$ scale can increase the energy use by about 10% [153]. If one can prevent or mitigate fouling on heat transfer surfaces, it not only increases heat exchanger efficiency, but also reduces the expenses associated with the cleaning of fouled heat exchangers. In addition to the benefit of reduced mineral fouling, the COC can be increased, resulting in water savings by reduced make-up and blowdown [118,119,154,155]. Blowdown is the water drained from cooling equipment to remove mineral build-up.

Various chemical and non-chemical methods have been used to prevent the mineral fouling. Among them the scale-inhibiting chemicals like chlorine and brominated compounds were the best choices, as they had a relatively high success rate. However, there were also many disadvantages and concerns in their use. Aside from the high cost of chemicals, more stringent environmental laws increased the costs associated with their storage, handling, and disposal. These chemicals also pose danger on human health and to the environment with accidental spills or accumulated chemical residues over a long period of time. Thus, there is a need for a new approach which is safe and clean from both environmental and cost points of view in cleaning and maintenance of heat exchangers. PWT is a non-chemical method to mitigate

mineral fouling, which utilizes electric or magnetic fields [156–158], catalytic surfaces [125,126], solenoid coils [159–161], or ultrasounds [118]. Numerous studies have been reported for the effectiveness of ultrasonic, solenoid coils, magnetic fields, catalytic material, and electrolysis. Recently, Yang and his coworkers [128] reported that oversaturated hard water treated by underwater pulsed spark discharge may induce the precipitation of $CaCO_3$ in supersaturated water and produce a significantly greater number of particles than the untreated water. Note that the precipitation of dissolved mineral ions takes place in the bulk water instead of on the heat exchanger surfaces. This is the key process for all PWT methods, as the particles suspended in water tend to form a soft coating on heat transfer surfaces. If the shear force produced by flow is large enough to remove the soft coating, mineral fouling can be prevented or mitigated.

In this section, direct pulsed spark discharge generated in water is used to mitigate mineral fouling in a double-pipe heat exchanger. The new method of using microsecond-duration pulsed plasma in water is a major improvement over the aforementioned PWT because these previous PWT methods produce induced electric fields in water, where the field strength is often very small ($\sim$1 mV/cm) due to involved physics laws such as Faraday's law. In comparison, an electric field above 10^6 V/cm could be produced by pulsed plasma in water in the present study, leading to higher efficiency than previous PWT devices.

A. Experiment Setup

The present study conducted fouling experiments in a heat exchanger by circulating artificially-prepared hard water through a simulated cooling-tower system. Figure 56 shows the schematic diagram of the present test facility, which consisted of two separate loops for circulation of hot and cooling water, a pulsed spark discharge generation system, a cooling tower, a heat exchanger test section, pumps, and a data acquisition system.

1. Heat Transfer Fouling Tests

Figure 57 shows the schematic diagram of the counterflow concentric type heat exchanger. The length of the heat transfer test section was 600 mm. Hot water was circulated inside the inner tube, while artificial hard water (i.e., cold water) was circulated through the gap between the inner and outer tubes of the concentric heat exchanger. The inner tube was made of copper with internal and external diameters of 19.1 and 22.2 mm, respectively, while the outer tube was made of a clear acrylic tube for visual observation of scale deposits during the fouling tests with internal and external diameters of 28.6

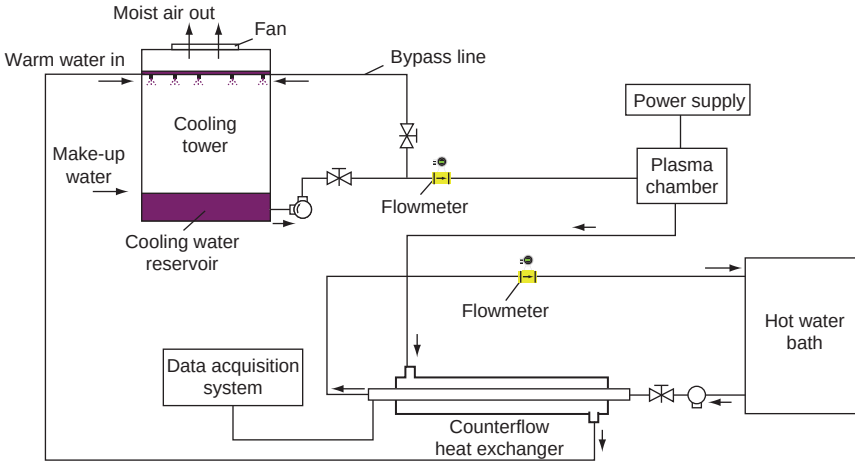

FIG. 56. Schematic diagram of the experimental set-up used by Yang *et al.* [162].

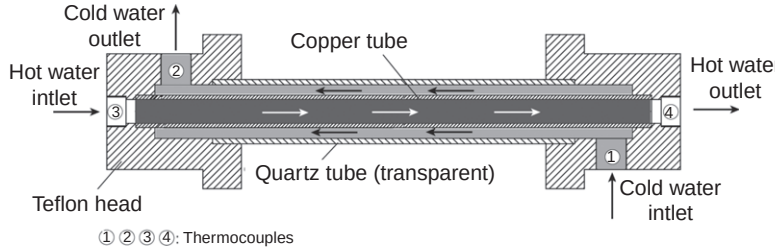

FIG. 57. Schematic diagram of the heat transfer test section used by Yang *et al.* [162].

and 34.9 mm, respectively. The annulus gap formed between the two tubes had a cross-sectional area of 0.000255 m^2. O-rings were used on grooves at the inlet and outlet sides of Teflon head blocks used for the mounting of copper tube to prevent any leakage between the hot water and the cold water.

The cold water passed through the annulus gap flowing in the opposite direction at two different velocities (0.1 and 0.5 m/s), while hot water flowed inside the copper tube at velocity ranging from 1.0 m/s to 1.2 m/s. The Reynolds number at the cold-water side (i.e., annulus gap) varied from 3000 to 15,000, whereas that at the hot-water side was varied from 43,000 to 52,000.

Four copper–constantan (type T) thermocouples were installed at the inlet and outlet sides of the counterflow heat exchanger (as shown in

Fig. 57) and temperatures measured every 1 min for a test period of 24–48 h. The temperature values were sent to a data acquisition system for automatic data storage during the fouling test. The heat transfer test section, copper tube lines, plasma generation system, and other equipment were all connected to ground to accurately measure temperatures as well as to prevent any adverse effects of static electricity. The inlet temperature of cooling water was maintained at 20 ± 3°C by means of a mini cooling tower throughout the entire experiments, whereas the inlet temperature of hot water was maintained at 95 ± 3°C using a hot water heater and re-circulating pump.

The heat transfer rate, Q, was calculated from both hot- and cooling-water sides as

$$Q = \dot{m}_{\mathrm{h}} c_{\mathrm{p}} \Delta T_{\mathrm{h}} = \dot{m}_{\mathrm{c}} c_{\mathrm{p}} \Delta T_{\mathrm{c}} \tag{80}$$

where $\dot{m}_{\mathrm{h}}$ and $\dot{m}_{\mathrm{c}}$ are the mass flow rates of hot and cooling water, respectively; c_{p} is the specific heat of water; and ΔT_{h} and ΔT_{c} are the temperature differences between inlet and outlet of hot and cooling water, respectively. The heat transfer rates at hot and cooling water sides should be equal to each other under ideal conditions. In reality, the heat transfer rate in the hot water side was less, approximately 5%, than that in the cold water side as parasitic heat loss takes place to the surroundings in spite of insulation. Hence, the heat transfer rate measured from the cooling water side was used to calculate the overall heat transfer coefficient. The heat transfer rate Q varied from 1.9 kW to 3.2 kW depending on the flow velocity at the cold-water side.

The overall heat transfer coefficient U was calculated using the following equation [151]:

$$U = \frac{Q_{\mathrm{c}}}{A_{\mathrm{o}} \Delta T_{\mathrm{LMTD}}} \tag{81}$$

The heat transfer surface area A_{o} was calculated using the outer diameter of the copper tube ($d_{\mathrm{o}} = 22.2$ mm) with an effective heat transfer length of 600 mm (i.e., $A_{\mathrm{o}} = \pi\ d_{\mathrm{o}} L_{\mathrm{effective}}$). The log mean temperature difference, ΔT_{LMTD}, was determined as follows [151]:

$$\Delta T_{\mathrm{LMTD}} = \frac{(T_{\mathrm{h,o}} - T_{\mathrm{c,i}}) - (T_{\mathrm{h,i}} - T_{\mathrm{c,o}})}{\ln\ \left[\frac{(T_{\mathrm{h,o}} - T_{\mathrm{c,i}})}{(T_{\mathrm{h,i}} - T_{\mathrm{c,o}})}\right]} \tag{82}$$

The fouling resistance, R_{f}, was calculated using the following equation [151]:

$$R_f = \frac{1}{U_f} - \frac{1}{U_i} \tag{83}$$

where U_f is the overall heat transfer coefficient for fouled states, while U_i is the overall heat transfer coefficient corresponding to the initial clean state. The latter (U_i) was determined using distilled water (without chemicals) and without the use of PWT device during the initial calibration run prior to the fouling tests with artificial hard water. All experimental procedures, materials, equipment, and inlet temperature settings for hot and cold water sides were identical for all tests.

Detailed uncertainty analysis using the present test method proposed by Kline and McClintock [163] has been provided elsewhere [164]. In summary, the flow rate measurement had 3% error, temperature measurements had 1% error, heat transfer rate measurement had 4.4% error, surface area measurement had 0.2% error, universal heat transfer coefficient measurement had 5.3% error, and fouling resistance measurement had 10% error.

2. *Pulsed Spark Discharge Generation System*

Figure 58 shows a schematic drawing of a spark discharge generation system used in the present study. The system consisted of two components: a discharge chamber utilizing point-to-plain electrode system immersed in water (left) and a HV power supply with a capacitive energy storage (right). In a typical experiment, an 8.5-nF capacitor bank stored energy ($E_{CB} \approx 2.65$ J) at voltage ($V_{CB} = 25$ kV) was discharged through a 5-mm electrode gap into the discharge chamber. The peak current of these pulses was about 90 A. Upon charging the electrodes, local ohmic heating created vapor microbubbles within the gap. The energy effectively delivered during the discharge process was estimated to be 2 J/pulse. These discharges simultaneously generated a localized hot spot, high electric field, and traveling

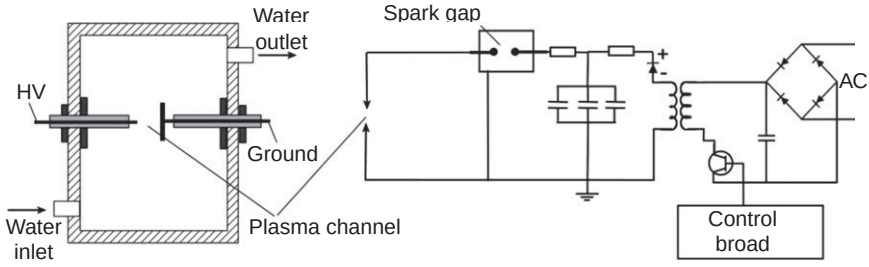

FIG. 58. Schematic diagram of the discharge chamber and electric circuit used in the study by Yang *et al.* [162].

shockwaves. The details of the electric circuit diagram and electric waveforms were discussed elsewhere [165].

3. *Artificial Hard Water*

The hardness of water varied from 250 ppm to 500 ppm in the present fouling experiments. The desired water hardness was obtained by mixing two chemicals, $CaCl_2$ and sodium bicarbonate ($NaHCO_3$), to Philadelphia city tap water at right proportions. The chemical reaction occurring in the artificially-prepared hard water can be described as follows:

$$CaCl_2 + 2NaHCO_3 \rightarrow CaCO_3 + 2NaCl + H_2O + CO_2 \quad (84)$$

To obtain the desired hardness in cooling water, the proportions as shown in Table VI were used.

The hard water reservoir was first filled with tap water at a volume of 250 L after cleaning. With the use of a bypass line, the tap water in the reservoir was continuously circulated (not through the whole fouling system setup, but only in the reservoir). $CaCl_2$ powder was added to the reservoir with gentle stirring using an electric stirrer and was left for 10 min to dissolve. Subsequently, $NaHCO_3$ powder was also added to the reservoir and was gently stirred. After 5–7 min, about 100 mL of water sample was taken out from the bottom of the reservoir and used for water chemistry measurements. The measurement results were used as the initial water hardness (at time zero). Water samples of 100 mL were collected every hour at 12–24 h intervals during each fouling test.

During the fouling test, the artificial water in the reservoir was automatically added to the reservoir of the cooling tower by gravity via a floating-ball valve, which was installed to control the inflow of make-up water to the cooling tower. Thus, the water volume at the cooling tower was maintained constant during the fouling test. Note that the blowdown was not used in the present study.

TABLE VI

AMOUNT OF $CaCl_2$ AND $NaHCO_3$ USED IN ARTIFICIAL HARD WATER

Tap water volume: 0.250 m^3	Hardness (ppm)	
	250 ppm	500 ppm
Calcium chloride (110.98 g/mol)	69.38 g	138.75 g
Sodium bicarbonate (84 g/mol)	105 g	210 g

4. Scanning Electron Microscopy (SEM) and X-Ray Diffraction (XRD) Measurements

SEM images and XRD analyses were obtained from the fouled copper tubes by resident technicians at Drexel SEM and XRD laboratories. SEM (FEI XL30) images were obtained to examine the topography and geometry of $CaCO_3$ scales. Scale samples of approximately $0.5\,cm \times 0.5\,cm$ were obtained from fouled copper tubes for all cases by manually cutting through the tubes using a saw blade. The scale samples were coated with platinum through low-vacuum sputter coating in order to prevent the accumulation of static electric charge during the irradiation of electron. XRD (Siemens D500) analyses were conducted on scale powders taken from fouled copper tubes manually cut using a saw blade to characterize the crystallographic structure of the scale deposits for both no-treatment and plasma-treated cases.

B. Results and Discussion

1. Cycle of Concentration (COC)

The COC is often defined as the ratio of the dissolved solids in cooling-tower water to those in makeup supply water. Figure 59 shows variations in COC over time for the case of 250-ppm hard water with a flow velocity of 0.5 m/s. The value of COC increased almost linearly with time because of zero blowdown. The COC reached approximately 2.8 at the end of the

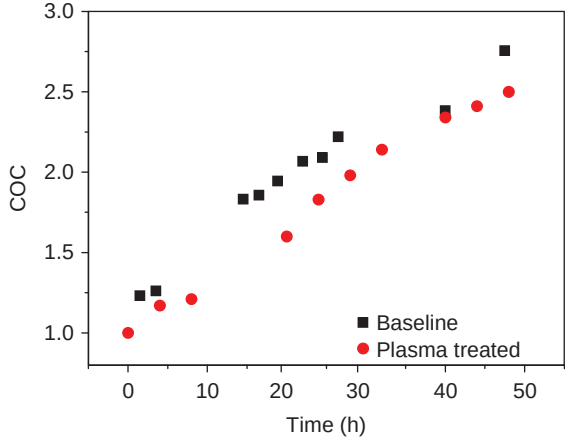

FIG. 59. Variations in cycle of concentration (COC) vs. time for 250 ppm hard water under no-treatment and plasma-treated cases with a flow velocity of 0.5 m/s [162].

fouling test for the no-treatment case, whereas it arrived at 2.4 for the plasma-treated case. Since the hardness of the makeup water was 250 ppm, the hardness of circulating water became approximately 600–700 ppm at the end of the fouling tests for both cases. In addition, the COC value for the plasma-treated case was consistently smaller by about 0.3–0.5 than those for the no-treatment cases during the entire fouling test, reflecting the fact that the pulsed spark discharge was continuously precipitating calcium ions from water. Note that the COC for other cases studied in the study (i.e., at different flow velocities and different hardness) also reached approximately three at the end of fouling tests with zero blowdown, indicating that the water hardness was about 750 and 1500 ppm for 250 and 500 ppm cases, respectively, near the end of the test. Such extremely harsh fouling conditions were utilized in the study in order to expedite the fouling process and examine the performance and limitation of the pulsed spark discharge system.

2. *Fouling Resistance*

Figure 60 shows the results for the fouling tests obtained using water hardness of 250 ppm for the no-treatment and plasma-treated cases at a flow velocity of 0.1 m/s. Due to high water hardness, there was no induction period in both cases. An induction period is usually depicted by a straight horizontal line in the beginning of the fouling curve, which indicates lateral

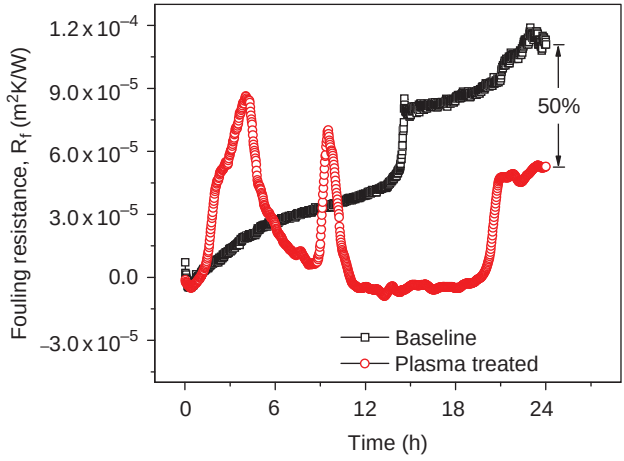

FIG. 60. Fouling resistances for 250 ppm hard water under no-treatment and plasma-treated cases with a flow velocity of 0.1 m/s [162].

spreading of scale deposits on heat transfer surface. In the present study, the artificial hard water that contained calcium and bicarbonate ions reacted quickly to the hot heat transfer surface, making immediate depositions of calcium salt particles on the surface as soon as the fouling test begun.

The scale deposition involved the cumulative effect of a direct diffusion of dissolved calcium ions to the heat transfer surface and the deposition of precipitated calcium salt particles due to supersaturated conditions and accelerated precipitation of calcium salts by PWT [4]. The fouling resistance in the no-treatment case demonstrated a slow increase in the first 14 h of operation. At $t = 15$ h, the fouling resistance increased dramatically as the entire surface of copper tube was fully covered by mineral scales. After that, at $t = 16$ h, the fouling resistance began to rise as the thickness of the scale layer slowly increased until the end of test, indicating that the deposition rate of the scales was consistently larger than the removal rate during this period because of the slow flow velocity.

The fouling resistance curves obtained in the cases of the plasma treatment depicted a completely different trend compared to that obtained for the no-treatment case. The fouling resistance had a steep increase to a maximum value in the first 4 h of operation. Note that there are two different categories of fouling: particulate fouling and precipitation fouling. The former refers to the adhesion of suspended particles to the heat transfer surface in the form of soft sludge. This type of fouling can easily be removed by shear forces created by flow rather than those deposits produced from the precipitation of mineral ions directly on the solid heat transfer surface, i.e., precipitation fouling. It was demonstrated in the authors' previous study that the precipitation of $CaCO_3$ could be induced by application of pulsed spark discharge in supersaturated hard water and thus creating a significantly greater number of $CaCO_3$ particles than the untreated water [25]. Hence, much faster particulate fouling took place at the first several hours of the test, causing the dramatic increase in the fouling resistance. At $t = 4$ h, the fouling resistance showed a significant drop, indicating that large-scale pieces were dislodged due to the shear stress of the water flow. The similar particulate fouling build-up and dislodge process were repeated during the period between 9 and 12 h. The final asymptotic fouling resistance at the end of the test was 50% lower than that obtained from baseline test, clearly indicating the beneficial effect of the plasma discharge on the mitigation of mineral fouling.

Figure 61 shows photographs of sections of fouled copper tubes for the no-treatment and plasma-treated cases, which were taken after the copper tubes were removed from the heat transfer test section and completely dried. Visual inspection on the fouled tubes indicated that there were thick scale deposits (>1 mm) over the entire tube surface for the no-treatment case.

FIG. 61. Photographic images of the scales for (a) no-treatment; (b) plasma treatment cases ($CaCO_3$ hardness of 250 ppm and a flow velocity of 0.1 m/s) [162].

For the case of the plasma treatment, the scale deposits appeared to be much thinner than that observed in the no-treatment case. One could clearly see the copper-tone color of the tube at the end of fouling test for the plasma-treated case, indicating that the pulsed spark discharge could significantly mitigate the scale deposits on the tube surface.

Figure 62 shows the results for the fouling tests obtained using water hardness of 250 ppm for both cases at a flow velocity of 0.5 m/s with zero blowdown. The overall fouling resistance showed a significant drop comparing with that obtained at 0.1 m/s, mainly because of the higher removal rate caused by a higher flow velocity. For the no-treatment case, the fouling resistance had a steep increase to a local maximum value in the first 3 h of operation. At $t = 3$ h, the fouling resistance stopped increasing and the value remained unchanged for the next 16 h, indicating that there must have been some balance between the deposition rate and removal rate for the no-treatment case due to the higher shear stress produced by a high flow

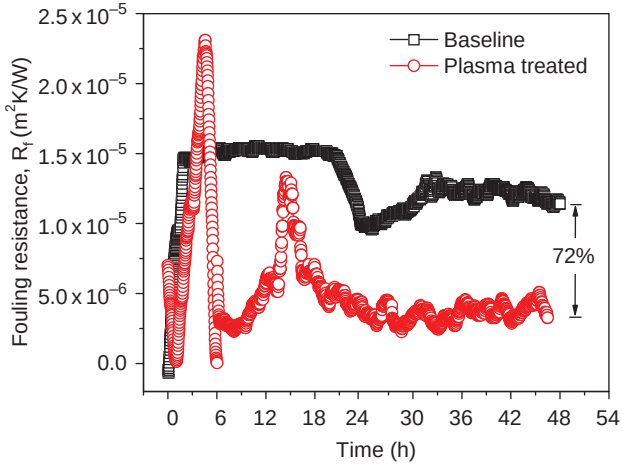

FIG. 62. Fouling resistances for 250 ppm hard water under no-treatment and plasma-treated cases with a flow velocity of 0.5 m/s [162].

velocity. At $t = 19$ h, the no-treatment case showed a significant drop in the fouling resistance. After $t = 30$ h, the fouling resistance showed slight up-and-down trends with its mean value slightly decreasing with time till the end of the test.

The fouling resistance curves obtained in the case of plasma treatment at 0.5 m/s depicted similar trend as the 0.1 m/s case shown in Fig. 60 at the first 20-h period, although at a much lower value. The fast rise and fall of fouling resistance observed in the first 6-h period indicated both accumulation and removal of particulate fouling on the heat exchanger surface. After $t = 20$ h, the fouling resistances slightly went up and down numerous times until the end of the test. The up-and-down trends of the fouling resistance clearly indicated that the old scales were repeatedly removed from the heat transfer surface as the new scales continued to develop. The surface was not fully covered by scales at the end of the test, and the final fouling resistance was reduced by 72% comparing to that for the no-treatment case. The improved efficiency in mitigating fouling observed in the plasma-treated case can be explained as follows: calcium ions were continuously precipitated to calcium salt particles by the spark discharge. Subsequently, particulate fouling took place as calcium particles adhered to the heat transfer surface, creating a soft sludge coating on the surface. The coating can be more easily removed due to high flow. Similar results were reported previously with a solenoid coil by Cho *et al.* [120–122], who showed better mitigation results at a high flow rate in the study.

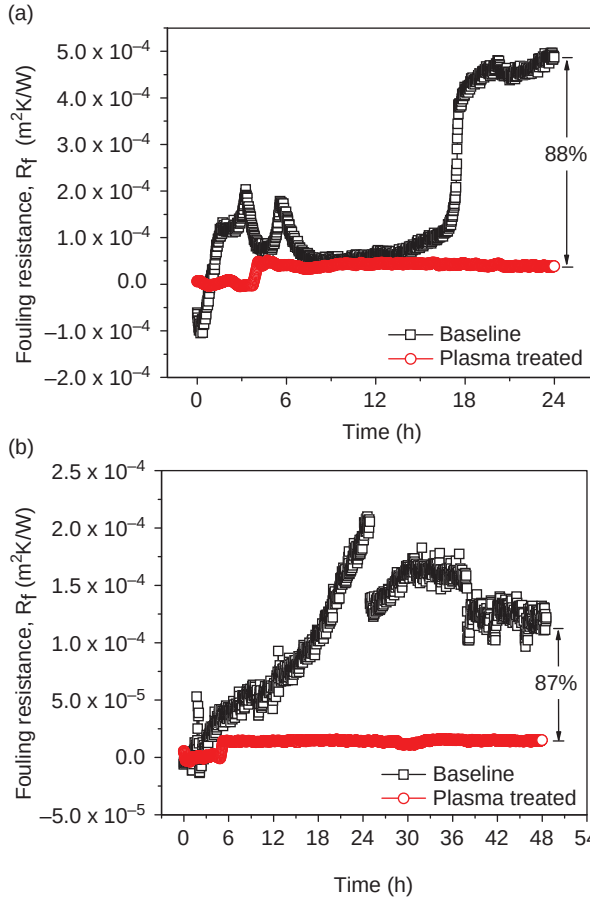

FIG. 63. Fouling resistances for 500 ppm hard water under no-treatment and plasma treatment cases with two different flow velocities: (a) 0.1 m/s; (b) 0.5 m/s [162].

Figure 63 (a) and (b) shows the results for the fouling tests obtained for the case of water hardness of 500 ppm and flow velocities of 0.1 and 0.5 m/s for the plasma-treated and no-treatment cases. Due to high water hardness, the rate of increase in the fouling resistance was very steep for the no-treatment case at 0.1 m/s, which reached the local maximum at $t = 3$ h. After this point, the fouling resistance significantly decreased till $t = 5$ h, indicating that the removal of scale particles was greater than the new deposits during this period, probably due to a reduced opening in the heat transfer test section by the scale deposits and subsequently increased wall

shear stress. Again, the similar cycle repeated during 5–9 h period. Note that the supersaturation level in the cooling water was extremely high so that there must have been a large number of suspended $CaCO_3$ particles in water even in the no-treatment case, leading to particulate fouling on the heat transfer surface. Thus, one might expect that the scale deposits might have been soft, which helped increasing the removal rate.

For the cases of plasma treatment, there was an induction period of approximately 3 h before a sudden but brief increase of fouling resistance, indicating that the heater exchanger surface was fully covered by the scales at $t \approx 3$ h. After $t \approx 4$ h the fouling resistance impressively remained constant till the end of the test. The asymptotic value for the plasma-treated case was about 88% lower than that for the no-treatment case.

Figure 63 (b) presents the fouling resistance for the flow velocity of 0.5 m/s, showing that there was also no induction period for the no-treatment case. As the velocity of cold water in the heat transfer test section was increased from 0.1 m/s to 0.5 m/s, there was less fouling deposit in general as the removal rate increased due to increased shear force, a phenomenon which was also reported by a recent study [111]. Note that at a high velocity, there was a high mass deposition rate. However, the shear force created by the flow increased such that the scales are more efficiently removed, resulting in reduced fouling resistances. An 87% drop in the fouling resistance was obtained for the plasma-treated case compared with the no-treatment case, again confirming the effectiveness of the plasma treatment of water on mitigating the mineral fouling. It is of note that even for the case of 500 ppm, where the hardness became about 1500 ppm near the end of test with zero blowdown, the plasma-treated case could reduce the fouling resistance by 88 and 87% for flow velocities of 0.1 and 0.5 m/s, respectively.

Figure 64 shows photographs of sections of fouled copper tubes for both no-treatment and plasma-treated cases for 500 ppm hardness water. The photographs taken for 500 ppm case were similar to those obtained for 250 ppm case, but the scale was thicker due to the higher hardness and smaller flow velocity.

3. *Scanning Electron Microscope Images*

Figure 65 (a) and (b) shows SEM images of $CaCO_3$ scales for both the no-treatment and plasma-treated cases for 250 ppm hard water at a flow velocity of 0.5 m/s. The SEM images for the no-treatment case showed particles less than 10 μm in size, with sharp and pointed tips in crystal structures, whereas those obtained with plasma treatment showed particles of 15 μm in size and above, due to the precipitation effect of spark discharges, with blunt-edged crystals. The sharp and pointed crystal tips observed in the no-treatment case

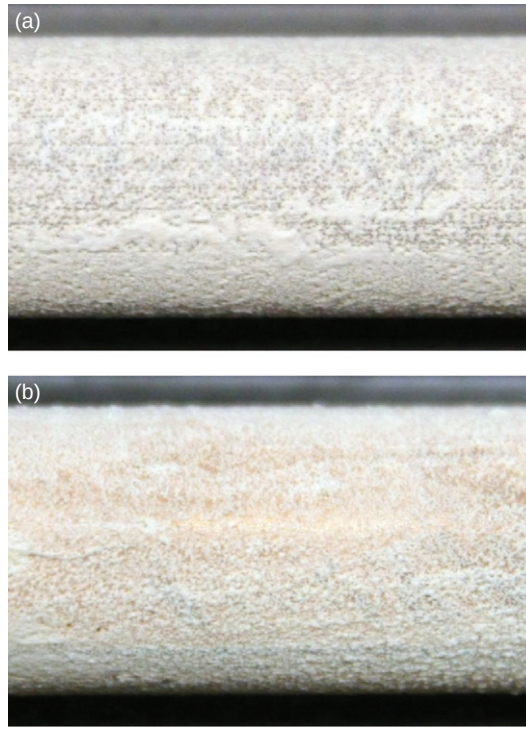

FIG. 64. Photographic images of the scales obtained for (a) no-treatment; (b) plasma treatment cases ($CaCO_3$ hardness of 500 ppm and a flow velocity of 0.1 m/s) [162].

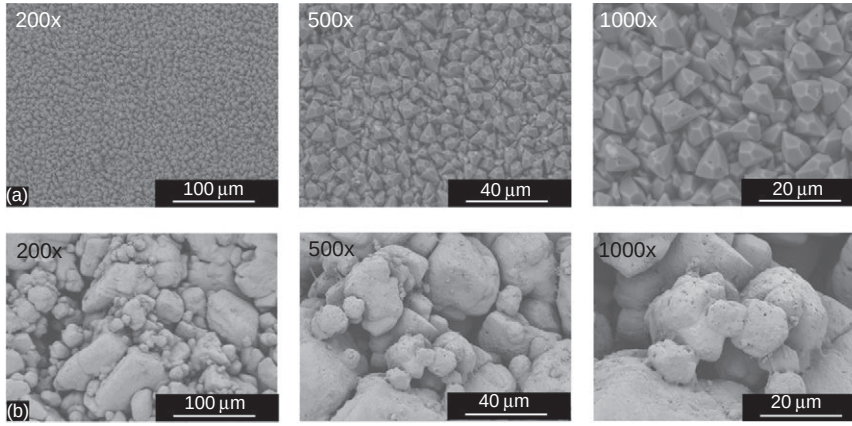

FIG. 65. SEM photographs of the scales obtained for (a) no-treatment; (b) plasma-treated cases ($CaCO_3$ hardness of 250 ppm and a flow velocity of 0.5 m/s) [162].

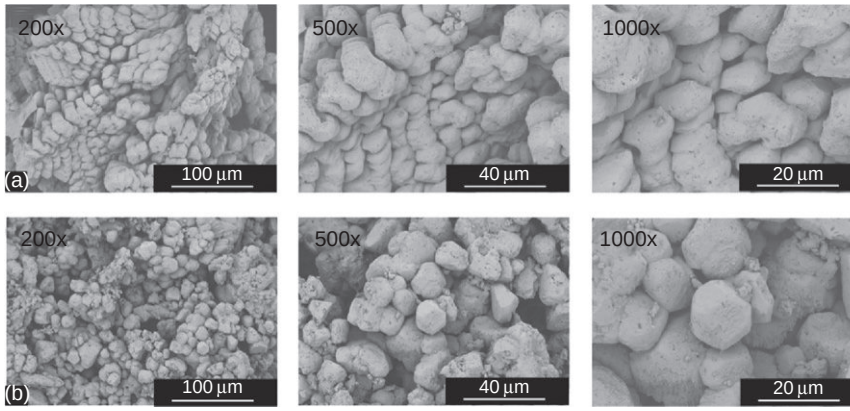

FIG. 66. SEM photographs of the scales obtained for (a) no-treatment; (b) plasma-treated cases ($CaCO_3$ hardness of 500 ppm and a flow velocity of 0.1 m/s) [162].

are believed to be produced through precipitation reactions of mineral ions on the heat transfer surface, thus adhering to the heat transfer surface more strongly than blunt crystals observed in the plasma case.

Figure 66 (a) and (b) shows similar SEM images (200×, 500×, and 1000×) of $CaCO_3$ scales for the no-treatment and plasma-treated cases for 500 ppm hard water at a flow velocity of 0.1 m/s. The SEM images obtained from the no-treatment case showed a more organized regular structure, which can be attributed to the aforementioned particulate fouling on the heat exchanger surface. For plasma treatment, the images showed random rounded particles with a less organized structure. The size of the particles obtained from the plasma treatment case was slightly larger than that retrieved from no-treatment case.

C. X-RAY DIFFRACTION TESTS

$CaCO_3$ is a crystalline substance that exists in three polymorphs: calcite, aragonite, and vaterite [166]. Each polymorph has a unique crystallographic structure with a unique XRD spectrum that serves as its fingerprint. The present XRD analyses were conducted to determine the crystallographic phase of scale deposits so that the focus was on spectrum peaks and not on the intensity. Figure 67 (a) shows the standard XRD spectra of the calcite phases of $CaCO_3$ as a reference, which has a prominent peak of intensity at $2\theta = 29.5°$.

Figure 67 (b) and (c) presents the results of the XRD analyses for the no-treatment and plasma-treated cases at water hardness of 500 ppm and a flow

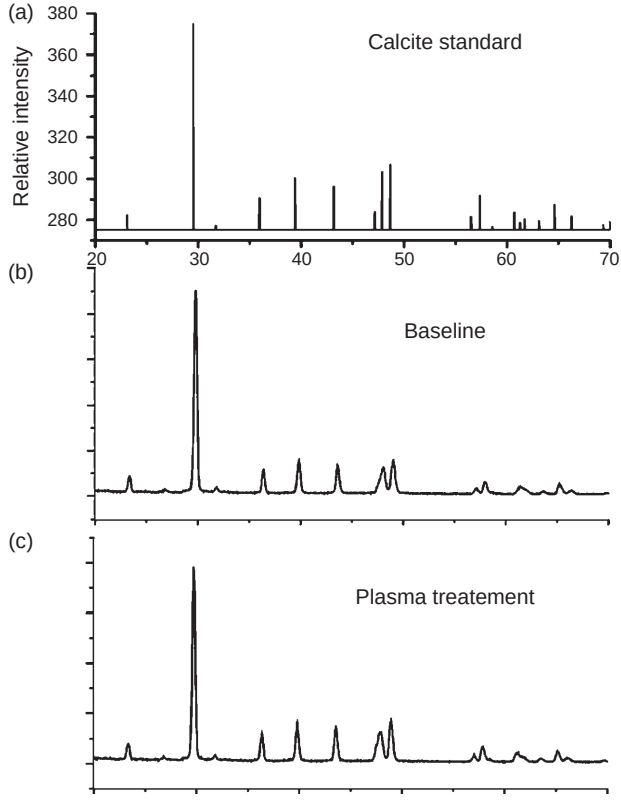

FIG. 67. XRD analyses of the scales for (a) standard calcite; (b) no-treatment; (c) plasma-treated cases (500 ppm $CaCO_3$ hardness and a flow velocity of 0.1 m/s) [162].

velocity of 0.1 m/s. The results were compared to the standard XRD spectra of $CaCO_3$ given in Fig. 67 (a). For both cases, the peaks depicted that of a calcite crystal. Although most previous studies reported aragonite crystals for no-treatment cases [120,167], the present XRD result did not show aragonite for the no-treatment case. It can be attributed to the fact that even for the no-treatment cases there must have been a large number of suspended calcium particles in water in the present study due to extremely supersaturated states of cooling water and no blowdown in the study. Hence, even for the no-treatment case, one might expect to have a large number of suspended particles in water, thus leading to a calcite form of $CaCO_3$ scales on the heat transfer surface.

For the cases of plasma treatment, spark discharge would produce more suspended calcium particles in hard water than the no-treatment cases [128],

producing particulate fouling or calcite form of calcium crystal at the heat transfer surface. The XRD results for the no-treatment and plasma-treated cases at water hardness of 250 and a flow velocity of 0.5 m/s were similar to the results given in Fig. 67.

VIII. Application for Water Sterilization

Pulsed plasma technology is a cost-effective and environmentally friendly technology for the destruction of microorganisms in contaminated potable water and wastewater [27,168–170]. Plasma discharges in water can produce high electric field, strong UV radiation, shockwaves, ozone, short-living active species ($^{\bullet}OH$, $^{\bullet}H$, $^{\bullet}O$, $^{1}O_2$, $^{\bullet}HO_2$, O_2^-, H_2O_2), and charged particles for the effective sterilization of water [171]. There are two main approaches of using high-voltage pulse discharges for water sterilization: one is to use high-energy pulses of ≥ 1 kJ [172] and the other is to use low-energy pulses of $\sim$1 J [168,173]. The second approach is especially interesting due to the simplicity in designing the discharge system that can readily be integrated into a household water delivery system. It can also be developed into a portable water supply system for safe drinking water in remote areas and/or underdeveloped countries. Next, recent advances in the plasma applications for water sterilization will be briefly reviewed.

A. Previous Studies on Plasma-Assisted Water Sterilization

Schoenbach and his colleagues at Old Dominion University studied the feasibility of the use of electrical pulses in a microsecond range for the sterilization of biological cells for the past two decades [174–177]. For example, a 600-ns, 120-kV square wave pulse was used to generate pulsed corona discharge for bacterial (*E. coli* and *Bacillus subtilis*) decontamination of water. They reported three orders of the magnitude reduction in the concentration of *E. coli* (gram-negative bacterium) with an energy expenditure of 10 kJ/L. For *B. subtilis* (gram-positive bacterium), it took about 40 kJ/L to reduce the three-order reduction. However, it was observed that plasma had no effect on *B. subtilis* spores. They attributed the phenomena to the accumulation of electrical charges at the membrane of the spores, which could shield the interior of the cell from the external electrical fields. Since the typical time required to charge mammalian cell membranes is on the order of 1 μs [178], microsecond pulses could not penetrate into cells once the membrane is charged. Hence, a short pulse in a nanosecond range might be able to penetrate the entire cell, nucleus, and organelles and affect

cell functions, thus disinfecting them, a hypothesis that needs to be validated.

Researchers at the Eindhoven University of Technology, Netherlands, applied pulsed electric fields and pulsed corona discharges to inactivate microorganisms in water [179]. They utilized four different types of discharge configurations, including a perpendicular water flow over two wire electrodes, a parallel water flow along two electrodes, air-bubbling through a hollow needle electrode toward a ring electrode, and wire cylinder with the application of 100-kV pulses with a 10-ns rise time and 150-ns pulse duration. Inactivation rate was found to be 85 kJ/L per 1-log reduction for *Pseudomonas flurescens* (gram-negative bacterium) and 500 kJ/L per 1-log reduction for *Bacillis sereus* spores.

Researchers at the General Physics Institute, Russian Academy of Science, Moscow, studied if plasma systems could eradicate microorganisms such as *E. coli* and *coliphages* in water distribution systems [180,181] and reported that the active species, UV, ozone, and hydrogen peroxide effectively could sterilize bacteria in water.

Sato and his colleagues at Gunma University, Japan, investigated the feasibility of using plasma discharges for sterilization and removal of organic compounds in water [46–49]. In particular, they studied the formation of chemical species and their effects on microorganisms and reported that hydroxyl radicals had extremely short lifetime of 70 ns and diffused only 20 nm before they were absorbed in water. They also reported that hydrogen peroxide was produced through the recombination of hydroxyl radicals, rather than by electrolytic reaction. They measured the emission spectrum between 200 and 750 nm and found that the largest peaks were in the UV range, which were believed to be molecular emissions from hydroxyl radicals (see Fig. 68).

Researchers at the University of Wisconsin, Madison, USA, studied the feasibility of using dense medium plasma reactors for the disinfection of water [52,53,172] and found that the UV radiation emitted from the electrohydraulic discharge was the lethal agent for the inactivation of *E. coli* colonies rather than the thermal/pressure shocks or other active chemical species.

Akiyama and his colleagues at Kumamoto University, Japan, studied the possibility of using streamer discharges in water to produce high-energy electrons, ozone, other chemically active species, UV radiation, and shock-waves [26,50,51]. A thin wire electrode was used to produce a large-volume discharge needed for industrial water treatments. Since the influence of the electric conductivity of water was found to be small, they speculated that bulk heating via ionic current did not contribute to the initiation of the breakdown process.

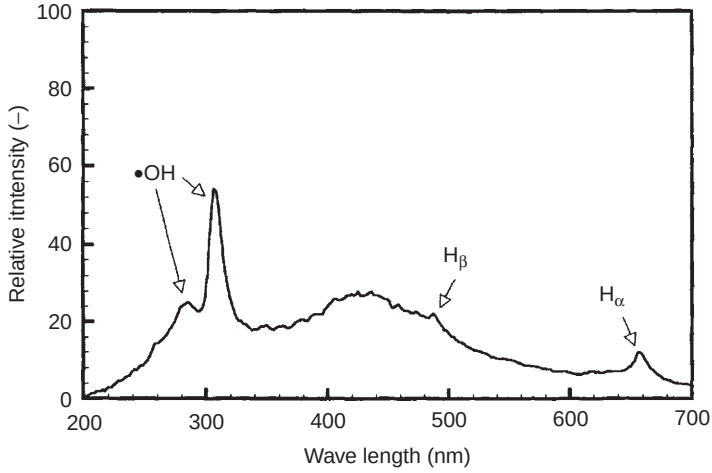

FIG. 68. Emission spectra from pulsed streamer discharge in distilled water with applied voltage of 14 kV [46].

Based on the previous researches, it is clear that plasma discharge has the ability to effectively inactivate microorganisms in water. A plasma-based water treatment system has a number of advantages compared to chemical or mechanical water treatment methods, such as minimal maintenance, low operating power, and minimal pressure loss through the discharge device. Therefore, a plasma-based water treatment can be implemented as a point-of-use water treatment system and in a large industrial water treatment system.

B. TEST METHODS

The present study examined the sterilization efficiency of a point-to-plane plasma discharge system. A spark-gap generator was used to produce a pulsed voltage capable of initiating desired breakdowns.

Validation and characterization of the plasma discharge were conducted by measuring pH, conductivity, temperature, voltage, and current waveforms. To validate whether or not the present design effectively inactivated microorganisms, a series of experiments were conducted with active *E. coli*, which was considered as the most reliable measure of public risks in drinking water since its presence was an indicator of fecal pollution and the possible presence of enteric pathogens [140].

A non-pathogenic strain of *E. coli* bacterium, K12, was used in all experiments. Cell stocks of *E. coli* were prepared by incubating cultures in

Luria–Bertani–Miller (LB) broth (10 g of tryptone, 5 g of yeast extract, 10 g of sodium chloride per liter), for 20–22 h at 37°C. *E. coli*, obtained in a stationary phase, were then centrifuged at 3500 rpm for 10 min, washed twice in sterile spring water, and finally resuspended to population densities of 10^6 and 10^8 CFU/mL of water. Two suspensions of different concentrations were chosen to check any dependence of initial bacterial concentration on *D*-value. Water whose conductivity varied from 100 μS/cm to 200 μS/cm was used in the experiments. Samples for determining the initial population were taken before applying the plasma discharge.

To analyze the treatment results, serial dilutions of the samples were prepared using sterile water and enumerated using a spread-plate counting method. The 100-μL aliquots of diluted samples were spread on brain heart infusion (BHI) agar plates and incubated at 37°C for 12–18 h and the colony-forming units (CFU) were counted. The effectiveness of the spark discharge in inactivating *E. coli* is often expressed as *D*-value, which is identified as the energy required to achieve one-$\log_{10}$ reduction in bacterial concentration at a specific plasma treatment condition [182,183].

C. Results and Effect of Plasma-Induced UV Radiation on Sterilization

1. Inactivation of E. coli *in Water by a Pulsed Spark Discharge*

Results from inactivation experiments with water having *E. coli* concentrations of 10^6 and 10^8 CFU/mL are given in Figs. 69 and Fig. 70, which show the survival curves obtained for these concentrations using spark discharge in water.

For the case of an initial *E. coli* concentration of 10^6 CFU/mL, the *D*-value was found to be 14 J/L of water, while for the case of a higher initial concentration of 10^8 CFU/mL, a high *D*-value of 174 J/L was obtained. This indicates some dependence of the *D*-value on the initial bacterial concentration. As the initial bacterial concentration increased, the *D*-value also increased. Thus, it was postulated that this loading effect might have been due to the inability of UV radiation, produced by spark discharge, to reach *E. coli* through water lacking transparency. Also at a high concentration, *E. coli* could aggregate to each other, partially shielding one another, thus preventing the active plasma species from effectively attacking them.

In an attempt to optimize the spark discharge system for effective water sterilization, the energy per pulse was varied by varying the capacitance of the capacitor source. This was achieved by varying the number of capacitors in the capacitor bank. Figure 71 shows the survival plot of *E. coli* for

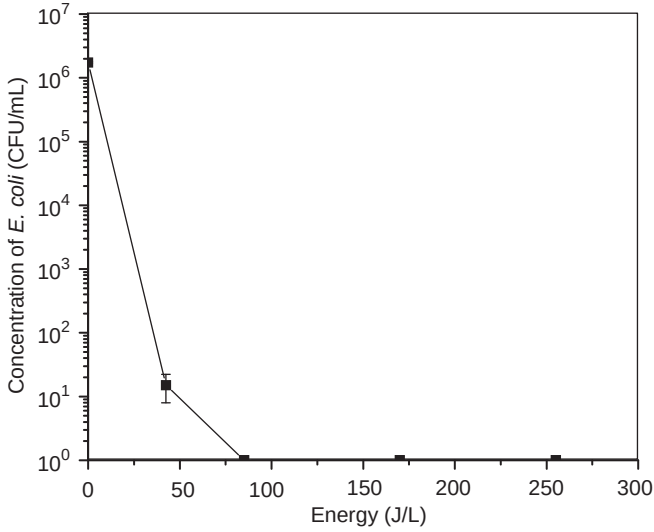

FIG. 69. Survival plot obtained for an *E. coli* concentration of 10^6 CFU/mL.

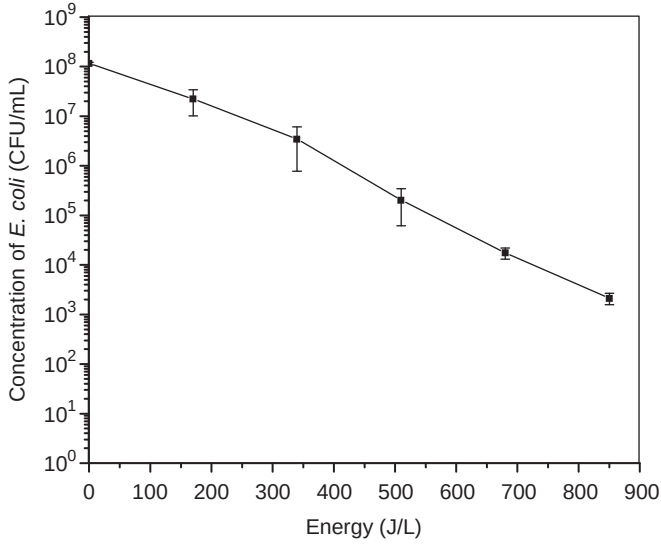

FIG. 70. Survival plot obtained for an *E. coli* concentration of 10^8 CFU/mL.

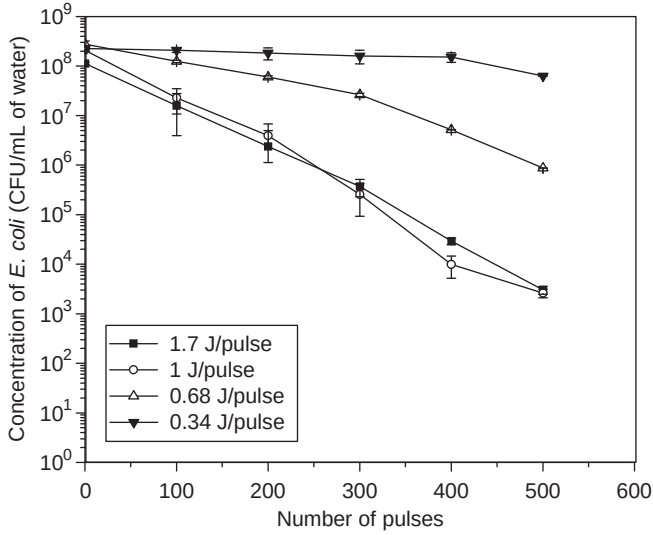

FIG. 71. Survival plot of *E. coli* for different energies per pulse.

different energies per pulse. The *D*-value obtained for an energy per pulse of 1.7 was 187 J/L. A low *D*-value of 98 J/L was obtained for an energy per pulse of 1 J. It may be assumed that only a portion of the energy input into water contributes to the inactivation of microorganisms, while the rest of the energy is dissipated into the water. For energies per pulse of 0.68 and 0.34 J, *D*-values were 140 and 366 J/L, respectively. The optimized treatment system corresponded to a minimum *D*-value of 187 J/L and energy per pulse of 1 J.

2. *Role of UV Radiation in the Inactivation of Microorganisms*

The transmission spectrum for wavelengths between 200 and 300 nm was obtained for BP-9 solutions of concentrations 1, 3, 10, 30, 100, 300, 1000, and 3000 mg/L. Figure 72 shows the relative transmittance for various concentrations of the BP-9 solution. Intensities were normalized at 500 nm. It can be seen that the BP-9 solution of a concentration of 3 mg/L absorbed some portion of UV-C but transmitted a major portion of UV-B and UV-A. The BP-9 solution of a concentration of 30 mg/L absorbed a significant amount of UV-C and UV-B and some portion of UV-A. The BP-9 solution of a concentration of 3000 mg/L completely absorbed UV-A, B, and C. The concentrations 3, 30, and 3000 mg/L were, hence, selected for conducting the

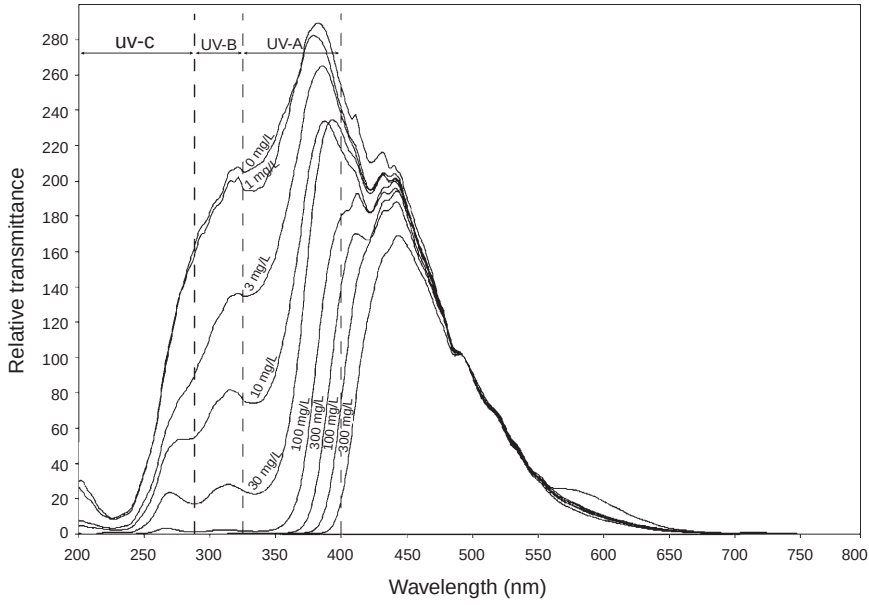

FIG. 72. Fluorescence spectra for different concentrations of BP-9 solution.

present inactivation experiments. As a control, the sensitivity of *E. coli* to BP-9 was tested by exposing the bacteria with an initial concentration of 1.44×10^7 CFU/mL to a BP-9 solution with a concentration of 7500 mg/L of water for 2 h. No change in bacterial concentration was observed.

Figure 73 shows the survival curves for various concentrations of BP-9. It can be observed that the disinfection of *E. coli* in water was almost completely suppressed at a concentration of 30 mg/L of BP-9. These results are in agreement with the results of similar experiments done earlier by other researchers [184]. UV radiation is known to kill microorganisms in water [185,186]. DNA has an important absorption peak near 254 nm [187]. UV photons can cause irreparable damage to the bacterial DNA, thus inactivating them [182,188]. The present results indicate that UV radiation produced by spark discharge in water plays a major role in inactivating microorganisms.

3. *Comparison of Different Plasma Discharges for Water Sterilization*

The possible applications for plasma water sterilization span a wide range of areas and industries, including foreign aid and disaster relief, providing a

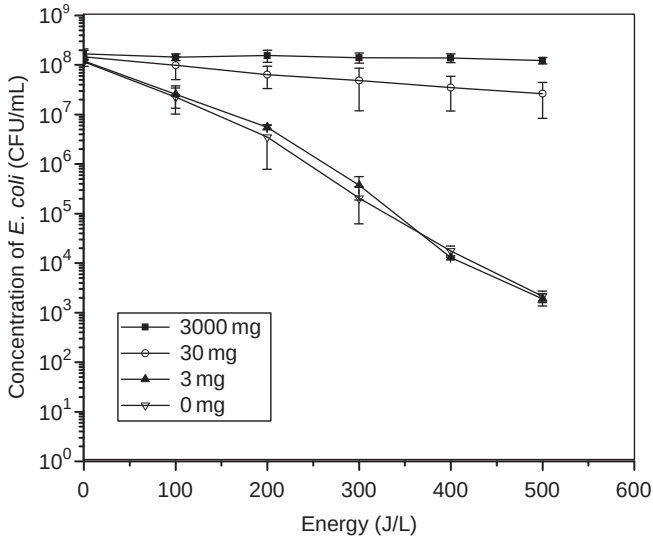

FIG. 73. Survival plot of *E. coli* for various concentrations of BP-9.

TABLE VII
COMPARISON OF DIFFERENT PLASMA DISCHARGES USED IN PLASMA-BASED WATER TREATMENT METHODS

	Pulsed arc discharge	Pulsed spark discharge	Pulsed corona discharge
Energy per liter for 1-log reduction of *E. coli*	860 J/L	77 J/L	30–150 kJ/L
Power requirement for household (6 gpm)	0.326 kW	0.148 kW	11.4–56.8 kW
Power requirement for village (1000 gpm)	54.3 kW	4.9 kW	1892–9463 kW
Efficiency	Good	Excellent	Poor
Central lethal biological agent of discharge	UV and chemical radicals	UV and chemical radicals	Chemical radicals

means for developing countries to sustain potable water sources, integrating into household water delivery systems in developed countries, and improving power plant wastewater treatment facilities. Table VII shows a chart comparing different plasma discharges found in plasma-based water treatment methods. The typical discharges applied in research can be found on two

ends of the spectrum: either a highly energetic thermal discharge, i.e., arc discharge, or a less energetic non-thermal discharge, i.e., corona discharge. The pulsed spark discharge used in the present study belongs somewhere between these two extremes. The properties of this type of discharge are quite unique and beneficial with regard to water treatment. First and most importantly, according to the present experiments it requires a very low power in comparison to other systems. A minimum *D*-value of 98 J/L was obtained, which means that the electric energy requirement was 148 W to achieve a 4-log reduction for a typical household flow rate of 6 gpm (22.7 L/min). The low energy consumption enables the plasma water treatment system to be powered by solar cells or hand-crank power supplies in third world countries where electricity is a scarce commodity. Secondly, the pH and temperature of the surrounding water did not significantly change during the treatment, indicating that the energy of the discharge was not wasted in the form of bulk heating of water and was used very effectively for the treatment. Thirdly, the flow rates that can be treated by the present plasma discharge (i.e., pulsed sparks) could be significantly larger than other plasma systems.

IX Final Remarks

Plasma discharge in water is an interesting and relatively new topic for consideration from the standpoint of classical water treatment technologies and is gaining importance in modern technologies. One of the major advantages of underwater plasma is that it combines different effects, including radical species (OH, O, HO_2), molecular species (H_2O_2), UV radiation, electric field, and shockwaves, in a single process. The synergy between these effects is usually believed to provide a higher efficiency than traditional chemical treatment methods. Secondly, the *in situ* production of active chemical species eliminates the need of transportation, storage, and the residual remediation of external chemical sources.

In this chapter the authors tried to consider all the major types of underwater plasma sources and their uses at different conditions that influence the energy transfer between the plasma and surrounding liquids. Also different media that the plasma interacts with have a significant influence on the energy transfer. Such examples include the electric conductivity of water, dissolved ions, solid particles, solid surfaces, and living microorganisms. Surely, this area of research is too broad to be comprehensively considered in one chapter, but the present study attempted to give some general idea on the state-of-the-art in this branch of science.

Acknowledgments

This work was partly supported by U.S. Department of Energy, National Energy Technology Laboratory, through contract DE-NT0005308.

References

1. Feeley, T. J., Skone, T. J., Stiegel, G. J., Jr, McNemar, A., Nemeth, M., Schimmoller, B., Murphy, J. T., and Manfredo, L. (2008). Water: a critical resource in the thermoelectric power industry. *Energy* **33**(1), 1–11.
2. Feeley, T.J. (2008). Department of Energy/Office of Fossil Energy's Power Plant Water Management R&D Program.
3. El-Wakil, M. M. (1984). "Powerplant Technology." McGraw-Hill, New York, NY.
4. World Water Assessment Programme. (2009). "The 3rd United Nations World Water Development Report: Water in a Changing World." UNESCO, Paris.
5. United States Environmental Protection Agency Office of Water, National Water Quality Inventory: Report to Congress. (2009). "2004 Reporting Cycle." EPA 841-R-08-00.
6. Ghezzar, M. R., Abdelmalek, F., Belhadj, M., Benderdouche, N., and Addou, A. (2007). Gliding arc plasma assisted photocatalytic degradation of anthraquinonic acid green 25 in solution with TiO2. *Appl. Catal. B* **72**(3–4), 304–313.
7. Grabowski, L., van Veldhuizen, E., Pemen, A., and Rutgers, W. (2006). Corona above water reactor for systematic study of aqueous phenol degradation. *Plasma Chem. Plasma Process.* **26**(1), 3–17.
8. Joanna, P. and Satoshi, I. (2007). Removal of color caused by various chemical compounds using electrical discharges in a foaming column. *Plasma Process. Polym.* **4**, 753–759
9. Nicolae Bogdan, M. (2008). Decomposition of methylene blue in water using a dielectric barrier discharge: optimization of the operating parameters. *J. Appl. Phys.* **104**(10), 103306.
10. Magureanu, M., Piroi, D., Mandache, N. B., David, V., Medvedovici, A., and Parvulescu, V. I. (2010). Degradation of pharmaceutical compound pentoxifylline in water by non-thermal plasma treatment. *Water Res.* **44**(11), 3445–3453.
11. Gao, J., Wang, X., Hu, Z., Deng, H., Hou, J., Lu, X., and Kang, J. (2003). Plasma degradation of dyes in water with contact glow discharge electrolysis. *Water Res.* **37**(2), 267–272.
12. Magureanu, M., Piroi, D., Gherendi, F., Mandache, N., and Parvulescu, V. (2008). Decomposition of methylene blue in water by corona discharges. *Plasma Chem. Plasma Process.* **28** (6), 677–688.
13. Nicolae Bogdan, M. (2008). Decomposition of methylene blue in water by corona discharges. *Plasma Chem. Plasma Process.* **28**, 677–688.
14. Zhang, R. B., Wang, L., Wu, Y., Guan, Z., and Jia, Z. (2006). Bacterial decontamination of water by bipolar pulsed discharge in a gas-liquid-solid three-phase discharge reactor. *IEEE Trans. Plasma Sci.* **34**, 1370–1374.
15. Yong Cheol, H., Hyun Jae, P., Bong Ju, L., Won-Seok, K., and Han Sup, U. (2010). Plasma formation using a capillary discharge in water and its application to the sterilization of E. coli. *Phys. Plasmas* **17**, 53502–53506.
16. Lee, H. Y., Uhm, H. S., Choi, H. N., Jung, Y. J., Kang, B. K., and Yoo, H. C. (2003). Underwater discharge and cell destruction by shockwaves. *J. Korean Phys. Soc.* **42**, S880–S884.

17. Sakiyama, Y., Tomai, T., Miyano, M., and Graves, D. B. (2009). Disinfection of E. coli by nonthermal microplasma electrolysis in normal saline solution. *Appl. Phys. Lett*. **94**, 16.
18. Sun, B., Kunitomo, S., and Igarashi, C. (2006). Characteristics of ultraviolet light and radicals formed by pulsed discharge in water. *J. Phys. D Appl. Phys*. **39**(17), 3814–3820.
19. Vankov, A. and Palanker, D. (2007). Nanosecond plasma-mediated electrosurgery with elongated electrodes. *J. Appl. Phys*. **101**, 12.
20. Volenik, K., Nop, P., Kopoeiva, P., Kolman, B., and Dubsky, J. (2006). Isothermal oxidation of metallic coatings deposited by a water-stabilized plasma gun. *Metal. Mate*. **44**, 40–48.
21. Suzuki, T., Saburi, T., Tokunami, R., Murata, H., and Fujii, Y. (2006). Dominant species for oxidation of stainless steel surface in water vapor plasma. *Thin Solid Films* **506–507**, 342–345.
22. Sridharan, K., Harrington, S. P., Johnson, A. K., Licht, J. R., Anderson, M. H., and Allen, T. R. (2007). Oxidation of plasma surface modified zirconium alloy in pressurized high temperature water. *Mater. Des*. **28**, 1177–1185.
23. Snizhko, L. O., Yerokhin, A. L., Gurevina, N. L., Patalakha, V. A., and Matthews, A. (2007). Excessive oxygen evolution during plasma electrolytic oxidation of aluminium. *Thin Solid Films* **516**, 460–464.
24. Matsushima, Y., Yamazaki, T., Maeda, K., Noma, T., and Suzuki, T. (2006). Plasma oxidation of a titanium electrode in dc-plasma above the water surface. *J. Am. Ceram. Soc*. **89**, 799–804.
25. Chu, P. K., Tian, X. B., Wei, C. B., Yang, S. Q., and Fu, R. K. Y. (2006). Water plasma implantation/oxidation of magnesium alloys for corrosion resistance. *Nucl. Instrum. Methods Phys. Res. B* **242**, 300–302.
26. Akiyama, H. (2000). Streamer discharges in liquids and their applications. *IEEE Trans. Dielectr. Electr. Insul*. **7**, 646–653.
27. Locke, B. R., Sato, M., Sunka, P., Hoffmann, M. R., and Chang, J. S. (2006). Electrohydraulic discharge and nonthermal plasma for water treatment. *Ind. Eng. Chem. Res*. **45**, 882–905.
28. Sunka, P. (2001). Pulse electrical discharges in water and their applications. *Phys. Plasmas* **8**, 2587–2594.
29. Bruggeman, P. and Leys, C. (2009). Non-thermal plasmas in and in contact with liquids. *J. Phys. D: Appl. Phys*. **42**, 53001–53027.
30. Joshi, R. P., Kolb, J. F., Shu, X., and Schoenbach, K. H. (2009). Aspects of plasma in water: streamer physics and applications. *Plasma Process. Polym*. **6**, 763–777.
31. Jun, Q., Joshi, R. P., Schoenbach, K. H., Woodworth, J. R., and Sarkisov, G. S. (2006). Model analysis of self- and laser-triggered electrical breakdown of liquid water for pulsed-power applications. *IEEE Trans. Plasma Sci*. **34**, 1680–1691.
32. Qian, J., Joshi, R. P., Kolb, J., Schoenbach, K. H., Dickens, J., Neuber, A., Butcher, M., Cevallos, M., Krompholz, H., Schamiloglu, E., and Gaudet, J. (2005). Microbubble-based model analysis of liquid breakdown initiation by a submicrosecond pulse. *J. Appl. Phys*. **97** (Copyright 2005, IEE), 113304–113301.
33. Schoenbach, K., Kolb, J., Shu, X., Katsuki, S., Minamitani, Y., and Joshi, R. (2008). Electrical breakdown of water in microgaps. *Plasma Sources Sci. Technol*. **17**, 24010 (10 pp.).
34. Schoenbach, K. H., Hargrave, B., Joshi, R. P., Kolb, J. F., Nuccitelli, R., Osgood, C., Pakhomov, A., Stacey, M., Swanson, R. J., White, J. A., Shu, X., Jue, Z., Beebe, S. J., Blackmore, P. F., and Buescher, E. S. (2007). Bioelectric effects of intense nanosecond pulses. *IEEE Trans. Dielectr. Electr. Insul*. **14**, 1088–1109.

35. Locke, B. R., Burlica, R., and Kirkpatrick, M. J. (2006). Formation of reactive species in gliding arc discharges with liquid water. *J. Electrostat*. **64** (Copyright 2006, IEE), 35–43.
36. Mededovic, S., Finney, W. C., and Locke, B. R. (2008). Electrical discharges in mixtures of light and heavy water. *Plasma Process. Polym*. **5**, 76–83.
37. Sahni, M. and Locke, B. R. (2006). Quantification of reductive species produced by high voltage electrical discharges in water. *Plasma Process. Polym*. **3**, 342–354.
38. Sato, K. and Yasuoka, K. (2008). Pulsed discharge development in oxygen, argon, and helium bubbles in water. *IEEE Trans. Plasma Sci*. **36**, 1144–1145.
39. Sato, K., Yasuoka, K., and Ishii, S. (2008). Water treatment with pulsed plasmas generated inside bubbles. *Trans. Inst. Electr. Eng. Jpn. A* **128**, 401–406.
40. Sato, K., Yasuoka, K., and Ishii, S. (2010). Water treatment with pulsed discharges generated inside bubbles. *Electr. Eng. Jpn*. **170**, 1–7.
41. Sato, M. (2008). Environmental and biotechnological applications of high-voltage pulsed discharges in water. *Plasma Sources Sci. Technol* **17**, 24021–24027.
42. Sato, M., Tokutake, T., Ohshima, T., and Sugiarto, A. T. (2008). Aqueous phenol decomposition by pulsed discharges on the water surface. *IEEE Trans. Ind. Appl*. **44**, 1397–1402.
43. Lukes, P., Clupek, M., Babicky, V., and Sunka, P. (2008). Pulsed electrical discharge in water generated using porous-ceramic-coated electrodes. *IEEE Trans. Plasma Sci*. **36**, 1146–1147.
44. Lukes, P., Clupek, M., Babicky, V., and Sunka, P. (2009). The role of surface chemistry at ceramic/electrolyte interfaces in the generation of pulsed corona discharges in water using porous ceramic-coated rod electrodes. *Plasma Process. Polym*. **6**, 719–728.
45. Sunka, P., Babicky, M., Clupek, M., Fuciman, M., Lukes, P., Simek, M., Benes, J., Locke, B., and Majcherova, Z. (2004). Potential applications of pulse electrical discharges in water. *Acta Phys. Slovaca* **54**, 135–145.
46. Sato, M., Ohgiyama, T., and Clements, J. S. (1996). Formation of chemical species and their effects on microorganisms using a pulsed high-voltage discharge in water. *IEEE Trans. Ind. Appl*. **32**, 106–112.
47. Sugiarto, A. T., Ohshima, T., and Sato, M. (2002). Advanced oxidation processes using pulsed streamer corona discharge in water. *Thin Solid Films* **407**, 174–178.
48. Sun, B., Sato, M., and Clements, J. S. (1999). Use of a pulsed high-voltage discharge for removal of organic compounds in aqueous solution. *J. Phys. D: Appl. Phys*. **32**, 1908–1915.
49. Sugiarto, A. T., Ito, S., Ohshima, T., Sato, M., and Skalny, J. D. (2003). Oxidative decoloration of dyes by pulsed discharge plasma in water. *J. Electrostat*. **58**, 135–145.
50. Katsuki, S., Akiyama, H., Abou-Ghazala, A., and Schoenbach, K. H. (2002). Parallel streamer discharge between wire and plane electrodes in water. *IEEE Trans. Dielect. Elect. Insul*. **9**, 498–506.
51. Lisitsyn, I. V., Nomiyama, H., Katsuki, S., and Akiyama, H. (1999). Streamer discharge reactor for water treatment by pulsed power. *Rev. Sci. Instrum*. **70**, 3457–3462.
52. Manolache, S., Somers, E. B., Wong, A. C. L., Shamamian, V., and Denes, F. (2001). Dense medium plasma environments: a new approach for the disinfection of water. *Environ. Sci. Technol*. **35**, 3780–3785.
53. Ching, W. K., Colus, A. J., and Hoffmann, M. R. (2003). Soluble sunscreens fully protect E. coli from disinfection by electrohydraulic discharges. *Environ. Sci. Technol*. **37**, 4901–4904.
54. Destaillats, H., Lesko, T. M., Knowlton, M., Wallac, H., and Hoffmann, M. R. (2001). Scale-up of sonochemical reactors for water treatment. *Ind. Eng. Chem. Res*. **40**, 3855–3860.
55. Robinson, J. W., Ham, M., and Balaster, A. N. (1973). Ultraviolet radiation from electrical discharges in water. *J. Appl. Phys*. **44**, 72–75.
56. Sun, B., Sato, M., and Clements, J. S. (1997). Optical study of active species produced by a pulsed streamer corona discharge in water. *J. Electrostat*. **39**, 132–189.

57. Laroussi, M. (2005). Low temperature plasma-based sterilization: overview and state-of-the-art. *Plasma Process. Polym.* **2**, 391–400.
58. Laroussi, M., Dobbs, F. C., Wei, Z., Doblin, M. A., Ball, L. G., Moreira, K. R., Dyer, F. F., and Richardson, J. P. (2002). Decontamination of water by excimer UV radiation. *IEEE Trans. Plasma Sci.* **30**, 1501–1503.
59. Hurst, C. J. (2005). "Manual of Environmental Microbiology." 2nd edn. ASM Press, Washington, DC.
60. Sunka, P., Babicky, V., Clupek, M., Lukes, P., Simek, M., Schmidt, J., and Cernak, M. (1999). Generation of chemically active species by electrical discharges in water. *Plasma Sources Sci. Technol.* **8**, 258–265.
61. Krcma, F., Stara, Z., and Prochazkova, J. (2010). Diaphragm discharge in liquids: fundamentals and applications. *J. Phys. Conf. Ser.* **207**, 12010–12016.
62. De Baerdemaeker, F., Monte, M., and Leys, C. (2005). Capillary underwater discharges. *IEEE Trans. Plasma Sci.* **33**, 492–493.
63. De Baerdemaeker, F., Simek, M., Schmidt, J., and Leys, C. (2007). Characteristics of ac capillary discharge produced in electrically conductive water solution. *Plasma Sources Sci. Technol.* **16**, 341–354.
64. De Baerdemaeker, F., Simek, M., and Leys, C. (2007). Efficiency of hydrogen peroxide production by ac capillary discharge in water solution. *J. Phys. D: Appl. Phys.* **40**, 2801–2809.
65. Malik, M. A., Minamitani, Y., Xiao, S., Kolb, J. F., and Schoenbach, K. H. (2005). Streamers in water filled wire-cylinder and packed bed reactors. *IEEE Trans. Plasma Sci.* **33**, 490–491.
66. Yang, Y., Kim, H., Starikovskiy, A., Fridman, A., and Cho, Y. I. (2010). Pulsed multichannel discharge array in water with stacked circular disk electrodes. *IEEE Trans. Plasma Sci.*
67. Sato, M., Yamda, Y., and Sugiarto, A. (2000). Decoloration of dyes in aqueous solution by pulsed discharge plasma in water through pinhole. *Trans. Inst. Fluid Flow Machinery* **107**, 95–104.
68. Chen, Y.-S., Zhang, X.-S., Dai, Y.-C., and Yuan, W.-K. (2004). Pulsed high-voltage discharge plasma for degradation of phenol in aqueous solution. *Sep. Purif. Technol.* **34**, 5–12.
69. Kostyuk, P. V. (2008). Effect of Ni and TiO_2 on hydrogen generation from aqueous solution with non-thermal plasma. *J. Phys. D: Appl. Phys.* **41**(9), 95202.
70. Shin, W.-T., Yiacoumi, S., Tsouris, C., and Dai, S. (2000). A pulseless corona-discharge process for the oxidation of organic compounds in water. *Ind. Eng. Chem. Res.* **39**(11), 4408–4414.
71. Miichi, T., Ihara, S., Satoh, S., and Yamabe, C. (2000). Spectroscopic measurements of discharges inside bubbles in water. *Vacuum* **59**(1), 236–243.
72. Akishev, Y., Grushin, M., Karal'nik, V., Monich, A., Pan'kin, M., Trushkin, N., Kholodenko, V., Chugunov, V., Zhirkova, N., Irkhina, I., and Kobzev, E. (2006). Generation of a nonequlibrium plasma in heterophase atmospheric-pressure gas-liquid media and demonstration of its sterilization ability. *Plasma Phys. Rep.* **32**(12), 1052–1061.
73. Takeda, T., Jen-Shih, C., Ishizaki, T., Saito, N., and Takai, O. (2008). Morphology of high-frequency electrohydraulic discharge for liquid-solution plasmas. *IEEE Trans. Plasma Sci.* **36**(4), 1158–1159.
74. Yukhymenko, V. V., Chernyak, V. Y., and Olshevskii, S. V. (2008). Plasma conversion of ethanol-water mixture to synthesis gas. *Ukr. J. Phys.* **53**, 409–413.
75. Hironori, A. (2008). Plasma generation inside externally supplied Ar bubbles in water. *Plasma Sources Sci. Technol.* **17**(2), 25006.

76. Ishijima, T., Hotta, H., Sugai, H., and Sato, M. (2007). Multibubble plasma production and solvent decomposition in water by slot-excited microwave discharge. *Appl. Phys. Lett.* **91**(12), 121501–121503.
77. Ishijima, T. (2010). Efficient production of microwave bubble plasma in water for plasma processing in liquid. *Plasma Sources Sci. Technol.* **19**(1), 15010.
78. Nomura, S. and Toyota, H. (2003). Sonoplasma generated by a combination of ultrasonic waves and microwave irradiation. *Appl. Phys. Lett.* **83**(22), 4503–4505.
79. Nomura, S., Toyota, H., Mukasa, S., Yamashita, H., Maehara, T., and Kuramoto, M. (2006). Microwave plasma in hydrocarbon liquids. *Appl. Phys. Lett.* **88**(21), 211503–211503.
80. Nomura, S., Toyota, H., Mukasa, S., Takahashi, Y., Maehara, T., Kawashima, A., and Yamashita, H. (2008). Discharge characteristics of microwave and high-frequency in-liquid plasma in water. *Appl. Phys. Exp.* **1**, 46002.
81. Yang, Y., Cho, Y. I., Fridman, A., and Starikovskiy, A. (2010). Non-equilibrium plasma in liquid water: dynamics of generation and quenching. *Plasma Sources Sci. Technol.*
82. An, W., Baumung, K., and Bluhm, H. (2007). Underwater streamer propagation analyzed from detailed measurements of pressure release. *J. Appl. Phys.* **101**, 53302.
83. Beroual, A. (1993). Electronic and gaseous processes in the prebreakdown phenomena of dielectric liquids. *Appl. Phys.* **73**, 4528–4533.
84. Jones, H. M. and Kunhardt, E. E. (1995). Development of pulsed dielectric breakdown in liquids. *J. Phys. D: Appl. Phys.* **28**, 178–188.
85. Lewis, T. and New, A. (1998). Model for the primary process of electrical breakdown in liquids. *IEEE Trans. Dielectr. Electr. Insul.* **5**, 306–315.
86. Lewis, T. (2003). Breakdown initiating mechanisms at electrode interfaces in liquids. *IEEE Trans. Dielect. Elect. Insul.* **10**, 948–955.
87. Qian, J., Joshi, R., Kolb, J. F., and Schoenbach, K. H. (2005). Microbubble-based model analysis of liquid breakdown initiation by a submicrosecond pulse. *J. Appl. Phys.* **97**, 113304–113313.
88. Qian, J., Joshi, R., and Schoenbach, K. H. (2006). Model analysis of self- and laser-triggered electrical breakdown of liquid water for pulsed-power applications. *IEEE Trans. Plasma Sci.* **34**, 1680–1691.
89. Joshi, R., Qian, J., Zhao, G., Kolb, J. F., and Schoenbach, K. H. (2004). Are microbubbles necessary for the breakdown of liquid water subjected to a submicrosecond pulse? *J. Appl. Phys.* **96**, 5129–5139.
90. Lisitsyn, I. V., Nomiyama, H., Katsuki, S., and Akiyama, H. (1999). Thermal processes in a streamer discharge in water. *IEEE Trans. Dielec. Dielectr. Electr. Insul.* **6**, 351–356.
91. Watson, P. and Chadbank, W. (1991). The role of electrostatic and hydrodynamic forces in the negative-point breakdown of liquid dielectrics. *IEEE Trans. Electr. Insul.* **26**, 543–559.
92. Yang, Y., Starikovskiy, A., Fridman, A., and Cho, Y. I. (2011). Analysis of streamer propagation for electric breakdown in liquid/bioliquid. *Plasma Med.* **1**, 65–83.
93. Kupershtokh, A. L. and Medvedev, D. A. (2006). Anisotropic instability of dielectric liquids and decay to vapor-liquid system in strong electric fields. *Tech. Phys. Lett.* **32**, 634–637.
94. Fridman, A. and Kennedy, L. (2006). "Plasma Physics and Engineering." Taylor & Francis Group, New York, NY.
95. Morch, K. A. (2007). Reflections on cavitation nuclei in water. *Phys. Fluids* **19**, 72104–72110.
96. Gidalevich, E. and Boxman, R. (2006). Sub- and supersonic expansion of an arc channel in liquid. *J. Phys. D: Appl. Phys.* **39**, 652–659.
97. Lama, W. and Gallo, C. (1977). Systematic study of the electrical characteristics of the tricel current pulses from negative needle-to-plane coronas. *J. Appl. Phys.* **45**, 103–113.

98. Beroual, A., Zahn, M., and Badent, A. (1998). Propagation and structure of streamers in liquid dielectrics. *IEEE Electr. Insul. Mag.* **14**, 6–14.
99. Woodworth, J. R., Lehr, J. M., and Elizondo-Decanini, J. (2004). Optical and pressure diagnostics of 4-MV water switches in the Z-20 test facility. *IEEE Trans. Plasma Sci.* **32**, 1778–1789.
100. White, F. M. (2006). "Viscous Fluid Flow." 3rd edn. McGraw-Hill Companies, Singapore.
101. Itikawa, Y. (1974). Electron-impact vibrational excitation of H_2O. *J. Phys. Soc. Jpn.* **36**, 1127–1132.
102. Parry, W., Bellows, J., Gallagher, J., and Harvey, A. (2008). "ASME International Steam Tables for Industrial Use." The American Society of Mechanical Engineers, New York, NY.
103. Lange, H. and Huczko, A. (2004). Carbon Arc discharge: plasma emission spectroscopy and carbon nanostructure formation. *Trans. Mater. Res. Soc. Jpn.* **29**, 3359–3364.
104. Eggers, J. (1997). Nonlinear dynamics and breakup of free-surface flows. *Rev. Mod. Phys.* **69**, 865–930.
105. Kenyon, K. E. (1998). Capillary waves understood by an elementary method. *J. Oceanogr.* **54**, 343–346.
106. Kenyon, K. E. (1983). On the depth of wave influence. *J. Phys. Oceanogr.* **13**, 1968–1970.
107. Lu, X., Pan, Y., and Liu, K. (2002). Spark model of pulsed discharge in water. *J. Appl. Phys.* **91**, 24–31.
108. Bluhm, H., Frey, W., and Giese, H. (2000). Application of pulsed HV discharges to material fragmentation and recycling. *IEEE Trans. Dielec. Dielectr. Electr. Insul.* **7**, 625–636.
109. Akiyama, H., Sakugawa, T., and Namihira, T. (2007). Industrial applications of pulsed power technology. *IEEE Trans. Dielec. Dielectr. Electr. Insul.* **14**, 1051–1064.
110. Wilson, M. P., Balmer, L., and Given, M. J. (2006). Application of electric spark generated high power ultrasound to recover ferrous and non-ferrous metals from slag waste. *Miner. Eng.* **19**, 491–499.
111. Yang, Y., Gutsol, A., Fridman, A., and Cho, Y. I. (2009). Removal of CaCO3 scales on a filter membrane using plasma discharge in water. *Int. J. Heat Mass Transf.* **52**, 4901–4906.
112. Joseph, B. K. and Miksis, M. (1980). Bubble oscillations of large amplitude. *J. Acoust. Soc. Am.* **68**, 628–633.
113. Inoue, Y. and Kobayashi, T. (1993). Nonlinear Oscillation of a gas-filled spherical cavity in an incompressible fluid. *Fluid Dyn. Res.* **11**, 85–97.
114. Prosperetti, A. and Lezzi, A. (1986). Bubble dynamics in a compressible liquid. I. First-order theory. *J. Fluid Mech.* **168**, 457–478.
115. Lezzi, A. and Prosperetti, A. (1987). Bubble dynamics in a compressible liquid. II. Second-order theory. *J. Fluid Mech.* **185**, 289–321.
116. Panchal, C. B. and Knudsen, J. G. (1998). Mitigation of water fouling: technology status and challenges. *Adv. Heat Transf.* **31**, 431–474.
117. Somerscales, E. F. C. (1990). Fouling of heat exchangers: an historical review. *Heat Transf. Eng.* **11**(1), 19–36.
118. Muller-Steinhagen, H. (2000). "Handbook of Heat Exchanger Fouling—Mitigation and Cleaning Technologies." Publico Publications, Germany.
119. Radler, S. and Ousko-Oberhoffer, U. (2005). Optimised heat exchanger management—achieving financial and environmental targets. *In* "Sixth International Conference on Heat Exchanger Fouling and Cleaning." Irsee, Germany.
120. Cho, Y. I., Fridman, A. F., Lee, S. H., and Kim, W. T. (2004). Physical water treatment for fouling prevention in heat exchangers. *Adv. Heat Transf.* **38**, 1–72.

121. Cho, Y. I., Lee, S. H., and Kim, W. T. (2003). Physical water treatment for the mitigation of mineral fouling in cooling-water applications. *ASHRAE Trans.* **109**, 346–357.
122. Cho, Y. I., Lane, J., and Kim, W. (2005). Pulsed-power treatment for physical water treatment. *Int. Commun. Heat Mass Transf.* **32**, 861–871.
123. Fathi, A., Mohamed, T., Gabrielli, C., Maurin, G., and Mohamed, B. A. (2006). Effect of a magnetic water treatment on homogeneous and heterogeneous precipitation of calcium carbonate. *Water Res.* **40**, 1941–1950.
124. Xiaokai, X. (2008). Research on the electromagnetic anti-fouling technology for heat transfer enhancement. *Appl. Therm. Eng.* **28**, 889–894.
125. Coetzee, P. P., Yacoby, M., Howell, S., and Mubenga, S. (1998). Scale reduction and scale modification effects induced by Zn and other metal species in physical water treatment. *Water SA* **24**, 77–84.
126. Lee, G. J., Tijing, L. D., Pak, B. C., Baek, B. J., and Cho, Y. I. (2006). Use of catalytic materials for the mitigation of mineral fouling. *Int. Commun. Heat Mass Transf.* **33**(1), 14–23.
127. Gabrielli, C., Maurin, G., Francy-Chausson, H., Thery, P., Tran, T. T. M., and Tlili, M.(2006). Electrochemical water softening: principle and application. *Desalination* **206**, 150–163.
128. Yang, Y., Kim, H., Starikovskiy, A., Fridman, A., and Cho, Y. I. (2010). Application of pulsed spark discharge for calcium carbonate precipitation in hard water. *Water Res.* **44**, 3659–3668.
129. Snoeyink, V. L. and Jenkins, D. (1982). "Water Chemistry." Wiley, New York, NY.
130. Yang, Y., Kim, H., Starikovskiy, A., Fridman, A., and Cho, Y. I. Precipitation of calcium ions from hard water using pulsed spark discharges and its mechanism. *Plasma Chem. Plasma Process.*
131. Muller-Steinhagen, H. (1999). Cooling water fouling in heat exchangers. *Adv. Heat Transf.* **33**, 415–496.
132. He, F. and Hopke, P. K. (1993). Experimental study of ion-induced nucleation by radon decay. *J. Chem. Phys.* **99**(12), 9972–9978.
133. Chibowski, E., Holysz, L., and Wojcik, W. (1994). Changes in zeta potential and surface free energy of calcium carbonate due to exposure to radiofrequency electric field. *Colloids Surf. A Physicochem. Eng. Asp.* **92**, 79–85.
134. Katz, J. L., Fisk, J. A., and Chakarov, V. M. (1994). Condensation of a supersaturated vapor IX. Nucleation on ions. *J. Chem. Phys.* **101**(3), 2309–2318.
135. Dhanasekaran, R. and Ramasamy, P. (1986). Two-dimensional nucleation in the presence of an electric field. *J. Cryst. Growth* **79**, 993–996.
136. Gehr, R., Zhai, Z. A., Finch, J. A., and Rao, S. R. (1995). Reduction of soluble mineral concentration in CaSO4 saturated water using a magnetic field. *Water Res.* **29**, 933–940.
137. Baker, J. S. and Judd, S. J. (1996). Magnetic amelioration of scale formation. *Water Res.* **30**, 247–260.
138. Higashitani, K. and Oshitan, J. (1997). Measurements of magnetic effects on electrolyte solution by atomic force microscopy. *Process Saf. Environ. Prot.* **75**, 115–119.
139. Levine, I. N. (1978). "Physical Chemistry." McGraw-Hill, New York, NY.
140. Probstein, R. F. (1989). "Physicochemical Hydrodynamics." Butterworths, Boston, MA.
141. Lin, L., Johnston, C. T., and Blatchley, III, E. R. (1999). Inorganic fouling at quartz: water interfaces in ultraviolet photoreactors-I. chemical characterization. *Water Res.* **33**, 3321–3329.
142. Wait, I. W. (2005). "Fouling of Quartz Surfaces in Potable Water Ultraviolet Disinfection Reactors." Purdue University, West Lafayette, IN.

143. Joshi, A., Locke, B. R., Arce, P., and Finney, W. C. (1995). Formation of hydroxyl radicals, hydrogen peroxide and aqueous electrons by pulsed streamer corona discharge in aqueous solution. *J. Hazard. Mater*. **41**, 3–30.
144. Sun, B., Sato, M., Harano, A., and Clements, J. S. (1998). Non-uniform pulse discharge-induced radical production in distilled water. *J. Electrostat*. **43**, 115–126.
145. Buxton, G. V. and Elliot, A. J. (1986). Rate constant for reaction of hydroxyl radicals with bicarbonate ions. *Radiat. Phys. Chem*. **27**, 241–243.
146. Crittenden, J. C., Hu, S., Hand, D. W., and Green, S. A. (1999). A kinetic model for H_2O_2/UV process in a completely mixed batch reactor. *Water Res*. **33**, 2315–2328.
147. Siegal, F. and Reams, M. W. (1966). Temperature effect on precipitation of calcium carbonate from calcium bicarbonate solutions and its application to cavern environments. *Sedimentology* **7**, 241–247.
148. Nagasaka, Y. and Nagashima, A. (1981). Simultaneous measurement of the thermal conductivity and the thermal diffusivity of liquids by the transient hot-wire method. *Rev. Sci. Instrum*. **52**, 229–232.
149. Xie, H., Gu, H., Fujii, M., and Zhang, X. (2006). Short hot wire technique for measuring thermal conductivity and thermal diffusivity of various materials. *Meas. Sci. Technol*. **17**, 208–214.
150. Assael, M. J., Karagiannidis, L., Malamataris, N., and Wakeham, W. A. (1998). The transient hot-wire technique: a numerical approach. *Int. J. Thermophys*. **19**, 379–389.
151. Incropera, F. P., Dewitt, D. P., Bergman, T. L., and Lavine, A. S. (2007). "Fundamentals of Heat and Mass Transfer." 6th edn. Wiley, New York, NY.
152. Staack, D., Fridman, A., Gutsol, A., Gogotsi, Y., and Friedman, G. (2008). Nanoscale corona discharge in liquids, enabling nanosecond optical emission spectroscopy. *Angew. Chem. Int. Ed*. **47**, 8020–8024.
153. The US Department of Energy. (1998). "Non-Chemical Technologies for Scale and Hardness Control." DOE/EE-0162.
154. Tijing, L. D., Kim, H., Kim, C., Lee, D., and Cho, Y. I. (2009). Use of an oscillating electric field to mitigate mineral fouling in a heat exchanger. *Exp. Heat Transf*. **22**, 257–270.
155. Demadis, K. D., Mavredaki, E., Stathoulopoulou, A., Neofotistou, E., and Mantzaridis, C. (2007). Industrial water systems: problems, challenges and solutions for the process industries. *Desalination* **213**, 38–46.
156. Parsons, S. A., Judd, S. J., Stephenson, T., Udol, S., and Wang, B. L. (1997). Magnetically augmented water treatment. *Process Saf. Environ. Prot*. **75**, 98–104.
157. Donaldson, J. and Grimes, S. (1988). Lifting the scales from our pipes. *New Sci*. **18**, 43–46.
158. Smith, C., Coetzee, P. P., and Meyer, J. P. (2003). The effectiveness of a magnetic physical water treatment device on scaling in domestic hot-water storage tanks. *Water SA* **29**, 231–236.
159. Xiaokai, X., Chongfang, M., and Yongchang, C. (2005). Investigation on the electromagnetic anti-fouling technology for scale prevention. *Chem. Eng. Technol*. **28**, 1540–1545.
160. Quan, Z., Chen, Y., Ma, C., Wang, C., and Li, B. (2009). Experimental study on anti-fouling performance in a heat exchanger with low voltage electrolysis treatment. *Heat Transf. Eng*. **30**, 181–188.
161. Ushakov, G. V. (2008). Antiscaling treatment of water by an electric field in heat-supply networks. *Therm. Eng*. **55**, 570–573.
162. Yang, Y., Kim, H., Starikovskiy, A., Fridman, A., and Cho, Y. I. (2010). Application of pulsed spark discharge for mineral fouling mitigation in a heat exchanger. *J. Heat Transf*.
163. Kline, S. J. and McClintock, F. A. (1953). Describing uncertainties in single-sample experiments. *Mech. Eng*. **75**, 3–8.

164. Kim, W. T. (2001). "A Study of Physical Water Treatment Methods for the Mitigation of Mineral Fouling." Drexel University, Philadelphia, PA.
165. Yang, Y., Kim, H., Fridman, A., and Cho, Y. I. (2010). Effect of a plasma-assisted self-cleaning filter on the performance of PWT coil for the mitigation of mineral fouling in a heat exchanger. *Int. J. Heat Mass Transf.* **53**, 412–422.
166. Smith, W. F. (1986). "Principles of Materials Science and Engineering." McGraw-Hill Book Co, Singapore.
167. Kontoyannis, C. G. and Vagena, N. V. (1999). Calcium carbonate phase analysis using XRD and FT-Raman spectroscopy. *Analyst* **125**, 251–255.
168. Anpilov, A. M., Barkhudarov, E. M., Christofi, N., Kop'ev, V. A., Kossyi, I. A., Taktakishvili, M. I., and Zadiraka, Y. (2002). Pulsed high voltage electric discharge disinfection of microbially contaminated liquids. *Lett. Appl. Microbiol.* **35**, 90–94.
169. Sun, B., Sato, M., Harano, A., and Clements, J. S. (1998). Non-uniform pulse discharge-induced radical production in distilled water. *J. Electrostat.* **43**, 115–126.
170. Sunka, P., Babicky, V., Clupek, M., Lukes, P., Simek, M., Schmidt, J., and Cernak, M. (1998). Generation of chemically active species by electrical discharges in water. *Plasma Sources Sci. Technol.* **8**, 258–265.
171. Fridman, A. (2008). "Plasma Chemistry." Cambridge University Press, Cambridge.
172. Ching, W. K., Colussi, A. J., Sun, H. J., Nealson, K. H., and Hoffmann, M. R. (2001). Escherichia coli disinfection by electrohydraulic discharges. *Environ. Sci. Technol.* **35**, 4139–4144.
173. Anpilov, A. M., Barkhudarov, E. M., Christofi, N., Kop'ev, V. A., Kossyi, I. A., Taktakishvili, M. I., and Zadiraka, Y. V. (2004). The effectiveness of a multi-spark electric discharge system in the destruction of microorganisms in domestic and industrial wastewaters. *J. Water Health* **2**(4), 267–277.
174. Abou-Ghazala, A., Katsuki, S., Schoenbach, K. H., and Moreira, K. R. (2002). Bacterial decontamination of water by means of pulsed-corona discharges. *IEEE Trans. Plasma Sci.* **30**, 1449–1453.
175. Schoenbach, K. H., Peterkin, F. E., Alden, R. W. J., and Beebe, S. J. (1997). The effect of pulsed electric fields on biological cells: experiments and applications. *IEEE Trans. Plasma Sci.* **25**, 284–289.
176. Joshi, R. P., Hu, Q., Schoenbach, K. H., and Beebe, S. J. (2002). Simulations of electroporation dynamics and shape deformations in biological cells subjected to high voltage pulses. *IEEE Trans. Plasma Sci.* **30**, 1536–1546.
177. Joshi, R. P., Qian, J., and Schoenbach, K. H. (2002). Electrical network-based time dependent model of electrical breakdown in water. *J. Appl. Phys.* **92**, 6245–6251.
178. Schoenbach, K., Joshi, R., Kolb, J., Chen, N., Stacey, M., Blackmore, P. F., Buescher, E. S., and Beebe, S. J. (2004). Ultrashort electrical pulses open a new gateway into biological cells. *Proc. IEEE* **92**(7), 1122–1137.
179. Heesch, E. J. M., Pemen, A. J. M., Huijbrechts, A. H. J., van der Laan, P. C. T., Ptssinski, K. J., Zanstra, G. J., and de Jong, P. (2000). A fast pulsed power source applied to treatment of conducting liquids and air. *IEEE Trans. Plasma Sci.* **137**, 137–140.
180. Anpilov, A. M., Barkhudarov, E. M., Bark, Y. B., Zadiraka, Y. V., Christofi, N., Kozlov, Y. N., Kossyi, I. A., Silakov, V. P., Taktakishvili, M. I., and Temchin, S. M. (2001). Electric discharge in water as a source of UV radiation, ozone and hydrogen peroxide. *J. Phys. D: Appl. Phys.* **34**, 993–999.
181. Anpilov, A. M., Barkhudarov, E. M., Christofi, N., Kopiev, V. A., Kossyi, I. A., Taktakishvili, M. I., and Zadiraka, Y. (2002). Pulsed high voltage electric discharge disinfection of microbially contaminated liquids. *Lett. Appl. Microbiol.* **35**, 90–94.

182. Moisan, M., Barbeau, J., Moreau, S., Pelletier, J., Tabrizian, M., and Yahia, L. H. (2001). Low temperature sterilization using gas plasmas: a review of the experiments and an analysis of the inactivation mechanisms. *Int. J. Pharm.* **226**, 1–21.
183. Moisan, M., Barbeau, J., Crevier, M.-C., Pelletier, J., Philip, N., Saoudi, B., and Sterilization., P., and (2002). Methods and mechanisms. *Pure Appl. Chem.* **74**(3), 349–358.
184. Ching, W. K., Colussi, A. J., and Hoffmann, M. R. (2003). Soluble sunscreens fully protect E. coli from disinfection by electrohydraulic discharges. *Environ. Sci. Technol.* **37**, 4901–4904.
185. Hayamizu, M., Tenma, T., and Mizuno, A. (1989). Destruction of yeast cells by pulsed high voltage application. *Proc. Inst. Electrostat. Jpn.* **13**, 322.
186. Wolfe, R. L. (1990). Ultraviolet disinfection of potable water. *Environ. Sci. Technol.* **24**, 768.
187. Labas, M. D., Brandi, R. J., Martin, C. A., and Cassano, A. E. (2006). Kinetics of bacteria inactivation employing UV radiation under clear water conditions. *Chem. Eng. J.* **121**, 135–145.
188. Sun, B., Sato, M., and Clements, J. S. (2000). Oxidative processes occurring when pulsed high voltage discharges degrade phenol in aqueous solutions. *Environ. Sci. Technol.* **34**, p. 509–513.

AUTHOR INDEX

A

Abdelmalek, F., 182
Abou-Ghazala, A., 186, 274, 275, 276
Achten, E., 9, 59, 61, 91
Addou, A., 182
Akishev, Y., 194
Akiyama, H., 182, 186
Aktas, M., 16, 17, 18, 19, 20, 21, 22, 23, 24, 25, 27, 28, 29, 31, 32
Aktas, M. K., 7, 9, 59
Alden, R. W. J., 274
Alexeev, A., 30
Allen, T. R., 5
Amiroudine, S., 2, 119
An, W., 197, 201, 205, 207, 211, 212, 245
Anderson, M. H., 182
Andrade, E. N., 4
Andres, J. M., 3
Angstadt, M., 149, 150, 155
Anpilov, A. M., 274, 275
Anzai, Y., 149
Arce, P., 248
Arora, P., 144
Assael, M. J., 250

B

Babicky, M., 184
Babicky, V., 184, 189, 192, 193, 203, 208, 244, 248, 274
Badent, A., 205
Baek, B. J., 228, 259
Bailey, M. R., 161, 167, 169
Bailly, D., 10
Baker, J. S., 245
Balaster, A. N., 186, 188
Ball, L. G., 188
Balmer, L., 219
Banerjee, R. K., 137, 148
Barbeau, J., 277
Bark, Y. B., 275
Barkhudarov, E. M., 274, 275
Bau, H. H., 8
Baum, J., 165
Baumung, K., 197, 201, 205, 207, 211, 212, 245
Bayazitoglu, Y., 110
Beard, P., 144
Beebe, S. J., 183, 274
Belhadj, M., 182
Bellows, J., 211
Benderdouche, N., 182
Benes, J., 184
Berg, R. F., 11
Bergman, T. L., 251, 261
Beroual, A., 201, 205
Beysens, D., 10
Bhowmick, S., 172
Bischof, J. C., 172
Black, K. L., 149
Blackmore, P. F., 183, 274
Blackstock, D. T., 16
Blatchley, III, E. R., 247
Bluhm, H., 197, 201, 205, 207, 211, 212, 219, 245
Bohris, C., 165
Boluriaan, S., 3
Bonetti, M., 10
Bong Ju, L., 182
Boris, J. P., 10, 14
Boukari, H., 10
Boxman, R., 203
Brandi, R. J., 280
Briggs, M. E., 10
Brown, M. A., 8, 9, 125
Bruggeman, P., 182, 183, 187
Buescher, E. S., 183, 274
Burlica, R., 183
Butcher, M., 183
Butts, K., 165, 186, 188
Buxton, G. V., 248

C

Calderon, A., 165
Campbell, P., 162

Carles, P., 2, 119
Cassano, A. E., 280
Cathignol, D., 149, 165
Cernak, M., 189, 203, 208, 244, 248, 249, 274
Cevallos, M., 183
Chadbank, W., 201, 207
Chakarov, V. M., 244
Chang, I., 137
Chang, J. S., 182, 186, 187
Chang, X., 161
Chen, D., 149, 150
Chen, N., 274
Chen, Y., 259
Chen, Y.-S., 194
Chernyak, V. Y., 194
Chester, W., 22
Chi, E., 161
Chibowski, E., 244
Ching, W. K., 274, 275, 280
Cho, Y. I., 192, 196, 197, 198, 199, 200, 202, 205, 206, 207, 209, 211, 212, 213, 216, 217, 220, 221, 223, 225, 226, 227, 228, 229, 230, 231, 234, 235, 236, 237, 239, 241, 248, 250, 251, 252, 253, 254, 255, 256, 257, 258, 259, 260, 262, 263, 264, 265, 267, 268, 269, 270, 271, 272, 273
Choi, H. N., 182
Chongfang, M., 259
Christofi, N., 274, 275
Chu, P. K., 182
Chugunov, V., 194
Churchill, S. W., 8, 9, 88, 125
Civale, J., 138, 139
Clarke, R., 138, 139
Clements, J. S., 186, 187, 248, 274, 276, 280
Cleveland, R. O., 139, 149, 153
Clupek, M., 184, 189, 192, 193, 203, 208, 244, 248, 274
Coetzee, P. P., 228, 259
Colus, A. J., 186, 275
Colussi, A. J., 274, 275, 277
Coppens, A. B., 182, 183
Corelli, J. C., 4
Crittenden, J. C., 248
Crum, L. A., 137, 161
Cunitz, B. W., 167, 169
Curra, F. P., 137
Cuschieri, A., 162

D

Dai, S., 194
Dai, Y.-C., 194
Daniel, B. L., 186, 188
Daryoush, A., 144
Daryoush, A. S., 144
Dasgupta, S., 137, 148
David, V., 182
De Baerdemaeker, F., 191
de Jong, P., 275
De Poorter, J., 165
Deene, Y. D., 165
Demadis, K. D., 258
Denes, F., 186
Deng, H., 182
DeSalles, A., 149, 164
Destaillats, H., 186
Dewey, W. C., 172
Dewitt, D. P., 251, 261
Dhanasekaran, R., 244
Dickens, J., 183
Dobbs, F. C., 188
Doblin, M. A., 188
Donaldson, J., 259
Dubsky, J., 182
Dyer, F. F., 188

E

Edwards, D. K., 153
Eggers, J., 214
Eicher, L., 10
Eisenmenger, W., 144
Elizondo-Decanini, J., 205, 211
Elliot, A. J., 248
El-Sherif, M., 144
El-Wakil, M. M., 180, 246

F

Fan, T., 149, 150
Farahani, K., 149, 164
Farhanieh, B., 155
Farouk, B., 16, 17, 18, 19, 20, 21, 22, 23, 24, 25, 27, 28, 29, 31, 32
Fathi, A., 228
Feeley, T. J., 179, 180
Ferrell, R. A., 10

Finch, J. A., 245
Finney, W. C., 183, 248
Fisk, J. A., 244
Francy-Chausson, H., 228, 242
Frank, T., 162
Frenkel, V., 149, 150, 155
Frey, W., 219
Fridman, A., 192–193
Fridman, A. F., 228, 268, 273
Friedman, G., 253
Friend, D. G., 12, 59, 111, 120, 125, 127
Fry, R. B., 149, 153
Fry, W. J., 149, 153
Fu, R. K. Y., 182
Fuciman, M., 184
Fujii, M., 250
Fujii, Y., 182
Fusegi, T., 9, 69, 78, 94

G

Gabrielli, C., 228, 242
Gallagher, J., 211
Gallo, C., 204
Gammon, R. W., 10
Gandhi, G., 144
Gao, J., 182
Garrabos, Y., 10
Gaudet, J., 183
Gehr, R., 245
Gessert, J. E., 143
Gherendi, F., 182
Ghezzar, M. R., 182
Gidalevich, E., 203
Giese, H., 219
Gilbert, J., 4
Gillis, K. A., 112
Given, M. J., 219
Gogotsi, Y., 253
Gompf, B., 144
Gopinath, A., 5, 6
Gopinath, R., 144
Grabowski, L., 182
Graves, D. B., 182, 183
Green, S. A., 184, 192, 193
Grimes, S., 259
Grushin, M., 194
Gu, H., 250
Guan, Z., 182
Guenoun, P., 10
Gurevina, N. L., 182
Gutfinger, C., 5, 30
Gutsol, A., 220, 221, 223, 225, 226, 227, 253, 270

H

Hallez, L., 140
Ham, M., 186, 188
Hamilton, D. R., 6, 7, 20, 21, 46, 47, 48
Han Sup, U., 182
Han, Z. H., 139
Hand, D. W., 248
Hao, H., 10
Harano, A., 248, 274
Hargrave, B., 183
Hariharan, P., 137, 148
Harland, A. R., 144
Harrington, S. P., 182
Harris, G. R., 139, 140, 141, 150, 155, 156
Harris, J. G., 4
Harvey, A., 211
Haupt, A., 10
Hayamizu, M., 280
Hazle, J. D., 173
He, F., 244
He, G. B., 138
He, X., 172
Heesch, E. J. M., 275
Herman, B., 150
Herman, B. A., 150, 155, 156
Heydari, M. M., 155
Higashitani, K., 245
Hihn, J. Y., 140
Hironori, A., 194, 195
Hodenett, M., 140
Hoffmann, M. R., 182, 186, 187, 244, 274, 280
Holt, R. G., 139, 149, 150, 153
Holtsmark, J., 4
Holysz, L., 244
Hopke, P. K., 244
Hos, P., 110
Hotta, H., 195
Hou, J., 182
Howard, S. M., 143
Howell, S., 228, 259
Hu, Q., 274

Hu, S., 248
Hu, Z., 182
Huang, J., 139, 149, 150, 153
Huang, Y., 8
Huber, P. E., 165
Huczko, A., 211
Huijbrechts,A. H. J., 275
Hunt, J. W., 139
Hurrell, A., 144
Hurst, C. J., 188
Hynynen, K., 153, 165
Hyun Jae, P., 182

I

Igarashi, C., 182
Ihara, S., 194
Incropera, F. P., 251, 261
Ingard, U., 3, 120
Inoue, Y., 224
Irkhina, I., 194
Ishihara, Y., 186
Ishii, S., 184
Ishijima, T., 195
Ishizaki, T., 194
Itikawa, Y., 208
Ito, S., 186, 275

J

Jenkins, D., 232, 239, 242, 243
Jenne, J., 165
Jen-Shih, C., 194
Jia, Z., 4, 182
Joanna, P., 139
Johnsen, I., 4
Johnson, A. K., 5
Johnson, R. E., 4
Johnston, C. T., 247
Jolesz, F. A., 165
Jones, H. M., 201
Joseph, B. K., 224
Joshi, A., 248
Joshi, R., 183, 201, 274
Joshi, R. P., 183, 274
Judd, S. J., 245, 259
Jue, Z., 183
Jun, Q., 183
Jung, Y. J., 182

K

Kaczkowski, P. J., 167
Kallel, F., 173
Kammoun, P., 10
Kang, B. K., 182
Kang, J., 182
Karagiannidis, L., 250
Karal'nik, V., 194
Kassoy, D. R., 8
Katsuki, S., 183, 186, 201, 274
Katz, J. L., 244
Kawashima, A., 195
Kennedy, L., 125, 202, 203, 208, 256
Kenyon, K. E., 215, 216
Kettenbach, J., 165
Khalil, B., 10
Khokhlova, V. A., 167
Kholodenko, V., 194
Kim, C., 258
Kim, H., 192, 193, 229, 230, 231, 234, 235, 236, 237, 239, 241, 258, 260, 263, 264, 265, 267, 271, 272, 273
Kim, W., 268
Kim, W. T., 228, 262
King, R. L., 150, 155, 156
Kirkpatrick, M. J., 183
Klima, J., 140
Kline, S. J., 102, 262
Knowlton, M., 186
Knudsen, J. G., 228, 258
Kobayashi, T., 224
Kobzev, E., 194
Kohler, M., 144
Kolb, J., 183, 274
Kolb, J. F., 183, 192, 201
Kolios, M. C., 139
Kolman, B., 143
Kontoyannis, C. G., 273
Kop'ev, V. A., 274
Kopoeiva, P., 182
Kossyi, I. A., 274, 275
Kostyuk, P. V., 194
Kozlov, Y. N., 275
Krcma, F., 191
Krompholz, H., 183
Krouskop, T. A., 173
Kunhardt, E. E., 201
Kunitomo, S., 182, 202

Kupershtokh, A. L., 202
Kuramoto, M., 195
Kuroda, K., 165
Kuznetsov, A. V., 6, 7, 149, 164

L

Labas, M. D., 280
Lagarias, J. C., 159
Lama, W., 204
Lane, J., 228, 258
Lange, H., 211
Larkin, B. K., 7
Laroussi, M., 188
Lauxmann, P., 144
Lavine, A. S., 251, 261
Le Neindre, B., 10
Lee, C. P., 3
Lee, D., 6
Lee, G. J., 228
Lee, H. Y., 182
Lee, S. H., 228, 258
Lee, Y. S., 158
Lehr, J. M., 205, 211
Lei, Z., 111
Lele, S. K., 15
Lemmon, E. W., 59, 111, 125, 127
Lepper, P., 144
Lesko, T. M., 186
Levine, I. N., 245
Lewin, P. A., 144
Lewis, T., 201
Leys, C., 182, 183, 191
Lezzi, A., 224
Li, B., 259
Li, K. P. C., 149, 150, 155
Licht, J. R., 182
Lin, L., 247
Lin, Y., 7, 33, 35, 36, 40, 45, 47, 68, 77, 125
Lisitsyn, I. V., 186, 201
Liu, D., 138
Liu, K., 219, 224
Liu, Y., 150
Locke, B., 184
Locke, B. R., 182, 183, 248
Lu, D., 167
Lu, X., 182, 219, 224
Luftkin, R., 149, 164
Lukes, P., 184, 244, 274

M

Ma, C., 259
Maeda, K., 182
Maehara, T., 195
Magureanu, M., 182
Majcherova, Z., 184
Malamataris, N., 250
Malik, M. A., 192
Mandache, N., 182
Mandache, N. B., 182
Manfredo, L., 179, 180
Manolache, S., 186, 275
Mantzaridis, C., 258
Marshall, B., 162
Martin, C. A., 280
Martin, R. W., 161
Martinez, E. G. E., 155
Maruvada, S., 150, 155, 156
Matsushima, Y., 182
Matthews, A., 182
Maurin, G., 228, 242
Mavredaki, E., 258
McClintock, F. A., 102, 262
McDannold, N. J., 153, 165
McLean, D., 162
McLinden, M. O., 59, 111, 125, 127
McNemar, A., 179–180, 227
Mead, R., 159
Mededovic, S., 183
Medvedev, D. A., 202
Medvedovici, A., 182
Melodelima, D., 149, 165
Menguy, L., 4
Meyer, J. P., 259
Miichi, T., 194
Miksis, M., 224
Minamitani, Y., 183, 192
Mingzhu, Lu., 161
Miyano, M., 182–183
Mizuno, A., 280
Mohamed, B. A., 228
Mohamed, T., 228
Moisan, M., 277, 280
Moldover, M. R., 11, 112
Monich, A., 194
Monte, M., 191
Moonen, C., 149, 165
Moore, W., 143
Morch, K. A., 202

Moreau, S., 277, 280
Moreira, K. R., 188, 274
Morris, H., 149, 153–154
Morris, P., 144
Morris, P. J., 3
Mougenot, C., 149, 165
Mu, C., 144
Mubenga, S., 228, 259
Mukasa, S., 195
Muller-Steinhagen, H., 228, 243, 258–259
Murata, H., 182
Murphy, J. T., 179–180, 227
Myers, M. R., 137, 139, 145, 147–149, 155–156, 159, 172

N

Nagasaka, Y., 250
Nagashima, A., 250
Namihira, T., 219
Nealson, K. H., 274
Nelder, J. A., 159
Nell, D. M., 139, 155
Nelson, P. I., 161
Nemeth, M., 179–180, 227
Neofotistou, E., 258
Neuber, A., 183
New, A., 201
Nicolae Bogdan, M., 182
Nitsche, K., 10
Noma, T., 182
Nomiyama, H., 186, 201
Nomura, S., 195
Nop, P., 182
Nuccitelli, R., 183
Nyborg, W. L., 16

O

Ohgiyama, T., 275–276
Ohshima, T., 184, 275
Okamoto, K., 165
Olshevskii, S. V., 194
O'Neill, B., 2, 7
Onuki, A., 10
Ophir, J., 173
Oran, E. S., 9, 14–15, 68–70, 72, 77–78, 94
Osgood, C., 183
Oshiro, T., 167
Oshitan, J., 245
Ouazzani, J., 2, 119
Ousko-Oberhoffer, U., 228, 258
Ozoe, H., 8

P

Pak, B. C., 228, 259
Pakhomov, A., 183
Palanker, D., 182
Pan, Y., 219, 224
Pan'kin, M., 194
Panchal, C. B., 228, 258
Parang, M., 9
Paredes, G. E., 155
Parry, W., 211
Parsons, S. A., 259
Parvulescu, V., 182
Parvulescu, V. I., 182
Patalakha, V. A., 182
Patankar, S. V., 110
Pauly, J. M., 165
Pelletier, J., 277, 280
Pemen, A., 182
Pemen,A. J. M., 275
Perrot, F., 10
Peskin, A. P., 12, 59, 111, 120, 125, 127
Peterkin, F. E., 274
Petzing, J. N., 144
Piroi, D., 182
Poinsot, T. J., 15
Pomeroy, O., 165
Pratt, R., 149
Preston, R., 144
Preston, R. C., 140
Price, R. E., 173
Pritchard, W. F., 150
Probstein, R. F., 245, 276
Prosperetti, A., 224
Ptssinski, K. J., 274

Q

Qi, Q., 4
Qian, J., 183, 201, 274
Qian, Z. W., 149, 164
Quan, Z., 259
Quinn, T., 149–150, 155

R

Radhwan, A. M., 8
Radler, S., 228, 258
Ramasamy, P., 244
Raney, W. P., 4
Rao, S. R., 245
Rayleigh., L., 16
Reed, J. A., 9, 88
Reeds, J. A., 159
Ren, X. L., 138
Richardson, J. P., 188
Rieke, V., 165
Righetti, R., 173
Rivens, I., 138–139, 149, 153–154
Robinson, J. W., 186, 188
Robinson, S., 144
Roy, R. A., 149, 153
Rutgers, W., 182

S

Saburi, T., 182
Sahni, M., 183
Saint-Martin-Tillet, X. N., 15
Saito, N., 194
Sakiyama, Y., 182–183
Sakugawa, T., 219
Salah-Eddine, A., 9
Salomir, R., 149, 165
Sanders, J. V., 4
Saperato, S., 172
Sarkisov, G. S., 183
Sato, K., 184
Sato, M., 184, 275–276, 187, 194
Sato, N., 275
Satoh, S., 194
Satoshi, I., 182
Schafer, M. E., 143
Schamiloglu, E., 183
Schimmoller, B., 179–180, 227
Schlichting, H., 3
Schmidt, J., 189, 191, 203, 208, 244, 248, 274
Schoenbach, K., 183, 274
Schoenbach, K. H., 183, 192, 201, 274
Schreiber, W. G., 165
Shamamian, V., 275
Shao, D., 149, 164
Shaw, A., 140–141, 143–144, 149, 153–154
Sherar, M. D., 139
Shi, X., 161
Shin, W.-T., 194
Shinder, I. I., 112
Shu, X., 183
Shumeyer, J. N., 10
Sibbet, W., 162
Sikkeland, T., 4
Silakov, V. P., 275
Simek, M., 184, 191, 193, 189, 203, 208, 244, 248, 274
Singer, S., 165
Sinha, S., 167
Sinha, U., 167
Skalny, J. D., 161
Skavlem, S., 4
Skone, T. J., 179–180, 227
Smith, C., 259
Smith, D. N., 165
Smith, W. F., 272
Snizhko, L. O., 182
Snoeyink, V. L., 232, 239, 242–243
Somers, E. B., 275
Somerscales, E. F. C., 228, 258
Sommer, G., 165
Song, C., 162
Sridharan, K., 182
Staack, D., 253
Stacey, M., 183, 274
Stafford, R. J., 173
Starikovskiy, A., 192–193
Stathoulopoulou, A., 258
Stephenson, T., 259
Stiegel, G. J., Jr., 2
Straub, J., 188
Sugai, H., 195
Sugiarto, A., 194
Sugiarto, A. T., 184, 194, 275–276
Sun, B., 18, 275, 187, 248
Sun, H. J., 274, 280
Sunka, P., 182, 184–185, 187–189, 192–193, 203, 208, 244, 248, 274
Suzuki, T., 182
Suzuki, Y., 165
Swanson, R. J., 183

Swift, C., 144
Swift, G. W., 2

T

Tabrizian, M., 277, 280
Takahashi, Y., 195
Takai, O., 194
Takeda, T., 194
Taktakishvili, M. I., 274
Temchin, S. M., 275
Tenma, T., 280
ter Haar, G., 139, 149, 153–154
ter Haar, G. R., 137–139, 140, 142–143
Theobald, P., 144
Thery, P., 228, 242
Thompson, A., 144
Thomsen, C., 165
Tian, X. B., 182, 266
Tijing, L. D., 228, 258–259
Tlili, M., 228, 242
Tokunami, R., 182
Tokutake, T., 184
Tomai, T., 182–183
Touyeras, F., 140
Toyota, H., 195
Tran, T. T. M., 228, 242
Trilling, L., 3, 7
Trushkin, N., 194
Tsouris, C., 194
Tyrer, J., 144
Tyrer, J. R., 144

U

Udol, S., 259
Uhm, H. S., 189
Umchid, S., 144
Ushakov, G. V., 259

V

Vaezy, S., 161
Vagena, N. V., 273
Vainshtein, P., 4–5
van der Laan, P. C. T., 275
van Veldhuizen, E., 182
Vankov, A., 182
Vigen, K., 165
Vo, H., 149, 164, 183
Volenik, K., 182

W

Wagner, H., 110
Wagter, C. D., 165
Wait, I. W., 247
Wakeham, W. A., 250
Wallac, H., 186
Wan, M., 161
Wan, Q., 6–7
Wang, B. L., 259
Wang, C., 259
Wang, L., 182
Wang, T. G., 3
Wang, X., 161, 182
Wang, Z. Q., 144
Wansapura, J., 149
Watanabe, H., 165
Watson, P., 201, 207
Wear, K. A., 150, 155–156
Wei, C. B., 182, 266
Wei, Z., 188
West, G. D., 4
Westervelt, P. J., 4, 16
White, F. M., 206
White, J. A., 183
Wilson, M. P., 219
Witte, D., 149
Wojcik, W., 244
Wolfe, R. L., 280
Wong, A. C. L., 275
Won-Seok, K., 182
Woodworth, J. R., 183, 211
Wright, M. H., 159
Wright, P. E., 159
Wu, J., 149–150
Wu, X., 149, 164
Wu, Y., 182
Wurster, C., 144

X

Xiao, S., 192
Xiaokai, X., 228, 259
Xie, H., 250
Xiong, L., 149, 164
Xu, F., 159

Y

Yacoby, M., 228
Yahia, L. H., 277, 280
Yamabe, C., 194
Yamashita, H., 195
Yamazaki, T., 182
Yamda, Y., 194
Yan, R. L., 138
Yang, S. Q., 182
Yang, Y., 192–193, 196–200, 202, 205–207, 209, 211–213, 216–217, 220–221, 223, 225–227, 229–230, 234–239, 241, 248, 250–256, 257, 259–260, 262–265, 267–269, 270–274, 373
Yano, T., 7, 22, 150
Yasuoka, K., 184
Yerokhin, A. L., 182
Yiacoumi, S., 194
Yong Cheol, H., 182
Yongchang, C., 259
Yoo, H. C., 182
Yu, J., 149, 164
Yu, M., 138
Yuan, W.-K., 194
Yuebing, W., 144
Yukhymenko, V. V., 194

Z

Zadiraka, Y., 274–275
Zadiraka, Y. V., 274
Zahn, M., 205
Zanelli, C. I., 143
Zanstra, G. J., 275
Zappoli, B., 2, 10, 119
Zeqiri, B., 140
Zhai, Z. A., 245
Zhang, D., 149
Zhang, E., 144
Zhang, J., 138,
Zhang, R. B., 182
Zhang, X., 250
Zhang, X.-S., 194
Zhao, G., 201
Zheng, M. J., 138
Zhirkova, N., 194
Zhou, X. D., 138
Zhu, H., 149, 164
Zimmereli, G. A., 11

SUBJECT INDEX

A

Accounting for boiling, cavitation, and nonlinearity, 173
Acoustic absorptivity, calculation of intensity and, 137–40
Acoustically driven cylindrical enclosure, flows in, 33
  experimental apparatus, 33–4
  experimental results, 34–7
    pressure fluctuation, instantaneous, 35
  numerical study, 38–42
    schematic of computational domain, 38
    variation of pressure along axis of enclosure, 39
Acoustically driven enclosure, flows in
  cylindrical enclosure, 33–43
  rectangular enclosure, 16–33
Acoustic Mach number, 7
  classical streaming/irregular streaming, 7
Acoustic Peclet number, 5–6
Acoustic Reynolds number, 30
Acoustic standing waves, formation of, 42
Acoustic streaming, 1, 3, 16, 58–9
  based method, 145–8
  cases considered for analysis, 18
  cycle averaged flow field showing, 50
  differential heating, 51
  effect of compressibility, 4
  end wall oscillation induced, 46
  experiment, 146
  as heat transfer enhancement mechanism, 5
  motion, 33
  non-linear source of, 4
  Reynolds number, 16
  standing wave is formed in resonator, 44
  360^{th} cycle, 51, 57
  120^{th} cycle, isothermal top and bottom walls, 56, 58
Acoustic-viscous boundary layer interactions, 32
Acoustic wave induced flows and heat transfer, 1–3
  experimental study in gases, 88
    apparatus and procedure, 88–92
    results and discussion, 90–110
  experimental study in supercritical fluids, 124–5
    apparatus and procedures, 125–7
    results and discussion, 127–30
  mathematical model, 11–14
  mechanically driven acoustic waves, 3–7
  mechanically driven acoustic waves in
    gas-filled enclosures, 15–16
    flows in cylindrical enclosure, 33–43
    flows in rectangular enclosure, 16–33
    interactions with heat transfer in rectangular chamber, 43–9
  numerical model, 14–15
  numerical study in gases, 59
    in atmospheric and high pressure gases, 59–67
    bottom-wall heated enclosure, 76–88
    side-wall heated enclosures, 68–76
  thermally induced acoustic waves in gases, 7–9
  thermally induced acoustic waves in supercritical fluids, 110–12
    numerical results for supercritical carbon dioxide, 113–24
    thermodynamic properties of supercritical carbon dioxide, 112–13
  thermoacoustic waves in supercritical fluids, 9–11
Acoustic waves
  with charge voltage, variation of unattenuated amplitude of, 99
  in compressible media, generation, 130–1
  effects of capacitance on, 101
  fluid velocities induced by, 2
  generation in compressible media, 1
  thermally induced, in confined medium, 8

Acoustic waves in supercritical fluids, thermally induced, 110–12
  equation of state and thermodynamic properties of supercritical carbon dioxide, 112–13
  numerical results for supercritical carbon dioxide, 113–24
Acoustic waves with heat transfer in rectangular chamber, 43–4
  interaction between acoustic waves and heat transfer, 45–6
  problem geometry, 44–6
    list of cases, 45
    schematic of computational domain, 45
  results and discussion
    effect of enclosure width on Nu, 56
    parametric case studies, 47–58
    validation results, 46–7
  steaming patterns, 56
Aristo-Craft ART-29308 U-25B, 34
Artificial hard water, 263
  amount of $CaCl_2$ and $NaHCO_3$ used in, 263
Atmospheric and high pressure gases, thermally induced acoustic waves in, 59–67
Average mass transport velocity, 18–19
Axis of enclosure, variation of axial velocity along, 40

B

Bottom-wall heated enclosure
  effects of aspect ratio, 84–6
  effects of gravity, 78–82
  effects of heating rate, 82–3
  increasing bottom wall temperature, 78
  list of computational cases, 79
  problem statement, 76–8
  results and discussion, 78
  summary of observations, 77
  variation of pressure, 80, 83, 85
  variation of temperature, 82
  velocity vectors, 80, 81, 84, 85, 86, 87
Boundary conditions, evaluation of, 15
"Boundary layer driven" streaming, 3
Boundary layer streaming, 4
Brüel & Kjær 4193 condenser microphone, 90, 91
Bubble discharges in liquid, 194–5
  electrode geometries for, 195
"Bulk dissipation driven" streaming, 3
Buoyancy induced flows, 87
  interaction of thermally induced acoustic waves with
    effects of aspect ratio, 84–6
    effects of gravity, 78–82
    effects of heating rate, 82–3
    increasing bottom wall temperature, 78
    list of computational cases, 79
    problem statement, 76–8
    results and discussion, 78
    summary of observations, 77
    variation of pressure, 80, 83, 85
    variation of temperature, 82
    velocity vectors, 80, 81, 84, 85, 86, 87
  interactions of thermally induced acoustic waves with, 68–76
    problem statement, 68
    results and discussion, 68–9
    spatially nonuniform gradual heating at zero gravity, 73–4
    spatially nonuniform gradual heating under normal gravity, 74–5
    spatially uniform gradual heating under zero gravity, 71–3
    uniform impulsive heating at zero gravity, 69–71
    variation of pressure and x-component of velocity, 73
    variation of pressure at mid point of enclosure for three grid sizes, 70

C

$CaCO_3$ precipitation, 242
Calorimetry method, 140
Carbon dioxide
  exists as supercritical fluid, 63
  as function of pressure
    variation of density for, 60
    variation of heat conductivity, 62
    variation of internal energy for, 60
    variation of sound speed for, 61
    variation of viscosity, 62
"Charge voltage," 96
Classical acoustic streaming flow patterns, 32
Classical streaming/irregular streaming, 7
Classical streaming patterns, regions, 31
Compressible fluid, speed of sound waves in, 13

Condenser microphone, 89
Conventional electrical breakdown in water, process of, 184–9
Copper–constantan (type T) thermocouples, 260–1
Critical free energy for nucleation, 244
Critical Reynolds number for transition, 31
Cycle-averaged flow field, 46–7, 56
Cycle-averaged temperature
  along vertical plane of enclosure, variation of, 53
  contours, 51, 53, 57
    in 360th cycle, 54, 55
Cycle of concentration (COC), 264–5
  vs. time, variations in, 264
Cylindrical filament, capacitance of, 210

D

Data acquisition system (DAQ), 125
Density, solid wall, 15
Dhanasekaran's theory, 245
Digital particle image velocimetry (DPIV), 145
Dynamics of non-equilibrium plasma in liquid water
  experimental setup, 196
  from nanosecond-duration power supply, 196
  results and discussions, 197–200
  from subnanosecond-duration power supply, 197

E

Eckert streaming, 3
Electrostatic model, 201–207
  bubble formation and, 202
  force balance for, 205
Electrostatic pressure, 213–14
Enclosure, mean flow field in, 23
Endevco 4428A pressure signal conditioner, 33
Endevco 8507C-1 piezoresistive pressure transducer, 33, 90, 91, 95
Energy balance equation for foil, 103
Energy dispersion spectrometer (EDS), 236
Extension of inverse heat transfer method, 173–4

F

Fabricated tissue phantom, 151
FCT algorithm, 124
Fiber-optic hydrophones, 143–4
  Raman spectroscopy images of, 144
FIDAP software, 158
Filament
  disturbance at surface of, 213
  electric conductivity, 203
  radius, variations of, 206, 211
  space outside, 204
Flexible EPDM, 88
Flow field in enclosure, mean, 20, 24, 27, 29
Flux corrected transport (FCT) algorithm, 14, 32
Fouling resistance, 261
Freshwater consumption
  for thermoelectric power generation 2005–2030, 180
  U.S., 181

G

Gases, experimental study of thermally induced acoustic waves in, 88
  apparatus and procedure, 88–92
  capacitance on acoustic wave, 101
  capacitance on temperature response, 100
  capacitance on voltage drop across foil, 100
  charge voltage on pressure, 98
  charge voltage on temporal decay of voltage drop across foil, 97
  estimation of experimental uncertainty, 102
  extrapolation of measured foil temperature, 106
  foil temperature and thermocouple measurements, 105
  maximum voltage drop across foil, 98
  measured and calculated foil temperature, 107
  measured foil voltage and calculated foil temperature, 104
  numerical and experimental results, 103
  pressure ($p - p_{atm}$) measurement, 96
  pressure probes, details of, 90
  pressure waves, 108, 109, 110
  results and discussion, 90–110
  schematic of experimental set up, 89
  specifications for experimental system, 90

Gases, experimental study of thermally induced acoustic waves in, (*Cont.*)
temperature profile for foil, 105
temporal foil temperature, 103
trace of pressure, 94, 95
transient temperature of foil, 93
transient voltage drop across foil, 93
variation of unattenuated amplitude of acoustic wave, 99
variation of unattenuated amplitude of pressure, 101
Gases, numerical study of thermally induced acoustic waves in, 59
in atmospheric and high pressure gases, 59–67
bottom-wall heated enclosure, 76–88
side-wall heated enclosures, 68–76
Gibbs free energy, 243

H

Heat-flux, component of, 112
Heat flux vector, 12
Heating effect of continuous wave ultrasound, 163
Heat transfer coefficient, 261
Heat transfer fouling tests, 259–62
Heat transfer rate, 261
HIFU. *See* High-intensity focused ultrasound (HIFU)
HIFU ablation procedure with thermocouple array, 160
HIFU devices, pre-clinical testing of, 139
HIFU free-field characterization in liquid medium, 140–8
alternate characterization methods
acoustic streaming-based method, 145–8
nonintrusive alternate characterization methods, 144–5
robust hydrophones, 143–4
established characterization methods, 140
calorimetry method, 140
hydrophones, 140–1
limitations, 142
radiation force balance, 141–2
intensity *vs.* axial distance, 148
HIFU heating of continuous wave, 163
HIFU Heat Source, calculation of, 157
HIFU-induced transient temperature profiles, 167
HIFU lesion volume *vs.* sonication time, 171
HIFU thermal field characterization
invasive method, 149–55
direct sonication of thermocouple junction, 149–50
experimental transient temperature profiles, 152
limitations in use of thermocouples, 150–3
localized temperature measurement, 155
measured temperature profile and calculated profile, 154
thermocouple artifacts, 153
noninvasive method, 160–73
diagnostic ultrasound, 161
lesion size measurement, 168–72
magnetic resonance imaging method, 164–5
magnified view of lesion boundary, 170
MRI calibration curve, 166
MRI images of lesions, 169
of MRI scanner for temperature measurement, 166
noninvasive temperature measurement, 165
temperature rise as function of time, 168
thermography method, 162–4
validation of computational models, 172–3
nonperturbing method, 155–60
application specific to HIFU studies, 156
derivation of beam location and angular orientation, 156
heat transfer analysis, application in, 155–6
thermocouples remote from beam, 156
in tissue medium, noninvasive method, 149
HIFU transducer, 147
aligned with tissue sample in MRI machine, 164
HIFU tumor ablation procedure, 138
High-intensity focused ultrasound (HIFU), 137
cell necrosis time for, 137
High-intensity focused ultrasound-induced thermal field, 137–40
accounting for boiling, cavitation, and nonlinearity, 173
calculation of intensity and acoustic absorptivity, 173–4

HIFU free-field characterization in liquid medium, 140–8
HIFU thermal field characterization
invasive method, 149–55
noninvasive method, 160–73
nonperturbing method, 155–60
in tissue medium, 148–9
High-pressure gas, *P*-ρ-*T* relations, 59
Hydrodynamic pressure, 215–18
instability growth rate, 216
Hydrophones, 140–1
limitations, 142

I

Ideal gas, internal energy of, 13
Ideal gas law, 64
"Impulsive heating," 669
"Inner streaming." *See* Schlichting streaming
Inverse heat transfer algorithm, 158

K

Khokhlov–Zabolotskaya–Kuznetsov (KZK) acoustic wave equation, 145
Kirkwood–Bethe model, 224

L

LabView 7.0 software, 92
Laplace transform technique, 7
Linear streaming, 7
Local micro-heating, 256
Loudspeaker powers
driving power 22.4mW, pressure amplitude, 35
91.5mW, peak-to-peak value, 36
RMS value of standing pressure, 36

M

Mathematical model and numerical methods, 11
mathematical model, 11–14
numerical model, 14–15
Mechanically driven acoustic waves, 3–7
in gas-filled enclosures, 15–16
cylindrical enclosure, 33–43
interactions with heat transfer in rectangular chamber, 43–9
rectangular enclosure, 16–33
with heat transfer in rectangular chamber, 43–9
Microsecond streamer propagation, analysis of, 200–201
electrostatic model, 201–207
stability analysis, 212–18
thermal mechanism, 209–12
Mineral fouling mitigation in heat exchangers, application for, 258–9
experiment setup, 259–64
amount of $CaCl_2$ and $NaHCO_3$ used in artificial hard water, 263
artificial hard water, 253
heat transfer fouling tests, 259–62
heat transfer test section, 260
no-treatment/plasma treatment cases scales, 267
pulsed spark discharge generation system, 262–3
schematic diagram, 260
SEM and XRD measurements, 264
results and discussion, 264–72
cycle of concentration (COC), 264–5
fouling resistance, 265–70
scanning electron microscope images, 270–2
x-ray diffraction tests, 272–4
XRD analyses of scales, 273

N

Nanosecond-duration discharge in water, 198
dynamics of, 198, 199
Navier-Stokes equations, 6, 7, 8
in 2-D Cartesian coordinate system, 32
generation/propagation in supercritical carbon dioxide, 111
simulating flow field, 44
Nelder–Mead scheme, 159
multidimensional optimization algorithm, 145–6
NIST standard reference database 12, 59, 64, 69, 111, 112, 127
Nonintrusive alternate characterization methods, 144–5
Nonlinear sound fields, irregular flow structure for, 28

Non-thermal effect of plasma, 252–5
Normalized maximum wall displacement and enclosure aspect ratio, function of, 32
Normalized pressure amplitude at resonance *vs.* dimensionless parameter, 31
Numerical study of thermally induced acoustic waves in gases, 59
  interactions with buoyancy induced flows, 68–76
  interaction with buoyancy induced flows, 76–88
  thermally induced acoustic waves in atmospheric and high pressure gases, 59–67
Nusselt number, 5–6

O

Oscillatory flow field
  in enclosure, 26
  maximum velocity in, 31
Oscillatory flow velocities, maximum, 30
Oscillatory velocity, maximum, 20
"Outer streaming." *See* Rayleigh streaming

P

Perfect gas, state for, 12
Perturbation method, 6
Perturbation, surface of, 213
Physical water treatment (PWT), 228
Piezoelectric ceramic hydrophone, 141
Piezoresistive pressure transducer, 33, 89
Piston effect, 10–11, 118
Plasma-assisted calcium carbonate precipitation, 227–9
  double spark-gap configuration, 253
  experiment setup, 229–33
    chemical compositions of water samples, 230
    energy deposited into spark discharge, 231
    laboratory cooling tower, 229
    pulsed power and water circulation system, 230
    pulsed spark discharge generation system, 229–32
    spark discharge in water, 231
    water preparation, 229
  mechanism study, 241–58
    calcium carbonate hardness reduction *vs.* input energy, 251
    effect of micro heating, 249–52
    effect of reactive species, 248–9
    effect of UV radiation, 247–8
    modified discharge chamber, 248
    non-thermal effect of plasma, 252–5
    possible mechanisms, 241–6
    SEM images, 252
  results, 233–41
    effect of immediate plasma exposure, 233–40
    effect of spray circulation, 233–41, 240
    elemental composition of particles, 238
    results obtained by laser particle counting, 236
    SEM images of calcium carbonate crystals, 238
    variations of $CaCO_3$ hardness/pH value, 241
  SEM image of calcium carbonate particles, 256
  variations of calcium carbonate hardness and pH, 254
  variations of hardness over time with and without plasma treatment, 234
  water treatment, 232–3
Plasma discharge in water
  analysis of microsecond streamer propagation, 200–201
    electrostatic model, 201–207
    stability analysis, 212–18
    thermal mechanism, 209–12
  application for mineral fouling mitigation in heat exchangers, 258–9
    experiment setup, 259–64
    results and discussion, 264–72
    x-ray diffraction tests, 272–4
  application for water sterilization, 274
    plasma-assisted water sterilization, 274–6
    plasma-induced UV radiation on sterilization, 277–82
    test methods, 276–7
  discharges generated using wire–cylinder geometry, 192
  dynamics of non-equilibrium plasma in liquid water
    experimental setup, 196
    results and discussions, 197–200

final remarks, 282
images of, 186
through pinhole, 191
multichannel pulsed electrical discharge in water, 193
needs for plasma water treatment, 179–82
oxidation potential of active species produced by, 187
plasma-assisted calcium carbonate precipitation, 227–9
experiment setup, 229–33
mechanism study, 241–58
results, 233–41
previous studies on plasma water treatment, 182–4
process of conventional electrical breakdown in water, 184–9
pulsed multichannel discharge array, 193
scale removal on filter membranes, 218–19
experiment setup, 219–22
results and discussion, 222–7
underwater plasma sources
bubble discharges in liquid, 194–5
direct discharges in liquid, 190–3
Plasma-filled filaments, propagation of, 203
Plasma water treatment
needs for, 179–82
cooling water management, 179–81
water sterilization, 181–2
previous studies on, 182–4
Polytetrafluoroethylene (PTFE) cylinder, 232
Polyvinylidene fluoride (PVDF) hydrophones, 140
Pressure along horizontal mid-plane of enclosure, variation of, 49
Pressure along symmetry axis of enclosure, variation of, 22
Pressure amplitude in enclosure, 17f
Pressure fluctuation, instantaneous, 35, 37
computed, at $3L/4$ for different left wall vibration amplitudes, 41
frequency spectra of, 38
Pressure profiles, 24
variation of pressure along symmetry axis of enclosure, 25
Pulsed arc, 186
characteristics of, 186
Pulsed corona, 186
characteristics of, 186
Pulsed power system, 220, 221
pulsed discharge in water, 221
Pulsed spark discharge generation system, 229–32, 262–3
discharge chamber and electric circuit, 262

R

Radial electric field, 204
Radiation force balance, 141–2
Rayleigh streaming, 3
and Couette flow, 4
vs. irregular streaming flow pattern, 25
Reaction rate coefficient, 244
Resistance-capacitance (R-C) circuit, 88, 124
Resonator, compression driver with mounted, 34
flow visualization experiments in, 34
formation of streaming vortices observed in, 37
in symmetric computational domain, mean flow field in, 42
RF-excited discharges in argon bubbles, 194–5
RMS value of standing pressure wave, 41
comparison of, 43
Robust hydrophones, 143–4

S

Scanning electron microscopy (SEM), 264
Schlichting streaming, 3
Side-wall heated enclosures, thermally induced acoustic waves, 68–76
problem statement, 68
results and discussion, 68–9
spatially nonuniform gradual heating at zero gravity, 73–4
spatially nonuniform gradual heating under normal gravity, 74–5
spatially uniform gradual heating under zero gravity, 71–3
uniform impulsive heating at zero gravity, 69–71
variation of pressure and x-component of velocity, 73
variation of pressure at mid point of enclosure, 70
Silicon-controlled rectifier (SCR), 124
Silver adhesive, 91

Spark discharge for scale removal on filter membranes, 218–19
energy deposited into spark discharge, 222
energy transferred to acoustic energy, 219
experiment setup, 219–22
pressure drop across filter membrane, 227
pressure drop at different flow rates, 223
pressure drop under repeated pulsed spark discharges, 225, 226
results and discussion, 222–7
spark discharge, 222
testing loop, 220
Spatially nonuniform gradual heating
geometry and boundary conditions of problem, 69
under normal gravity, 74–5
at zero gravity, 73–4
Spatially uniform gradual heating under zero gravity, 71–3
Spectra-Physics 120S Helium-Neon 15mW laser system, 34
Steady acoustic streaming, 40
Steady second-order acoustic streaming, 58
Steady streaming flow field, 49
Streamer propagation, 206
Streamer, variations of Mach number of, 207, 212
Streaming, 44
Streaming fields, forms of, 31
Streaming Reynolds number, 22
Streaming structure, results, 30
Streaming velocities, 19–20
along vertical-plane, *y*-component, 52
comparison of transverse distribution of *y*-component, 48
effect of temperature difference on, 50
maximum, 20
non-dimensional, 21
variation along semi-height of enclosure, 21
Streaming velocity components, 51
Streaming velocity contour, 146
Streaming vortices, formation of, 37
Streamlines, 51
Stress component, 112
Subnanosecond-duration discharge development for different voltages, 200
Supercritical fluids, 9
carbon dioxide exists as, 63
P-ρ-T relations, 59
thermally induced
acoustic waves in, 110–30
thermoacoustic waves in, 9–11
Supercritical fluids, experimental study of thermally induced acoustic waves in, 124–5
comparison of numerical and experimental results, 129
experimental apparatus and procedures, 125–7
experimental results and discussion, 127–30
generating thermally induced acoustic waves, 125–7
schematic of experimental tubing system, 126
temporal variation of foil temperature, 128
temporal variation of pressure, 128, 129
Supercritical fluids, thermally induced acoustic waves in, 110–12
bulk viscosity of carbon dioxide, 115
experimental and computational temporal variations of pressure, 130
internal energy for carbon dioxide, 114
numerical and experimental results, 129
numerical results for supercritical carbon dioxide, 113–24
parametric results, 116
thermally induced acoustic (pressure) wave profiles, 116
pressure for carbon dioxide as function of temperature and density, 113
schematic of problem geometry, 111
spatial variations of temperature, 120, 121, 123, 124
spatial variations of temperature waves, 117
temporal variation of left wall temperature, 115
temporal variations of pressure, 118
at center point, 119, 121, 122, 123
thermal diffusivity for carbon dioxide, 114
thermodynamic properties of supercritical carbon dioxide, 112–13
Surface tension, 214–15
Suspended solid contents in water, 236

T

Temporal foil temperature, 103
Thermal-acoustic interactions, 2
Thermal-dose parameter, 172
Thermally induced acoustic (pressure) wave profiles, 116

Thermally induced acoustic waves in atmospheric and high pressure gases
effect of initial pressure, 67
geometry and boundary conditions of problem, 63
list of computational cases, 64
problem statements, 61–3
property variations, 59–61
results and discussions, 63–7
temperature, 63
variation of pressure with time at mid point of enclosure, 65, 66
at different heating rates, 66
for different initial pressures, 67
Thermally induced acoustic waves in gases, 7–9
experimental study of. *See* Gases, experimental study of thermally induced acoustic waves in
numerical study of. *See* Gases, numerical study of thermally induced acoustic waves in
Thermally induced acoustic waves in supercritical fluids, 124–5
experimental study. *See* Supercritical fluids, experimental study of thermally induced acoustic waves in
See also Supercritical fluids, thermally induced acoustic waves in
Thermally induced pressure waves, 3
Thermal mechanism, 209–12
force balance for thermal model, 209
Thermoacoustic engine, 2
Thermoacoustic refrigerator, 2
Thermoacoustic waves in supercritical fluids, 9–11
Thermo-chemical data of reactions, 239
Thermocouple artifacts, 153
Thermocouple junction, direct sonication of, 149–50
Time-averaged flow fields, 40
Time evolution of left wall pressure at mid-point, 23, 28
Tissue damage via ultrasound, 137
Tissue-mimicking material/tissue phantom, 157
Tissue temperature rise, calculation, 158
Transient hot-wire method, 250
Transport velocity, average mass, 40
Transverse distribution of x-component streaming velocity, comparison of, 47
Two-dimensional cylindrical coordinates, conservation equations in, 11–14

U

Ultrasound surgery system, image-guided 256-element phased-array focused, 161, 162
Underwater plasma sources
bubble discharges in liquid, 194–5
direct discharges in liquid, 190–3
electrode geometries used for plasma discharges in liquid, 190
Uniform impulsive heating at zero gravity, 69–71
U.S. freshwater withdrawal, 180
US Geological Survey's (USGS), 179

V

Velocity vectors, 70
at four different times, 75, 76
at two different times, 72, 74
variation of pressure and x-component of velocity, 71
x-component of velocity with time, 72
Vibrating boundary, 17
Vibrating wall, displacement of, 39
Viscous dissipation, 12
Viscous dissipation rate, 12

W

Water sterilization, application for, 274
plasma-induced UV radiation on sterilization, 277–82
previous studies on plasma-assisted water sterilization, 274–6
test methods, 276–7

X

X-ray diffraction (XRD) measurements, 264
XRD pattern of calcium carbonate crystals, 239